Direct search for dark matter with the DarkSide-20k experiment

Marie van Uffelen

Aix*Marseille université
Socialement engagée

NNT : 2024AIXM0263

THÈSE DE DOCTORAT

Soutenue à Aix-Marseille Université
le 26 Septembre 2024 par

Marie van Uffelen

Direct search for dark matter with the DarkSide-20k experiment

Discipline
Physique et Sciences de la Matière

Spécialité
Physique des Particules et Astroparticules

École doctorale
ED352: Physique et Sciences de la Matière

Laboratoire/Partenaires de recherche
Centre de Physique des Particules de Marseille, Aix-Marseille Université - CNRS/IN2P3
Laboratoire d'Astrophysique de Marseille, Aix-Marseille Université - CNRS/INSU

Composition du jury

Corinne Augier Professeure des Universités, IP2I	Rapporteure
Fabrice Hubaut DR CNRS, CPPM	Directeur de thèse
Eric Kajfasz DR CNRS, CPPM	Président du jury
Julien Lavalle DR CNRS, LUPM	Examinateur
Julien Masbou Maître de Conférences, Subatech	Rapporteur
Jocelyn Monroe Professor, University of Oxford	Examinatrice
Emmanuel Nezri CR CNRS, LAM	Co-directeur de thèse

Institut Physique de l'Univers
Aix*Marseille Université

LAM
LABORATOIRE D'ASTROPHYSIQUE DE MARSEILLE

CENTRE DE PHYSIQUE DES PARTICULES DE MARSEILLE
CPPM

Affidavit

Je soussignée, Marie van Uffelen, déclare par la présente que le travail présenté dans ce manuscrit est mon propre travail, réalisé sous la direction scientifique de Fabrice Hubaut et Emmanuel Nezri, dans le respect des principes d'honnêteté, d'intégrité et de responsabilité inhérents à la mission de recherche. Les travaux de recherche et la rédaction de ce manuscrit ont été réalisés dans le respect à la fois de la charte nationale de déontologie des métiers de la recherche et de la charte d'Aix-Marseille Université relative à la lutte contre le plagiat.

Ce travail n'a pas été précédemment soumis en France ou à l'étranger dans une version identique ou similaire à un organisme examinateur.

Fait à Marseille le 26 Juin 2024

Liste de publications et participation aux conférences

Liste des publications réalisées dans le cadre du projet de thèse:

1. DarkSide-20k collaboration, « DarkSide-20k sensitivity to light dark matter particles », submitted to Nature Communications (2024). arXiv: 2407.05813 [hep-ex].

2. Marie van Uffelen « The simulation of the DarkSide-20k calibration ». In : 57th Rencontres de Moriond on Electroweak Interactions and Unified Theories. Nov. 2023. arXiv: 2311.07437 [hep-ex].

3. Marie van Uffelen « The calibration of a direct search for dark matter experiment: the TPC of DarkSide-20k ». JRJC 2022 - Journées de Rencontres Jeunes Chercheurs. Book of Proceedings. 2023. hal: 04118967.

Participation aux conférences et écoles d'été au cours de la période de thèse:

1. 15^{th} international workshop on the Identification of Dark Matter (IDM), 2024, L'Aquila, Italy.

2. 57^{th} Rencontres de Moriond - Electroweak Interactions & Unified Theories, 2023, La Thuile, Italy.

3. Journées de Rencontres Jeunes Chercheurs, 2022, Saint Jean de Monts, France.

4. IN2P3 School of Statistics, 2022, Carry-le-Rouet, France.

Résumé

La nature de la matière noire reste un mystère de la physique fondamentale. Un modèle, motivé par la cosmologie et la physique des particules, fait l'hypothèse de l'existence d'une particule dont les propriétés répondent aux conditions pour être de la matière noire. Cette particule s'appelle Particule Massive qui Interagit Faiblement (notée WIMP), elle est la particule de matière noire la plus recherchée depuis des décennies par plusieurs générations d'expériences qui ont déjà exclu une grande partie de l'espace des phases. La prochaine expérience qui recherchera le WIMP en utilisant une Chambre à Projection Temporelle double phase fonctionnant avec de l'argon s'appelle DarkSide-20k, actuellement en construction. DarkSide-20k utilisera 50 tonnes d'argon liquide de basse radioactivité dans la partie la plus centrale de son volume de détection. Dans le contexte de la préparation de DarkSide-20k à la prise de données, les premières simulations de la calibration du détecteur avec des sources externes ont été effectuées, ainsi que des tests instrumentaux du système de calibration conduits avec des maquettes. Cela a permis de valider la conception et de prouver la faisabilité du système de calibration externe. En outre, la sensibilité attendue de DarkSide-20k aux WIMPs de basse masse ($< 10\,\mathrm{GeV/c^2}$), ainsi qu'à d'autres candidats de matière noire de faible masse, a été évaluée pour la première fois. Par rapport aux actuels résultats d'autres expériences, une amélioration de sensibilité de plus d'un ordre de grandeur est attendue après seulement un an de prise de données. Comme le signal dépend de la modélisation du halo de matière noire de la Voie Lactée, l'impact des incertitudes astrophysiques sur les sensibilités de DarkSide-20k aux WIMPs de haute et basse masses a été quantifié.

Mots clés : Détection directe de Matière Noire, Physique des détecteurs, Simulations, Phénoménologie

Abstract

The very nature of dark matter is still a critical question mark in fundamental physics. A paradigm, driven by both cosmology and particle physics, hypothesises the existence of a Weakly Interacting Massive Particle, which fulfils the requirements to be a dark matter candidate. To date, the Weakly Interacting Massive Particle is the most seeked for dark matter candidate, with a large phase space already excluded by several generations of experiments. The next generation argon dual-phase Time Projection Chamber, called DarkSide-20k, is under construction. It will employ 50 tons of low radioactivity liquid argon in its most central detection volume. In the context of preparing DarkSide-20k before operation, the first simulations of the detector calibration using external sources as well as hardware tests with mock-ups have been performed. They validate the design and prove the feasibility of the external calibration system. Besides, the sensitivity of DarkSide-20k to low mass Weakly Interacting Massive Particles ($< 10\,\mathrm{GeV/c^2}$) and other light dark matter candidates has been assessed for the first time. One expects more than one order of magnitude sensitivity improvement with respect to previous research results to a wide range of dark matter models, already with one year of data. As the signal spectrum depends on the modelling of the Milky Way dark matter halo, the impact of the astrophysical uncertainties on the sensitivity of DarkSide-20k to high and low mass Weakly Interacting Massive Particles has been quantified.

Keywords: Dark matter direct detection, Detector physics, Simulations, Phenomenology

Synthèse en Français

Plusieurs observations indépendantes de notre Univers à différentes échelles montrent qu'il doit exister une forme de matière dont on voit les effets gravitationnels mais dont on ignore l'origine et la nature [1, 2, 4]. On appelle cette matière "matière noire", car elle n'interagit pas électromagnétiquement. Presque un siècle après le premier soupçon de son existence, la matière noire n'a toujours pas été détectée directement. La solution est envisagée sous la forme d'une ou plusieurs particules hypothétiques qui interagissent très faiblement avec la matière décrite par le Modèle Standard de la physique des particules. Pour répondre aux observations, ces particules doivent avoir une masse, être neutres au regard des interactions fortes et électromagnétiques, être stables (ou avoir une durée de vie supérieure à l'âge de l'Univers) et être "froides", c'est-à-dire être non-relativistes. Dans ce contexte, plusieurs particules émergeant naturellement de modèles au-delà du Modèle Standard de la physique des particules satisfont les critères pour être de la matière noire. L'une des particules hypothétiques les plus plébiscitées jusqu'alors est le WIMP (en anglais Weakly Interacting Massive Particule : Particule Massive qui Interagit Faiblement). En effet, cette particule émerge naturellement de modèles de mécanisme de production de matière dans l'Univers primordial, et dans les bonnes proportions pour concorder avec les observations astrophysiques actuelles. Cela s'appelle le miracle du WIMP. Le WIMP est cherché dans toute la gamme de masse entre $\approx 1\,\mathrm{GeV/c^2}$ et $> 1\,\mathrm{TeV/c^2}$.

Depuis le début des années 2000, plusieurs expériences terrestres ont été construites pour rechercher une interaction directe entre le WIMP et les nucléons composant les noyaux des atomes des détecteurs. Afin de se protéger du bruit de fond provenant de l'Univers (produits de désintégration des rayons cosmiques), différentes expériences de recherche directe de WIMP sont mises en service sous terre. Ces expériences se consacrent à la réduction du bruit de fond d'origine radiogénique (rayons X et γ, particules $\beta^{\pm}$, particules α, neutrons) grâce à des choix méticuleux de matériaux. Parmi les expériences de recherche directe de WIMP, la technologie la plus prometteuse est celle des Chambres à Projection Temporelles double phase (TPC). Cette technologie utilise un élément noble (xenon ou argon), principalement liquéfié, avec en addition une couche de gaz. Les informations clés permettant d'identifier les interactions à l'interieur du détecteur sont fournies grâce à la collection d'électrons d'ionisation et de photons de scintillation : interaction simple ou multiple, énergie déposée et position (en trois dimensions). Ces infomations permettent de discriminer le bruit de fond (toutes les interactions régies par le Modèle Standard de la physique des particules) et le signal (interaction entre un WIMP et un noyau). À l'heure actuelle, les TPCs les plus sensibles à la recherche de WIMP au-dessus de $3.6\,\mathrm{GeV/c^2}$ sont celles qui utilisent du xenon [35, 37, 36]. Entre

1.2 $\mathrm{GeV/c^2}$ et 3.6 $\mathrm{GeV/c^2}$, c'est la plus grande TPC double phase utilisant de l'argon construite à ce jour qui mène la recherche de WIMP, DarkSide-50.

La prochaine TPC double phase utilisant de l'argon est DarkSide-20k, actuellement en construction au Laboratoire National du Gran Sasso en Italie. DarkSide-20k aura une masse active de 50 tonnes –environ 1.000 fois plus que DarkSide-50– et de 20 tonnes dans le volume central de recherche de WIMP, appelé volume fiduciel. Un détecteur de 32 tonnes servant de veto actif à neutrons englobe la TPC, lui même installé au cœur d'un cryostat cubique de 8.5 m de haut. La présente thèse est focalisée sur la préparation de DarkSide-20k, de la simulation de sa calibration à l'évaluation de ses performances futures dans la recherche de matière noire de faible masse. Enfin, cette thèse étudie la dépendence de la sensibilité de DarkSide-20k aux WIMPs de haute et basse masse à la modélisation du halo galactique de matière noire.

La calibration de DarkSide-20k

Avant toute prise de données physiques, une expérience doit calibrer son détecteur afin de mesurer avec précision sa réponse en énergie et en position, de vérifier son uniformité et sa stabilité, et de les corriger a posteriori le cas échéant. La calibration dite "externe" de DarkSide-20k, qui utilise des sources radioactives de longue durée de vie et de haute activité, est un défi à cause de la taille de l'expérience : il faut acheminer une source au cœur de l'expérience, dans un cryostat de 8.5 m de haut, et l'approcher suffisamment proche de la TPC pour rendre la calibration efficace. La solution optée par DarkSide-20k est de faire circuler des sources radioactives dans deux tubes qui les guident autour de la TPC, à l'interieur du veto et qui sortent par le toit du cryostat. Ces sources sont attachées à une corde contrôlée par deux moteurs synchrones par tube situés sur le cryostat (un par sortie de tube). Elles sont de deux types : productrices de neutrons (pour imiter le signal WIMP qui interagit avec le noyau de l'argon), et productrices de photons (pour imiter le bruit de fond). Dans cette thèse, deux sources de neutrons (AmBe et AmC) et cinq sources de photons (^{57}Co, ^{133}Ba, ^{22}Na, ^{137}Cs et ^{60}Co) ont été envisagées pour la calibration de DarkSide-20k.

Le but de ce travail était de préparer cette calibration externe. Premièrement, en simulant les interactions entre les neutrons (recul nucléaire, NR) et photons (recul électronique, ER) émis par les sources externes et l'argon de la TPC de DarkSide-20k. Un exemple de spectre en énergie qu'on obtiendrait suite à la calibration NR et ER est montré sur la Figure 1 gauche et droite, respectivement. Dans ces spectres, les événements particulièrement intéressants pour la calibration sont les interactions uniques (histogrammes rouges), labellisés "single scatters", car ils imitent un signal de matière noire. En prenant en compte la saturation du système d'acquisition de données par les événements non intéressants pour la calibration (histogramme bleu) ainsi que le taux d'événements intéressants, l'activité optimale de chaque source de calibration a pu être calculée et par conséquent le temps nécessaire pour atteindre 10.000 événements intéressants pour la calibration. Ces deux informations sont présentées dans la Table 1.

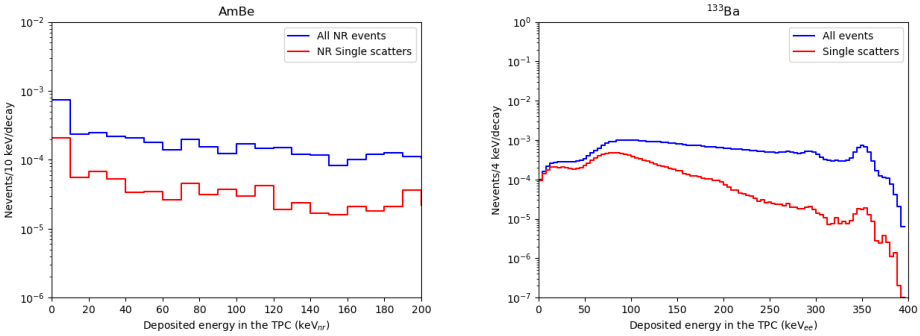

FIGURE 1. : Spectres en énergie resultant de la simulation de l'exposition de la TPC à une source de neutron (AmBe, gauche) et de photons (^{133}Ba, droite) placées sur le côté de la TPC. La résolution en énergie attendue de DarkSide-20k est prise en compte. Les histogrammes bleus représentent la proportion d'événements simulés qui interagissent dans la TPC, les rouges sont les événements utiles à la calibration (interactions uniques).

Source	AmBe	AmC	^{57}Co	^{133}Ba	^{22}Na	^{137}Cs	^{60}Co
Energie initiale (keV)	[0.2, 12].10^3	[2, 7].10^3	122	356	511	662	1173
Activité (côté) (kBq)	0,14	0,15	18	1,9	0,36	2,2	0,36
Activité (dessous) (kBq)	0,18	0,18	100	5,0	0,67	4,6	0,6
Temps par position (côté)	19 h	28 h	3,7 min	6,6 min	10,8 min	9 min	12,6 min
Temps par position (dessous)	23 h	25 h	3,8 min	5,9 min	9 min	7,8 min	10,8 min
Durée de calibration	8 j	10 j	4,2 h	4,6 h	5,2 h	5,0 h	5,4 h

TABLE 1. : Activité optimale et temps de calibration correspondant nécessaire pour atteindre 10.000 interactions simples (un unique NR pour la calibration utilisant des neutrons et un unique ER pour celle utilisant des photons), pour les deux sources de neutrons (AmBe et AmC) et les cinq sources de photons (^{57}Co, ^{133}Ba, ^{22}Na, ^{137}Cs et ^{60}Co) considérées pour la calibration externe de DarkSide-20k.

La calibration externe devrait être complétée en environ un mois de prise de données.

Ce travail a également démontré que la présence du système de calibration à l'interieur du veto et très proche de la TPC va introduire un bruit de fond radioactif négligeable et ne va pas altérer la collection de la lumière de scintillation dans le veto.

Deuxièmement, la faisabilité de la calibration a été prouvée par des tests techniques mettant à l'épreuve le système de calibration dans divers contextes expérimentaux (à température cryogénique, avec une géométrie de tubes proches de la réalité, pour une durée de tests au delà des besoins finaux), en utilisant à chaque fois des maquettes spécifiques pour le besoin du test. Un exemple de maquette est montré sur la Figure 2 gauche. Un exemple de la stabilité du fonctionnement du système motorisé (à travers la mesure de la tension appliquée sur la corde pour mettre une pseudo source en mouvement dans un tube) est montré sur la Figure 2 droite.

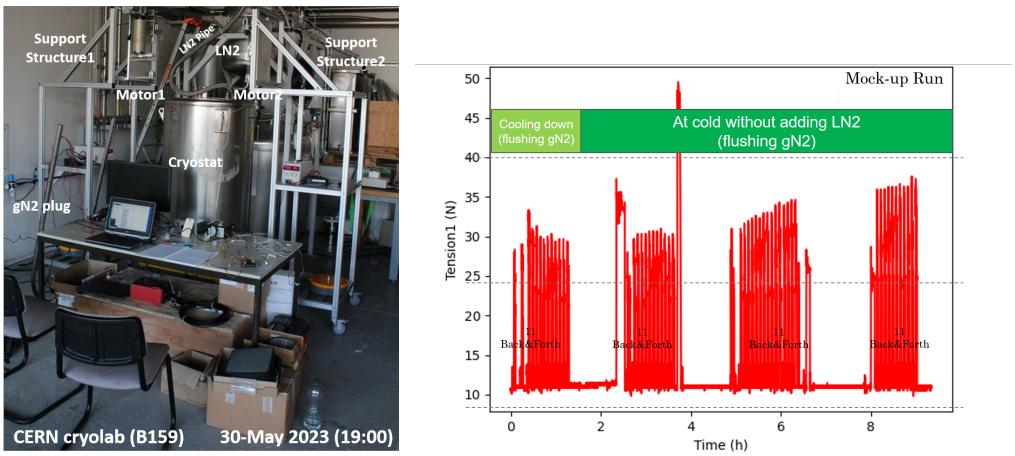

FIGURE 2. : Gauche : Photo de l'équipement de tests du système de calibration installé au CERN. Droite : Mesure typique de la tension appliquée sur la corde pour mettre une pseudo-source en mouvement lors d'un test du système de calibration.

En somme, ce travail a prouvé la faisabilité de la calibration externe, tant sa portée scientifique grâce à des simulations que sa faisabilité technique grâce à des tests utilisant des maquettes du système final.

Sensibilité de DarkSide-20k aux particules de matière noire de basse masse

Les TPC double phase ont pour premier objectif de détecter une interaction directe entre des WIMPs de "haute" masse ($M_\chi \geq 10\,\mathrm{GeV/c^2}$) et un noyau d'argon grâce à la collection de photons de scintillation et d'électrons d'ionisation. Cependant, comme prouvé par DarkSide-50, la recherche de WIMP peut s'étendre à plus basse masse (entre $O(1\,\mathrm{GeV/c^2})$ et $10\,\mathrm{GeV/c^2}$) grâce aux dépôts de basse énergie, au prix d'une recherche dominée par le bruit de fond ER à modéliser. En effet, en dessous de $\lesssim 1\,\mathrm{keV_{er}}$ ou $\lesssim 5\,\mathrm{keV_{NR}}$, le signal de scintillation n'est plus détecté, et seul le signal d'ionisation est utilisé. Cela empêche la discrimination entre signal NR et bruit de fond ER. Le modèle est donc une prédiction du nombre d'électrons N_{e^-} collectés suite à une interaction entre une source de bruit de fond et l'argon du détecteur.

Pour estimer la sensibilité de DarkSide-20k à la recherche de WIMPs de basse masse, la réponse du détecteur a été modélisée et les différentes contributions de bruit de fond ER ont été évaluées. Le modèle complet est montré sur la Figure 3 gauche, il est composé de :

1. Bruit de fond interne, réparti dans tout le volume interne de la TPC, provenant de la désintégration des composants radioactifs ^{39}Ar et ^{85}Kr. Le niveau de radioactivité du premier est supposé égal à celui de DarkSide-50 (0.73 mBq/kg) alors que

celui du deuxième est supposé réduit d'un facteur 100 par rapport à DarkSide-50 (18.6 μBq/kg). Les spectres de désintégration β des deux composants proviennent de calculs théoriques récents. Des systématiques de morphologie des spectres en énergie de ces radio-contaminants sont propagées sur les spectres d'ionisation. Ces erreurs proviennent de l'effet d'écrantage des électrons de l'atome, des effets d'échanges atomiques, de la chaleur de réaction Q et de la réponse du détecteur aux ionisations d'origine ER. Une erreur supplémentaire est attribuée à la normalisation de ces deux composantes. Le bruit de fond ^{39}Ar domine le modèle total pour $N_{e^-} \geq 4$.

2. Bruit de fond externe, provenant des rayons X et γ produits par les matériaux du détecteur interne (photo-détecteurs de la TPC et du veto, "PDMs", structure de la TPC, "TPC", contenant du détecteur interne, "vessel"). Les spectres d'ionisation resultent de simulations d'interactions entre ces photons et le détecteur. Le niveau de radio-activité de chaque composant est estimé grâce à des campagnes dédiées de mesure de radio-contamination. L'erreur sur les spectres N_{e^-} provient de la normalisation des différents composants et de la réponse du détecteur aux ionisations d'origine ER. Les trois composantes de ce bruit de fond sont visibles sur la Figure 3 gauche, dominé par les PDMs, puis la TPC et enfin le contenant du détecteur interne, négligeable.

3. Le bruit de fond provenant d'"électrons parasites". Ce bruit de fond a été observé dans DarkSide-50, mais non modélisé. Cette composante est constituée de quelques électrons d'ionisation, provenant possiblement d'électrons qui ont été piégés par des impuretés présentes dans le volume du détecteur puis relâchés ensuite. Dans DarkSide-50, cette composante était dominante pour $N_{e^-} < 4$. Pour pouvoir descendre la région d'interêt à $N_{e^-} \geq 2$ dans l'analyse de DarkSide-20k, le bruit de fond parasite a été extrapolé à partir des mesures de DarkSide-50. L'extrapolation prend en compte le comportement de ce bruit de fond, à la fois en morphologie N_{e^-} et temporelle. Des erreurs d'extrapolation sur la morphologie du bruit de fond et sur sa normalisation sont prises en compte dans l'étude. Comme visible sur la Figure 3 gauche, ce bruit de fond domine pour $N_{e^-} < 4$. À $N_{e^-} = 4$, il est 18 fois plus faible que le bruit de fond dû à l'argon.

4. Le bruit de fond neutrinos, provenant à la fois des neutrinos solaires et atmosphériques et interagissant avec le noyau (CEνNS, Diffusion élastique cohérente entre le neutrino et le noyau) ou les électrons (ν-ES, Diffusion élastique entre neutrino et électron) de l'argon, a été modélisé. Ce bruit de fond est entre deux et quatre ordres de grandeur sous le niveau du bruit de fond ^{39}Ar, comme en atteste la Figure 3 gauche. Une erreur sur la normalisation du flux est prise en compte ainsi qu'une systématique sur la réponse du détecteur (NR pour CEνNS, ER pour ν-ES).

Grâce à la modélisation du bruit de fond parasite (point 3) extrapôlé à partir des données de DarkSide-50, la région d'interêt a pu être étendue jusqu'à $N_{e^-} = 2$. Cependant, ce travail a montré que la sensibilité de DarkSide-20k est plus robuste vis à vis de la modélisation du bruit de fond parasite si l'ajustement du modèle est fait à partir de

$N_{e^-} = 4$ (au prix d'une sensibilité plus faible). Le signal WIMP est simulé à partir du modèle du halo standard, un exemple de spectre de ionisation attendu pour un WIMP de masse 2 GeV/c^2 et de section efficace d'interaction avec un nucléon de $\sigma_{SI} = 3.10^{-44}$ cm^2 est montré sur la Figure 3 gauche. Le signal est confiné à bas N_{e^-}, typiquement en dessous de 30 electrons. Afin de mieux contraindre le bruit de fond, les spectres d'ionisation sont simulés jusqu'à $N_{e^-} = 170$.

Le modèle est alors ajusté sur les pseudo-données, définies comme la somme des valeurs centrales des bruits de fond. Cette procédure donne lieu à l'estimation de la sensibilité de DarkSide-20k aux sections efficaces d'interaction entre un WIMP de masse entre 0.8 GeV/c^2 et 10 GeV/c^2 et un nucléon d'argon, ici montrée comme limite d'exclusion du signal à 90% de niveau de confiance. La Figure 3 droite montre la sensibilité de DarkSide-20k à des WIMPs de basse masse, après une année complète de prise de données, dans les deux scenarios d'ajustement de données : ajustement à partir de $N_{e^-} = 2$ (sensibilité ultime) ou à partir de $N_{e^-} = 4$ (sensibilité robuste). Cette sensibilité est comparée à celle d'autres expériences dans ce domaine de masse. DarkSide-20k améliorera l'espace de phases recherché d'au moins un ordre de grandeur, et dominera la recherche de WIMPs entre 800 MeV/c^2 et ≈ 5 GeV/c^2.
Il a été montré que cette sensibilité dépend faiblement de la modélisation de la réponse du détecteur. La principale source d'amélioration ou de dégradation de la sensibilité de DarkSide-20k viendrait respectivement d'un niveau de bruit de fond interne plus faible pour l'argon (car c'est actuellement le bruit de fond dominant) et d'une résolution de collecte d'un unique électron dégradée d'un facteur 2.

En utilisant le potentiel "effet Migdal", un effet atomique qui prédit la libération d'un électron lors d'un NR, il est possible de rechercher une interaction entre un WIMP de masse ≤ 1 GeV/c^2 et un noyau d'argon via la collecte de la composante ER. La sensibilité de DarkSide-20k dans ce paradigme est montrée sur la Figure 4 en haut à gauche pour un an de prise de données. DarkSide-20k devrait mener la recherche de WIMP entre 40 MeV/c^2 et ≈ 5 GeV/c^2.
Avec le même modèle de bruit de fond de basse énergie, il est possible d'étendre la portée de DarkSide-20k à d'autres candidats de matière noire de basse masse interagissant avec les électrons, comme les Axion-Like-Particles (ALPs), le photon sombre (Dark Photon, DP), le neutrino stérile ou la matière noire légère (Light Dark Matter, LDM). Ce dernier candidat diffuse élastiquement sur les électrons de l'argon via un médiateur qui peut être léger ou lourd. La sensibilité de DarkSide-20k à ces cinq modèles est montrée sur la Figure 4 gauche milieu et bas pour LDM, respectivement médiateur lourd et léger. La Figure 4 droite haut montre la sensibilité aux ALPs ; milieu, la sensibilté aux DP ; et basse, aux neutrinos stériles.
Pour tous ces candidats, DarkSide-20k améliorera d'au moins un ordre de grandeur l'espace des phases de recherche directe sur une certaine gamme en masse après un an de prise de données. Pour le neutrino stérile, l'espace des phases investigué par DarkSide-20k et les autres détecteurs directs est déjà exclu par des expériences de recherche indirecte [94].

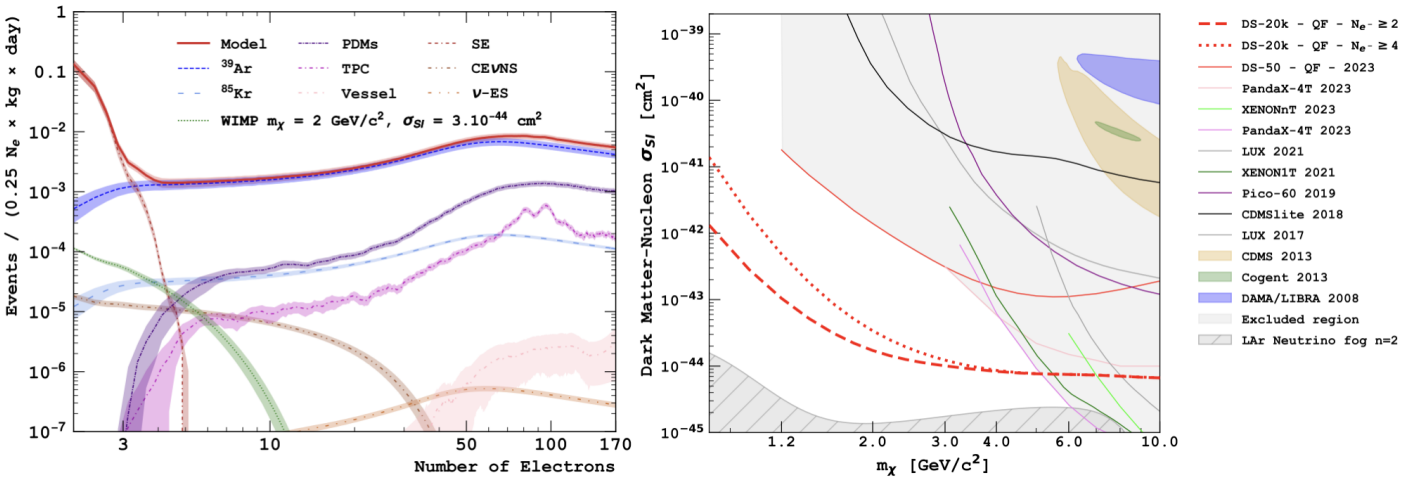

FIGURE 3. : Gauche : Modèle de signal WIMP (de masse $M_\chi = 2\,\mathrm{GeV/c^2}$ et de section efficace d'interaction de $\sigma_{SI} = 3.10^{-44}$ cm^2) et de bruits de fond. Droite : Sensibilité de DarkSide-20k au WIMP de masse entre $0.8\,\mathrm{GeV/c^2}$ et $10\,\mathrm{GeV/c^2}$, pour deux stratégies d'ajustement ($N_{e^-} \geq 2$ en tirets, $N_{e^-} \geq 4$ en pointillés), comparée aux limites d'exclusion à 90% de niveau de confiance de diverses expériences [56, 75, 104, 105, 106, 110, 111, 112, 113].

En conclusion, cette étude pionnière a permis de renforcer le potentiel de découverte de DarkSide-20k, en évaluant sa sensibilité aux particules de matière noire de basse masse.

Impact de la modélisation du halo de matière noire sur la sensibilité de DarkSide-20k

Dans les figures de résumé de recherche directe de matière noire qui montrent les limites hautes sur la section efficace d'interaction entre un WIMP et un nucléon, le taux de signal WIMP à un point donné de l'espace des phases est calculé dans un cadre théorique particulier : le Modèle du Halo Standard (Standard Halo Model, SHM). Ce modèle fait désormais référence dans l'estimation du taux de signal dans le domaine de recherche directe de WIMPs [40]. Il décrit le halo de matière noire de la Voie Lactée de manière simpliste, pratique pour estimer l'ordre de grandeur du taux de signal attendu et permettre aux expériences de se comparer entre elles, mais peu réaliste physiquement. Le SHM décrit la distribution de vitesse et la densité massique de matière noire au voisinage du système solaire. Dans le SHM, chaque composante de la vitesse d'une particule de matière noire du halo galactique est distribuée selon une gaussienne, centrée en zéro et de largeur v_0, décrivant un système isotherme, ce qui manque de réalisme. Un tel modèle induit une distribution de vitesse (en norme) décrite par une maxwellienne, forcée de manière ad-hoc à zéro au delà de la vitesse d'échappement au niveau du système solaire v_{esc}. En outre, pour estimer le taux d'événements attendus dans une expérience de recherche de matière noire, cette distribution de vitesse doit être tranformée pour être décrite dans

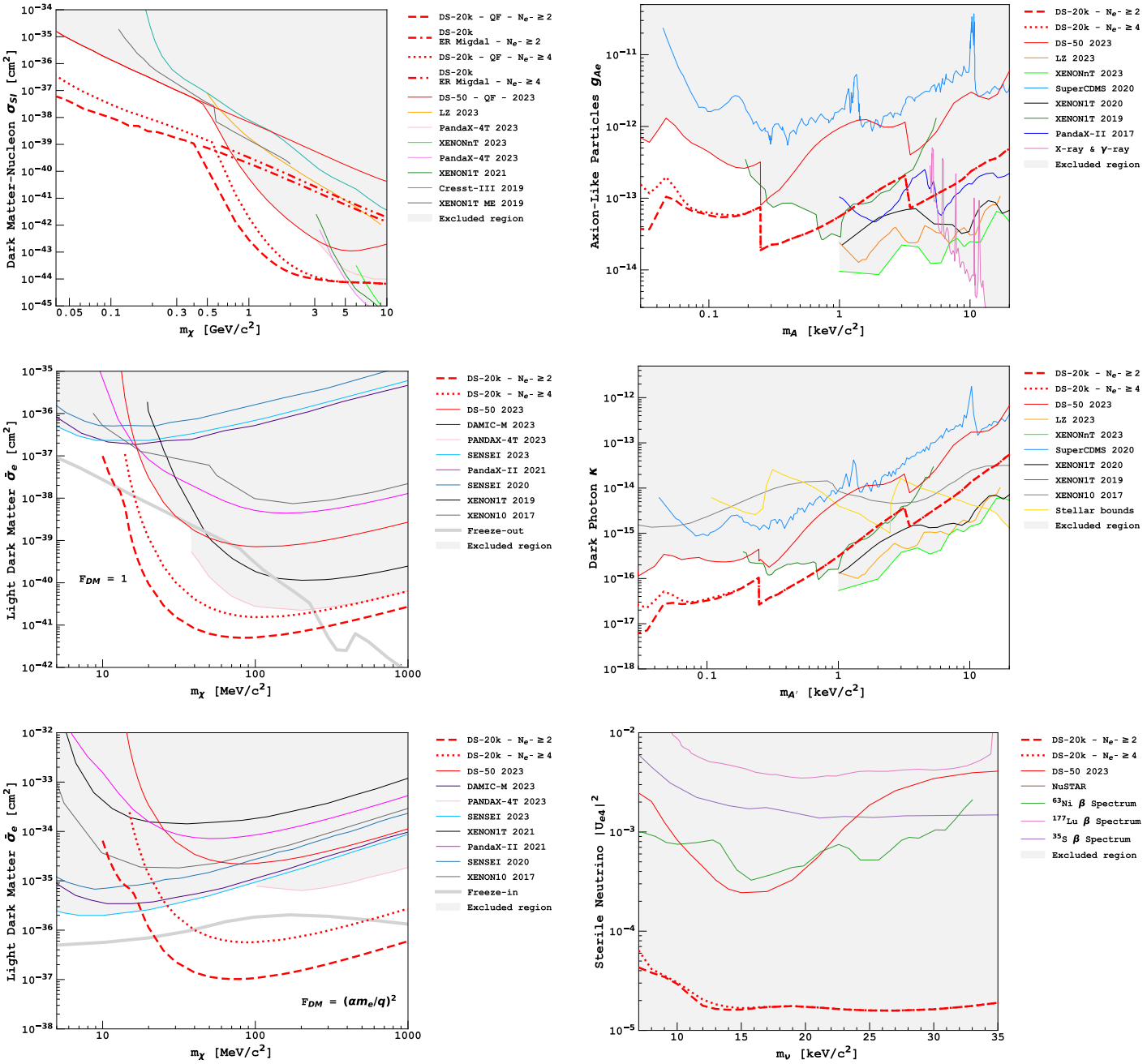

FIGURE 4. : Sensibilité de DarkSide-20k à différents modèles de signal, avec deux différentes stratégies d'ajustement : à partir de 2 N_{e^-} (courbes en pointillés) ou à partir de 4 N_{e^-} (courbes en tirets). Gauche : Matière noire de masse dans la gamme MeV/c^2-GeV/c^2 (Haut : WIMP léger utilisant l'effet Migdal, milieu et bas : matière noire légère leptophilique, dont le recul électronique est véhiculé par un médiateur lourd (milieu) ou léger (bas)). Droite : Autres candidats légers de masse autour du keV/c^2 (haut : ALP, milieu : photon sombre, bas : neutrino stérile). La sensibilité de DarkSide-20k est comparée aux limites d'exclusion à 90% de niveau de confiance d'autres expériences recherchant ces mêmes candidats [32, 57, 75, 89, 90, 104, 105, 106, 119, 122, 123, 124, 125, 120, 126, 127].

le référentiel terrestre. Cela nécessite l'utilisation de la vitesse du Soleil sur son orbite circulaire v_c. Le taux d'événements attendus dans une expérience est normalisé par la densité massique de matière noire au niveau du Soleil, ρ_0. Ces quatre paramètres qui permettent de décrire l'environnement galactique dans lequel se trouvent les expériences de recherche de matière noire sont estimés indépendamment les uns des autres, alors que la dynamique du système devrait être prise en compte pour les corréler les uns aux autres, ainsi qu'à la distribution de masse (et donc au modèle de distribution de vitesse) du système.

Les valeurs de ces quatre paramètres sont : $\rho_0 = 0.3\,(\mathrm{GeV/c^2})/\mathrm{cm^3}$, $v_c = v_0 = 238\,\mathrm{km/s}$ et $v_{esc} = 544\,\mathrm{km/s}$. [43].

Afin d'estimer l'erreur induite sur l'estimation du taux de signal et en conséquences sur l'évaluation de la sensibilité de DarkSide-20k à observer de la matière noire de haute et basse masse, trois méthodes ont été adoptées dans cette thèse :

A Estimer l'incertitude provenant de l'erreur induite par chaque paramètre astrophysique indépendamment, en faisant varier ces paramètres un à un dans leur gamme de mesure dans le cadre du SHM. Cette méthode est une première approche naïve ;

B Estimer l'incertitude provenant de l'erreur induite par l'ensemble des paramètres astrophysiques, en utilisant des ensembles contraints d'estimation de ces quatre paramètres dans le cadre du SHM ;

C Estimer l'incertitude provenant de l'erreur induite par la distribution maxwellienne de vitesse de matière noire dans le halo galactique, en considérant à la place des distributions de vitesse modélisées par des simulations cosmologiques à N corps.

La bande d'incertitude telle qu'estimée par chacune des trois méthodes sur la sensibilité de DarkSide-20k dans le régime de basse masse ($800\,\mathrm{MeV/c^2} < M_\chi < 10\,\mathrm{GeV/c^2}$) est montrée sur la Figure 5.

L'incertitude sur la sensibilité telle qu'estimée avec la méthode A est dominée par l'effet de ρ_0, directement proportionnel au taux d'événements de signal attendus dans une expérience de matière noire. Les effets des vitesses sur la sensibilité de l'expérience sont faibles et principalement localisés à basse masse de WIMP, près du seuil en énergie. L'incertitude combinée des quatre paramètres propagée sur la sensibilité de DarkSide-20k est montrée sous forme de bande rouge sur la Figure 5 gauche, labellisée "Independent variation of parameters".

Une deuxième bande d'incertitude, estimée par la méthode B, est montrée en vert sur la Figure 5 gauche et labellisée "Dependent variation of parameters". L'estimation cohérente des quatre paramètres astrophysiques donne dans deux cas sur trois une estimation de ρ_0 plus faible que $0.3\ \mathrm{GeV/c^2/cm^3}$ et induit donc une estimation plus conservative de la sensibilité de DarkSide-20k que lorsqu'elle est calculée avec le SHM. Une troisième estimation donne lieu à une valeur de ρ_0 élevée, donc une sensibilité plus optimiste que celle calculée avec le SHM.

Enfin, la troisième bande d'incertitude (jaune) de la Figure 5 droite, labellisée "N-body simulations", a été estimée grâce à la méthode C, en prenant le résultat de simulations

cosmologiques à N corps (incluant matière noire et baryons) comme distribution de vitesse pour le calcul du signal. Les simulations cosmologiques ne permettant pas de prédire la densité locale de matière noire, cette approche permet de tirer des conclusions qualitatives sur l'utilisation d'une Maxwellienne comme distribution de vitesse. Seule la sensibilité aux WIMPs de plus basse masse est impactée car ρ_0 est gardé à sa valeur nominale : seule la distribution de vitesse est affectée par cette méthode.

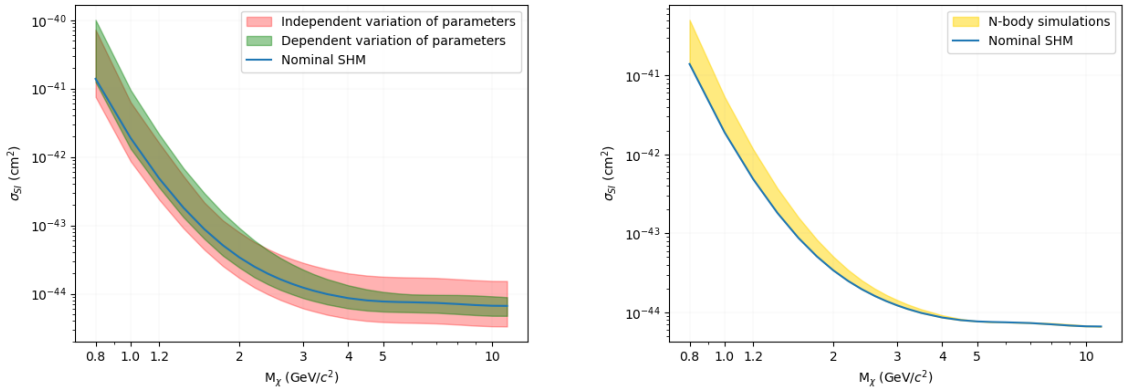

FIGURE 5. : Sensibilité de DarkSide-20k à basse masse exprimée sous forme de limite d'exclusion à 90% de niveau de confiance, utilisant le SHM pour le modèle de halo de matière noire (courbe bleue pleine). Les incertitudes systématiques, montrées sous forme de bandes autour de cette limite, proviennent du manque de connaissances sur le halo de matière noire de la Voie Lactée (voir texte). Elles sont estimées dans trois cas : à gauche : la variation des quatre paramètres astrophysiques (indépendante : bande rouge, cohérente : bande verte) et à droite : utilisation de deux halos simulés (bande jaune).

Conclusions

Ce travail s'inscrit dans le contexte de la préparation de DarkSide-20k à la prise de données physiques à partir de 2027.

En premier lieu, il a démontré la faisabilité de la calibration de la TPC de DarkSide-20k, d'un point de vue physique et technique. Un mois sera nécessaire pour calibrer la plus grande TPC jamais contruite dans le but de chercher de la matière noire. Puis, la sensibilité de DarkSide-20k à la recherche de WIMPs de basse masse a été déterminée pour la première fois. La sensibilité de l'expérience à des particules de matière noire leptophiliques a également été calculée grâce aux mêmes modèles de détecteur et de bruit de fond. Quel que soit le candidat recherché, DarkSide-20k devrait pouvoir investiguer plus d'un ordre de grandeur de chacun des espaces de phase non encore exploré, après seulement un an de prise de données. Enfin, l'incertitude sur la sensibilité de DarkSide-20k à basse masse de WIMPs, provenant de la modélisation du halo galactique de matière noire a été évaluée. Elle est principalement confinée dans les gammes de basse masse de chaque régime, près du seuil de détection de l'expérience.

Remerciements

I would like to thank all the people who helped me achieving this work, in a scientific or human way, during my three years as a PhD student.

First, I would like to thank my jury, chaired by Eric Kajfasz, who accepted to review my work : many thanks to Julien Masbou and Corinne Augier, my rapporteurs, who gave relevant and important feedbacks on the content of the manuscript, as well as Jocelyn Monroe and Julien Lavalle for accepting to be my reviewers and attending the defense in person.

I would also like to thank my PhD advisors : Emmanuel Nezri and Fabrice Hubaut, for the support provided during these three years working together. In particular, I would like to address the most sincere thanks to Fabrice for all the help, motivation and knowledge you gave me during my time being your student, I am deeply grateful for that and for all the work we did together.

Beyond Fabrice, my collegues at CPPM and beyond were of great help and support : thanks to Pascal Pralavorio, Emmanuel Le Guirriec and Davide Franco for all the discussions we had to improve my work and my skills as a speaker. Of course, many thanks to Isabelle Wingerter-Seez and Pierre Barillon for all the fun moments during the calibration tests, as well as the personal attention you showed me.

De toute évidence, mes ami.e.s et ma famille ont été d'un soutien indispensable pour me permettre de mener à bien ces dernières années d'étude.

Tout d'abord, un grand merci à mes amis du labo, les thésards : Jeannot, Gaya, Artich, Luluc, Maxou, Grode, Vince et Tyannou, que j'élargie évidemment à doudou, juju et HichHich, pour votre soutien sans faille au quotidien. Merci pour les pauses cafés, les lundis sham, les mardi papamousse et toutes nos autres soirées signatures. Ces années à Marseille auraient de toutes façons été cools mais vous les avez rendues extraordinaires. Je suis infiniment fière de vous compter parmi mes ami.e.s.

Je me dois aussi de remercier mes amies de toujours, mes Quiches –Tropi, Vio, Chlo, Khelef, Plou, Lolympe, Glo et Jazou– pour votre présence au quotidien malgré notre éloignement physique. Je remercie également mes deux amies adorées qui forment avec moi un trio de choc : Vio (encore toi, oui) et Maïwennou. Toutes, à l'autre bout de la France comme à l'autre bout du Monde, vous avez toujours été mes pilliers et ça ne va pas s'arrêter maintenant. Merci pour ces 15 ans d'amitié, et pour les nombreuses autres années à venir, je vous aime mes stars.

Il y aurait énormément d'autres ami.e.s à remercier, comme Lisou, Tross, Mathilde, Maxence, les autres thésards, canouche et bien d'autres. Merci merci merci.

Enfin, merci infiniment à ma famille, mes parents, grand-parents et mes soeurs. Vous avez toujours témoigné de la fierté et du soutien dont j'ai besoin en temps que petite dernière. Merci pour tout. Pour finir, mon dernier merci revient à mes deux grand-pères qui sont très certainement la raison pour laquelle j'ai fini docteure.

Table of Contents

Introduction

Dark matter is one of the biggest puzzles that physics is currently facing. The measurement of the mass of the same luminous object but with different methods leads to a striking finding : telescopes are blind to most of the Universe matter. This statement is further supported by the spectral shape of the Cosmic Microwave Background that permits to estimate that 85% of the mass content of the Universe is unknown. This dark form of matter escapes direct detection since almost a century. The solution is envisaged to be under the form of one or a set of particles. The latter are at least interacting via gravitation but hopefully also interacting –very feebly– with Standard Model matter. Among the different hypothetical dark matter particles, the one on which most attention was driven in the last decades is the Weakly Interacting Massive Particle (WIMP). It is indeed very well motivated theoretically as it naturally emerges from beyond the Standard Model theories and from simple cosmology predictions of dark matter production. It has driven a race of experiments around the world to directly detect WIMP interactions in sensitive terrestrial detectors. Up to now, experiments have been able to exclude a large accessible parameter space. To achieve so, they rely on detection features with large signal-background separation power and put strong efforts in reducing the background sources that could hide the faint signal. Next generation experiments are expected to keep investigating the un-probed parameter space, down to lower masses and down to the so-called neutrino floor. This is allowed thanks to technological improvements at the same time as further backgrounds reduction and dramatical exposure increase. A typical example is the DarkSide-20k experiment.

DarkSide-20k is the next generation experiment of the Global Argon Dark Matter Collaboration. It will search for dark matter with a dual-phase Time Projection Chamber (TPC) by employing at its heart 50 tons of purified argon at liquid phase for its considerable signal-background separation power. DarkSide-20k will be the result of merging technologies employed by previous argon experiments : the O(50 kg) dual-phase TPC DarkSide-50 (and other smaller ones, ArDM and miniCLEAN) and the O(3.6 tons) single-phase experiment DEAP3600. From DarkSide-50 to DarkSide-20k, the full volume is multiplied by a factor $\approx$ 1,000, the material contamination is expected to be reduced by a factor $\approx$ 10 per unit mass, and the photo-detection technology will improve from Photo-Multiplier Tubes to Silicium Photo-Multipliers. DarkSide-20k –that is introduced in Chapter 2– is currently under construction phase at Laboratori Nazionali del Gran Sasso, Italy. Science data collection should start in 2027 and last for a decade, reaching 200 ton $\times$ year exposure.

The primary objective of this thesis work is the preparation of DarkSide-20k, with

instrumental, experimental and phenomenological contributions. In that regard, I was responsible for the first simulation work of the calibration of the DarkSide-20k TPC using external sources, to validate the design of the proposed system. It encompasses several aspects, from its physics reach to the evaluation of its adverse impact on the inner detector performances. In addition, I took part, throughout the whole thesis period, in all the hardware tests of the external calibration system to prove its feasibility. These instrumental and experimental contributions are developed in Chapter 3. As DarkSide-20k is primarily designed to search for high mass WIMPs ($> 10\,\mathrm{GeV/c^2}$), its sensitivity at low mass ($< 10\,\mathrm{GeV/c^2}$) had never been computed, even though DarkSide-50 leads the search in the [$1.2\,\mathrm{GeV/c^2}$, $3.6\,\mathrm{GeV/c^2}$] mass range. Hence, this work was dedicated to the very first assessment of the DarkSide-20k sensitivity to low mass WIMPs and to a variety of other light dark matter particles. The analysis, based on ionisation signals, and its results are reported in Chapter 4. The sensitivity of a dark matter experiment depends on the signal modelling, itself driven by the theoretical predictions for the Milky Way dark matter halo. This dependency has been quantified in this work, leading to the estimate of the astrophysical systematic uncertainties of DarkSide-20k sensitivities to high mass and low mass WIMPs. This phenomenological work is presented in Chapter 5.

1. The Dark Matter problem

Summary

Astrophysical observations lead since the 1930s are consistent with the existence of an unseen component in the Universe, called dark matter. It is estimated to represent 85 % of the mass of the Universe and 27 % of its energy content.
The suspicion of the existence of dark matter as we think of it nowadays is mainly driven by inconsistencies between some astrophysical measurements and the related theoretical predictions. These inconsistencies will be described in the first section of the present chapter.

Since then, the dark matter paradigm became a pillar of modern cosmology, and cosmologists proposed some production mechanisms of dark matter. Yet, its properties remain unknown to date. Section 1.2 describes the different possibilities for dark matter, with a special focus on particles candidates. Indeed, particle physicists develop models that can imply the existence of new kind of particles that are massive, neutral and stable (or very long lived), which fit the astrophysical observations to be dark matter candidates. One of these particles is the WIMP, Weakly Interacting Massive Particle, on which this thesis is focused.
Dark matter search is at the heart of physics of the two infinities, with particle physics expected to solve problems seen at astrophysical and cosmological scales. For now, dark matter still has to be detected. The most flagship candidates are more and more searched for via different techniques : around colliders, by doing indirect measurements of its interaction products looking at dense astrophysical objects, or by designing dedicated terrestrial experiments that intend to measure a direct interaction of dark matter with standard matter. Section 1.3 will focus in particular on the latter technique as this thesis has been conducted within the DarkSide collaboration, currently building the DarkSide-20k detector (see Chapter 2).

1.1. Main evidences for Dark Matter

The motion of most astrophysical objects, from stellar velocity in galaxies to galaxy motion in galaxy clusters, is expected to behave according to Newtonian dynamics. The so-called baryonic mass (that is actually the summed mass from the contribution of all matter of the Standard Model of particles, not only baryons) of these astrophysical objects can be inferred from their luminosity. From 1932, several astrophysical observations at different scales showed a discrepancy between Newtonian predictions and measurements of astrophysical objects motion. All these observations lead to the hypothesis of the existence of an unseen massive component in the Universe, hence called dark matter. The goal of this section is to briefly introduce the problem of the mass discrepancy problem thanks to a set of astrophysical measurements.

1.1.1. First hints for dark matter

First suspicion The first idea of the existence of dark matter in its modern concept followed a measurement by Oort in 1932 [1]. Oort was a Dutch astronomer studying stars motion in the Milky Way. From his measurement, he found that one third of the mass of

the Milky Way was bright enough to be visible. In his definition of dark matter, both un-luminous, not-bright-enough stars and gaseous components were included, though. His idea of dark matter is not exactly the one of today, and more importantly, he expected a low proportion of dark matter in the Milky Way, but he was the first to talk about a dark component in our own galaxy.

First striking evidence One year after Oort, in 1933, Zwicky observed an un-expected behaviour of individual galaxies in the so-called Coma cluster of galaxies [2]. By measuring the line-of-sight velocity of different galaxies of the Coma cluster, he noticed they were moving too fast compared to the amount of bright matter seen in the cluster, thus they should escape the cluster. He then estimated the mass of the cluster, not by measuring its luminosity (typical way to measure the baryonic content of an astrophysical object), but by applying classical Newtonian mechanics to the cluster using the Virial theorem ($M = RV^2/G$, where M, R and V are respectively the mass, the characteristic radius and the velocity spread of the system and G is the gravitational constant). From this method, he estimated the dark content of the cluster to be several hundreds of times higher than the luminous one. It is the first assumption of the existence of dark matter in extra-galactic objects. Since 1933, other galaxy clusters were studied, and the same conclusion was obtained : a mass-to-light ratio of more than two orders of magnitude is measured.

1.1.2. Dark matter evidences on a galactic scale

After Zwicky's measurement of individual galaxies motion in clusters of galaxies, three possibilities for the dark matter location can be thought of :

- the dark matter can be located in the cluster. More precisely, the mass of the galaxies are well estimated and dark matter would be intergalactic matter ;
- the dark matter is a full-fledged component of individual galaxies, and the mass of the galaxies are wrongly measured using only their luminous component ;
- a mix of the two approaches.

Independent measurements of the velocity rotation curve of several galaxies, i.e. the velocity of tracers [1] vs their radial position in galaxies, have been conducted in the last century. In 1939, Babcock measured the rotation curve of the Andromeda galaxy up to 24 kpc from its center. Above a certain threshold radial position in the galaxy, he observed a constant circular velocity while a Keplerian decline ($v_c = \sqrt{\frac{GM(r)}{r}} \propto 1/\sqrt{r}$ outside the baryonic disk) is expected from Newtonian dynamics considering the purely baryonic mass distribution. Even though Babcock didn't consider the dark matter hypothesis to explain this phenomenon, the problem of stars velocity was raised on galactic scales.

[1] tracers can be stars, 21 cm Hydrogen line, Nebulae or interstellar gas.

With the increase of the computing power, first N-body simulations of the Milky Way were done in the 1970s. The simulations confirm that the baryonic mass of the Milky Way alone cannot bind galaxies together when stars have velocities of the order of their measured ones (the kinetic pressure overcomes the gravitational potential) [3]. However, by adding a dark halo to the galaxy (increasing its mass), Peebles and Ostriker could stabilise the galaxy, which suggests that real galaxies should have a dark matter halo.

In turn, Rubin and Ford became interested in measuring the rotation curve of the Andromeda galaxy, taking Nebulae as tracers, and observed a flatten rotation curve. Their analysis lead to the conclusion that there might be a dark matter halo surrounding Andromeda [4]. Since then, a lot of independent measurements asserted the necessity to have a dark matter halo in spiral galaxies such as the Milky Way [3].

Rotations curves measurements can be fitted by different matter components and one can infer some halo properties from the fit. Figure 1.1 shows such a fit of the Milky Way data as taken by the recent GAIA survey (data release number 3 [5]) and analysed by Ref. [6]. The rotation curve is measured and interpreted as the sum of a baryonic matter component (blue dashed line, divided into four sub-categories : bulge, disk, dust and gas) and a dark matter component (red dashed line). In this work, the model used to fit the dark matter halo is the Einasto profile as it is motivated by various studies of structures formation [7, 8] :

$$\rho(r) = \rho_0 \quad exp\left[-\left(\frac{r}{h}\right)^{1/n}\right], \tag{1.1}$$

where $\rho(r)$ is the dark matter mass density vs radius r, ρ_0 is the characteristic dark matter density, h is a scale radius and n accounts for the shape of the density profile, determining how fast the density decreases with the radius r. The best fit values by Ref. [6] are $n = 0.43$, h=11.41 kpc, and $\rho_0 = 0.019\,92\,\mathrm{M}_\odot\mathrm{pc}^{-3}$.

1.1.3. Gravitational lensing

According to the General Relativity, massive objects –producing a gravitational field– can deflect the light and become lenses [9]. Depending on the configuration [2], it will lead to strong lensing or weak lensing. In the case of strong lensing, the image of the background galaxy is repeated in the sky, spread around the lens, like in Figure 1.2 left. Thanks to the image properties, this method gives estimates of the gravitational mass of the lens that are consistent with other methods such as the Virial theorem. In weak lensing, the image will only be distorted, as in Figure 1.2 right, allowing to map the matter distribution. Last, there also exists microlensing which consists of temporary brightening of the background object due to the lens. One can use these effects to probe the existence of a dark matter object, by measuring the mass of the lens thanks to its gravitational effect and compare the measurement to the lens luminosity, which relates

[2]The configuration can be lens-object distance or their alignment.

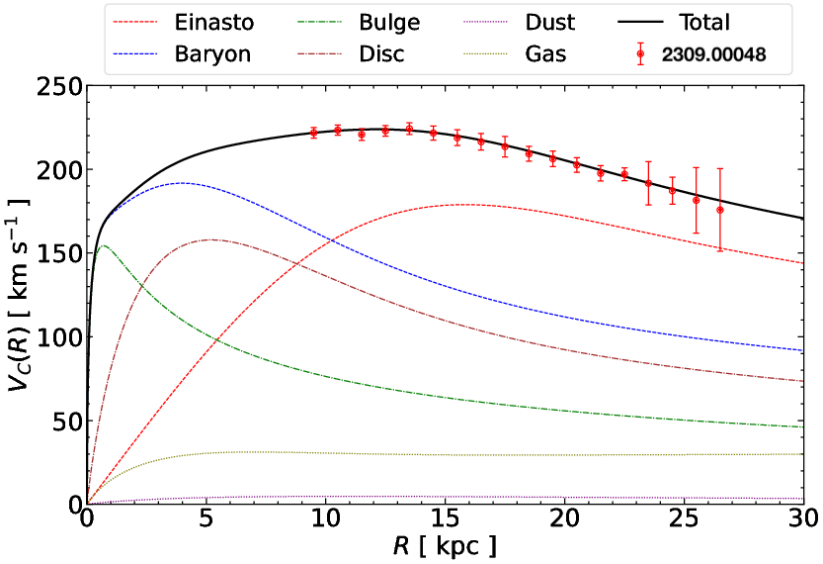

FIGURE 1.1. : Circular velocity of the Milky Way as observed by recent GAIA survey (data release 3) and analysed by Ref. [6]. The red data points are GAIA measurements, with error bars from statistics and systematics. The dashed lines are the components of the fitted model, containing baryonic matter (bulge, disc, gas and dust) and a Einasto dark matter halo (red dashed line). The solid black line is the sum of the fitted model. The figure is adapted from [6].

to its baryonic mass. An example of the evidence of dark matter presence inferred from this technique is showed in the next subsection. The use of microlensing is discussed in Section 1.2.

1.1.4. The Bullet cluster of galaxies

The so-called Bullet cluster is actually a collision of two clusters of galaxies. Figure 1.3 shows a view of the collision of the two clusters, observed with two different techniques. First, in pink, one can see the matter in the cluster as measured by X-rays (collisioning baryonic mass from interstellar gas, thus hot and producing photons). Second, in blue, one can see the total matter distribution as measured with weak gravitational lensing. The discrepancy of the center of mass of the clusters from two measurements of the same astrophysical object gives evidence that all the mass of the cluster is not from baryonic matter. Observations lead to the conclusion that the two matter components were separated during the collision, the baryonic components of each cluster –with high interaction rate– interact, are heated and slowed down, while the two dark matter components crossed each other without interacting [10]. This discovery is of peculiar importance for the dark matter paradigm as such observation cannot be explained by alternative theories of gravitation [9]. In addition to the evidence of the existence of dark matter, one can conclude that the dark components are dominant and collisionless.

FIGURE 1.2. : Left : Example of the effect of strong lensing as observed in telescopes. Here, the alignment is so good that the background object almost forms a perfect Einstein ring (Credits : NASA/ESA/Acknowledgement : Judy Schmidt). Right : Example of the effect of weak lensing, showing background galaxies behind the Abell 370 cluster of galaxies as seen by the Hubble telescope (Credits : NASA, ESA, and J. Lotz and the HFF Team (STScI)). One can see the distortion of the picture, characteristic of weak lensing.

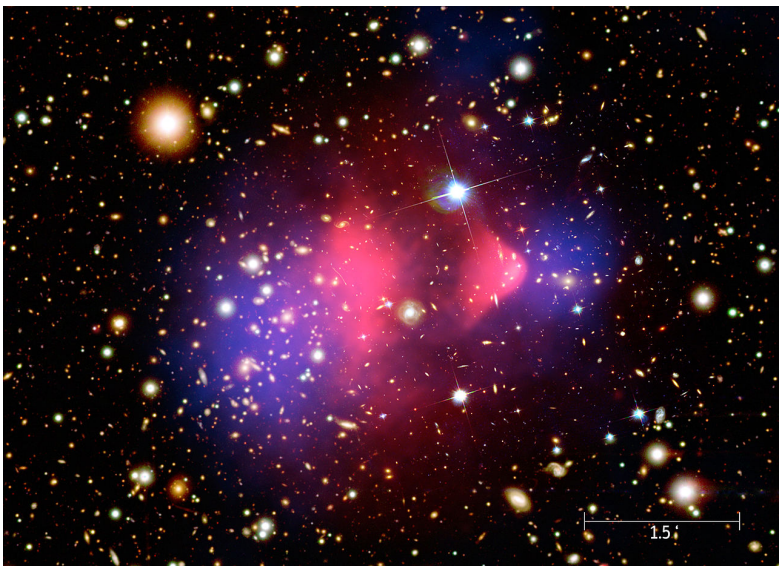

FIGURE 1.3. : Picture of the Bullet Cluster as seen with X-rays (pink mass distribution) and gravitational lensing (blue mass distribution). (Credits : NASA/CXC/M. Weiss)

1.1.5. Cosmological hints for dark matter

At its early stage, the Universe was a hot and dense plasma of matter and radiation, as inferred from observational evidences of an expanding Universe. At that time in the primordial Universe, nucleosynthesis was prevented by high energy photons that interacted with charge particles and prevented recombination. The plasma is opaque to photons which hence could not travel freely in the Universe.

With the expansion of the Universe (following a sudden and extreme accelerated expansion phase called inflation), the temperature decreased as well as the photons energy. Ionised matter (electrons and protons) could recombine and photons travel through our Universe : it is called recombination. These primordial photons travelling from the early times of the Universe are called the Cosmic Microwave Background (CMB), their time of emission is measured to be 380,000 years after the Big Bang [11]. The CMB acts as a snapshot of the density fluctuations of the Universe at that time. COBE, WMAP and PLANCK missions measured the CMB, the most recent measurement by PLANCK is shown in Figure 1.4 left [11]. It is mostly a black body spectrum with temperature T = 2.73 K (this low temperature is caused by the expansion of the Universe since emission). Although almost perfectly homogeneous in all directions, the CMB displays some small fluctuation features ($\frac{\delta T}{T}$ of the order of 10^{-3} - 10^{-5}) that testify of small density fluctuations at the time of radiation decoupling. By gravitational attraction, these fluctuations grew into the structures that we see today in the Universe. To achieve so, a type of matter needed to be non-relativistic before the recombination time in order to let gravitational wells form into density fluctuations, without interacting with photons (this kind of matter decoupled from photons earlier than the baryons). After the recombination, these wells allowed matter to cluster and form structures at different scales (dwarf galaxies, galaxies, galaxy clusters) by trapping baryons into these wells. These hierarchical scenarios of structures formation in the Universe could not be possible without this form of collisionless matter, that is dark matter.

By fitting the power spectrum of the CMB (decomposition into spherical harmonics of the fluctuations around the mean temperature), shown in Figure 1.4 right, one can estimate the abundance of different energy components of the Universe as the position and size of the peaks are sensitive to the cosmological parameters. The analysis of the CMB power spectrum by PLANCK concluded that baryonic matter accounts for 4.9 % of the energy content of the Universe, dark energy contributes to 68.3 % and dark matter to 26.8 %.

1.2. What is Dark Matter ?

The observations presented in the previous section provide evidence for the existence of dark matter, as well as some hints on the basic properties that dark matter must have. Dark matter should be :

- **Massive** : there is obviously a missing mass problem in the Universe, at different scales (astrophysical and cosmological scales) ;

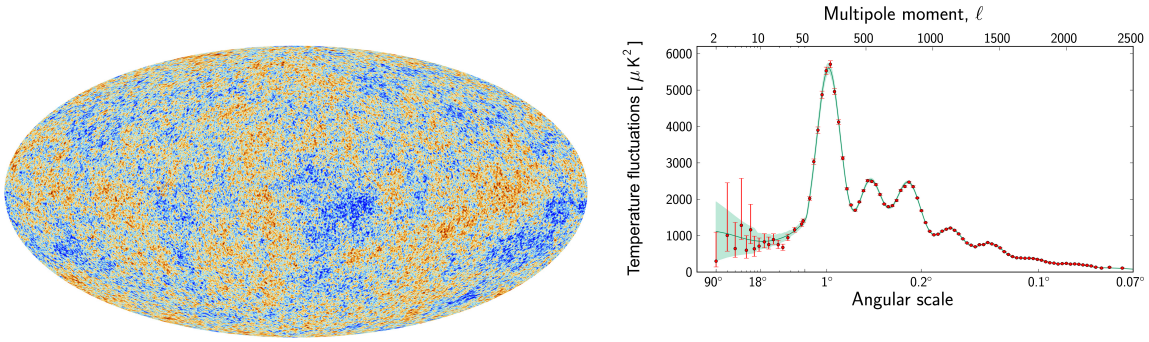

FIGURE 1.4. : Left : Picture of the CMB as measured by the PLANCK telescope. Right : Power spectrum of the CMB measured by PLANCK. (Credits : ESA and the PLANCK Collaboration)

- **Neutral** regarding the electromagnetic and strong interactions. Otherwise, dark matter would be visible (directly or via its interaction products) ;
- **Collisionless** : dark matter must interact very weakly to fit the observation of the collision of the Bullet clusters of galaxies, as well as the CMB measurements ;
- **Stable**, or at least long lived compared to the age of the Universe, because we still observe its effects to date ;
- **Cold enough**, in order to be able to form large scale structures.

However, no information of the precise content of what dark matter actually is can be inferred from observations.

1.2.1. Astrophysical objects

One assumption could be that massive compact objects in our Universe, such as black holes or neutron stars, are not all discovered yet. These dark objects are called MAssive Compact Halo Objects (MACHOs). Even though, as baryonic objects, they cannot be the complete solution to the dark matter problem, they have been searched for by the MACHO and EROS experiments, using microlensing. These experiments came to the conclusion that MACHOs are not numerous enough. However, Primordial Black Holes (PBH) –non baryonic black holes that were formed in the primordial Universe, resulting from density fluctuations– can be candidates for dark matter providing they are massive enough ($M > 3 \cdot 10^{-19}$ $M_\odot$, with $M_\odot$ the mass of the Sun) so that their lifetime is longer than the age of the Universe. PBHs are massive, long-lived, electrically neutral, collisionless and cold, thus are good dark matter candidates. Even if PBHs exist –and are part of the dark matter content of the Universe– their contribution is limited to ≈ 10 % at maximum in most of the allowed mass range [12].

1.2.2. Particles

In parallel of the observations leading to the suspicion of dark matter, particle physicists have developed the Standard Model of Particles along the second half of the 20^{th} century. It makes use of quantum field theory and symmetries to model, to the best of today's knowledge, the standard elementary particles content of the Universe and their interactions. Particles are divided into two categories : fermions and bosons. Fermions are matter particles that interact by exchanging interaction mediators (vector fields of spin 1) : the bosons. There exists three fundamental interactions : the electromagnetic interaction mediated by the photon (massless), the weak interaction mediated by the $W^{\pm}$ and Z^0 bosons (massive) and the strong interaction mediated by gluons (eight massless gluons). The mediators are the gauge bosons of the force they carry. Matter (and similarly anti-matter particles, that have the same properties as matter particles with opposite charges) particles (fermions) are divided into categories according to the interactions they are sensitive to : quarks and leptons. Quarks carry a color and an electric charge, thus interact strongly, weakly and electromagnetically. On the contrary, leptons do not carry colour charge thus interact only via weak and electromagnetic (only for the charged leptons) interactions. The fermions are divided into three generations that share the same quantum numbers (except their mass), each composed of two quarks and two leptons (one electrically charged lepton and one neutrino). The weak interaction allows to change generation, by conservation of their quantum numbers, hence the least massive generation is stable : it is the first generation (quark up, quark down, electron and electronic neutrino). A fifth boson, called the Higgs boson, has been detected in 2012 by the ATLAS and CMS experiments, confirming the Standard Model theory. Although it is a boson, the Higgs does not mediate a force (it has a spin 0) but is at the origin of the mass of particles (both fermions and bosons) thanks to a process called the Higgs mechanism [13, 14, 15]. Figure 1.5 summarises the classification of matter, mediator and Higgs boson particles of the Standard Model of particle physics, as well as their mass and charges.

While the Standard Model has been well tested and its predictions have not been contradicted in experiments around the Large Hadron Colliders (LHC) in France and Switzerland, some questions remain un-answered [3]. In order to solve these problems, theoretical physicists develop models based on new symmetries –in the same vein as the Standard Model of Particles– that sometimes involve the existence of a new kind of particle that fulfills requirements for being a dark matter candidate. The present section describes the most favoured dark matter candidates inferred from these particle physics models.

Figure 1.6 summarises the different dark matter models, their most motivated regions of existence in mass as well as the mean to detect them. The lower mass bound –10^{-22} eV/c^2– is originating from Heisenberg's uncertainty principle and considering that the dark matter is a boson. In the fermionic case, the Pauli exclusion principle applies and the lowest

[3] Among others : the matter - antimatter asymmetry, the fine-tuned mass of the Higgs, the neutrino mass origin, the mass hierarchy.

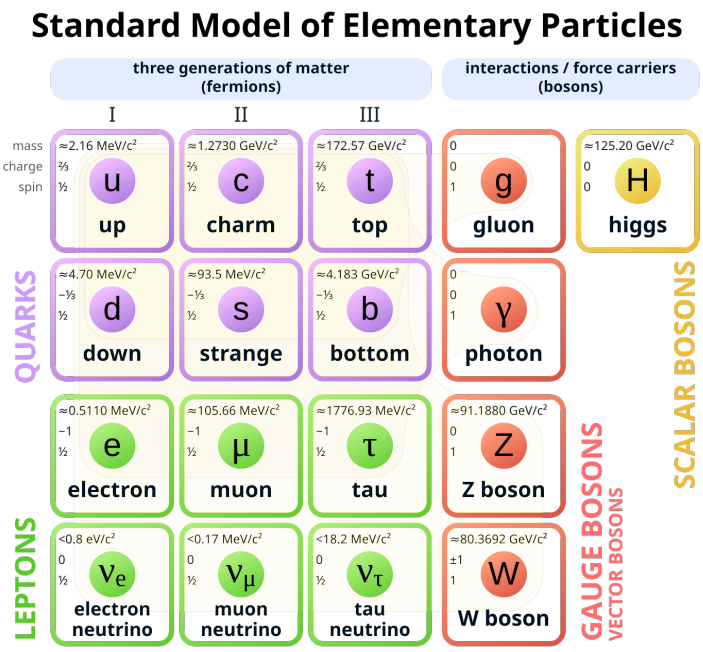

FIGURE 1.5. : Classification of the known elementary particles into quarks and leptons (matter), vector bosons serving as force mediators and the Higgs boson. Some of their quantum numbers (mass, electric charge and spin) are also shown.

mass possible for the dark matter is O(0.1 keV/c^2). The upper bound in possible mass of dark matter, $M_\chi \approx 30\ M_\odot \approx 10^{66}$ eV/c^2, comes from PBH measurements [16]. One can see that the dark matter mass is not well theoretically constrained, its possible mass range spans 88 orders of magnitude.

1.2.2.1. The Weakly Interacting Massive Particle

The Weakly Interacting Massive Particle (WIMP) is the most favoured dark matter candidate to date as its existence is both motivated by cosmology (notably because of the WIMP miracle described later) and beyond Standard Model particle physics. The WIMP candidate is a massive, electrically neutral, color neutral and stable particle that interacts at least via the standard weak interaction. In particle physics, the WIMP is a generic neutral particle interacting weakly that can appear in a variety of beyond the standard model theories. It is for example the case of SUperSYmmetry (SUSY) theories. Among these theories, the so-called Minimal Supersymmetry Standard Model (MSSM) [17] assumes a new set of particles called 'super-partners', with the same quantum numbers as Standard Model particles except their spin, plus a new symmetry exchanging bosons and fermions. In addition, it assumes the so-called R-parity, linked to the conservation of the Baryon and Lepton numbers [18]. This paradigm can provide a WIMP candidate (when the lightest neutralino is the lightest SUSY Particle) : a massive, neutral and stable (assuming the R-parity) particle that hence is a viable dark matter candidate. The

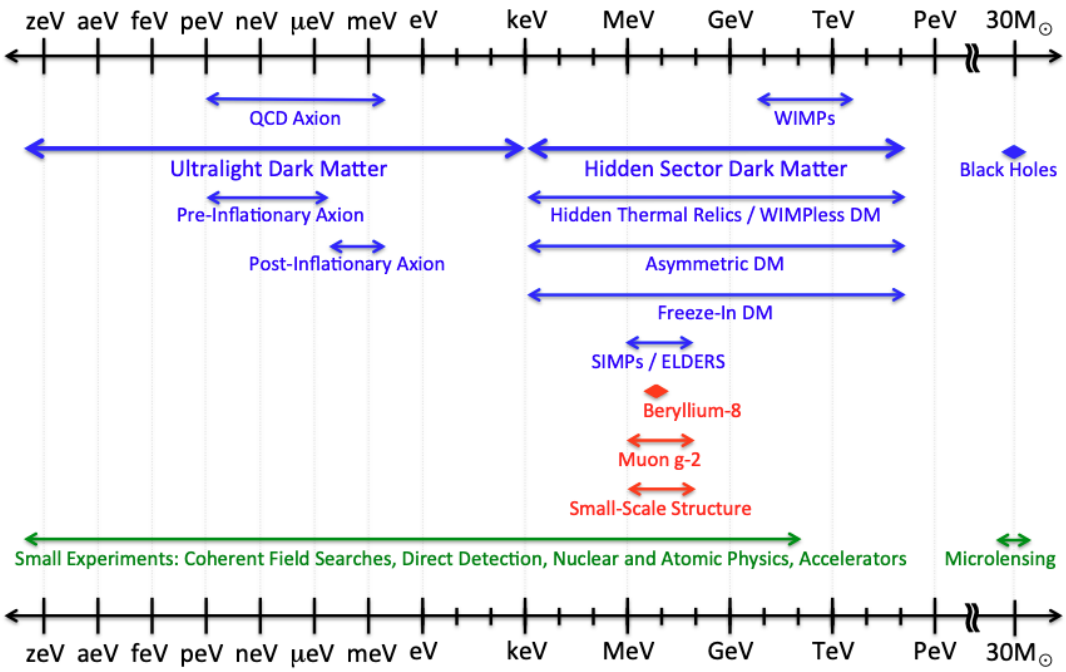

FIGURE 1.6. : Scheme of the theoretical mass range of some motivated dark matter candidates and the associated methods to look for them [16].

weak interaction constitutes a portal that enables the detection of the WIMP following an interaction with standard matter. The WIMP mass is most expected to be between $\approx 1\,\mathrm{GeV/c^2}$ and $\approx 10\,\mathrm{TeV/c^2}$ [4]. With such high mass, the WIMP is naturally cold. The WIMP search will be further described in the following of the present chapter.

The WIMP miracle The content of today's Universe is expected to originate from the inflation. As the dark matter is stable or long lived (we still observe its effects at present), it should be a thermal relic of the Big Bang.

At its beginning, the Universe was hot and dense, composed of standard matter and dark matter all at thermal equilibrium (the population of each component is stable, their production rate is equal to their annihilation rate). The Universe then cooled down, decreasing the dark matter production rate according to $e^{-m_\chi/T}$ (Boltzmann suppressed), with m_χ the mass of the dark matter particle and T the temperature of the Universe [19]. At the same time, the Universe expanded thus the annihilation also ceased. Without production and annihilation, the number of dark matter particles became constant, this is called the *freeze-out*.
The competition between the production of dark matter particles and their annihilation is characterised by the evolution of the number density n as function of time t, described

[4] A lower or higher mass neutral particle interacting via weak interaction could still be a candidate WIMP, though. They are usually called Light Dark Matter and Heavy Dark Matter.

by the Boltzmann equation [20] :

$$\frac{dn}{dt} = -3Hn - < \sigma_{ann} v > (n^2 - n_{eq}^2), \tag{1.2}$$

with H the Hubble constant, $< \sigma_{ann} v >$ the thermally-averaged dark matter annihilation cross section, and n_{eq} the dark matter number density at thermal equilibrium. The production rate is accounted for by the term $< \sigma_{ann} v > n_{eq}^2$, $-3Hn$ accounts for the volumic dilution due to expansion, and the $- < \sigma_{ann} v > n^2$ term represents the annihilation rate. At freeze-out, the interaction rate is equal to the expansion rate ($n < \sigma_{ann} v >= H$), giving –with hypothesis that freeze-out happened in the radiation dominated era of the Universe– $n_f = \frac{T_f^2}{M_{Planck} < \sigma_{ann} v >}$, with M_{Planck} the Planck mass and "f" quantities being the quantity value at freeze-out. This ratio is independent of dark matter particle properties. The thermal relic density is, with "0" quantities, the quantities at their current value, ρ_c the critical density, h the reduced Hubble parameter and $x_f = m_\chi / T_f$:

$$\Omega_X h^2 = \frac{m_\chi n_0}{\rho_c} \sim \frac{x_f T_0^3}{\rho_c M_{Planck} < \sigma_{ann} v >} \tag{1.3}$$

By computing $\frac{x_f T_0^3}{\rho_c M_{Planck}}$, one has

$$\Omega_X h^2 = \frac{(3 \cdot 10^{-27}) cm^3/s}{< \sigma_{ann} v >} \tag{1.4}$$

or

$$< \sigma_{ann} v >= \frac{(3 \cdot 10^{-27}) cm^3/s}{\Omega_X h^2} \approx 2.5 \cdot 10^{-26} \text{cm}^3/\text{s}, \tag{1.5}$$

which is close to the weak interaction cross section, $\sigma_W = \frac{\alpha_{weak}^2}{m_W^2} = 1.5 \cdot 10^{-26}$ cm^3/s (α_{weak} is the weak coupling constant and m_W the W boson mass). This suggests that a dark matter candidate is well fitted by a particle interacting via the weak interaction. This is the so-called WIMP miracle : weakly interacting particles naturally freeze out with the desired present relic density thus make excellent dark matter candidates [19].

1.2.2.2. The axion

Axions are also well motivated dark matter candidates. They are pseudo-scalar bosons that were postulated to "wash" the strong CP problem in particle physics (in Quantum Chromo-Dynamics, QCD) by introducing a new U(1) symmetry [5] [22]. The axion would be the pseudo-Goldstone boson of the spontaneous breaking of this symmetry. A viable QCD axion has a mass between 10^{-12} eV/c^2 and 10^{-2} eV/c^2. It is expected to be able to couple with some standard particles like photons and fermions. In particular, under a

[5] The strong Charge-Parity (CP) problem is the non-observation of CP violation in the strong sector, while nothing in the QCD Lagrangian suggests such apparent conservation. This results from the upper bound of experimentally measured electric dipole moment of the neutron that is 10^{10} larger than theoretically allowed [21].

strong magnetic field, axions are expected to transform into low energy photons. Thus the usual way to search for them is by using haloscope and helioscope, that target to transform axions into microwave photons inside a strong magnet, and detect the resulting electromagnetic field. Haloscopes and helioscopes search for axions from the galactic dark matter halo and axions produced by the Sun, respectively. Experiments able to directly search for axions can also search for Axion-Like-Particles (ALPs), that are hypothetical particles with the same particle properties as QCD axions but that do not solve the strong CP problem.

1.2.2.3. The dark photon

The dark photon is an hypothetical force carrier (a boson), similar to the standard photon but in the dark sector. It is introduced as the boson that breaks an abelian U(1) symmetry, and that couples weakly to standard particles carrying an electric charge, such as the electron, via kinetic mixing with the standard photon. This is how some experiments hunt for the dark photon : by looking at their absorption by electrons producing a monochromatic standard photon or by conversion of a dark photon into a standard photon in the cavity of the axion experiment. From CMB measurements, the dark photon must have a mass lower than $m_{A'} = 1\,\mathrm{MeV/c^2}$ [23].

1.2.2.4. The sterile neutrino

The sterile neutrino is a hypothetical kind of neutrino with very feeble interaction rate, making it a possible dark matter candidate. The standard neutrinos have a mass, as demonstrated by the observation features of the neutrino oscillation phenomenon (neutrinos oscillate like L/E, with L the oscillation length and E the neutrino energy), however their mass is not predicted by the Standard Model of particles [6]. A way to explain that neutrinos have a mass –and especially a tiny mass compared to other standard model massive particles– is the introduction of a new kind of neutrino (with potentially several generations like the standard neutrinos) : the sterile neutrino, mixing with standard neutrinos via the See-Saw mechanism [24]. The theoretical particle physics models don't predict a mass range for the sterile neutrino. Nevertheless, in order to be able to form small-scale structures, sterile neutrinos should be heavier than $\approx 10\,\mathrm{keV/c^2}$, as concluded by astrophysical observations. Sterile neutrinos might be detected thanks to their mixing with active neutrinos which is however very small. Several experiments, such as terrestrial double phase TPCs or indirect astrophysical measurements can constrain their mixing with the electronic neutrino ν_e : $|\mathrm{U}_{e4}|^2 = sin^2(2\theta)$, with θ the mixing angle.

[6] One could imagine that dark matter originates from the lack of knowledge we have on neutrinos. In particular, their exact mass is not yet known. However, we know that neutrinos are relativistic, thus hot, and cannot account for the full dark matter content of the Universe.

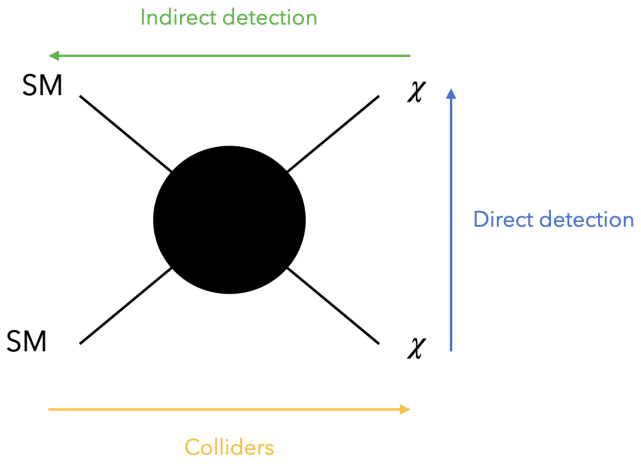

FIGURE 1.7. : Scheme illustrating how the search for WIMPs (called χ) is performed : looking at decay products of standard model particles (called SM, yellow arrow), looking at excesses of standard model particles in dense regions where dark matter particles interact with other dark matter particles (indirect detection, green arrow), and looking at direct interaction between standard model particles and dark matter particles (direct detection, in blue).

1.2.3. Modified gravitation

Another assumption could be that gravitation is misunderstood and Newtonian dynamics don't apply at galactic scales and above. Thus, instead of a missing ingredient in the Universe, the unexpected astrophysical observations would be explained by a new model for gravitation that accurately predicts the spatial observations. For example, the MOdified Newtonian Dynamics (MOND) theories have been developed to provide an explanation to the behaviour of the rotation curve of spiral galaxies (see reviews such as [25, 26]). MOND theories don't need an extra dark matter component to fit the observations. However, such theories don't predict correctly the velocity spread of galaxies in galaxy clusters (MOND theories would need an extra dark matter component). Hence, MOND theories cannot explain all astrophysical observations at once. In particular, MOND theories don't provide explanation for the obervation of the Bullet cluster discussed in Section 1.1.4.

1.3. Direct search for WIMP Dark Matter

From now on, this thesis will focus on the search for WIMP dark matter as it is the main candidate searched for by the DarkSide-20k experiment. The experimental search for WIMPs can be made three-ways –schemed in Figure 1.7 : at colliders, via indirect detection or via direct detection. The three methods are complementary.

Search at colliders First, the search at colliders is schemed reading Figure 1.7 from left to right (yellow arrow). Particle physics experiments located at the interaction points of the LHC in Switzerland, search for a range of different dark matter candidates including the flagship WIMP. Proton-proton interactions at the LHC could produce WIMP dark matter from interactions of the created particles. As they interact very weakly, the created WIMPs will not trigger the detector, hence physicists search for an associated particle (a photon, a jet, a boson, ...) emitted in the interaction or radiated from the incoming protons. Hence, they can search for missing transverse energy [27]. The backgrounds are events that mimic such signature, i.e. missing transverse energy resulting from neutrino production. The WIMP is searched for via deviation from background only Standard Model expectations.

Indirect search for WIMPs Second, one can search for WIMPs by looking at excesses of Standard Model particles in well-chosen regions of the Universe, where the medium is dense enough to enhance the interaction probability of dark matter particles with themselves, producing standard matter (reading Figure 1.7 from right to left). These dense regions also enhance the probability of detection of dark matter decays. This method relies on estimates of the production of standard particles by the astrophysical sources themselves, as well as a good understanding of the phenomena happening in the line of sight of the observed object [28, 29, 30].

Direct search for WIMPs The last method to search for WIMPs is the direct detection, shown in blue in Figure 1.7 when reading the scheme from bottom to top. Direct detection aims at tagging a direct interaction between a dark matter particle and the standard matter that composes the detector. Direct detection techniques are built relying on the double assumption that dark matter interacts with standard matter and that there is dark matter locally, i.e. in the Solar system vicinity. This PhD thesis focuses on direct detection method, using liquid argon as target material, thanks to the DarkSide-20k experiment (see Chapter 2), thus the present section focuses on the direct search for WIMP dark matter in more details.

A variety of experiments, employing different WIMP-matter interaction detection methods, have been built in the last decades, as reviewed in Ref. [31]. These experiments collect the heat, charge, light, or a combination of two of the three latter quantities, produced following an interaction in the detection bulk. For example, bolometers collect the heat via phonons produced after interactions. Typically, experiments that collect phonons also collect the scintillation light (like CRESST [32]) or ionisation electrons (like EDELWEISS [33] or superCDMS [34] experiments). It is also possible to combine the collection of ionisation electrons and scintillation photons to search for dark matter signal, as done in double phase noble liquid TPCs (Xenon-based (XENON [35], PandaX [36], LZ [37]) or Argon-based (DarkSide [38], ArDM [39])).

In direct detection, the backgrounds are all the interactions between Standard Model particles and the target material (mostly from cosmic rays and materials radioactivity).

Experiments mitigate these sources of background by selecting radio-pure materials to build the detector, by going deep underground to hide from cosmic rays-induced background (like in SNOLAB (Canada), LNGS (Italy), Modane (France), CJPL (China), etc) and by applying analysis criteria that discriminate signal-like and background-like interactions (see an example with the DarkSide-20k argon double phase time projection chamber in Chapter 2).

A significant part of the present thesis is dedicated to the sensitivity of the DarkSide-20k experiment, as shown in Chapter 4 and Chapter 5. In order to compute the sensitivity of a dark matter direct detection (DMDD) experiment, the signal rate has to be compared to the background rate, and a limit is set at a signal strength where an excess cannot be statistically ruled out by the signal + background fit of the data anymore. More details will be given in the next chapters of the thesis. Thus the aim of the present section is to describe the methodology employed to search for WIMPs via direct detection and to derive the theoretical framework that enables to estimate the signal rate in a dark matter direct detection experiment.

1.3.1. The Standard Halo Model

The Standard Halo Model (SHM) is a vanilla model which became the reference for signal rate computations in direct search for WIMP dark matter experiments [40]. It has been built to describe in a simple manner the dark matter halo of the Milky Way galaxy, relying on quite elementary yet relevant assumptions. The model is fine tuned by observations and some useful local halo properties are derived to permit dark matter experiments to compute their expected signal rate, after change of frame from galactic to terrestrial. The model is too simplistic, but it allows competitive experiments to compare their physics search results, which is especially important in case of positive result. The assessment of the impact of some more refined models is shown in Chapter 5.

As a proxy for the Milky Way dark matter halo, the SHM models the halo to be a non-collisional, spherically symmetric and isothermal gas of dark matter particles. Thus, the halo is three-dimensional, contrary to the baryonic content of the galaxy mostly contained in a two-dimensional disk. In the context of dark matter direct detection, the halo definition permits to compute the event rate by estimating the local (i.e. at the Sun vicinity in the Earth frame) velocity of the dark matter particles, hence estimate the interaction probability [41, 42]. Following the assumptions on the dark matter halo properties in the SHM framework (non-collisional, spherically symmetric and isothermal gas), the halo is described by a Maxwell-Boltzmann gas. The corresponding velocity distribution, $f_{gal}^{\text{No cut}}(\vec{v})$, reads

$$f_{gal}^{\text{No cut}}(\vec{v}) = \left(\frac{m}{2\pi k_B T}\right)^{\frac{3}{2}} \exp\left(-\frac{m|\vec{v}|^2}{2k_B T}\right), \tag{1.6}$$

where m is the mass of the dark matter particle in the gas, T is the temperature of the

gas and k_B is the Boltzmann constant. The root mean square velocity of this distribution is $\sigma_{\vec{v}} = \sqrt{\frac{3k_BT}{m}}$. Such distribution reaches its maximum at the most probable dark matter velocity, equal to $\mathrm{v}_0 = \sqrt{\frac{2}{3}}\sigma_{\vec{v}}$. It is convenient to express $f_{gal}^{\text{No cut}}(\vec{v})$ explicitly as function of the most probable dark matter velocity v_0, giving

$$f_{gal}^{\text{No cut}}(\vec{v}) = \left(\frac{1}{\pi^{3/2}v_0^3}\right)\exp\left(-\frac{|\vec{v}|^2}{v_0^2}\right), \tag{1.7}$$

It can also be useful to consider the speed distribution of dark matter particles in the halo, $f_{gal}^{\text{No cut}}(|\overrightarrow{v}|)$, obtained by integrating $f_{gal}^{\text{No cut}}(\overrightarrow{v})$ over the angles θ and ϕ :

$$f_{gal}^{\text{No cut}}(|\overrightarrow{v}|) = \int_0^{2\pi} d\phi \int_0^{\pi} v^2 \sin\theta d\theta f_{gal}^{\text{No cut}}(\overrightarrow{v}) \tag{1.8}$$

$$= 4\pi v^2 f_{gal}^{\text{No cut}}(\overrightarrow{v}). \tag{1.9}$$

In order to consider the local dynamics of the halo, one has to take into account the values of the astrophysical parameters of interest in the velocity distribution, modelled for example by Eq. (1.6). These parameters are :

- The dark matter mass density at the position of the Sun, called ρ_0. Its value is estimated to $\rho_0 = 0.3\ (\mathrm{GeV/c^2})/\mathrm{cm^3}$;
- The escape velocity at the position of the Sun, v_{esc}, defined as the threshold velocity beyond which an object would escape the gravitational potential. Its value is estimated to $\mathrm{v}_{esc} = 544$ km/s ;
- The circular velocity at the position of the Sun, v_c. Its value is set to $\mathrm{v}_c = 238$ km/s ;
- The most probable WIMP velocity (in norm) at the position of the Sun, v_0, set to $\mathrm{v}_0 = 238$ km/s.

The values of these four parameters have been set to the most accepted values of each parameter in the 2010s thanks to dynamic analyses of telescopes measurements of tracers velocity, and re-set by some new recommendations for dark matter experiments in 2021 [43].

Although these four parameters should be dependent on one another, and on the velocity and mass distribution of the halo, they have all been set to their best-fit value independently. In the framework of assessing competitiveness between different experiments, having such inconsistent values for the astrophysical parameters is not an issue as the signal model will still provide the right order of magnitude for the event rate. However, in the perspective to claim for detection or null-result when actually searching for WIMPs, these parameters can be decisive. Chapter 5 discusses the inter-dependency of the latter parameters, as well as their individual influence on the claimed detection limits.

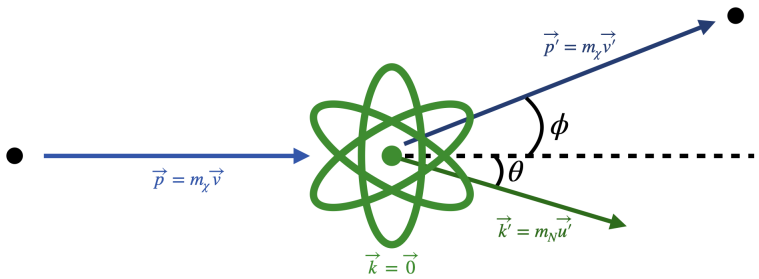

FIGURE 1.8. : Scheme of the elastic scattering between a WIMP and target nucleus.

With $v_0 = 238\,km/s$, Eq. (1.7) allows for velocities beyond the local escape velocity v_{esc}. The escape velocity has to be taken into account in the Velocity Probability Distribution Function (VPDF) to ensure that the VPDF velocity tail doesn't exceed the escape velocity. The chosen solution in the case of the SHM is to do a sharp cut at $v = v_{esc}$: $f(v > v_{esc}) = 0$, which gives :

$$f_{gal}(\vec{v}) = \begin{cases} \frac{1}{N_{esc}} \cdot e^{-\frac{|\vec{v}|^2}{v_0^2}} & \text{if } |\vec{v}| < v_{esc} \\ 0 & \text{if } |\vec{v}| \geq v_{esc} \end{cases} \tag{1.10}$$

The cut at v_{esc} changes the norm of the velocity distribution (the gaussian distribution is infinite). Hence, the normalisation factor of Eq. (1.7) becomes N_{esc} in Eq. (1.10).

1.3.2. Signal rate and time modulation

Due to the theoretically most motivated WIMP mass, in the range [1 GeV/c^2, 10 TeV/c^2], direct detection experiments expect the WIMP to scatter off target nuclei of the material. The available kinetic energy in the interaction is [7] :

$$E_{kin} = \frac{1}{2} \cdot m_\chi \cdot < v_\chi^2 > \tag{1.11}$$

To do an estimate of the kinetic energy, taking $v_\chi \approx 240$ km/s $\approx 10^{-3}$c and $m_\chi \approx 100$ GeV/c^2, E_{kin} is of the order of the keV. As the material nucleus is usually at cryogenic temperatures, one can suppose the target material at rest before the interaction. The scheme presented in Figure 1.8 lists all the kinetic variables needed to perform the computation of the recoil energy, assuming to be in the lab frame. Here, one only considers elastic scatterings due to the low initial WIMP velocity : they cannot break the bindings between nucleons in the atom. The chosen reference axis is the one of the initial momentum of the WIMP, hence the recoil angle in the final state is the one compared with the initial WIMP momentum.

By energy conservation during the interaction, the recoil energy of the atom nucleus

[7] the operation '< X >' represents the mean of X.

(of mass m_N) is the energy difference between the incoming and the outgoing WIMP, i.e. :

$$E_r \quad = \quad E_{kin}^{\chi'} - E_{kin}^{\chi} \quad = \quad E_{kin}^{Ar'} \quad = \quad \frac{|\overrightarrow{k'}|^2}{2m_N} \tag{1.12}$$

The energy and momentum conservations also provide :

$$\frac{v}{u'} = \frac{m_N + m_\chi}{2m_\chi} \frac{1}{cos\theta} \tag{1.13}$$

$$\frac{\frac{1}{2}m_\chi v^2}{\frac{1}{2}m_N u'^2} = \frac{m_\chi}{m_N} \left(\frac{m_N + m_\chi}{2m_\chi} \right)^2 \left(\frac{1}{cos\theta} \right)^2 \tag{1.14}$$

$$\frac{\frac{1}{2}m_\chi v^2}{\frac{1}{2}m_N u'^2} = \frac{(m_\chi + m_N)^2}{4m_\chi m_N} \frac{1}{cos^2\theta} \tag{1.15}$$

And gives :

$$E_r = \frac{4m_\chi m_N}{(m_\chi + m_N)^2} cos^2\theta \cdot \frac{1}{2} m_\chi v^2 \tag{1.16}$$

Finally, by introducing the reduced mass μ of a binary system (A, B) :

$$\mu = \frac{m_A m_B}{m_A + m_B} \ , \tag{1.17}$$

the recoil energy is expressed as :

$$E_r = \frac{2\mu^2 v^2 cos^2\theta}{m_N} \tag{1.18}$$

The energy of the recoil depends on the angle between the incident WIMP and the recoil direction of the nucleus, reaching a maximum value for a given initial WIMP velocity v. This value happens when $\theta = 0$, i.e. cos$\theta = 1$. This specific scenario gives :

$$E_r^{max} = \frac{2\mu^2 v^2}{m_N} \tag{1.19}$$

It can be seen the other way around, the WIMP needs a minimum initial velocity to be able to induce a recoil of the detector material with energy E_r :

$$v_{min} = \sqrt{\frac{E_r m_N}{2\mu^2}} \tag{1.20}$$

Experimentally, this v_{min} represents an energy threshold for experiments. The lighter the detector material, the lower the threshold, thus the larger the parameters space that can be explored. In addition, in the regime where $m_\chi << m_N$, the lighter the WIMP, the

larger its minimum velocity needed to induce a recoil in the detector (a direct consequence of the latter conclusion is visible in Chapter 5).

In parallel, one can compute the rate of collisions per unit time of a gas of dark matter particles off one target nucleus, $R_{coll,1}$. This rate depends on the cross section of interaction σ between the WIMP and the target nucleus, on the local number density of dark matter particles n_χ and on the WIMP-nucleus initial relative velocity v -which is the WIMP velocity in the Earth frame as the target nucleus is supposed at rest :

$$R_{coll,1} =< n_\chi \sigma v >_{coll,1} \tag{1.21}$$

In order to compute the differential rate of events in a dark matter direct detection experiment, one needs the differential collision rate for N_T target nuclei, thus :

$$\mathrm{d}R_{coll} =< n_\chi \cdot N_T \cdot \mathrm{d}(\sigma v) >_{coll} \tag{1.22}$$

The local number density of WIMPs can be written with more convenient variables, ρ_0 and the WIMP mass m_χ : $n_\chi = \frac{\rho_0}{m_\chi}$. Plus, in order to strengthen the dependency of the result on the exposure of larger and larger experiments, it is more straightforward to use mass variables, thus to express N_T as $N_T = \frac{M_{tot,DMDD}}{m_N}$, $M_{tot,DMDD}$ being the total mass of the target detection volume (e.g. $M_{tot,DMDD} = 20$ tons in the case of DarkSide-20k's fiducial volume). Besides, the initial WIMP velocity is not known. Thus, one needs to introduce the phase space VPDF of the WIMP in the Earth rest frame. For clarity purposes, quantities directly related to the Earth are labelled with the Earth astronomical symbol $\oplus$, and dark matter velocity variable is labelled with an apostrophe when defined in the Earth frame. The dark matter VPDF on Earth is then written as $f_\oplus(\overrightarrow{v'})$.

$f_\oplus(\overrightarrow{v'})$ is derived thanks to the VPDF of the WIMP in the galaxy, $f_{gal}(\overrightarrow{v})$, by using the vector composition of a velocity as seen on Earth $\overrightarrow{v'} = \overrightarrow{v_{\chi/\oplus}}$ with the corresponding velocity as seen in the galactic frame $\overrightarrow{v} = \overrightarrow{v_{\chi/\text{ galaxy}}}$, the velocity of the Sun (labelled $\odot$) in the galaxy $\overrightarrow{v_{\odot/\text{ galaxy}}}$ and the velocity of Earth with respect to the Sun $\overrightarrow{v_{\oplus/\odot}}(t)$:

$$\overrightarrow{v_{\chi/\oplus}} = \overrightarrow{v_{\chi/\text{ galaxy}}} - \overrightarrow{v_{\odot/\text{ galaxy}}} - \overrightarrow{v_{\oplus/\odot}}(t) \tag{1.23}$$

Swiping Eq. (1.23) and taking the result as input of $f_{gal}(\overrightarrow{v})$:

$$f_\oplus(\overrightarrow{v_{\chi/\oplus}}(t)) = f_{gal}\left(\overrightarrow{v_{\chi/\oplus}} + \overrightarrow{v_{\odot/\text{ galaxy}}} + \overrightarrow{v_{\oplus/\odot}}(t)\right) \tag{1.24}$$

In order to ease the reading, let's define :

$$\overrightarrow{v_\oplus}(t) = \overrightarrow{v_{\odot/\text{ galaxy}}} + \overrightarrow{v_{\oplus/\odot}}(t) \tag{1.25}$$

Which gives :

$$f_{\oplus}(\overrightarrow{v'}) = f_{gal}\left(\overrightarrow{v'} + \overrightarrow{v_{\oplus}}(t)\right) \tag{1.26}$$

The velocity distribution on Earth is then as stated by Equation (1.26) : one has to evaluate the velocity distribution model at $\overrightarrow{v'} + \overrightarrow{v_{\oplus}}(t)$. In the peculiar case of the spherically symmetric isothermal SHM, Eq. (1.26) has an analytical expression. One obtains :

$$f_{\oplus}(\overrightarrow{v'}) = \frac{1}{N'_{esc}(t)} \cdot e^{-\frac{\left(\overrightarrow{v'}+\overrightarrow{v_{\oplus}}(t)\right)^2}{v_0^2}}, \tag{1.27}$$

where $N'_{esc}(t)$ is the norm of $\mathrm{x} \mapsto e^{-\frac{(\vec{x}+\overrightarrow{v_{\oplus}(t)})^2}{v_0^2}}$.

This formula, expressed in the Earth frame, exhibits a time dependency. Indeed, while the Sun velocity around the galactic center can be considered constant at human time scale, obviously the Earth velocity cannot be treated as such as it orbits the Sun with a period of one year, smaller than the running time of most dark matter direct detection experiments. This time dependency enhances the maximum velocity value of the WIMP around the 2^{nd} of June, while it is lower the 2^{nd} of December. Thus, at a given WIMP mass and given bin of recoil energy, the interaction probability within a terrestrial detector is higher in June than in December. This signal characteristics allows for a detection feature called annual modulation : in case of detection, one can check that the amplitude of the signal is annually modulated as expected, which discriminates it against background, supposed to be constant vs time.

In its left plot, Figure 1.9 shows the dark matter velocity distribution in the galaxy and on Earth for the SHM. As expected from Eq. (1.27), the width of the distribution is larger in the Earth frame and the central value of the distribution is translated to higher velocities by the mean Earth velocity. The expected rate of events in a liquid argon TPC assuming a dark matter mass density $\rho_0 = 0.3$ GeV/c^2/cm^3, a WIMP mass $m_\chi = 100\,\mathrm{GeV/c^2}$ and a cross section $\sigma_0 = 10^{-48}$ cm^2, computed the 2^{nd} of June, is shown in the right plot of the same figure.

The differential rate of collisions between the WIMP halo and a dark matter direct detection experiment per unit time is then :

$$dR_{coll} = M_{tot,DMDD}\frac{\rho_0}{m_\chi m_N} \cdot \int_{v_{min}}^{v_{max}} d^3\overrightarrow{v'} \cdot f_{\oplus}(\overrightarrow{v'}) \cdot |\overrightarrow{v'}| \cdot d\sigma \tag{1.28}$$

The precise expression of σ can be determined using particle physics. However, in the following, $\frac{d\sigma}{dE_r}$ is derived from simple yet relevant assumptions. In the non-relativistic and isotropic case, the differential cross section of interaction between a WIMP χ and a nucleon N can be written as :

$$\frac{d\sigma}{dE_r} = \frac{m_N\sigma}{2\mu^2 v^2} \tag{1.29}$$

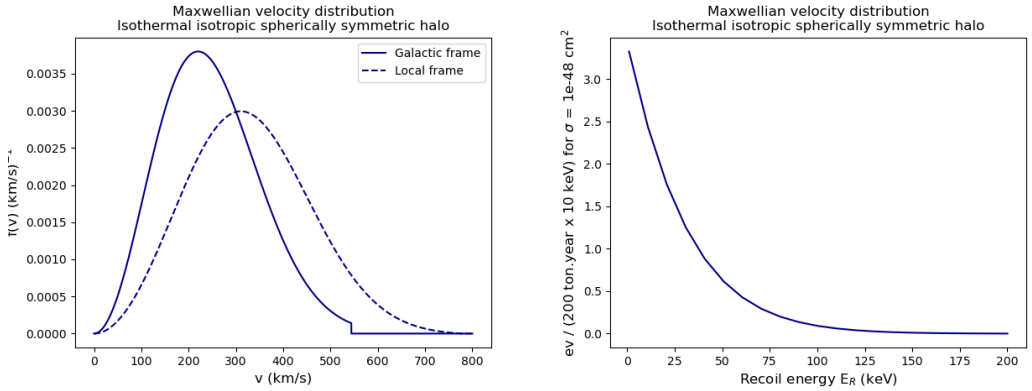

FIGURE 1.9. : Left : WIMP velocity distribution as expected from the SHM. The full blue curve is the VPDF represented in the Galaxy, in blue dashed one is in the Earth (lab) frame. Right : Expected rate of events in the main search volume of DS-20k, with an assumed cross section of interaction $\sigma_0 = 10^{-48}$ cm^2, a WIMP mass $m_\chi = 100$ GeV/c^2 and a WIMP density of $\rho_0 = 0.3$ GeV/cm^3.

When scaling the cross section to the whole nucleus, the shape of the nucleus has to be taken into account [44]. The spin independent [8] cross section of interaction between the nucleus and the WIMP can be -temporarily- written as :

$$\sigma_0^{SI} = \frac{4\mu^2}{\pi}\Big(Zf_p + (A-Z)f_n\Big)^2 \tag{1.30}$$

f_p and f_n being the WIMP-proton and WIMP-neutron coupling factors. If one assumes a low momentum transfer, the interaction is blind against neutrons and protons thus $f_p \approx f_n$ (this assumption is model-dependent) and $\sigma_0^{SI} \propto A^2$. It is thus possible to write $\sigma_0^{SI} = \sigma_0 A^2$. It becomes obvious that the cross section of interaction is enhanced for big nuclei. In other words, the heavier the nucleus, the more probable the interaction.
In order to take into account the shape of the nucleus (up to now, the interaction was considered point-like), the cross section of interaction is multiplied by a nuclear form factor. Such form factor allows keeping the simple description of the interaction by multiplying the cross section by this correction factor that maps the nucleus structure. It is noted F(q), q being the momentum transfer (q $= \sqrt{2m_N E_r}$), the squared value of F(q) is effectively used. Here, the Helm form factor [45, 40] is used, that has the mathematical expression :

[8] In this thesis, only the spin-independent interaction is presented, as the spin-dependent one is of negligible magnitude for most experiments -and null in the case of Argon target material (which is the case for DarkSide-20k using ^{40}Ar)- compared with the microscopic interactions occurring in the nucleus (especially in heavy ones).

$$F^2(q(E_r)) = \left(\frac{3j_1(q(E_r)R_1)}{q(E_r)R_1}\right)^2 \exp(-q(E_r)^2 s^2) \tag{1.31}$$

$$\text{where} \quad j_1(x) = \frac{sin(x)}{x^2} - \frac{cos(x)}{x} \tag{1.32}$$

$$\text{where} \quad R_1 = \sqrt{c^2 + \frac{7}{3}\pi^2 a^2 - 5s^2} \tag{1.33}$$

j_1 is the Spherical Bessel function, s is the nuclear skin thickness and R_1 the effective nuclear radius (c = $1.23\text{A}^{1/3}$-0.60 fm, a = 0.52 fm and s = 0.9 fm) [46].

Finally, the differential cross section of interaction between a WIMP and a -heavy-nucleus is :

$$\frac{d\sigma}{dE_r} = \frac{m_N \sigma_0 A^2 F^2(q(E_r))}{2\mu^2 v'^2} \tag{1.34}$$

This differential cross section is multiplied by $f_\oplus(\overrightarrow{v'}) \cdot |\overrightarrow{v'}| \cdot d^3\overrightarrow{v'}$ and integrated over v' in the rate of events of Eq. (1.28), giving :

$$\frac{\mathrm{d}R_{coll}}{\mathrm{d}E_r}(E_r, t) = M_{tot,DMDD}\frac{\rho_0}{m_\chi m_N} \cdot \int_{v_{min}}^{v_{max}} \frac{m_N \sigma_0 A^2 F^2(q(E_r))}{2\mu^2 |\overrightarrow{v'}|^2} \cdot f_\oplus(\overrightarrow{v'}, t) |\overrightarrow{v'}| \mathrm{d}^3\overrightarrow{v'} \tag{1.35}$$

$$\tag{1.36}$$

Which after simplification gives rise to the explicit differential event rate :

$$\frac{\mathrm{d}R_{coll}}{\mathrm{d}E_r}(E_r, t) = M_{tot,DMDD}\frac{\rho_0}{m_\chi}\frac{\sigma_0 A^2 F^2(q(E_r))}{2\mu^2} \cdot \int_{v_{min}}^{v_{max}} \frac{f_\oplus(\overrightarrow{v'}, t)}{|\overrightarrow{v'}|} d^3\overrightarrow{v'} \tag{1.37}$$

Calling $\eta(v_{min}, t)$ the mean inverse speed of the WIMP on Earth,

$$\eta(v_{min}, t) = \int_{v_{min}}^{v_{max}} \frac{f_\oplus(\overrightarrow{v'}, t)}{|\overrightarrow{v'}|} \mathrm{d}^3\overrightarrow{v'} \tag{1.38}$$

or equivalently,

$$\eta(v_{min}, t) = \int_{v_{min}}^{v_{max}} \frac{f_\oplus(|\overrightarrow{v'}|, t)}{|\overrightarrow{v'}|} \mathrm{d}v' \tag{1.39}$$

one can rewrite Eq. (1.37) as :

$$\frac{\mathrm{d}R_{coll}}{\mathrm{d}E_r}(E_r, t) = M_{tot,DMDD}\frac{\rho_0}{m_\chi} \cdot \frac{\sigma_0 A^2 F^2(q(E_r))}{2\mu^2} \cdot \eta(v_{min}, t) \tag{1.40}$$

The η factor gathers all the astrophysics (except for ρ_0) of the differential rate of

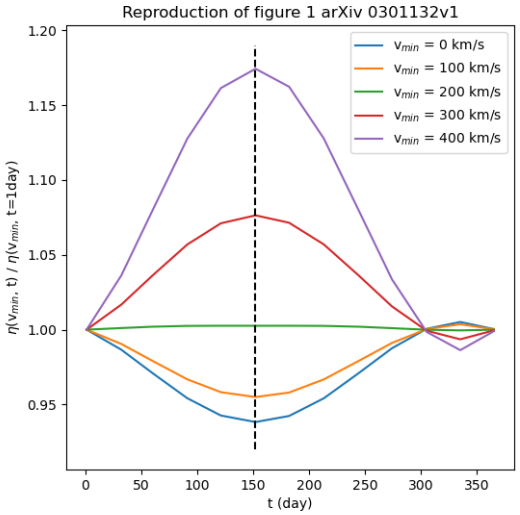

FIGURE 1.10. : The η factor along the year, for different values of v_{min} and in the SHM framework (assuming a Maxwellian isotropic velocity distribution). Each line is normalised by the value of the η factor of the 1st of January with the considered value of v_{min}. This Figure is reproduced from [47].

events, and is the only function taking the date of the event into account. As an example, the normalised value of the η factor vs the time of the year is shown in Figure 1.10, for different values of v_{min} and in the SHM framework. The modulation of the signal is clearly visible : the signal takes its maximum value the 152^{th} day of the year, i.e. the 2^{nd} of June, if $v_{min} > 200$ km/s. Still when $v_{min} > 200$ km/s, the η factor takes its minimum value the 335^{th} day of the year, i.e. the 2^{nd} of December. The modulation of the signal reaches 17% (resp. 7%) for $v_{min} = 400$ km/s (resp. $v_{min} = 300$ km/s).

This feature is useful in case of excess events : one can confirm the WIMP detection with the modulation of the signal along the year after several years of data taking.

Some of the previous expressions outlined relationships between detector features and benefits when searching for WIMPs. They are summarised in the following :

- The bigger the experiment, the more probable to detect an interaction between a WIMP and a target nucleus.
- The lighter the target nucleus, the lower the energy threshold of the experiment (see Eq. (1.20)).
- The larger the target nucleus (the larger the A), the more probable the interaction with an incoming WIMP ($\sigma \sim A^2$).
- For a given WIMP mass, the larger the target nucleus, the lower the form factor $F^2(q(E_r))$.

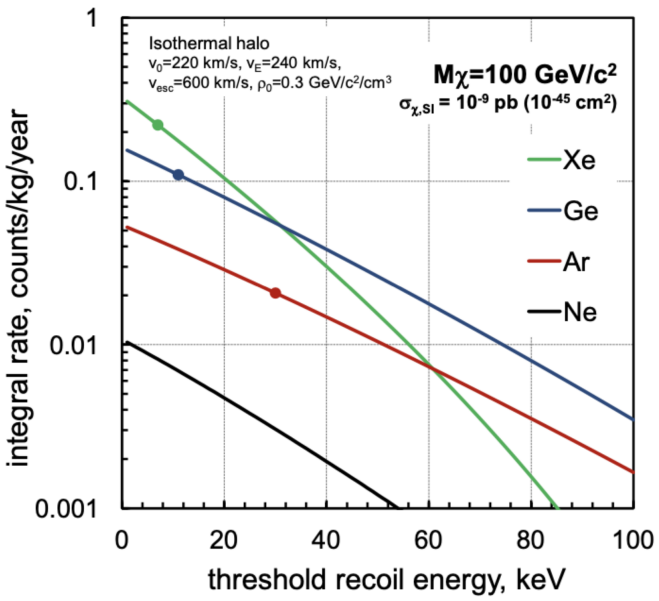

FIGURE 1.11. : Event rate per kg per year vs the threshold energy in keV for different target materials (xenon, germanium, argon, neon). The bullets point out the typical energy threshold for each technology [48].

A joint representation of the two last bullets is shown on Figure 1.11. This plot shows the rate of events (as expected from an isotropic Maxwellian velocity distribution) vs the threshold energy (in keV) for different target materials. Current noble liquid double phase TPCs are filled with xenon (XENON, Panda-X and LZ collaborations) or argon (GADMC collaboration). At 0 keV recoil energy threshold, the momentum transfer is null (q=0) so is the nuclear form factor (see Eq. (1.31), hence the rate of recoils off xenon nucleus is $\left(\frac{A_{Xe}}{A_{Ar}}\right)^2 \approx$ 10 times larger than the one off argon nucleus. At low and medium recoil energy thresholds ($E_r < 50$ keV), there is a competition between the ($\sigma \sim A^2$) effect and the $F(q(E_r))$ effect. At larger recoil energy thresholds, the effect of $F(q(E_r))$ overcomes the one of A^2 and the rate of recoils off argon nuclei becomes larger than rate of recoils off xenon. the markers indicate typical WIMP-search thresholds for each technology

1.3.3. Direct detection signatures

In case of an excess of events in a direct detection of dark matter experiment, the dark matter hypothesis can be strengthened by some experimental signatures based on some assumptions on the galactic halo and galactic motion. Of course, these signatures depend on the halo modelling, especially in the Sun vicinity, which is not well known. Up to now, we can mostly rely on cosmological simulations, which provide qualitative relationships between matter and velocity distributions. Yet, it is still possible to consider the following effects, with some uncertainty due to the halo modelling.

Annual modulation First, there is the annual modulation due to the motion of the Earth around the Sun, already hinted in 1.3.2. In the solar system, because of the Sun orbit around the galactic center pointing towards the Cygnus constellation, everything acts as if the dark matter halo was a wind coming from the latter point in the sky. In practice in experiments –where there is an energy threshold– at a given recoil energy, the event rate should be dependent on the time of the year. One expects a maximum the 2^{nd} of June (when the Earth faces the wind) and minimum the 2^{nd} of December (when the Earth is in the same direction as the wind). Nonetheless, the magnitude of the annual modulation is of the order of the %, or tens of % in extreme conditions, as seen in Figure 1.10, thus a lot of statistics (O(10^4) events [49]) is needed to leverage on such signature.

Directionality Linked with the annual modulation, if an experiment is sensitive enough to measure the direction of a recoil in its detection bulk, one can claim that the excess recoils come from the direction of Cygnus. This signature is especially strong as the background is not expected to be able to mimic such effect, as it should be uniformly distributed. For example, the MIMAC [50] and ReD [51] collaborations try to prove the feasibility of detecting dark matter using such signature.

1.3.4. State of the art of WIMP direct detection

Since the end of the 1980s, there has been an active race to detect the WIMP dark matter candidate, starting with crystals and cryogenic detectors. In the late 2000s, the DAMA/LIBRA collaboration [52] claimed a detection of dark matter with time modulation of the signal with each of the two running phases of the experiment (DAMA/NaI (2008) and DAMA/LIBRA (2010) [53]) using NaI crystals. Yet, other dark matter-sensitive experiments, relying on different technologies, have excluded the signal region claimed by the DAMA/LIBRA collaboration.

Since 2010, the double phase TPCs (collection of light and charge) lead the search for WIMP dark matter (xenon-based : XENON [35], LZ [37] and Panda-X [36] collaborations, argon-based : DarkSide-50 [38], ArDM [39] and DEAP [54] (single phase) collaborations). This technology is particularly competitive thanks to its scalability to very large exposures and powerful background discrimination, which is described in more details in Chapter 2. Figure 1.12 shows the strong commitment to search for the WIMP in the scientific community, here setting upper limits on the Spin-Independent cross section of interaction with nucleons. The figure outlines that xenon double phase TPCs are leading the race in the so-called high mass region –above 10 GeV/c^2. Currently, the upper limit on σ_{SI} is of the order of $\sigma_{SI} \approx 1$ x 10^{-47} cm^2 at $M_\chi \approx 30$ GeV/c^2 [55]. In the near future, second generation xenon double phase TPC experiments (XENONnT, LZ, PandaX-4T) will produce their final physics results, and are expected to reach sensitivities around 10^{-48} cm^2

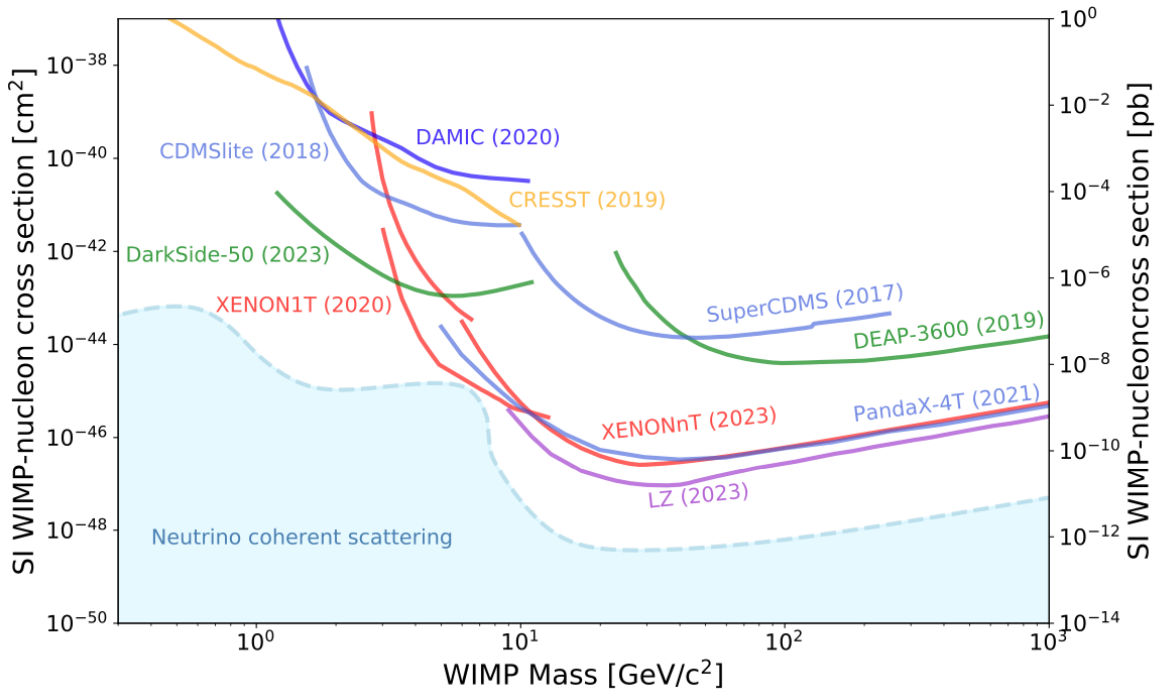

FIGURE 1.12. : Current upper limits on the spin-independent (SI) cross section of interaction between dark matter and nucleons, vs WIMP mass [55]. The blue area is the neutrino floor.

at 30 GeV/c^2. The next argon double phase TPC searching for WIMPs is DarkSide-20k (see Chapter 2), it is expected to be competitive with xenon-based experiments after ≈ 3 years and ultimately reach 10^{-48} cm^2 at $\approx$100 GeV/c^2. The next generation experiments (argon-based and xenon based) plan to reach the neutrino floor at high mass by the end of the next decade.

At WIMP masses in the [1, 10] GeV/c^2 mass range, thanks to the so-called ionisation-only analysis, double phase TPCs can extend the WIMP search below 10 GeV/c^2 (see Chapter 4), currently led by the argon-based experiment DarkSide-50 in the mass range [1.2, 3.6] GeV/c^2 [56] and by the xenon-based experiment XENON-1t in the range [3.6, 8] GeV/c^2 [57].

Finally, there is a strong effort from the community to lower the detection threshold and improve the sensitivity to masses below 1 GeV/c^2. Prospective experiments like superCDMS [58] and TESSERACT [59] (bolometers and ionisation charge collectors), DAMIC-1k [60] (Si CCDs (charge-coupled devices), ionisation charge collectors) and NEWS-G - DarkSPHERE [61] (spherical proportional counter, ionisation charge collectors), intend to probe the low mass WIMP existence down to O(1) MeV/c^2.

2. The DarkSide-20k experiment

Summary

The DarkSide-20k (DS20k) experiment will be the next generation detector of the Global Argon Dark Matter Collaboration (GADMC). GADMC is a collaboration gathering all WIMP dark matter experiments using argon target (the stable isotope ^{40}Ar). These experiments are DarkSide-50 [38] (DS50, located at Laboratori Nazionali del Gran Sasso (LNGS) in Italy), DEAP-3600 [54] (located at SNOLab in Canada), ArDM [39] (located at Laboratorio Subterráneo de Canfranc in Spain) and miniCLEAN [62] (located at SNOLab in Canada).
Like DS50, DS20k will be hosted in the Hall C of LNGS, under 1.4 km of rock in order to shield it from cosmic rays induced background. The design of DS20k was finalised in December 2021 by its Technical Design Report [63] ; the construction of the experiment began afterwards. DS20k should be ready for data collection by 2027.

The present chapter aims at describing dark matter detection principles in an argon double phase Time Projection Chamber (TPC), the expected backgrounds in the experiment and the associated detector design to mitigate it. Finally, the sensitivity projection of DarkSide-20k in the 10 GeV/c^2 - 10 TeV/c^2 WIMP mass range is shown for different exposures.

2.1. Detection features in an argon double phase Time Projection Chamber

The search for WIMPs in DS20k will be performed in the bulk of a double phase TPC with argon as target nucleus. The use of such apparatus for WIMP search was proven to be efficient by DS50, the predecessor of DS20k. As said in chapter 1, one primarily expects the WIMP to interact with the nucleus of argon [1], inducing a recoil of the latter, called Nuclear Recoil (NR).

When a particle interacts and deposits energy inside the bulk of a double phase TPC, the target material gets heated, excited and ionised [64, 65] with mecanism shown on the scheme of Figure 2.1 left. The energy from heating after interaction with the target nucleus (heat is negligible after interaction with the electrons) is deposited as phonons and lost, provoking quenching. However, the photons and electrons emitted after interaction provide information on the interaction if collected. A general scheme of the collection of scintillation photons (black wavy arrows) and ionisation electrons (white arrow) is shown on Figure 2.1 right, considering a generic incoming particle (green arrow). Provided they can be efficiently collected, information brought by the two components allows for energy and position reconstructions - described in the following - as well as particle identification further described in section 2.2.1.

[1] It is worth noting that, like DS50, DS20k will be sensitive to other dark matter candidates, especially light particles interacting with bound electrons of argon, producing an electron recoil. More details are given in chapter 4.

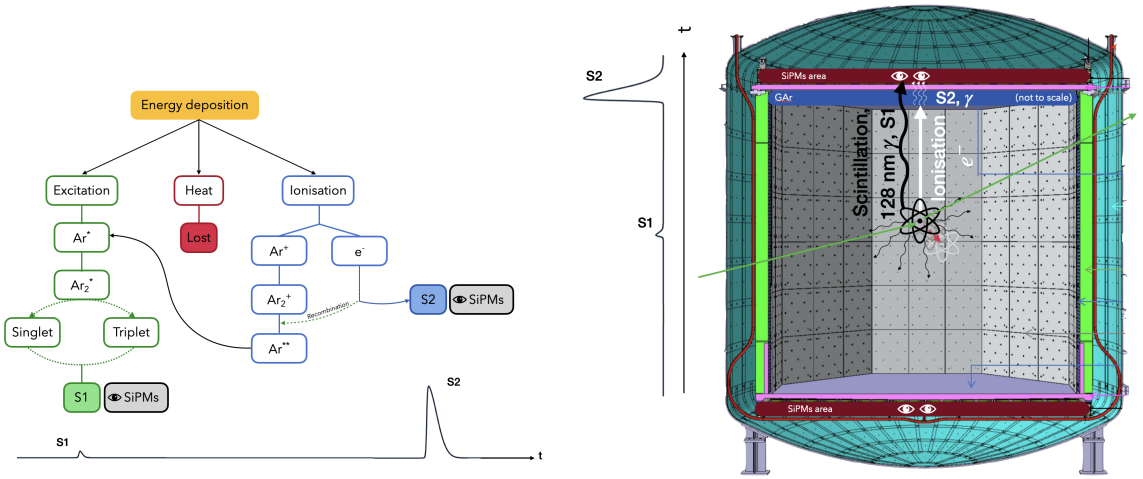

FIGURE 2.1. : Left : Excitation, ionisation and recombination after interaction in liquid argon. Right : Scheme of scintillation and ionisation after interaction in a double phase TPC.

2.1.1. Excitation

On the one hand, the target material of the detector is excited by an incoming particle resulting in scintillation. In argon, the excitation is schematised in the left branch of Figure 2.1 left and the de-excitation mechanism is :

$$Ar^* + Ar \rightarrow Ar_2^* \rightarrow 2\ Ar + h\nu \tag{2.1}$$

In argon, the hν photons are produced with a wavelength of 128 nm and yield of 51 photons/keV. Then, as illustrated by the wavy black arrows of Figure 2.1 right, the photons propagate isotropically in the TPC. After wavelength shifting and reflection on the walls of the TPC thanks to reflectors coated with peculiar wavelength shifter (WLS), photons are promptly (within tens of ns for second generation experiments) detected by photo-multipliers usually arranged in two arrays at the top and bottom of the TPC. The scintillation signal is called S1.

2.1.2. Ionisation

The ionisation and recombination mechanisms are schematised in the right branch of Figure 2.1 left and described here :

$$Ar^+ + Ar \rightarrow Ar_2^+ \tag{2.2}$$
$$Ar_2^+ + e^- \rightarrow Ar^{**} + Ar \tag{2.3}$$
$$Ar^{**} \rightarrow Ar^* + phonons \tag{2.4}$$
$$Ar^* + Ar \rightarrow Ar_2^* \rightarrow 2\ Ar + h\nu \tag{2.5}$$

First, Equation (2.5) evinces a contribution of ionisation to the scintillation signal S1, also depicted in the scheme 2.1 left. In addition, electrons released by ionisation but escaping recombination described by Equation (2.3) drift to the top of the TPC thanks to an uniform electric field called *drift field*. Once at the top of the TPC, electrons are extracted into a thin gaseous layer of argon thanks to a strong *extraction field*. Finally, they are accelerated under another strong electric field called *luminescence field*, and generate a flash of photons by electro-luminescence. The produced photons are proportional to the number of electrons reaching the gas pocket and, after being wavelength shifted, are detected by the top array of photo-multipliers. The secondary - and delayed - signal resulting from ionisation is called S2.

2.1.3. Event reconstruction

Thanks to the time difference between S1 and S2 arrivals (corresponding to the electron drift time), one can reconstruct the Z position of the interaction. Besides, the XY position of interaction is given by the S2 XY location on the top array of photo-multipliers. Hence, the use of a double phase TPC allows the 3D reconstruction of events position.

In addition, with S1 and S2 information, the deposited energy can be reconstructed thanks to the following expression, already used by the DS50 collaboration [66] :

$$E_{dep} = w \left(\frac{S1}{g1} + \frac{S2}{g2} \right), \tag{2.6}$$

where w is the effective work function i.e. the mean energy needed to extract a quantum. In the case of argon, the commonly used value is $w = (19.5 \pm 1.0)$ eV [67]. g1 represents the scintillation gain i.e. the number of photo-electron measured in S1 per released photon after interaction. g2 is the ionisation amplification factor corresponding to number of photo-electrons (pe) produced per ionisation electron. Both g1 and g2 depend on the electric fields and the detector design. In DS20k, one expects g1 ≈ 20 % and g2 ≈ 20 pe/e^- (DS50 measured g1 $= (16 \pm 1)$% and g2 $= (23 \pm 1)$ pe/e^- [66]).

Thanks to the long electron lifetime in the TPC and the high ionisation amplification g2, the efficiency to extract S2 in the gaseous layer of argon almost reaches 100 %. On the contrary, because of the poor S1 detection efficiency (g1), the low energy interactions - producing low number of scintillation quanta - have S1 inefficiency. In terms of WIMP search, this defines the so-called *high mass* and *low mass* search regions. The former have S1 efficiency for both signal (WIMP) and background events, it represents the [10 GeV/c^2, 10 TeV/c^2] WIMP mass range. The latter have S1 inefficiency for WIMP events, leading to S2-only analysis for WIMP search, possible with argon target in the [1 GeV/c^2, 10 GeV/c^2] WIMP mass range as proved by DS50 [56, 68]. Chapter 4 describes in details such low mass analysis for both DS50 and DS20k as well as search (or prospects) for other dark matter candidates with ionisation-only data.

In addition to position and energy reconstruction, the combination of S1 and S2 tells wether the incoming particle interacts once, such as the WIMP (doing a so-called single scatter), or several times (multiple scatter). Indeed, the photons propagation being extremely fast in the TPC compared to the electron drift time, all S1 photons will be recognised as a single signal, while each interaction should be seen separated through the multiple S2 signals. In section 2.3.3, one can discern the importance of such single-multiple scatter discrimination in background rejection.

2.2. Backgrounds

As WIMP direct detection experiments measure the recoil of target liquid argon (LAr) after interaction with a candidate WIMP, one expects background sources to produce either NR (heavy particles (neutrons and α)) or Electron Recoil (ER, from light particles : γ, β). Depending on their energy range, neutrinos are expected to produce either ER (elastic scattering between a neutrino and bound electrons) or NR (via Coherent Elastic Neutrino (ν) - Nucleus Scattering (CEνNS)). Once underground, most of the background (in terms of rate of interaction) comes from natural radioactivity, thus a peculiar attention is drawn to the choice of low radioactivity materials to decrease the background rate as much as possible. Yet, some backgrounds remain hence need to be vetoed thanks to additional detector features.

The following section shows that the use of argon target is a strong asset in terms of signal-background separation. Then the detector design, focused on tagging remaining backgrounds, is described.

2.2.1. Electron recoil backgrounds

The most numerous background comes from light particles such as electrons and photons emitted by the radio-active isotopes of detector materials. Light particles will interact with the bound electrons of target argon atoms, producing an ER.
The main ER contribution comes from the cosmogenic ^{39}Ar isotope, a β-emitter with 1 Bq/kg activity in atmosheric argon (AAr), produced by interactions between cosmic rays and the stable ^{40}Ar isotope present in the atmosphere. In order to reduce the background contribution from this isotope, the DarkSide experiments - already at the time of DS50 - make use of underground argon (UAr), extracted from mines in Colorado, USA thanks to the so-called Urania plant, especially designed for DarkSide. Such UAr has $\approx$ 1400 times lower activity than AAr [69] giving rise to an expected internal background rate of 36.5 Hz before analysis rejection with 49.7 t argon volume at 0.73 mBq/kg. In addition to the use of UAr to lower the internal background rate, the DS20k collaboration plans to perform cryogenic distillation of the extracted gas to reduce impurities in the bulk of the TPC, that gives rise to uncorrelated background and decreases the electron lifetime. This manoeuvre will be carried out in the so-called Aria facility in Sardinia, Italy [70, 71].

Other ER contributions come from the so-called external background : the radio-contamination of detector materials (Silicon Photo-Multipliers of both TPC and the inner veto, walls of the TPC and inner detector vessel - see section 2.3.1) by ^{238}U, ^{235}U, ^{232}Th, ^{137}Cs, ^{60}Co, ^{40}K, emitters of X-rays and γ-rays photons. Including the external background, the ER background rate increases to 82 Hz [63]. Thus the importance to be able to discriminate between ER background and NR signal.

To reject ER background, noble liquid double phase TPCs can use the distribution of light in S1 and S2 as discriminating variable because it depends on the type of interaction. Indeed, S2 $\propto$ $(1-r)N_i$, while S1 $\propto$ $N_{ex}+rN_i$, where N_{ex} and N_i are respectively the number of excitation and ionisation quanta released by the interaction and r the electron recombination probability. The excitation over ionisation ratio, $\alpha = \frac{N_{ex}}{N_i}$, has been measured to be 0.21 with electron as ionising particle (ER) [72, 73, 74], while it is estimated to be of the order of 1 for NR interactions. Thus, by computing the S1/S2 ratio for each event $\left(\frac{\mathrm{S1}}{\mathrm{S2}} \propto \alpha\,\frac{1+r}{1-r}\right)$, one gets a first discrimination between ER and NR, obtaining $\left(\frac{\mathrm{S1}}{\mathrm{S2}}\right)_{ER} < \left(\frac{\mathrm{S1}}{\mathrm{S2}}\right)_{NR}$. This method is the only ER-NR discrimination used by xenon-based experiments and proved to achieve a $\approx 10^2$ reduction factor [75].

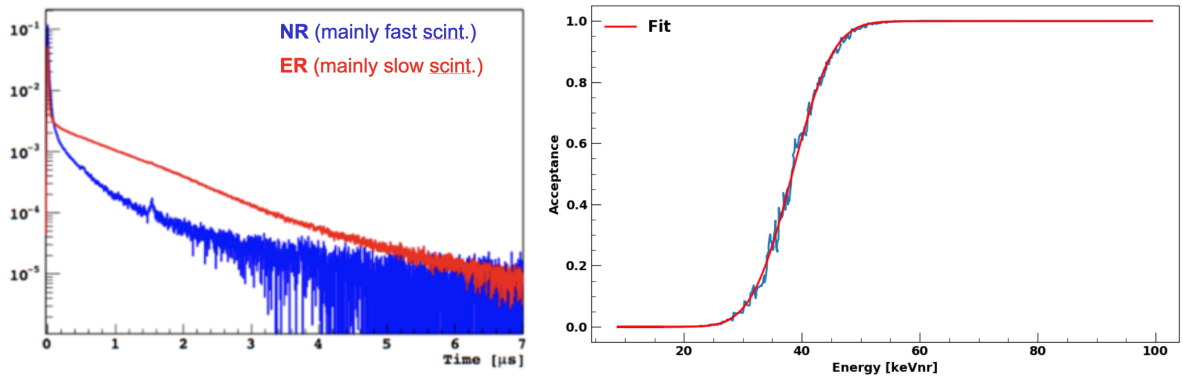

FIGURE 2.2. : Left : Normalised S1 pulse shape for an NR (blue) and an ER (red). Right : Signal efficiency versus energy with PSD cut for an ER background $<$ 0.1 events / 10 years [76].

In addition to this ratio, argon-based experiments can use the S1 pulse shape to discriminate between ER and NR. Indeed, in the scintillation mechanism described in section 2.1.1, the di-argon excited state Ar_2^* can be in spin singlet or spin triplet state. For NR, the singlet state is the most populated (75 %) while for ER, the triplet state is dominant (67 %). Argon de-excites significantly faster in the singlet state ($\approx$ 6 ns lifetime against $\approx$ 1400 ns for triplet state), thus the proportion of light in the first few hundreds of ns of S1 signal is higher in NR than in ER. This signal attribute is illustrated in Figure 2.2 left where S1 is shown in an ER (red) and NR (blue) scenario. Most of the NR

signal is in the first few tens of ns of S1 while the photons of the ER S1 pulse are more spread in time. This argon asset allows for S1 Pulse Shape Discrimination (PSD), it was exploited by DS50 and is still exploited by the DEAP-3600 collaboration. DEAP-3600 precisely measured the background reduction power allowed by S1 PSD to be 3.6 x 10^8 to 2.4 x 10^9 [77, 78]. Note that the singlet-triplet population depends on the energy of the interaction, reaching almost equal repartition below 10 keV leading to less performant discrimination [76].

It is worth underlining that the energy reconstruction proposed in Equation (2.6) depends on S1 and S2, which also serve as discriminating variables for ER and NR identifications. Keeping in mind that NR interactions can lead to quenching thus modify the energy reconstruction if misidentified, WIMP search experiments use the keV_{ee} and keV_{NR} units for energy. The former means *keV electron equivalent* (ER interaction), the latter *keV Nuclear Recoil* (NR interaction).

In DS20k, the discriminating variable representing the PSD is called f_p. f_p represents the fraction of photo-electrons measured in the p first ns of S1 signal. p is optimised for each experiment, for example in the case of DS50 $p = 90$ ns. In the case of DS20k, a dedicated PSD study was performed in [76], and maximal ER/NR separation was found at $p \approx 200$ ns, larger than the one of DS50 due to the drastically increased TPC size. Relying on such discrimination variable, DS20k expects a background-free search, with high mass ER background budget chosen to < 0.1 events / 10 years, corresponding to $10\,\text{GeV/c}^2 < \text{M}_\chi < 10\,\text{TeV/c}^2$. The resulting NR (signal) acceptance has been studied as function of energy, as shown on Figure 2.2 right. Above 50 keV_{NR}, one can see that the NR acceptance probability reaches ≈ 100 %. Background-free search was achieved by DS50 with their final high mass search result in 2018 [38]. Xenon-based experiments cannot benefit from such an asset because the two states lifetimes are too close to each other (4 ns and 22 ns for singlet and triplet respectively).
Apart from pure background events considerations, the rather high rate in a TPC with 3.7 ms drift time at maximum in the case of DS20k (see section 2.3.1) might induce pile-up (defined as two events occurring close in time and being un-resolvable). The impact of such pile-up on the low mass WIMP search is studied in chapter 4.

2.2.2. Nuclear recoil backgrounds

According to the previous statements, the most troublesome background is not the most numerous one, but the one that comes from interaction with the argon nucleus (producing an NR). Such particles are neutrons and α, emitted by ^{238}U, ^{235}U and ^{232}Th radio-contaminants in the detector materials or originating from the lab environment (rock and ^{222}Rn). In order to ensure low NR background from neutrons and α particles, material assays are performed by a dedicated working group in the collaboration. Radioactivity of each considered material of each sub-component of the detector is precisely measured. The NR background rate from exposure of the final materials is then derived thanks to Monte Carlo simulations, weighted by the volume and density of the sub-component.

As for γ-induced ER background, NR background remains and is tagged thanks to veto detectors.

α background α particles are mainly originating from ^{210}Pb (and its products ^{210}Bi and ^{210}Po) on surfaces due to exposition to ^{222}Rn present in the lab during construction. α being heavy and charged, they are mostly surface background.

Neutron background The predominant neutron background comes from material contamination through both (α, n) reactions and ^{238}U fission. In addition, a part of neutron background comes from cosmogenic muon showers in the cavern of LNGS (or directly in the detector), neutrons from the rock of Hall C or finally from ^{222}Rn diffusion. Neutrons are more dangerous than α as they are neutral : they interact less and penetrate more than α particles. In other words, neutron background can penetrate the innermost part of the TPC, where WIMP search analyses are performed.

ν background With a 1000 times bigger volume than DS50, DS20k is expected to highly improve the sensitivity reached by previous argon experiments and to get closer to the so-called neutrino floor. The latter is the (M_χ ; σ_{SI}) phase space region where WIMP signal becomes so low that neutrino background with same signal characteristics becomes dominant and prevents discovery. Both atmospheric and solar neutrinos contribute to this background. The neutrino floor isn't already reached by 2^{nd} generation experiments (such as DS20k, XENONnT or LZ) but as one approaches the limit, one begins to expect neutrino events interacting with LAr.

2.3. The DarkSide-20k experiment

2.3.1. Design of the detector

The geometry of DS20k aims at tagging NR background preceding or following interaction in the TPC, so that such background could be ruled out by data analysis. To achieve so, DS20k is designed as a layer detector shown in Figure 2.3. The left-hand Computer Assisted Design (CAD) is a view of the full detector (not including the cryogenic system) while the right-hand CAD focuses on the inner detector.
The inner detector is held in an oval-shaped radiopure stainless steel vessel and composed of two multitons UAr sub-detectors. The one at the center is the TPC which, in the case of DS20k, is a 3.48 m high octagon with inscribed diameter of 3.50 m, its active mass is 49.7 tons of purified UAr. Thanks to the purification of UAr, the electron lifetime in the DS20k TPC reaches $\approx$ 16 ms. In comparison, the maximum electron drift time is 3.7 ms, approximately four times lower than its lifetime.

Ionisation electrons drift under a 200 V/cm drift field to the top of the TPC, the extraction field is set to 2.8 kV/cm to allow electrons entering the 7 mm thin layer of argon where the 4.2 kV/cm luminescence field allows electro-luminescence. This configuration

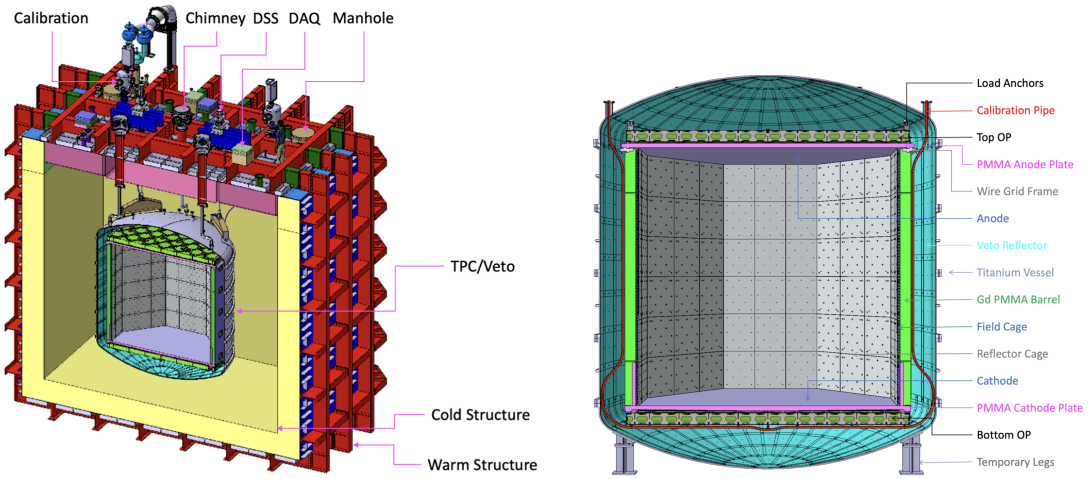

FIGURE 2.3. : Left : The DarkSide-20k experiment. Right : The inner detector of DarkSide-20k [63].

leads to both 1 mm resolution in Z and g2 $\approx$ 20 pe/e$^-$.

Scintillation and ionisation light emitted after interaction are collected by two 10.5 m^2 arrays of $\approx$ 1 cm^2 large Silicon Photo-Multipliers (SiPMs) located at the top (anode region) and bottom (cathode region) of the TPC. The green area at the top of the octagonal TPC of Figure 2.4 bottom represents the SiPMs array in the anode region. SiPMs are based on a counting photons technology thanks to Single Photon Avalanche Diodes (SPADs) inside them. SiPMs are 8 $\times$ 12 mm^2 arrays of 94,900 SPADs. SPADs are well adapted to the detection of low intensity signals made of photons as they can be functioning in avalanche mode, which multiplies dramatically the incoming signal up to macroscopic intensities. To achieve so, SPADs are made of $p-n$ junction semiconductors that are operated under a strong electric field. When a photon arrives and deposits energy, the charge carriers (electrons and holes in the substract) generate other charge carriers by ionisation which creates the avalanche with a known gain. This effect enables the detection of individual photons but has the drawback of a high dark noise rate. Thanks to resistors and capacitors that control the charge and discharge of the SPADs, the charge carriers transform into a macroscopic and detectable current that is released briefly (typically in O(1) ns). After the discharge of a SPAD, the SPAD is off until the circuit recharges it up to the "ready" state. During this moment, the detection is possible thanks to the other SPADs of the SiPM. Thanks to SPADs, SiPMs have a faster response, a higher signal to noise ratio, a lower level of noise and lower radio-activity compared to usual Photo-Multiplier Tubes (PMTs). In total in the TPC, there are 202,752 SiPMs grouped together to ease the read-out. Figure 2.4 top shows a scheme of SiPMs grouping. SiPMs are grouped by 24 into Tiles, themselves grouped by four into Photo-Detection Modules (PDMs) corresponding to one readout channel (one PDM is the analog sum of the four Tiles signals). PDMs are also grouped by four into Photo-Detector Units (PDUs) read by front-end

electronics modules and processed by further Data Acquisition System (DAQ). As a summary, there are 202,752 SiPMs into 8,840 Tiles into 2,112 PDMs (readout channels) into 528 PDUs allocated for the TPC. This layout allows a XY resolution lower than 3 cm.

Lastly, the walls structuring the TPC are 15 cm thick and made of acrylic (precisely PolyMethyl MethAcrylate (PMMA)) with high radio-purity. As a consequence of the almost null photodetection efficiency of SiPMs at 128 nm (scintillation wavelength of argon), the collaboration uses the TetraPhenyl-Butadiene (TPB), a WLS painted on top of the reflector (called Enhanced Specular Reflector, ESR) panels covering the TPC walls. TPB absorbs 128 nm photons and re-emits 420 nm photons. At 420 nm and at 80 K, the photodetection efficiency of SiPMs is $\approx$ 40 %.

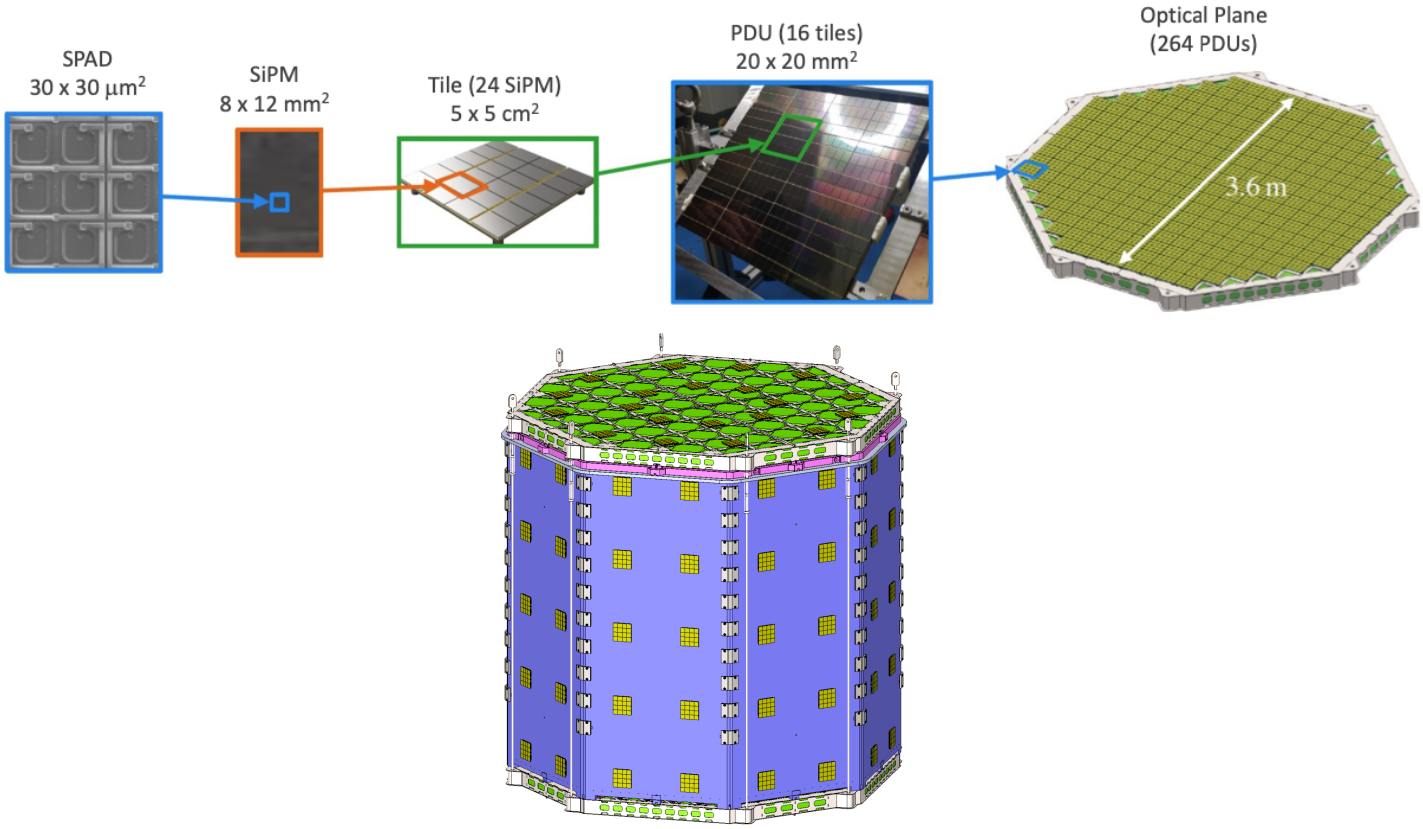

FIGURE 2.4. : Top : Grouping of SiPMs into Tiles, PDUs and final TPC optical plane. Note that in the veto, the grouping stops at (v)PDU level. Bottom : A CAD view of DS20k TPC from outside. The top optical plane of the TPC is the green area. Part of the veto PDUs are shown on the external walls of the TPC in yellow. [63]

The second sub-detector in the inner detector is the so-called inner veto that envelops the TPC with 32 tons UAr active mass. The inner veto aims at tagging background

(especially neutrons from radio-contamination of materials) before or after they interact in the TPC by collecting scintillation light - wavelength shifted thanks to PolyEthylene Naphthalate (PEN) - with SiPMs. There are 46,080 SiPMs grouped into 480 readout channels corresponding to 120 vPDUs (veto Photo-Detection Modules), disseminated on the inner surface of the stainless steel vessel and on the outer surface of the TPC as can be seen on Figure 2.4 bottom. They cover 3.2 % of the geometrical surface of the veto providing 4 % scintillation Light Collection Efficiency (LCE) in the veto.

Finally, the inner detector stands at the center of a 8.5 × 8.5 × 8 m^3 PEN-coated proto-DUNE like cryostat filled with 650 t of AAr at liquid phase. The first purpose of the cryostat is to keep the detector cold (boiling point of ^{40}Ar : 87.3 K) thanks to a specific cryogenic system not shown on Figure 2.3 left. The cryostat also acts as an active veto, tagging high energy neutrons (E > 10 MeV/c^2) produced in cosmic muon showers thanks to the scintillation light collected by 12,288 SiPMs, mounted into 32 vPDUs.

2.3.2. Construction status and schedule

The different parts of the DS20k experiment are built and tested around the world. First, UAr will be extracted in the USA, the construction of the Urania plant is on going since end of 2023. In the current schedule, UAr extraction should take place in 2025 and 2026. After extraction from mines, UAr will be shipped to the Aria facility in Sardinia, Italy for cryogenic distillation. There, a reduced size test column called Seruci-0 has reached final operation. Its goals were to test the physics of the cryogenic distillation and to prepare future shifters for operation with the final facility. Final distillation column has been in construction since beginning of 2024 and will last until mid 2026 when UAr is shipped and Seruci-1 operation starts.

In parallel, the 270,000 SiPMs of both the TPC and the veto have all been produced. They are now being mounted into PDUs and under cryogenic test phase in Italy, Poland and UK. 43 % of them have been tested by May 2024, showing a 94 % validation rate. The PDUs production and tests should be completed by mid 2025, followed by the assembly of the TPC optical planes and the TPC assembly itself.

Finally at LNGS, the building of the DS20k experiment began end of 2022, starting with the construction of the concrete floor of the cryostat. The mechanical structure of the cryostat was completed during the second half of 2023. Figure 2.5 shows a picture of the cryostat of DS20k in the Hall-C of LNGS. The radiopure stainless steel vessel should be ready by beginning of 2026, approximately at the same moment as the TPC optical planes for further inner detector assembly. The full detector is expected to be ready by mid 2027, for commissioning and first physics runs.

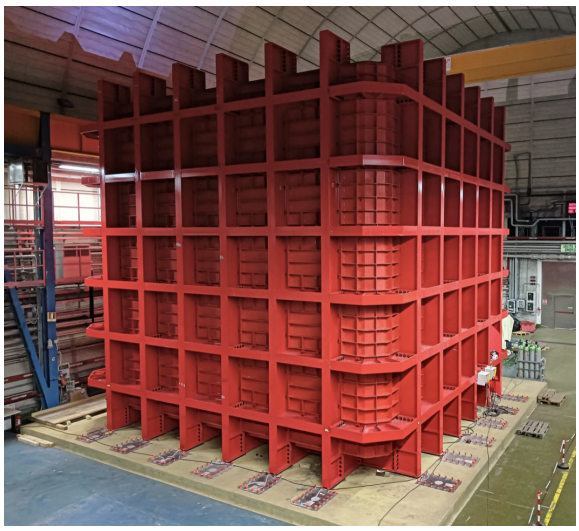

FIGURE 2.5. : Picture of the mechanical structure of the DS20k cryostat completed in 2023.

2.3.3. Nuclear recoil backgrounds rejection

The analysis for high mass WIMP search is a succession of selections aiming at describing and removing background events. Thus, background simulations and selection studies are done ahead of data collection.

α background The α background being a surface one, a way to remove it is to actually search for WIMPs in a reduced volume at the center of the TPC. This volume is called the fiducial volume (FV), an octagon reproducing the shape of the TPC but 30 cm (resp. 70 cm) are vetoed from the side walls (resp. from the top and bottom optical planes). The mass corresponding to the FV is 20 tons. [2] In addition, α background can be identified thanks to their decay energies.

Neutron background First of all, most neutrons are foreseen to interact several times in the TPC, generating so-called multiple scatters. On the contrary, WIMPs are expected to interact only once in the TPC. Thus, the NR single scatter requirement allows a preliminary cleaning of the data. In addition, the design of DS20k aims at detecting single scatter neutron background outside the TPC thanks to active vetoes allowing further neutron rejection searching for time coincidence between events in the TPC and the ones in the vetos.

[2] Of course, ER background rejection also benefits from such fiducialisation. Part of γ-rays emitted from the walls of the TPC and optical planes are vetoed by this FV.

ν background Such background events have the same characteristics as a WIMP event : only one interaction in the detector due to their very low interaction rate. The measurement of coherent astrophysical solar neutrino scattering off target nucleus was predicted to be possible since 1974 [79]. In 2024, XENONnT [80] and PandaX [81] xenon-based dual phase TPCs performed a dedicated search for ^{8}B solar neutrinos and both rejected the background-only hypothesis at more than 2-σ. In the case of DS20k with full 200 ton $\times$ year exposure, one expects three ν events via CEνNS in the energy Region of Interest (RoI) for WIMP signal.

With such a detector, the NR background budget after cuts is < 0.1 events / 10 years of data taking, in addition to the three CEνNS irreducible neutrino events.

2.4. DarkSide-20k sensitivity at high WIMP mass

Thanks to Monte Carlo simulations produced by a GEANT-4 based software (called g4ds in the following) [82], the collaboration could derive the DS20k background model after the different events selections.
In addition, toy Monte Carlo simulations were made to model the signal expected at different WIMP masses between 10 GeV/c^2 and 10 TeV/c^2 according to Equation (1.37). The sensitivity is then derived by a profile likelihood approach for different exposures. The targeted running time is 10 years, resulting in a 200 ton $\times$ year exposure for search in the fiducial volume, 500 ton $\times$ year exposure for search in the full volume.
Figure 2.6 top shows the sensitivity of DS20k in terms of exclusion power at 90 % Confidence Level (90 % C.L.) for 5 years (dotted lines) and 10 years (dashed lines) of data taking, both in the fiducial (blue lines) and full (red lines) volume [63]. 20 years of search in the full volume is also shown in full red line. For comparison purposes, second generation xenon-based experiments LZ [83] (grey line) and XENONnT [84] (green line) projected sensitivities at targeted exposure (respectively 15.3 ton $\times$ year and 20.2 ton $\times$ year) are shown. DS20k should be able to reach the sensitivity of the two xenon experiments above 10 GeV/c^2 after approximately three years. On that figure, the grey shaded area represents the neutrino floor for argon target, the dark green area represents XENON1T excluded region by their 2018 analysis [85] while the light green area represents the result of PandaX-4T from their 2021 analysis [36].
As DS20k expects a background-free search at high mass, it is also interesting to show the 5 σ discovery potential. On Figure 2.6 bottom, the discovery potential of DS20k is estimated for the same running times as the 90 % C.L. exclusion power limits [63], and again compared with the ones of XENONnT and LZ as well as XENON1t and PandaX-4T results.

Of course, such a sensitivity - depending on the crucial ability to suppress background thanks to signal features (S1/S2, PSD) and the detector itself (vetos) - strongly depends on simulations and event reconstruction, which rely on the detector calibration. The purpose of the next chapter is to describe the multi faceted calibration of DS20k, which

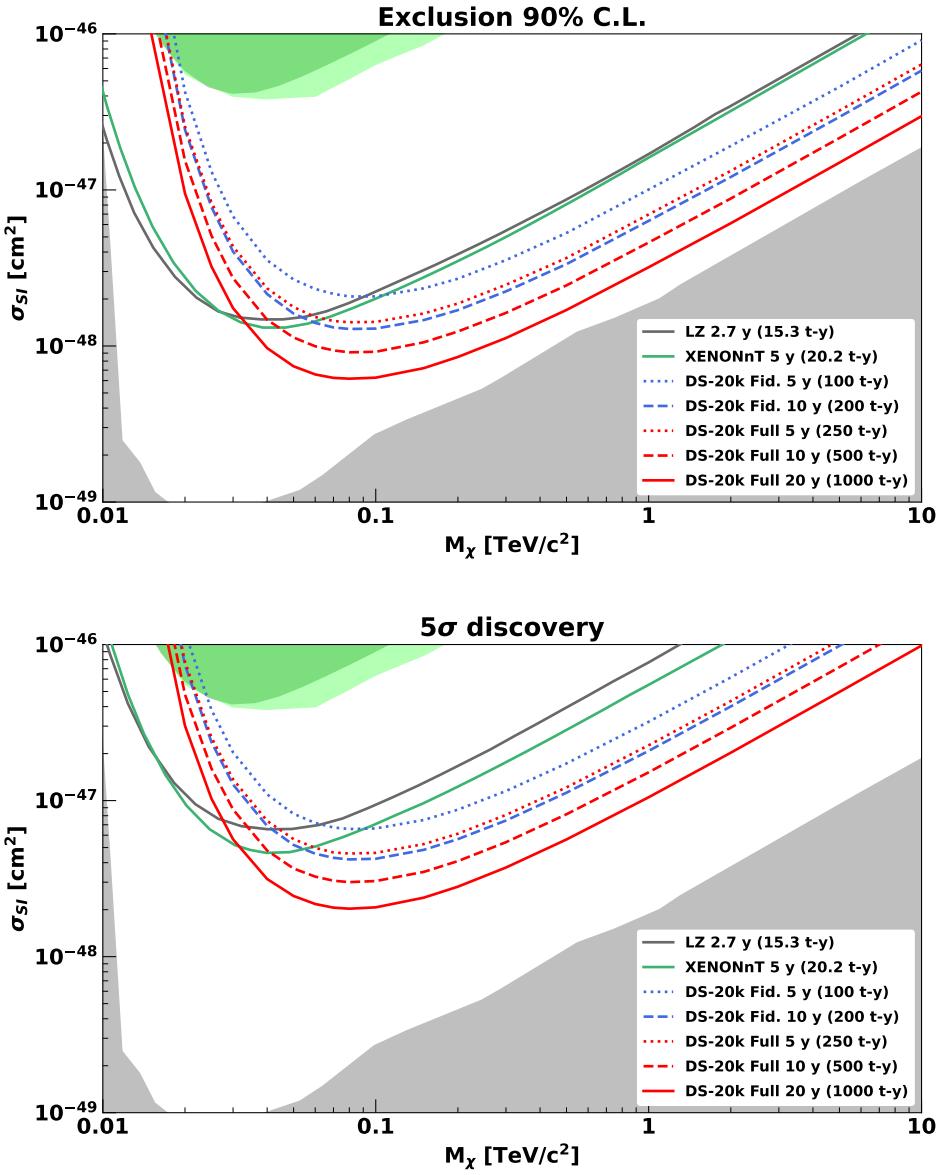

FIGURE 2.6. : DarkSide-20k exclusion limit for different running times (5 years dotted lines, 10 years dashed lines and 20 years full line) and different search volume considerations (fiducialised volume ('Fid.' curves, blue) or not ('Full' curves, red)). The limits are compared with the neutrino floor (grey shaded area), the result of PANDA-X (light green shaded) and XENON1T (dark green shaded) and the projection of LZ (grey) and XENONnT (green) experiments.
Top : Sensitivity computed in terms of exclusion power at 90 % Confidence Level.
Bottom : Sensitivity computed in terms of discovery potential (at 5 σ) [63].

will be the largest TPC ever built for dark matter search.

3. The DarkSide-20k calibration programme

Summary

The calibration of an experiment is a crucial landmark in the path towards high quality data collection as it permits the deep understanding of the detector response to signal and background processes. To achieve so, one uses radioactive sources of particles with known behaviour : nature of emitted particles, interaction type within the detector, particle energy spectrum at emission and activity. The calibration of the detector response to signal-like and background-like interactions permits to check the particle identification, and especially to quantify the pulse shape discrimination power, that enables to mitigate ER background during science runs. Furthermore, the WIMP dark matter candidate will be mainly searched through a NR with energy in a wide range depending on the mass regime considered in the analysis. Thus the characterisation of the energy response of the detector as well as the NR acceptance with respect to energy is of primary importance. In the case of DS20k, the detector will be large which might induce a significant pile-up rate and degrade the detector performance, because of the long ionisation electron drift time. Thanks to calibration data, one will be able to verify the capacity to reconstruct events. Last, as the detector will be run for a decade, different calibration runs will be needed along data collection to check the proper functioning of the detector and its stability versus time.

The design of the experiment (including its size, the layer structure of the detector and the choice of materials for the TPC walls) as well as the cryogenic environment challenge the calibration of the inner detector. This chapter describes first the whole calibration procedure, with a peculiar attention drawn on the external calibration using radioactive sources as my laboratory, the Centre de Physique des Particules de Marseille (CPPM), proposed to design and build the system that permits radioactive sources of photons and neutrons to approach the innermost part of the DS20k experiment. Then, section 3.2 presents the simulations that I have performed to assess the feasibility and efficiency of the external calibration. To finish, section 3.3 summarises the feasibility tests performed at CPPM and Organisation Européenne pour la Recherche Nucléaire (CERN) before design validation and final construction. These tests, to which I participated to, aim at demonstrating that the calibration set up design matches DS20k specifications.

3.1. Multi-faceted calibration

3.1.1. Motivations for calibration

The preparation of a robust physics analysis, as soon as data taking starts, includes to conduct a solid calibration of the detector response to signal-like events and background events as well as the foreseen means to separate them (such as the S1 PSD described in Chapter 2) but also to scrutinise its uniformity, firstly in space and later in time along data taking. In the peculiar case of DS20k, the calibration needs to address some key topics, catalogued in this introduction.
First, DS20k is expected to search for WIMP in a substantial energy range, from 0.5 keV_{nr}

to 200 keV_{nr}, corresponding to WIMP masses from a fraction of GeV/c^2 to multi-TeV/c^2. Below $M_\chi = 10$ GeV/c^2, the WIMP search is no longer background-free (see Chapter 4). The low energy data are expected to be dominated by ER background from ^{39}Ar β decays as well as X and γ decays from radioactive elements in the materials used to build the inner detector. The ER background energy range for a low mass analysis spans between 0.05 keV_{ee} and 20 keV_{ee}. DS50 proved that a comprehensive study of low energy calibration recoils permitted improving the low mass sensitivity of the detector by up to a factor 10 [56]. Hence the DS20k calibration should be able to provide means to measure the energy response linearity of the detector.
In addition, in the so-called high mass search ($M_\chi > 10$ GeV/c^2), the background-free search relies on the ability to discriminate between ER and NR events thanks to the S1 PSD. The goodness of the $p = 200$ ns estimate for PSD optimisation in DS20k with f_p variable (see Chapter 2) must be validated as well as the NR acceptance vs energy. Thus, it is essential to include radioactive sources of both NR and ER producers in the calibration programme of DS20k.
Plus, the spatial and time dependances of the detector response have to be understood for powerful and trustworthy physics analyses, especially in such a large TPC, 1,000 times larger than its predecessor. The calibration system should give the ability to regularly and reliably measure the detector performance and means to correct for any variation due to aging for instance.
To finish, the calibration should allow to measure all the important detector parameters like g1 and g2 (see Chapter 2), the single electron resolution, the electron lifetime in the TPC, the XY and Z spatial resolutions.

The forecasted calibration programme, that will encompass all the challenges at stake during calibration runs is three-faceted.

First, the SiPMs will be frequently calibrated thanks to LASER photons, in order to verify their good functioning and their time stability.

Second, in line with its predecessor DS50 and xenon-based dual phase TPCs, the collaboration foresees the injection of short lived diffuse radioactive sources with short decay chains, namely ^{83m}Kr and ^{220}Rn, in the bulk of the TPC. In addition, DS20k can also take advantage of the residual ^{39}Ar atoms in its volume to have a permanent source of calibration for detector response. Despite their unsuitability to provide means to measure the XY and Z resolutions (the position of emission is not known), diffuse sources will permit the characterisation of the spatial uniformity of the detector response, and to reach quickly high statistics calibration data.
On top, at the beginning of the run, the short lived cosmogenic radioactive ^{37}Ar ($T_{1/2} \approx 35$ days) is present in the bulk of the experiment. The isotope produces low energy positrons (O(200 eV)) by electron capture, permitting to extend the calibration to low energy deposits. In the case of DS50, ^{37}Ar allowed to measure the electron recoil response down to 179 eV_{ee}, corresponding to 8 ionisation electrons [66].

The number of suitable sources for bulk calibration is low and they are only providing electrons and positrons for ER calibration. Hence the need to have an additional calibration method, providing several NR and ER sources of calibration and also measure detector parameters of interest.

To do so, the DS20k collaboration will build a dedicated system to allow external calibration using long lived radioactive sources of photons and neutrons. The external calibration system, described in details in Section 3.1.2, will permit the XY and Z position reconstruction and to measure the position resolution as the position of the emitter is known. The energy response and NR acceptance vs energy will both be measured with better precision as several neutrons (three) and photons (five) sources, with different energy, are foreseen to be used. However, the ER calibration with external sources of photons is confined at the borders of the TPC, in the O(10 cm) from the walls and near the site of the calibration system. At first, external calibration runs are expected to be done once a year and to be performed again during the lifetime of the detector depending on its specific needs.

3.1.2. The external calibration set-up

The primary goal of the external calibration system is to approach radioactive sources near the TPC, inside the inner veto for TPC calibration. To achieve so, two almost U-shaped orthogonal tubes, that are shown in red on Figures 2.3 right and 3.1 top, are designed to guide the sources at a target position near the TPC. The integration of radioactive sources inside the tubes will be done on the roof of the detector cryostat, through glove boxes.

The two tubes are made in stainless steel, in order to have the same vertical shrinkage as the inner detector vessel while cooling. They have an inner diameter of 5 cm, the pipe thickness is 1.5 mm. The tubes are shaped in order to be as close as possible from the TPC lateral walls (3 cm) and 1 cm below the bottom optical plane, to maximise the rate of events in the TPC during calibration runs. The two tubes are orthogonal, in order to cross each other below the TPC, one tube is bended to bypass the other. Because of detector integration needs and detector maintenance requirements during the 10 years of operation, the exits of the tubes must be in the peripheral section of the cryostat. Hence, the tubes are bended with a sequence of 40 cm curvature radius bends to be as close as possible to the TPC yet reach large distance at the top of the cryostat. The individual total tube length is 20 m. The tubes are cut into smaller bended sub-parts and re-assembled together into the final tube thanks to a set of flanges. The precise shape of the tubes is shown in Figure 3.1 top left and their integration in the detector in Figure 3.1 top right. The use of two guide tubes is driven by the need to increase the volume of the detector that will be characterised.
To ensure the circulation of the radioactive sources, the latter will be attached to two ropes, themselves driven by two synchronous motorised systems. One, the puller, draws the source towards itself while the other, the follower, releases some rope length to allow

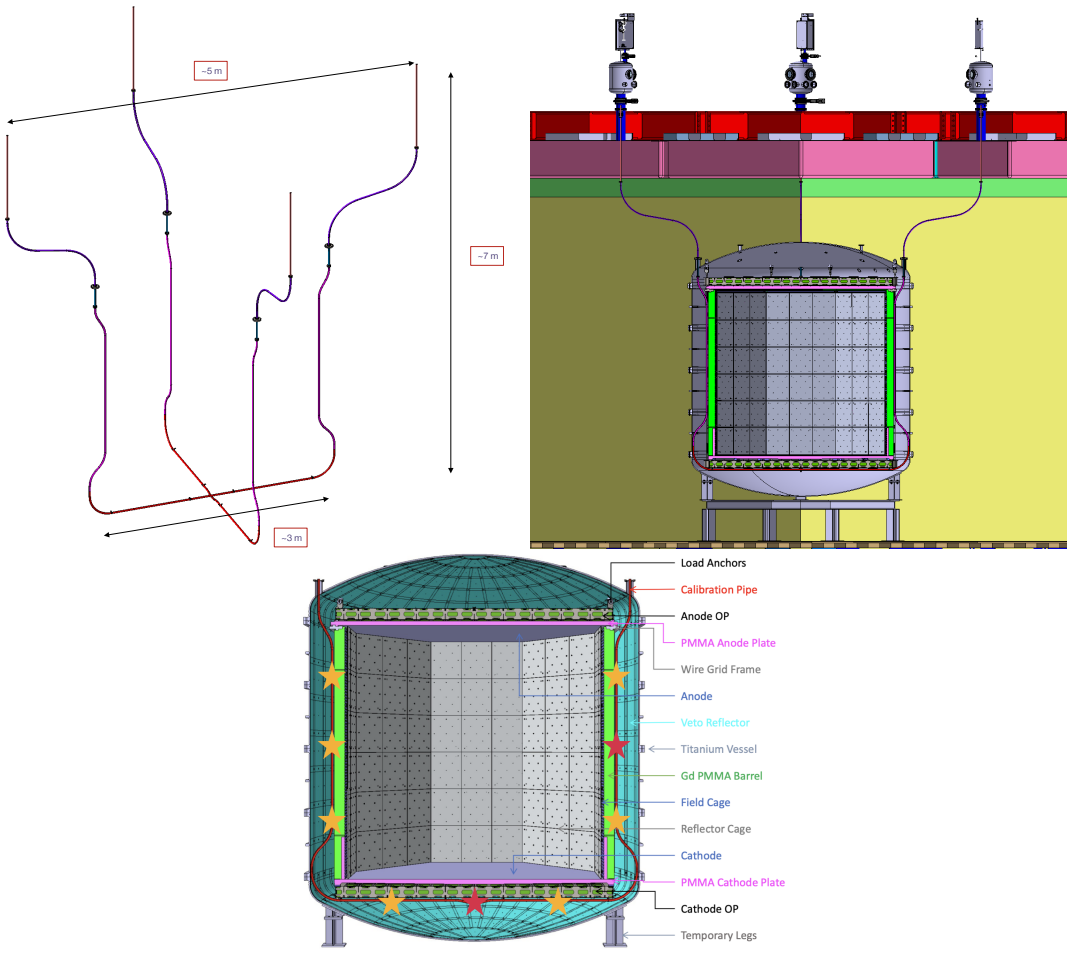

FIGURE 3.1. : Top : 3D view of the calibration guide tubes (left) and their integration in the full detector (right). Bottom : CAD view of the inner detector with the nine calibration positions shown with the stars. Red stars emphasise where the calibration simulations are performed.

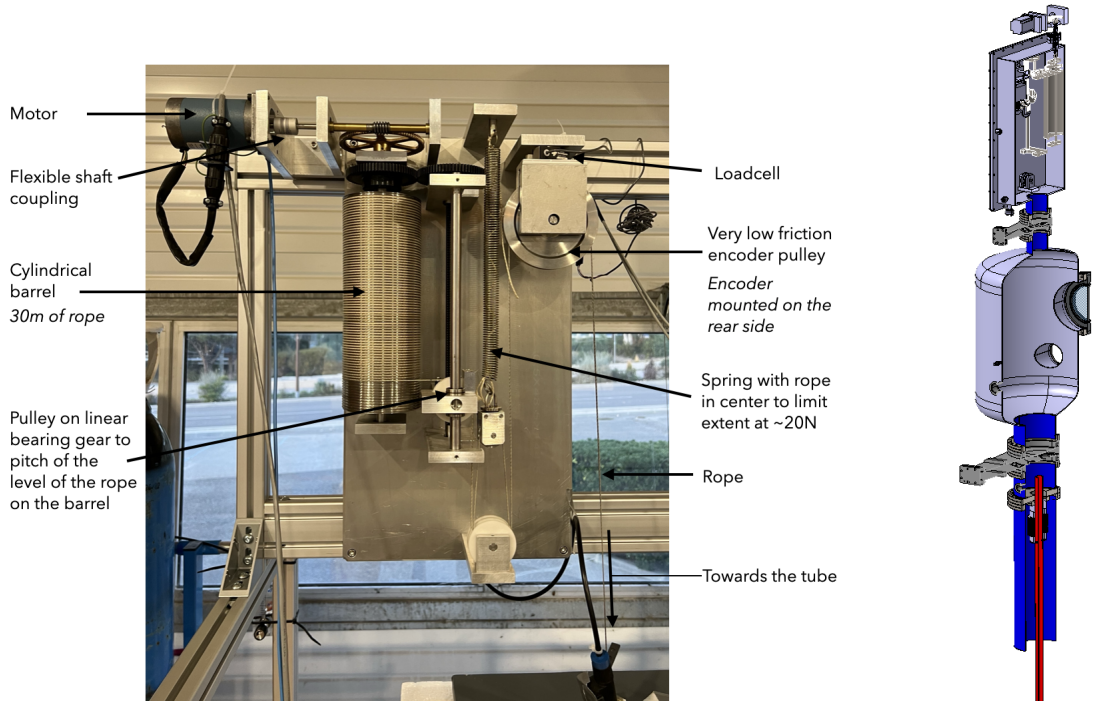

FIGURE 3.2. : Picture and legend of the motorised system and its sub-components (left) and CAD of the motorised system combined with the glove box below it (right).

the source to move towards the puller. To do so, the motorised systems are composed of barrels to store or deploy the rope. Sensors, called encoders, placed in the motorised systems measure the length of rope repatriated (resp. released) by the puller (resp. follower) motorised system by measuring the number of revolutions made by sheaves guiding the path of the rope through the motorised system. In order to measure the mechanical tension applied on each rope, sensors called loadcells are also integrated in the motorised systems. Useful information given by the sensors are measured by a dedicated DAQ (micro controller box of Figure 3.13 bottom and managed by the Controller box of the same Figure), stored and displayed to shifters in real time thanks to a custom software to ensure the good functionning of the motorised systems during the calibration runs. A picture of one motorised system is shown on Figure 3.2 left. The motorised systems are placed at the two exits of each tube (there are four motorised systems in total). Between the tube and the motorised systems, there are glove boxes which aim is to allow the safe insertion and handling of the sources before and after calibration runs. The glove box and motorised system CAD is shown on Figure 3.2 right.

During a standard calibration run, the radioactive source is placed at nine positions around the TPC (the positions are shown on Figure 3.1 bottom), with a target position resolution of $\approx 1\,\text{cm}$. The nine positions are splitted into three positions per side of the

TPC and three at its bottom. Having nine calibration positions is an adjusted choice driven by the low penetration of photons in the TPC (see Section 3.2.1.2 and Figure 3.8) and the need to have a reliable estimate of the position resolution in the detector. Once the source is placed and stopped at one of its calibration positions, the shifter waits until the collection of high enough statistics of interesting events, such as single scatters for example. The main goal of the next section is to determine the physics reach of such calibration system with a set of radioactive sources. The study also permits to derive the best-suited activity of these sources leading to the estimate of the time needed to perform a full external calibration run, taking into account detector design and DAQ limitations.

3.2. Simulation of the external calibration and derivation of the calibration procedure

The objective of this section is to present the first simulation work conducted to validate the design of the proposed guide tube system. This aims at exploring the physics potential of the external calibration discussed in section 3.2.1 and formulate a calibration strategy outlined in section 3.2.2. The latter includes a quantitative estimate of the activity of radioactive sources, adjusted to meet the requirements of the DAQ, and determining the time required for a complete calibration run. Finally, additional simulations were carried out to demonstrate the adverse negative effects of the presence of calibration tubes within the inner detector on its performance in terms of backgrounds and light collection efficiency (section 3.2.3).

3.2.1. Simulation of the calibration

The simulation of the calibration was performed thanks to a collaborative GEANT-4 based software, called g4ds [86], in which the geometry of DS20k is integrated. Note that at the time of the study, the TPC walls were foreseen to be loaded with Gadolinium (Gd), which is not the current option anymore. Neutron capture by the Gd induces the emission of photons. The consequences of this change on the external calibration of DS20k should be studied. The two guide tubes have been implemented in the g4ds package. Incident particles emitted by a peculiar radioactive source are simulated with Monte Carlo from their initial position. Two cases are studied : a particle emitted on the side of the TPC, at mid-height of the side wall, defining the position $z = 0$ cm (the position is the one shown by the red star on the right-hand side of the scheme of Figure 3.1 bottom), or a particle emitted at the bottom of the TPC, at the center of the TPC cross section (as shown by the red star at the bottom of the scheme of Figure 3.1 bottom). After emission, their simulated tracks inside the detector are recorded. The simulation tool provides high level information such as total energy deposited inside the TPC, number of clusters of interaction in the TPC, type of interaction (ER, NR or both in case of an event with a neutron with accompanying photon from Gd capture, for example), etc.

The total energy deposited in the TPC is taken as study variable for calibration. Energy spectra are derived, taking into account detector energy resolution effects. [1]

3.2.1.1. Calibration of nuclear recoils with sources of neutrons

WIMPs are expected to produce pure nuclear recoil single scatters (pure NR SS) as they merely interact with ordinary matter. This is why such events should be carefully calibrated. We define the Region Of Interest (ROI) as the expected energy deposit for a WIMP, E_{ROI} = [30, 200] keV_{nr} [44].

In this section, the study considers two neutron emitters, AmBe and AmC. AmBe (resp. AmC) provides neutrons with an initial energy between 0.2 and 12 MeV (resp. 2 and 7 MeV), following the spectra of Figure 3.3. At emission, neutrons from the two radioactive sources are accompanied by photons [2]. The two sources are complementary and their choice for DS20k is driven by the successful calibration of DS50. Indeed, the AmBe source allows for high energy nuclear recoil calibration, while AmC allows to extend the NR calibration down to low energies [66].

This study presents simulations with sources inside the tubes, on the side and at the bottom of the TPC, using 1e6 decay events per position. On the side, sources are at $z = 0$ (the middle of the TPC side) and 5.5 cm away from the wall (tubes are placed 3 cm from the wall and are 5 cm large with source at the middle). At the bottom of the TPC, sources are placed at $x = y = 0$ which represents the center of the octagonal TPC face. The tube is 1 cm below the TPC floor. This setup corresponds to the description of the external calibration system in 3.1.

On Figures 3.4 & 3.5, neutrons energy spectra are shown for energies of interaction below 200 keV_{nr} respectively on the side and at the bottom of the TPC. The Figures show all pure NR events and pure NR with one interaction in the TPC only (pure NR SS). Integrating the latter energy spectra leads to the rates of events per decay of the radioactive source, as depicted in Table 3.1.

The rates are quite low, which is a caveat for NR calibration but a huge asset for background rejection in the experiment. This is the consequence of thick Gd-doped PMMA walls around the TPC. Indeed, with such walls producing photons accompanying calibration neutrons, having pure NR becomes a challenge. Considering the two sources AmBe and AmC, only 54-65 % of initial emitted neutrons produce a recoil (of any type) in the TPC. Among these events, about 6-10 % is at least composed of one NR -that is already only 3-6 % of the initial emitted neutrons by the source. Yet in this study, the useful events are pure NR single scatters. Pure NR represent 7-16 % of events having at least one NR, i.e. 0.4-0.6 % of all initial events. In the end, between 0.06 % and 0.1 % of

[1] In this very first calibration simulation, only the signal has been considered. The tools to include the pile-up background (internal and external background in the TPC) have been recently made available. The pile-up probability is about 50 % when including the sources [87]. Assessing the impact of this background in the calibration programme derived in this section is the subject of a future work.

[2] Note that the collaboration also recently considered the use of AmLi neutron source, which emits single neutrons with an energy spectrum endpoint around 1.5 MeV, without accompanying gamma emission.

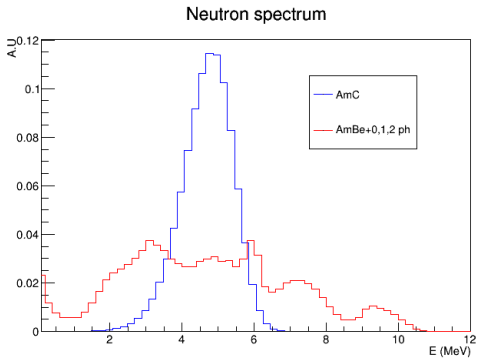

FIGURE 3.3. : Neutron initial energy spectra by the AmC (blue curve) and AmBe (red curve) sources.

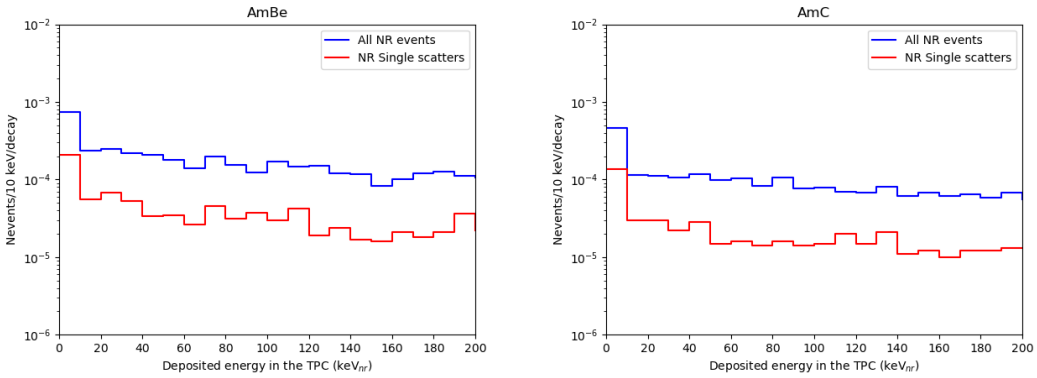

FIGURE 3.4. : Rates of events per decay as a function of the energy deposited in the TPC (keV_{nr}) for two sources of neutrons : AmBe (left, E ∈ [0.2, 12] MeV) and AmC (right, E ∈ [2, 7] MeV). The source is placed 3 cm from the side of the TPC.

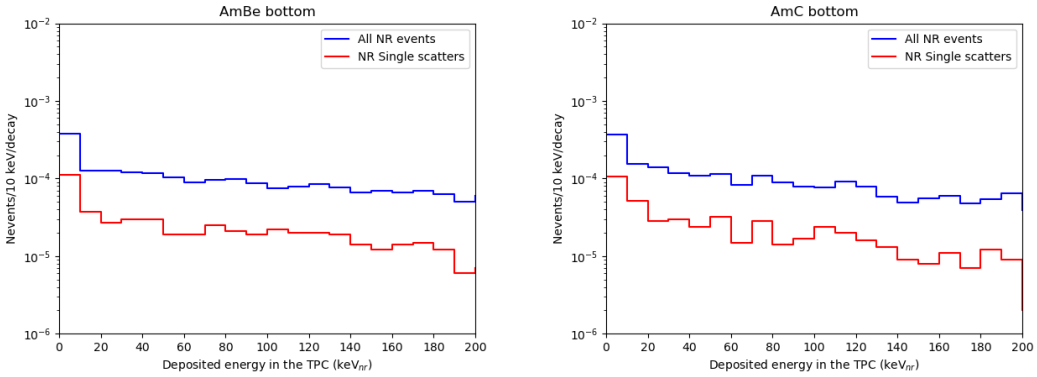

FIGURE 3.5. : Rates of events per decay as a function of the energy deposited in the TPC (keV_{nr}) for two sources of neutrons : AmBe (left, E ∈ [0.2, 12] MeV) and AmC (right, E ∈ [2, 7] MeV). The source is placed 1 cm below the bottom of the TPC.

Source	AmBe	AmC
Initial energy (MeV)	[0.2, 12]	[2, 7]
Rates side (events/decay)	1.1 x 10^{-3}	6.4 x 10^{-4}
Rates bottom (events/decay)	6.5 x 10^{-4}	6.1 x 10^{-4}

TABLE 3.1. : Rates of pure NR single scatters events detected in the TPC per decay of the calibration source inside the tube – on the side and at the bottom of the TPC.

the initial emitted neutrons are retrieved as pure NR single scatters events in the TPC (anywhere and of any energy).
In addition, if one wants to probe the detector response with events passing the Region of Interest (RoI) and the Fiducial Volume (FV) cuts, the rates of Table 3.1 decrease by a factor $\approx$ 2 when applying the selection of energy inside the RoI. Applying the FV cut, the rates decrease by a factor $\approx$ 9 on the side of the TPC (the fiducial volume begins 30 cm away from the side walls) and by a factor ≈ 30 (between 26.5 and 32) at the bottom, where the fiducial volume is 70 cm above the lower wall. Hence, the number of events for such calibration in the RoI and in the FV will decrease accordingly.

It has been shown by other members of the DS20k calibration working group that the material activation due to neutron captures is either negligible or short-lived [87]. Details are provided in Appendix A.

3.2.1.2. Calibration of electron recoils with sources of photons

The calibration of the detector response to ER is also of primary importance as background from photons and electrons is the most numerous one.

To calibrate them, five sources of photons (^{57}Co, ^{133}Ba, ^{22}Na, ^{137}Cs, ^{60}Co) whose energy span from 122 to 1332 keV (see Table 3.2) will be used [3]. The most useful ER events are single scatter (SS) events. The events considered in this study are pure ER SS whose energy corresponds to the one of the photon at emission [4].

Source	^{57}Co	^{133}Ba	^{22}Na	^{22}Na	^{137}Cs	^{60}Co	^{60}Co
Energy (keV)	122	356	511	1274	662	1173	1332

TABLE 3.2. : Initial photons energy for the five sources of photons used for DS20k ER calibration.

[3] Two other sources (^{241}Am and ^{109}Cd) have also been studied as they provide lower energy photons for low mass dark matter search. Yet, they are less efficient thus not shown here [87].
[4] Note that ^{22}Na (resp. ^{60}Co) has two peaks from two decays. When the photoelectric peak is used for analysis, the 511 keV (resp. 1172 keV) is considered.

Source	^{57}Co	^{133}Ba	^{22}Na	^{137}Cs	^{60}Co	^{22}Na	^{60}Co
Energy (keV)	122	356	511	662	1173	1274	1332
Rate - Side (events/decay)	5.7x10^{-3}	5.4x10^{-2}	2.8x10^{-1}	4.5x10^{-2}	2.8x10^{-1}	2.8x10^{-1}	2.8x10^{-1}
SS - Rate - Side (events/decay)	2.6x10^{-3}	1.3x10^{-2}	4.4x10^{-2}	8.3x10^{-3}	3.7x10^{-2}	4.4x10^{-2}	3.7x10^{-2}
Rate - Bot. (events/decay)	9.3x10^{-4}	2.0x10^{-2}	1.5x10^{-1}	2.2x10^{-2}	1.7x10^{-1}	1.5x10^{-1}	1.7x10^{-1}
SS - Rate - Bot. (events/decay)	4.4x10^{-4}	5.6x10^{-3}	2.8x10^{-2}	4.6x10^{-3}	2.6x10^{-2}	2.8x10^{-2}	2.6x10^{-2}

TABLE 3.3. : Rates of all events and separately SS events in the whole energy spectra per decay of the calibration source, as measured in the TPC. The source is positioned inside the tube on the side and at the bottom of the TPC.

Similarly to NR calibration simulations, the ER sources are placed inside the tubes, on the side and at the bottom of the TPC. As the rates of events are lower for ER calibration (photons interact more in the materials than neutrons), 1e7 decays per position were simulated.

Figure 3.6 (resp. Figure 3.7) represents the rate of events per decay as a function of the energy deposited in the TPC for each considered source of photons positioned on the side (resp. at the bottom) of the TPC.

In order to quantify the confinement of the ER external calibration, Figure 3.8 shows the X, Y, Z spot size of the single cluster events for a low energy source (^{57}Co) and a high energy one (^{60}Co), the sources being placed on the side and at the bottom of the TPC. In particular, the RMS of the Z distribution for the sources on the side of the TPC is 11.0 cm (resp. 22.2 cm) for ^{57}Co (resp. ^{60}Co), confirming the statement that the ER calibration will only be possible at the borders of the TPC.

Source	^{57}Co	^{133}Ba	^{22}Na	^{137}Cs	^{60}Co	^{22}Na	^{60}Co
Energy (keV)	122	356	511	662	1173	1274	1332
SS peak - Rate - Side (events/decay)	6.2x10^{-4}	1.1x10^{-4}	3.7x10^{-4}	4.0x10^{-5}	1.0x10^{-4}	5.9x10^{-5}	6.1x10^{-5}
SS peak - Rate - Bot. (events/decay)	8.2x10^{-5}	2.6x10^{-5}	1.6x10^{-4}	1.2x10^{-5}	5.2x10^{-5}	2.7x10^{-5}	2.2x10^{-5}

TABLE 3.4. : Rates of single scatters events with energy corresponding to the photoelecric peak of the spectra per decay of the calibration source, as measured in the TPC. The source is positioned inside the tube on the side and at the bottom of the TPC.

The Table 3.3 presents the rates of all events derived from the blue energy spectra of Figures 3.6 and 3.7. The rates are rather low because of the thickness of the TPC

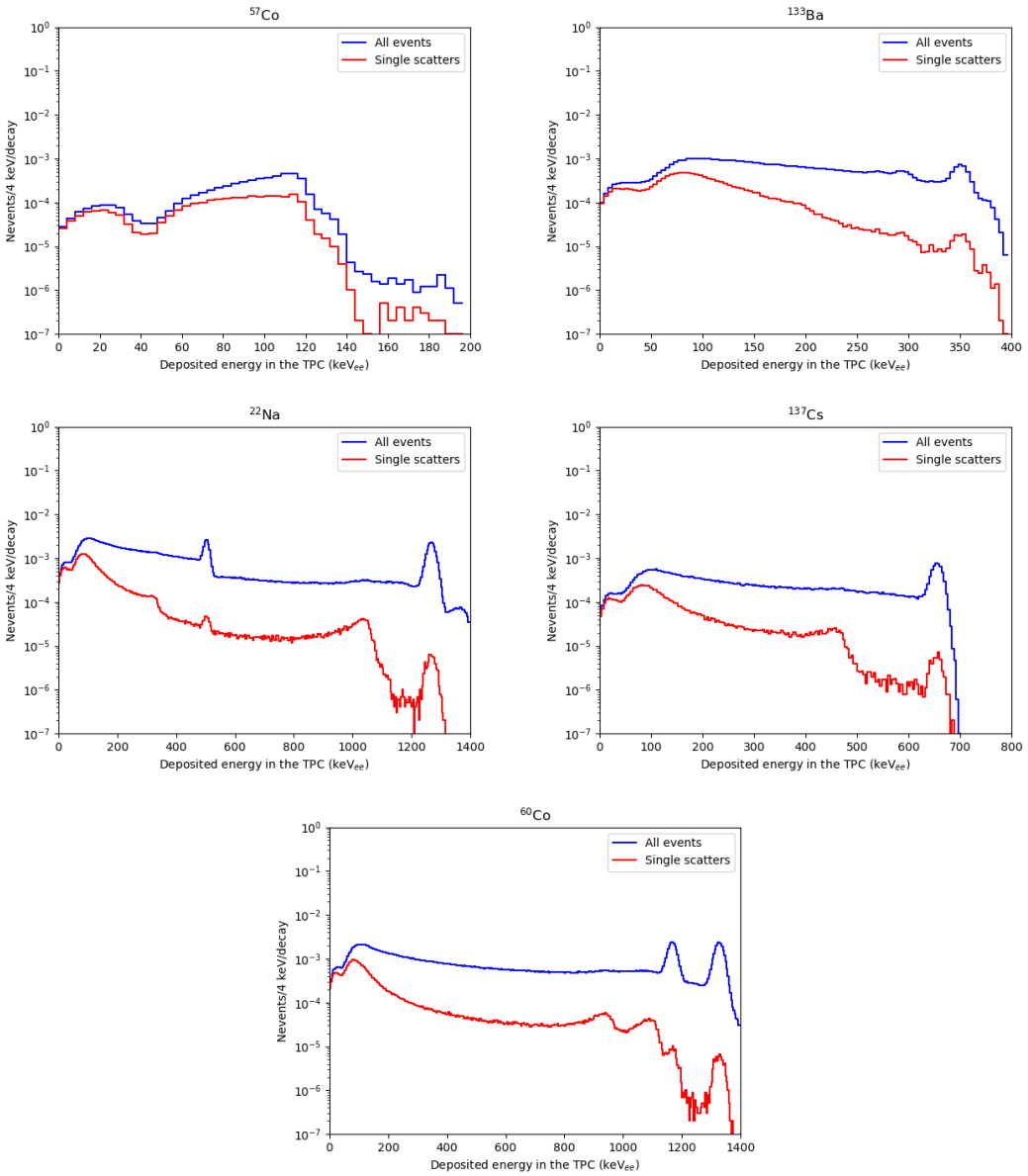

FIGURE 3.6. : Rates of events per decay of the source as a function of the energy deposited in the TPC, for five sources of photons. From left to right and top to bottom : ^{57}Co, ^{133}Ba, ^{22}Na, ^{137}Cs, ^{60}Co. ^{22}Na and ^{60}Co have two photoelectric peaks (see Table 3.2). The spectra are presented for all ER events (blue) and separately for single scatters (red). The source is positioned on the side of the TPC. The expected energy resolution of DS20k is applied.

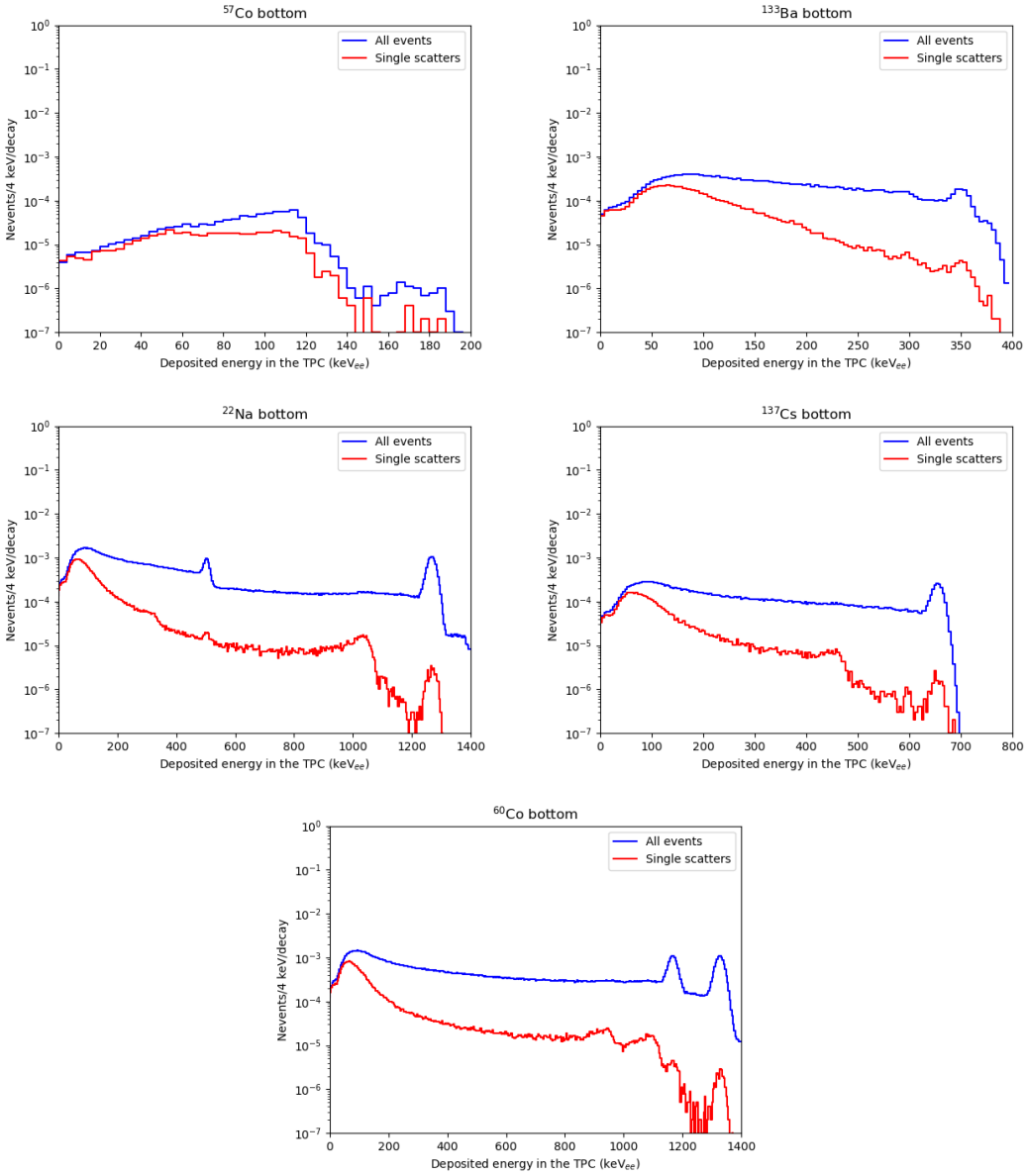

FIGURE 3.7. : Rates of events per decay of the source as a function of the energy deposited in the TPC, for five sources of photons. From left to right and top to bottom : ^{57}Co, ^{133}Ba, ^{22}Na, ^{137}Cs, ^{60}Co. The spectra are presented for all types of events (blue) and separately for single scatters (red). The source is positioned at the bottom of the TPC. The expected energy resolution of DS20k is applied.

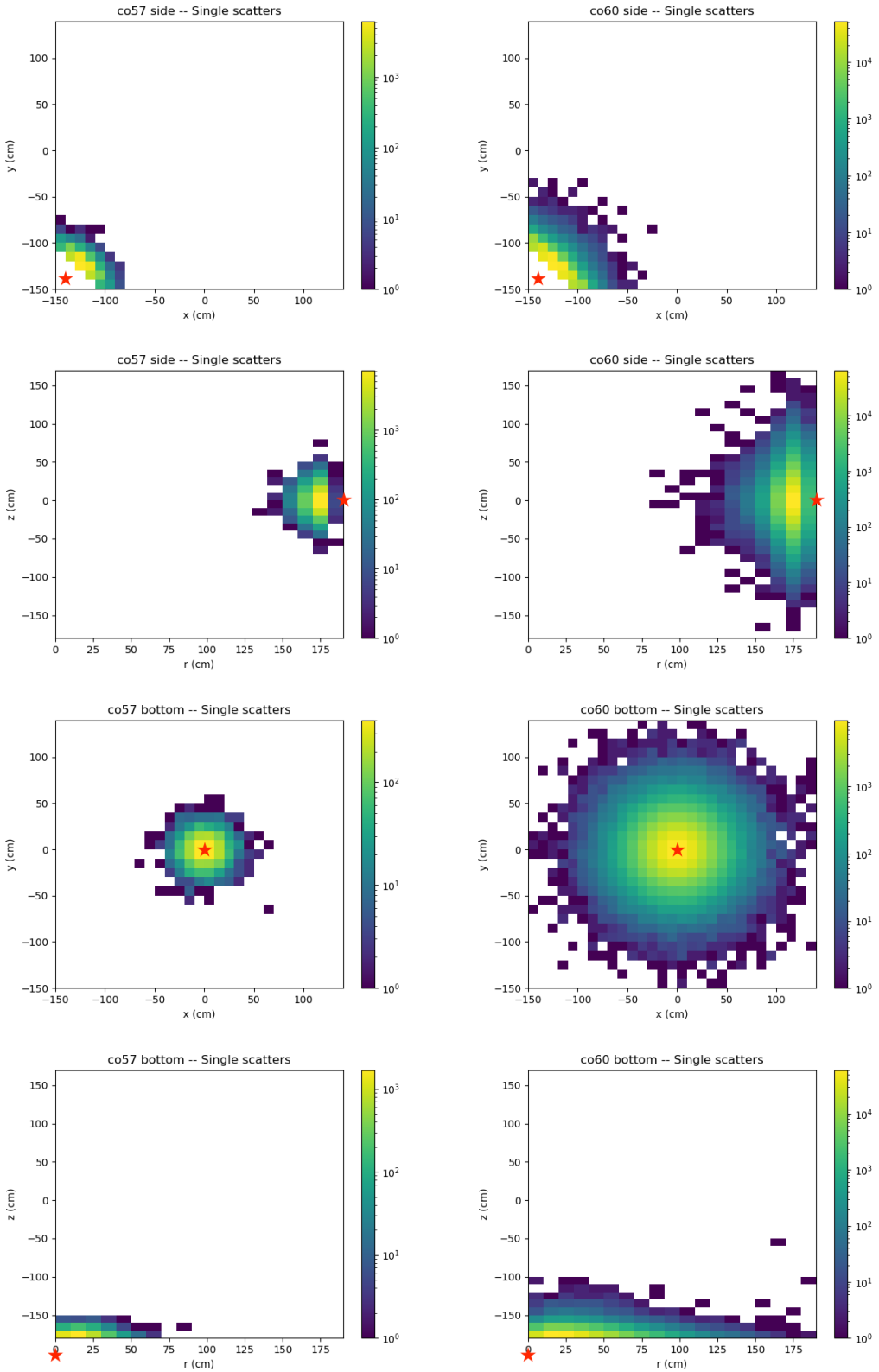

FIGURE 3.8. : XY and RZ distributions of ER single scatters events, for a low energy source (^{57}Co, left) and a high energy one (^{60}Co, right), for sources at the side (four top plots) and bottom (four bottom plots) of the TPC. The position of the source is indicated with a red star.

walls : GdPMMA absorbs photons and most of them never enter the TPC. The Table also displays the rates of all SS events (corresponding to the integral of the red spectra of Figure 3.6 and Figure 3.7). The latter rates on the side are two to four times higher than the ones at the bottom. Indeed, there is more passive material to cross at the bottom of the TPC than on the side (bottom optical plane populated with SiPMs).

Table 3.4 presents the rates of SS in the photoelectric peak of the same spectra computed between -2 σ and 2 σ of the peak. In average, the higher the energy, the lower the rate of SS in the peak. In general, in particle-matter interactions, the photoelectric effect dominates at low energy (from 10 to $\approx$ 80 keV) then becomes more and more unlikely at high energy. The Compton scattering dominates at middle energy ($\approx$ 80 keV to $\approx$ 5 MeV). This is why it is less and less probable to see the photoelectric peak at high energy in the ER spectra. Thus at higher energies, one could consider using the Compton edge instead of (or in addition to) the photoelectric peak as it is more discernable than the photoelectric peak in the SS spectra. The energy of the Compton edge is well known : $E_{edge} = E_{peak}\left(1 - \frac{1}{1+\frac{2E_{peak}}{m_e c^2}}\right)$, E_{peak} being the energy of the photoelectric peak. Using it would help increasing the statistics for energy calibration above 80 keV.

To validate and strengthen the study, a comparison with the energy spectra published by DS50 [86] when calibrating with ^{57}Co and ^{133}Ba sources is proposed in Figure 3.9. The very good agreement between data and g4ds simulation in DS50 can be appreciated. Figure 3.9 left shows the spectra from Figure 3.6 put in linear-y scale. The same shape as in DS50 is observed :

- At low energy the high rate comes from low energy deposits in the TPC due to energy losses in the materials before entering the TPC.
- At high energy a clear peak is visible, with similar reduction when asking for single scatter.

This comparison gives confidence in the reliability of the simulation results obtained. More generally the calibration strategy followed by DS20k, based on data-MC comparison, will follow closely that of DS50 [88].

3.2.2. Meeting DAQ requirements and calibration procedure

From the energy spectra and the tables summarising the rates of valuable events for each source, one can derive a time estimate of the duration of the calibration runs for one tube. The estimate is based on the following (conservative) hypotheses :

1. Two hours are needed to handle the sources (to place them inside the tubes and remove them at the end of the run).

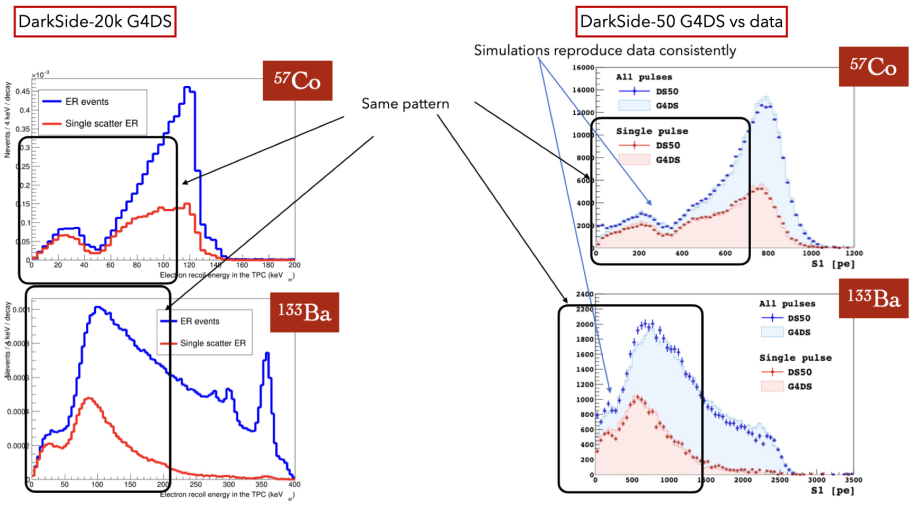

FIGURE 3.9. : DS50 calibration run using ^{57}Co and ^{133}Ba sources (right) [86] and DS20k simulation results from Figure 3.6 put in linear-y scale and normalised per event (left). Note that DS50 (DS20k) show S1 (total) energy distributions.

2. Data will be taken at nine positions : three on each side of the TPC and three others at the bottom of the TPC, 10 minutes are needed to move the source from one position to the next one.

3. At each position, the calibration waits until the targeted statistics of interesting events is reached. For NR, one wants to wait until the collection of 10,000 pure NR SS events. For ER, two options are considered : one waits until 1,000 SS events in the photoelectric peak or 10,000 SS in the whole energy range of the spectrum.

4. The DAQ system saturates at 100 Hz.

5. The activity of the sources are computed such that they saturate the DAQ system. Such activities are different for the positions on the side of the TPC and at the bottom (because the rates are different in both positions). If the activity needed to saturate the reconstruction system exceeds 100 kBq, it is set at 100 kBq in order to have reasonable activities.

Time needed for NR calibration The optimised activities of the NR sources (that induce saturation of the DAQ system at 100 Hz) are shown in Table 3.5. Calibrating with 10,000 pure NR SS events requires to wait up to one full day per calibration position, as pointed out by the Table. In total, more than one week is needed for a full calibration with each source.

Time needed for ER calibration The focus is first put on the whole ER energy spectra and especially on single scatter events. Table 3.3 presents the rates of these events, which

Source	AmBe	AmC
Initial energy (MeV)	[0.2, 12]	[2, 7]
Activity (side) (kBq)	0.14	0.15
Activity (bottom) (kBq)	0.18	0.18
Time per position (side) (h)	19	28
Time per position (bottom) (h)	23	25
Duration of calibration (day)	8	10

TABLE 3.5. : Activity needed and time estimation for the NR calibration (asking for 10,000 pure NR SS events) and for the two previously presented sources of neutrons. The overall time needed to perform the NR calibration run is 18 days.

are between 4.4 x 10^{-2} ER events/decay and 4.4 x 10^{-4} ER events/decay.

Table 3.6 presents the optimised activity of the sources (considering that the DAQ system will be saturated by any type of events) and the related time needed to perform the calibration run source by source. Within the outlined hypotheses, around five hours for each of the five sources are needed to reach 10,000 events per position. Therefore the ER calibration should last a full day. Such a procedure would provide spectra with reasonable statistics as presented in Figures 1 & 2 of Appendix A. In these figures, spectra are normalised to such that there are 10,000 SS events.

Source	^{57}Co	^{133}Ba	^{22}Na	^{137}Cs	^{60}Co
Energy (keV)	122	356	511	662	1173
Activity (side) (kBq)	18	1.9	0.36	2.2	0.36
Activity (bottom) (kBq)	100	5.0	0.67	4.6	0.6
Time per position (side) (min)	3.7	6.6	10.8	9	12.6
Time per position (bottom) (min)	3.8	5.9	9	7.8	10.8
Duration of calibration (h)	4.2	4.6	5.2	5.0	5.4

TABLE 3.6. : Activity needed and time estimation for the ER calibration using 10,000 SS events for the whole energy spectra of the sources. The time needed to perform the ER calibration run in one tube is one day straight.

However, calibration could be made easier using ER single scatters with their energy inside the peaks of the spectra of the source. Reaching 10,000 ER single scatters in the photo-electric peak (targeting 1 % statistical uncertainty) has been shown to take a large amount of time. Hence, the hypothesis to aim for the collection of 1,000 ER single scatters in the photo-electric peak has been considered to lower the ER calibration duration, leading to 3 % statistical uncertainty. Table 3.7 presents the calibration duration to reach such statistics in the photo-electric peak, source by source. With the previous set of hypotheses, the calibration should last one full week. This is reasonable, even considering calibration runs made to check the time stability of the detector response (such runs will take place during the data taking time). Within this time slot, it is possible to reach energy peaks with the shape of the ones on Figures 3 & 4 shown in Appendix A

Source	^{57}Co	^{133}Ba	^{22}Na	^{137}Cs	^{60}Co
Energy (keV)	122	356	511	662	1173
Activity (side) (kBq)	18	1.9	0.36	2.2	0.36
Activity (bottom) (kBq)	100	5.0	0.67	4.6	0.6
Time per position (side) (h)	2.5e-2	1.4	2.1	3.1	7.3
Time per position (bottom) (h)	3.4e-2	2.2	2.5	4.7	9.1
Duration of calibration (h)	3.84	18.72	23.52	36	74.4

TABLE 3.7. : Activity needed and time estimation for the ER calibration using 1,000 SS in the energy peak and for the five previously presented sources. The time needed to perform the ER calibration run is roughly one full week per tube.

(respectively made on the side and at the bottom of the TPC), where the number of events per 4 keV$_{ee}$ are presented vs energy. The integral of each portion of spectra signaled by dashed lines is 1,000.

It has been shown recently by other members of the DS20k calibration working group [87] that all photon sources, with activities computed in this section, will produce data rates below the DAQ maximum data output to the Front-End Processors of 125 MB/s. However, this is not the case for the neutron sources, for which the expected rates are above 125 MB/s by 30 % to 80 %. Lowering the neutron source activity would increase the calibration time accordingly. Work is ongoing with the DAQ group to investigate special trigger conditions for calibration. Alternatively, one could perform the calibration in fewer positions.

3.2.3. Impact of the calibration system on the inner detector performances

3.2.3.1. Backgrounds induced by the pipes in TPC

The following results have been obtained several years before construction, thus different types of stainless steel have been considered. First, one kind of stainless steel noted LZ and the other one noted ArDM, being evaluated respectively as best and worst case scenario. This chapter only presents the contamination results with LZ stainless steel, yet the background estimate with ArDM stainless steel is shown in Appendix A, section A.2.

The guide tube material can be contaminated by radioactive elements such as ^{238}U, ^{232}Th, ^{235}U, etc ... (see 2.2) [63]. When they decay, these radioactive elements will produce photons and neutrons which might penetrate the TPC and produce ER and NR backgrounds. In the current design, the calibration tubes are made of 50 kg stainless steel. The impact of the background from the tubes has been studied and compared to the background budget required by the DarkSide-20k collaboration.

Table 3.8 gives the list of the considered radioactive elements that pollute the stainless steel of the tubes. These radioactive elements will produce ER and in some cases NR

Element	^{238}U Upper	^{238}U Middle	^{238}U Lower	^{232}Th	^{235}U	^{40}K	^{60}Co	^{137}Cs
Contamination (mBq/kg) LZ stainless steel	1	0.72	1	0.83	0.046	0.49	3.1	0.86
Photon producer ?	Yes	Yes	Yes	Yes	Yes	Yes	Yes	Yes
Neutron producer ?	Yes	Yes	Yes	Yes	Yes	No	No	No
Neutron yield (neutron/decay) LZ stainless steel	1.1 x 10^{-9}	4.8 x 10^{-7}	1.06 x 10^{-9}	1.8 10^{-6}	3.7 x 10^{-7}	No	No	No

TABLE 3.8. : Considered radioactive elements polluting the stainless steel assuming LZ-type stainless steel, their contamination levels (in mBq/kg), background production and neutron yield.

background. Photons and neutrons are isotropically radiated from the whole tube, around the TPC. Hence, only a fraction of them will enter the TPC. To estimate the background nuisance induced by the tubes, 1e7 events are simulated for each radio-element (with their full chain radioactive decays), distributed within 5 cm diameter tubes. The fraction of events depositing part of their energy in the TPC are measured and analysis selections are applied. If no event passes the selections, an upper limit at < 2.3 events is set, corresponding to the limit of a poissonian distribution with mean zero at 90% C.L. After all these steps, the counts are normalised to the radioactive contamination of the material (see Table 3.8), the mass of the tubes and the time exposure (ten years of operation).

The study first scrutinises the most dangerous background case : NR background from neutrons. Only ^{232}Th, ^{238}U and ^{235}U produce neutrons, through (α, n) reactions. The final analysis events in the NR channel for WIMP search are pure NR events, doing single scatters in the fiducial volume, in the energy region of interest (30 keV$_{nr}$ < E < 200 keV$_{nr}$) [44], and not tagged by the veto (E$_{veto}$ < 200 keV$_{nr}$). These cuts are reproduced for the tubes contribution to the NR background. The normalisation also includes the production rate of neutrons by the contaminating radioactive elements, shown in the last line of Table 3.8.

Figure 3.10 presents the energy and spatial distributions of the NR background from the tubes for ^{232}Th radiocontaminant. The top-right and bottom-left plots display events localised near the tubes, a few events are in the fiducial volume. As seen in Figures 3.10-up left and 3.10-down right, four events resist the cuts after 10^7 simulated events from ^{232}Th in the tubes. Reproducing the study for ^{238}U, four events resisted the cuts. The final quantitative results of the study are shown in the Table 3.9, for the three radioactive contaminants. The background level from ^{235}U has an asterisk because this radio-contaminant isn't coded in g4ds. Thus the background level from the latter contaminant is estimated by renormalising the ^{238}U emission spectrum to the parameters of ^{235}U.

This study shows that the background from impurities in the tubes produce around

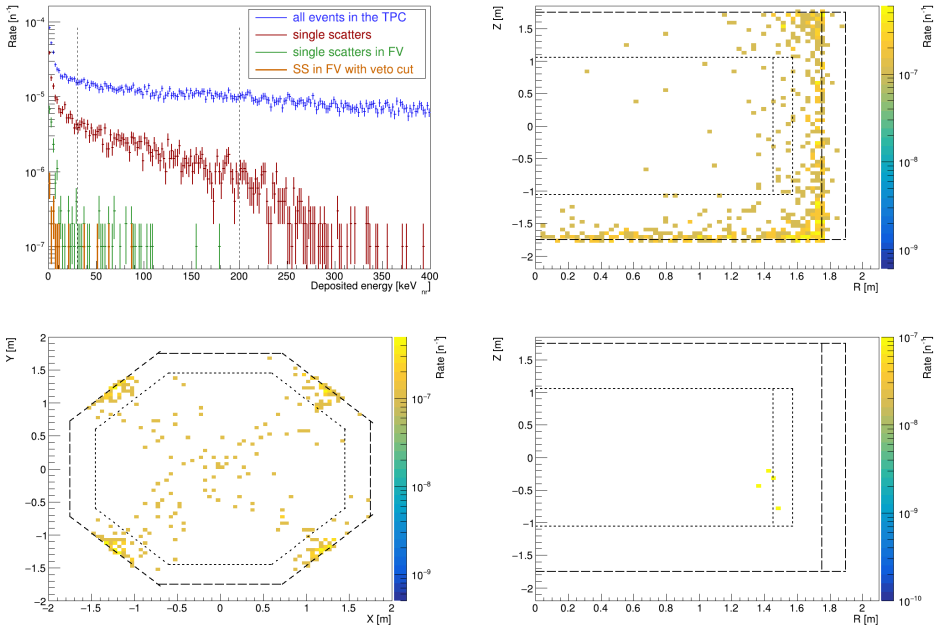

FIGURE 3.10. : Up left : energy spectrum of NR events induced by the presence of ^{232}Th in the guide tube system in four cases : all events, single scatters, single scatters in FV and single scatters in FV after the veto cut. Up right : geometric view of NR background events (from ^{232}Th decay) in the TPC in the RZ plane, after all cuts except ROI & FV. Down left : cut-view of NR background events (from ^{232}Th decay) in the TPC in the XY plane, after all cuts except FV. Down right : geometric view of NR background events (from ^{232}Th decay) in the TPC in the *RZ* plane, after every cuts.

Element	^{238}U Upper	^{238}U Middle	^{238}U Lower	^{232}Th	^{235}U
Contamination (mBq/kg)	1	0.72	1	0.83	0.046
Neutron yield (neutron/decay)	1.1 x 10^{-9}	4.8 x 10^{-7}	1.06 x 10^{-9}	1.8 10^{-6}	3.7 x 10^{-7}
Events/10years	6.7 x 10^{-9}	2.2 x 10^{-6}	6.7x 10^{-9}	9.5 x 10^{-6}	1.0 x 10^{-7} *

TABLE 3.9. : NR background rates induced by the radioactive contamination of the stainless steel tubes, assuming LZ-type stainless steel, after normalisation (which includes the neutron production rate of the three radioactive elements). The asterisk in the ^{235}U column highlights that this background estimate is derived based on ^{236}U simulations.

Element	^{238}U Upper	^{238}U Middle	^{238}U Lower	^{232}Th	^{235}U	^{40}K	^{60}Co	^{137}Cs
Contamination (mBq/kg)	1	0.72	1	0.83	0.046	0.49	3.1	0.86
Events/10years	< 3.3	< 2.5	< 3.3	< 3.3	< 0.2	< 1.7	< 11.7	< 3.3

TABLE 3.10. : ER background rates induced by the radioactive contamination of the stainless steel tubes, assuming LZ-type stainless steel, after normalisation.

10^{-5} events for 10 years of data taking. Considering that the background budget is settled at 0.1 events per 10 years, the NR background induced by the calibration system is fully negligible (it is more than four orders of magnitude less than the requirements). This low rate of events is achieved thanks to the Gd-PMMA walls which better stops neutrons than usual walls (plastic scintillator for instance). For the ArDM-type stainless steel, the tables are shown in Appendix A, displaying a background contamination from 24 to 68 times larger than the one that considers LZ-type stainless steel, depending on the radio-contaminant. However, conclusions remain the same as LZ-type stainless steel : the NR background from the tubes contamination is fully negligible.

Now, let's consider the ER case. All radioactive contaminators produce photons, which might produce ER signal in the TPC. This time, the set of cuts applied to the ER background analysis is : having single scatters inside the energy Region Of Interest ($7.5\ keV_{ee} < E < 50\ keV_{ee}$) and in the Fiducial Volume of DS20k (SS + ROI + FV). Figure 3.11-top shows the evolution of the energy distribution of ER background from ^{238}U cuts after cuts : zero event resist the cuts. Figure 3.11 bottom (left and right) shows that the background is located around the tubes and at the borders of the TPC. The same conclusions are obtained with all other ER-producer radiocontaminants.

ER background estimate is shown in Table 3.10. There are only upper limits as no event survived the cuts. The results shown in the Table are the ones before the S2/S1 ratio and the PSD computations (which will bring another 10^7 to 10^8 rejection, see Chapter 2). To conclude, the ER background induced by the tubes is fully negligible. The same conclusion holds for ArDM stainless steel.

Another important aspect to check is the rates (before cuts) induced by the tubes in the veto and the TPC. Indeed, in a scenario where all the background events could be rejected by analysis but the background rate actually saturates the DAQ, the WIMP search would be degraded. Between 1 and 20 % of all the events emitted by the contaminants in the stainless steel tubes will deposit energy in the TPC. Weighted by the contamination level, the latter events represent a rate of recorded events in the TPC between less than 0.002 Hz and 0.03 Hz. The summed background rate in the TPC DAQ readout induced by the calibration tubes is 0.03 Hz, which represents 0.07 % of the sum of the total rate of DS20k : it is fully negligible.
Similarly, between 11.8 and 97.1 % of events emitted by the contaminants of the stainless steel tubes will deposit energy in the veto, representing between less than 0.002 Hz and

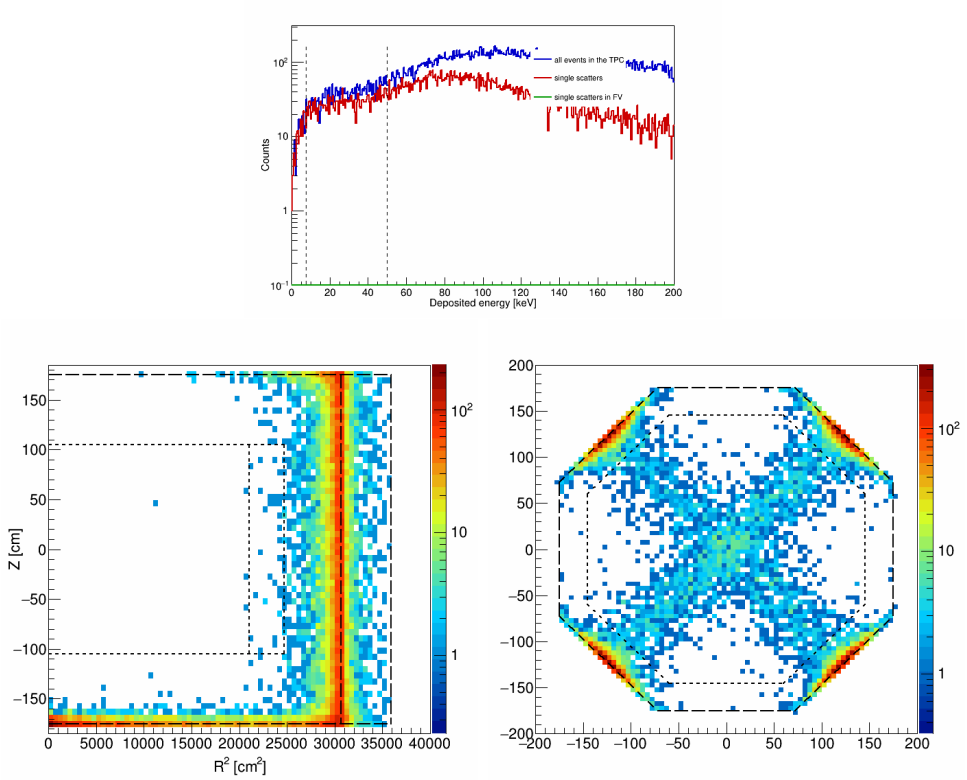

FIGURE 3.11. : Up : energy spectrum of ER events induced by the presence of ^{238}U in the guide tube system in three cases : all events, single scatters and single scatters in FV. The prospective resolution of the detector is applied. Bottom left : geometric view of ER background events (from ^{238}U decay) in the TPC in the R^2Z plane, before the FV cut. Bottom right : cut-view of ER background events (from ^{238}U decay) in the TPC in the XY plane, before the FV cut.

0.15 Hz of events in the veto DAQ. The summed background rate induced by the stainless steel calibration tubes in the inner veto is 0.2 Hz, which represents 0.15 % of the rate induced by all other materials in the veto. Again, the rate induced by the tubes in the veto DAQ is totally negligible.

3.2.3.2. Veto Light Collection Efficiency and choice of the surface of the pipes

The inner veto, in which the tubes are, collects the scintillation light to tag and reject background. Thus, the presence of the tubes inside the veto may reduce the Light Collection Efficiency (LCE), hence reduce the veto performances. This effect is evaluated by simulating 1,000,000 events - an event being the release of 1,000 isotropic photons of 128 nm (9.7 eV) - in the bulk of the veto, with 3 cm tubes [5] present in the veto. The simulations consider five cases for the optical surface of the tubes : either the tubes are untreated stainless steel (UT), either the tubes are electro-polished stainless steel (EP), either they are TPB-coated (TPB, with a reflector layer between the tube and the TPB), either they are PEN-coated (PEN, with a reflector layer between the tube and the PEN) or they are only wrapped with an ESR reflector foil (ESR).

In order to study the LCE, the following is considered :

- In a 3D view : four regions of the veto are taken into account : the full veto buffer, its bottom part (i.e. the veto volume below the floor of the TPC), its top part (i.e. the veto volume above the ceiling of the TPC) and its side-part (the in-between volume, shaped as a pipe).
- In a 2D cut-view : two octants of the circle are compared : one without tubes (between angles of $\frac{3\pi}{8}$ and $\frac{5\pi}{8}$) and one with a portion of the tubes (between angles of $\frac{\pi}{8}$ and $\frac{3\pi}{8}$ - see Figure 3.12).

Table 3.11 points out that the light collection efficiency is $\approx$ 3-4% in each case. The sectors with tubes have a lower efficiency than the ones without tubes as one can expect (the light can be absorbed by the tubes).

As a reference, the LCE without the calibration system in the veto is taken (see Table 3.12). At maximum, due to geometrical reasons, the inner veto can reach an efficiency of $\approx$ 4.04%. It is now possible to compute the relative loss of efficiency as an average in the veto, computed as

$$\frac{LCE^{Full}_{without-tubes} - LCE^{Full}_{UT-EP-TPB-PEN-ESR}}{LCE^{Full}_{without-tubes}} \tag{3.1}$$

and in the tube regions, computed as

$$\frac{LCE^{Tubes-octants}_{without-tubes} - LCE^{Tubes-octants}_{UT-EP-TPB-PEN-ESR}}{LCE^{Tubes-octants}_{without-tubes}} \tag{3.2}$$

[5] In this analysis, the tubes have a diameter of 3 cm as their design at the moment of the study was so. A discussion at the end of the section is given for 5 cm diameter tubes.

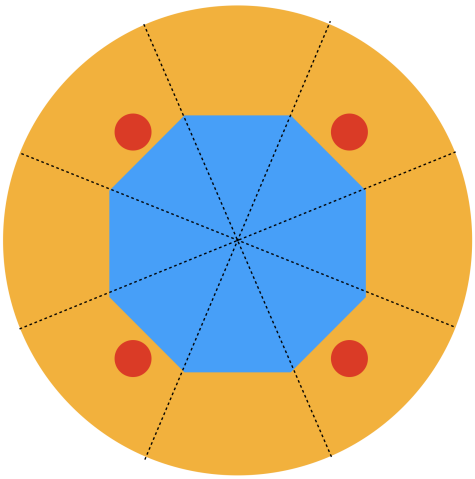

FIGURE 3.12. : 2D cut view scheme of the TPC (blue) with the veto buffer around it (yellow) and tubes inside (red). The scheme is not at scale. Separations of the veto buffer into eight sub-regions are depicted : four with tubes and four without.

LCE	Full Veto Buffer (mean) (%) :					Octants with tubes (mean) (%) :					Octants without tubes (mean) (%) :				
Optical Boundaries	UT	EP	TPB	PEN	ESR	UT	EP	TPB	PEN	ESR	UT	EP	TPB	PEN	ESR
All	3.66	3.72	3.97	3.94	4.00	3.59	3.67	3.94	3.90	3.99	3.73	3.78	4.00	3.97	4.01
Side	3.72	3.78	4.04	4.00	4.06	3.60	3.68	3.99	3.95	4.06	3.85	3.88	4.08	4.05	4.07
Top	3.85	3.89	4.03	4.01	4.03	3.84	3.88	4.02	4.01	4.03	3.86	3.90	4.04	4.02	4.04
Bottom	3.43	3.51	3.85	3.80	3.90	3.40	3.50	3.83	3.77	3.89	3.46	3.54	3.87	3.83	3.90

TABLE 3.11. : LCE in three 2D cut-view-areas of the veto buffer : an average inside the full veto, in the four octants where tubes are and in the four octants where tubes are not. For each of these three considerations, the Table shows the LCE in four volumes : inside the whole volume, on the side, the top part and the bottom part of the veto. This is done for five optical boundaries : untreated steel (UT), Electro-polished steel (EP), ESR-wrapped + TPB-coated tubes (TPB), ESR-wrapped + PEN-coated tubes (PEN) and ESR-only-wrapped tubes (ESR). Statistical errors on these numbers are less than 1 x 10^{-2}.

LCE	Full Veto Buffer (Mean) :
All	4.04 %
Side	4.09 %
Top	4.05 %
Bottom	3.97 %

TABLE 3.12. : Maximum LCE reachable in the veto buffer (case without tubes). Statistical errors on these numbers are less than 1 x 10^{-2}.

$\frac{\Delta LCE}{LCE}$	UT (%)	EP (%)	TPB (%)	PEN (%)	ESR (%)
All	9.4	7.9	1.7	2.5	0.91
Side	9.0	7.6	1.2	2.2	0.75
Top	4.9	4.0	0.5	0.99	0.32
Bottom	14	12	3.0	4.3	1.9

TABLE 3.13. : Relative loss of the average LCE. The reference is the LCE in the case where there are no tubes in the veto.

$\frac{\Delta LCE}{LCE}$	UT (%)	EP (%)	TPB (%)	PEN (%)	ESR (%)
All	11	9.2	2.5	3.5	1.1
Side	12	10	2.4	3.4	0.95
Top	5.2	4.2	0.7	0.99	0.31
Bottom	14	12	3.5	5.0	2.0

TABLE 3.14. : Relative loss of LCE in octants where the tubes are. The reference is the LCE in the case where there are no tubes in the veto.

Tables 3.13 and 3.14 show the results, respectively for average loss and loss in the tubes regions. The best situation is to have ESR-wrapped tubes, where the efficiency is the highest (between 3.89% and 4.07%). This is consistent with the reflectivity of the different considered surfaces [63], with a reflectivity of ESR foils at the level of 98 % for 420 nm photons. The presence of the tubes that are wrapped with an ESR foil do reduce the inclusive veto LCE by about 1 % (up to 2 % in sectors where the tubes are).

Finally, the veto needs to be as uniform as possible. The asymmetry between octants induced by the tubes is evaluated thanks to the ratio

$$\frac{LCE^{Octants-Without-Tubes} - LCE^{Octants-With-Tubes}}{LCE^{Octants-Without-Tubes}} \tag{3.3}$$

Table 3.15 displays the results. The asymmetry is ≈ 0.3 % for tubes treated with a reflector ESR. Such asymmetry is not of concern for the operation of the veto.

All above results with ESR-coated tubes have been repeated for 5 cm diameter tubes

Asymmetry	UT (%)	EP (%)	TPB (%)	PEN (%)	ESR (%)
All	3.8	2.9	1.5	2.0	0.3
Side	6.5	5.2	2.2	2.0	0.3
Top	0.5	0.5	0.5	0.2	0.05
Bottom	1.7	1.1	1.0	2.0	0.2

TABLE 3.15. : Asymmetry between octants computed as the relative difference of light collection efficiency between octants where tubes are not and octants where tubes are - for the five options of optical boundaries of the tubes.

instead of 3 cm, to check the impact of larger tubes. The relative loss of LCE for the inclusive case (all sectors) increases from 0.91% to 1.4%. For all sectors with tubes it goes from 1.1% to 1.7%. The inclusive asymmetry between the sectors increases from 0.3% to 0.6%. We can conclude that for 5 cm tubes, the impact on LCE is still very much acceptable.

3.3. Tests campaigns proving the calibration mechanical feasibility

Before operation at cold with the final detector, the mechanical feasibility and especially the risks and relevant emergency procedures associated with the external calibration system have to be tested and implemented for safe functioning.
Because of the cold temperature (T = 88 K in DS20k) and of the close and narrow environment, consequences would be detrimental in case of an accident during operation (e.g. a radioactive source trapped near the TPC, preventing further WIMP search). Consequently, a variety of tests with different mock-ups have been conducted throughout the design validation phase. The aim of these tests is to validate the design choices and check that the performances can be met : positioning of the source with $\pm$ 1 cm precision, reasonable source speed ($>$ 1 cm/s) and reasonable tension to apply on the rope ($<$ 150 N). It also allowed us to apprehend the behaviour of the whole calibration system and to derive emergency procedures in case of a dramatic event occurring during calibration runs. The following hypothetical scenarii were considered :

Cryo Problems related to the cryogenic environment

- C1 Ice formation in the tubes in case of humidity (from air) introduction in the pipes. Such scenario may block the radioactive source near the TPC, preventing science runs.
- C2 Especially, each neutrons source is expected to stay about one day at the same position before being moved to the next one. If there is humidity in the pipes, frozen water might stick the source to the pipe and prevent its transport.

Design Problems related to the design of the tubes

- D1 Shape of the tubes : the sequencing of 14 or 15 bends, along the 21.47 m path of the source from one side to the other, may induce a large tension to apply on the ropes by the motorised systems in order to be able to move the source. It could both degrade the motorised systems and degrade the source position accuracy.
- D2 Material of the tubes : as the source is expected to touch one side of the inner circle of the pipes, if the material of the tube is too scratchy, the tension may also increase drastically.

Operation Problems related to operation during calibration runs

O1 The source mounting (resp. dismounting) on the ropes before (resp. after) calibration runs is risky. If the procedure is not safe enough, the rope could accidentally fall in the tubes, which would require full rope re-deployment leading to a delay in the operation schedule. Even worse, the source could inadvertently fall in the tube, which is the most dramatic scenario that one can think of. Indeed, it would require stopping operation to empty and dismantle the detector to retrieve the fallen source.

O2 Three neutrons and five photons sources are expected to be used for calibration. Each source is expected to travel in the whole calibration tube that is $\approx 20\,\mathrm{m}$ long. Therefore the calibration system will be stressed during calibration runs : the motorised systems will move different sources on $\approx 160\,\mathrm{m}$ in total for a full calibration run (≈ 100 m/day at maximum).

O3 A minor issue would be the wrong interpretation of the source position in the tube, hence a degraded source position resolution and of course (x, y, z) calibration.

The present section aims at describing the main tests performed between 2021 and 2024 to validate the design of the external calibration system before Final Design Review and Production Readiness Review, which are internal procedures within the collaboration. Unless explicitly specified, all tests are conducted the same way : a set of back and forth travels in the tubes were done with a pseudo-source. This way, stress tests were achieved each time a calibration test was performed, addressing challenge O2 : all the tests proved the robustness of the calibration system. Similarly, the accuracy between software-reconstructed source position and the physical one was checked at each test, addressing challenge O3. The set of tests related to the operation at cold is detailed in 3.3.1 followed by some tests concerning the design of the system in 3.3.2. To finish, a discussion and a comparison with the requirements of DS20k are proposed in 3.3.3.

3.3.1. The operation at cold

Two different mock-ups were used to test the operation in a cryogenic environment and address the situation C1. The first one, called here $\mathrm{CPPM_{cryo}}$ allowed short duration tests with liquid Nitrogen ($\mathrm{LN_2}$, 77 K) at Centre de Physique des Particules de Marseille (CPPM), in Marseille, France. The second one, called $\mathrm{CERN_{cryo}}$, allowed long duration tests with $\mathrm{LN_2}$ and LAr (88 K) at CERN, in Geneva, Switzerland. Both mock-ups permitted training future shifters to handle safely the sources and to assess the source position accuracy, dealing with challenges O2 and O3. The source position accuracy was all the time measured to be within 1 cm for short ($< 20\,\mathrm{m}$) runs. The accuracy degrades with the number of travels, but stays within 0.1 % the travelled distance of the source.

Short test at 77 K To check the behavior of the calibration system at cryogenic temperature, a first mock-up has been built at CPPM and operated with $\mathrm{LN_2}$ (77 K)

several times. It consists of a stainless steel tank (1800 × 900 × 100 mm^3) insulated with polystyrene, and a 3 m long 3 cm diameter and 1.5 mm thickness titanium tube. Note that at the time of mock-up construction, the tube material was foreseen to be titanium, and the tube was foreseen to have an internal diameter of 3 cm. The mock-up tube is shaped as a U : it has two vertical and one horizontal sections of 60 cm, two curved sections with a curvature radius of 40 cm (as foreseen for the experiment), see Figure 3.13 top. The tube is equipped with four temperature sensors (called PT100), fixed at different locations along the tube in order to estimate the level of LN_2 inside the tank. Gaseous nitrogen (gN_2) is used to flush the tube and reduce the humidity to few %, as measured by a sensor located close to the tube entrance in the cryostat. To drive the source, the mock-up is equipped with the final version of the motorised systems at each extremity of the tubes, see Figure 3.13 bottom. The motorised systems consumption power, gN_2 flux, temperature in the tank and of course encoders and loadcells outputs are monitored and stored.

A preliminary test of source circulation inside the tube was carried out at room temperature. A position accuracy of ± 1 cm was measured and the circulation speed was of 3 cm/s, in agreement with the DS20k requirements. The tension applied on the rope was measured of 25-30 N when circulating the pseudo-source. Then, three training tests were conducted to apprehend the different involved procedures : best-suited way to deploy the rope in the tube, test of the resistance of the home-made cryostat to cold, apprehension of the controlling of the motorised systems, optimisation of the monitoring system (data recording, data display), etc.
Once the optimised test procedure was obtained, a short cold test of 8 h was carried out, filling the cryostat thanks to LN_2. For this test, the pipe was permanently flushed with gN_2. The rope tension showed a slight increase compared to room temperature tests yet never exceeding 40 N. Figure 3.14 bottom shows the variation of the tension measured during the run. For this run, more than 40 round trips were done corresponding to 300 m of travel.

Figure 3.14 top shows that a cryogenic environment colder than DS20k was kept for about 4 h in the bends. This is well below what will be needed for DS20k. This is why the calibration team have used a better insulated cryostat for longer runs, described in the next two paragraphs.

Long tests at 77 K Longer tests are needed to test the robustness of the calibration system at cold and to mimic a DS20k run, with maximal motorised systems usage and long stops (as described in Table 3.5). A second battery of tests were conducted at the CERN cryolab at LN_2 and then at LAr temperatures. The $CERN_{cryo}$ set-up is shown in Figure 3.15 left. The second pair of final motorised system were used. The tube, of 3.3 cm internal diameter, has an asymetrical U-shape : the left (resp. right) part has a 40 cm (resp. 10 cm) curvature radius to fit in the cryostat as schemed in Figure 3.15 right. Similarly to $CPPM_{cryo}$, four temperature probes are put along the left part of the tube. Ambient temperature and humidity are also measured. The tube is fixed to the cryostat

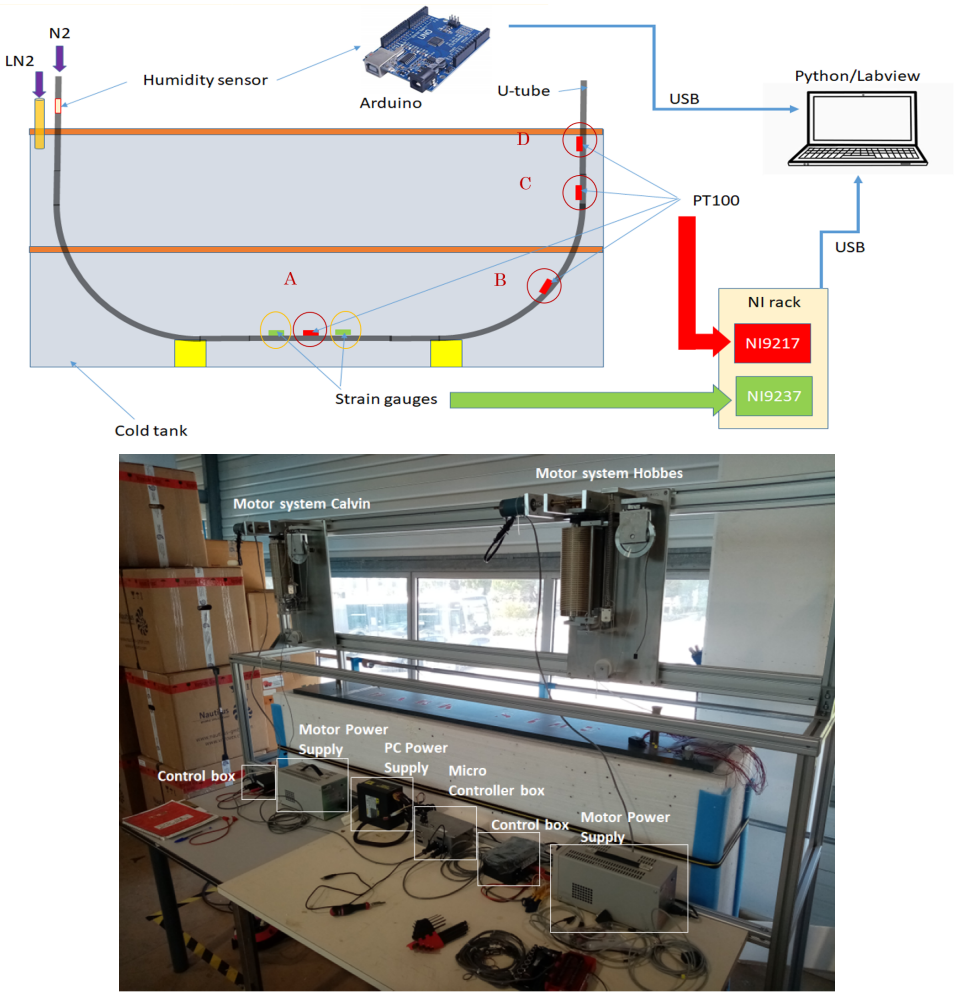

FIGURE 3.13. : Top : Simple schematic of the cryogenic mock-up built at CPPM. Bottom : Picture of the fully integrated system with the two motors including the power supply and the controller (the monitoring PC is not shown on this picture).

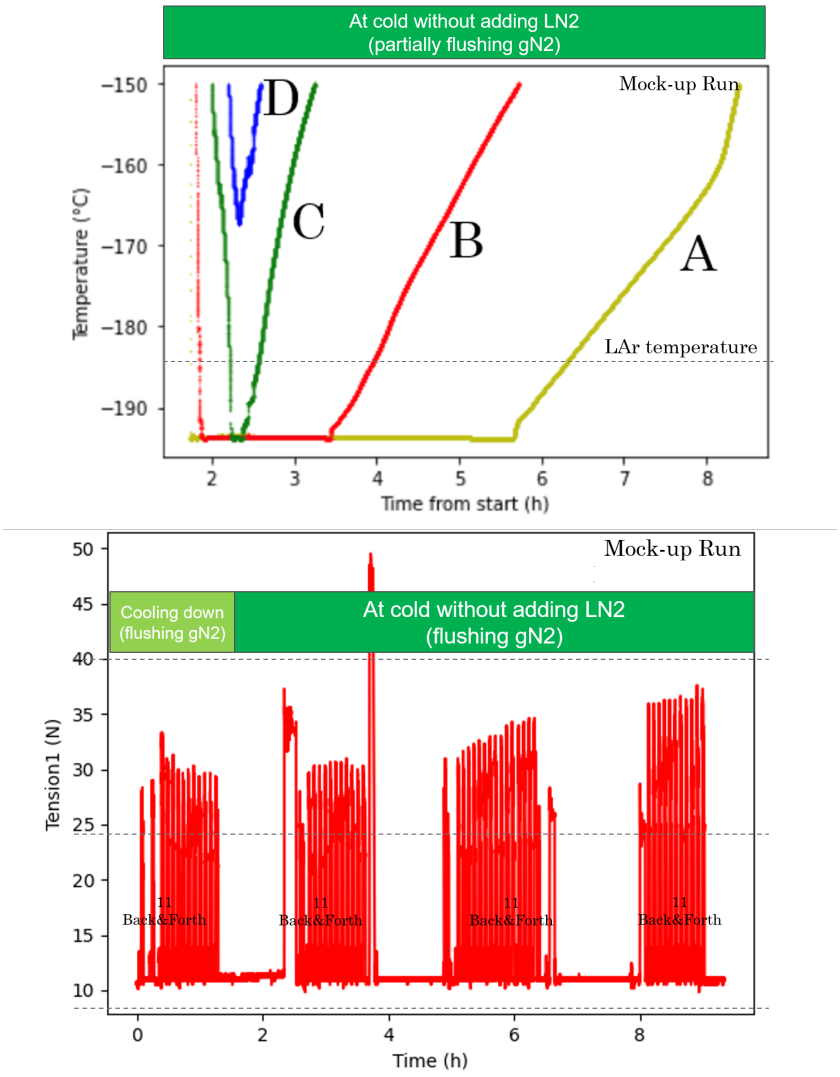

FIGURE 3.14. : Top : Temperature probe measurements during a typical cold test with the CPPM mock-up. Letters A, B, C, D correspond to PT100 probes of Figure 3.13 and the LAr temperature is indicated. Bottom : Measured tension during the cooling down and at cold.

and the cryostat is closed with a polystyrene cap. As the cryostat is not closed with an hermetic cover, it is necessary to refill the cryostat regularly. The level of cryogenic liquid is always kept sufficiently high for the tests, though.

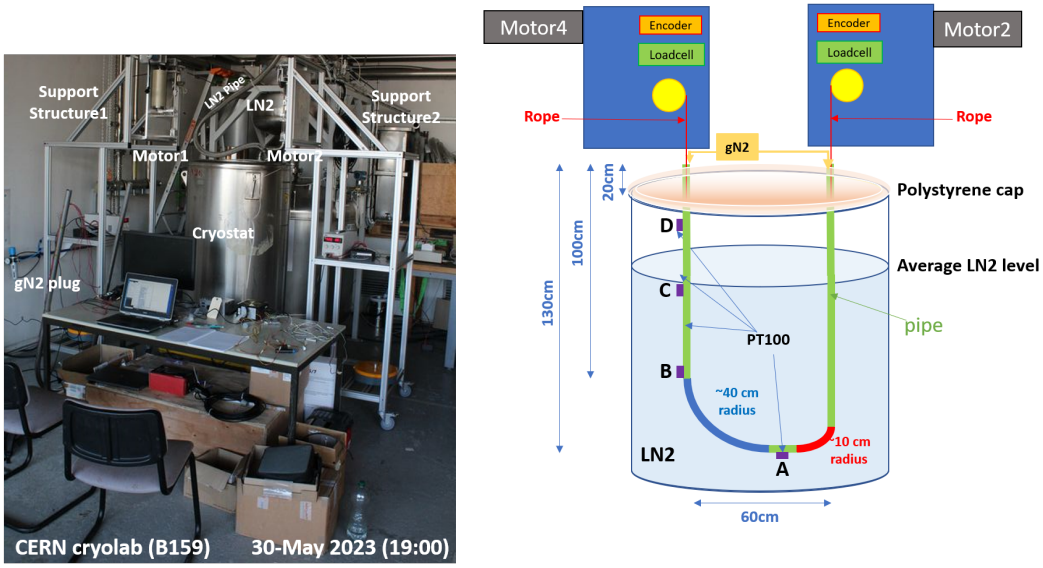

FIGURE 3.15. : Left : photograph of the cryostat set-up used for the CERN tests. The cryostat height is 120 cm and the inner diameter is 70 cm. Right : Scheme of the mock-up operated at CERN for long term measurements.

Each side of the tube is not perfectly hermetic causing humidity to enter in the tube. In addition, the flushed gN_2 was liquefied inside the tube, the liquid level was measured to be at 50 cm below the top of the tube. The liquefaction of gN_2 inside the tube is expected to originate from the low flushing rate, thus gN_2 might have had time to do thermal exchanges with outside LN_2 environment and got liquefied. The long-run $CERN_{cryo}$ LN_2 mock-up allowed to perform stress tests as well as long stay tests leaving the source at the same position for $\approx$ 1 day.

Beginning with stress tests, in total during two weeks, the pseudo-source travelled 750 m via 280 back and forth trips. This represents five times what will be done with the final system within one week only. Figure 3.16 shows the tension measured during these tests : motor 2 on the right in blue and motor 4 on the left in orange. A standard pattern of the tension along the course of the source is shown in Figure 3.16 top left and right. Depending on which motor is pulling, the tension is in average around 23 and 16 N, respectively, the asymmetry is assumed to come from the asymmetrical shape of the tube inside the cryostat.

On the other hand, during long stay tests, the source was put in a given position (A, B, C or D of Figure 3.16 top center) and left there from 1 minute to 2 hours – sometimes

over night and over the week-end. Figure 3.17 shows a typical example of tension applied on the left and right part of the rope during a run, respectively shown in orange and blue. A small peak in tension of few Newtons (circled in black) is visible after the restart, without preventing the displacement (the tension to move the source is large, yet the source is not stuck). The maximum value of the tension is within the 10 s after the restart.

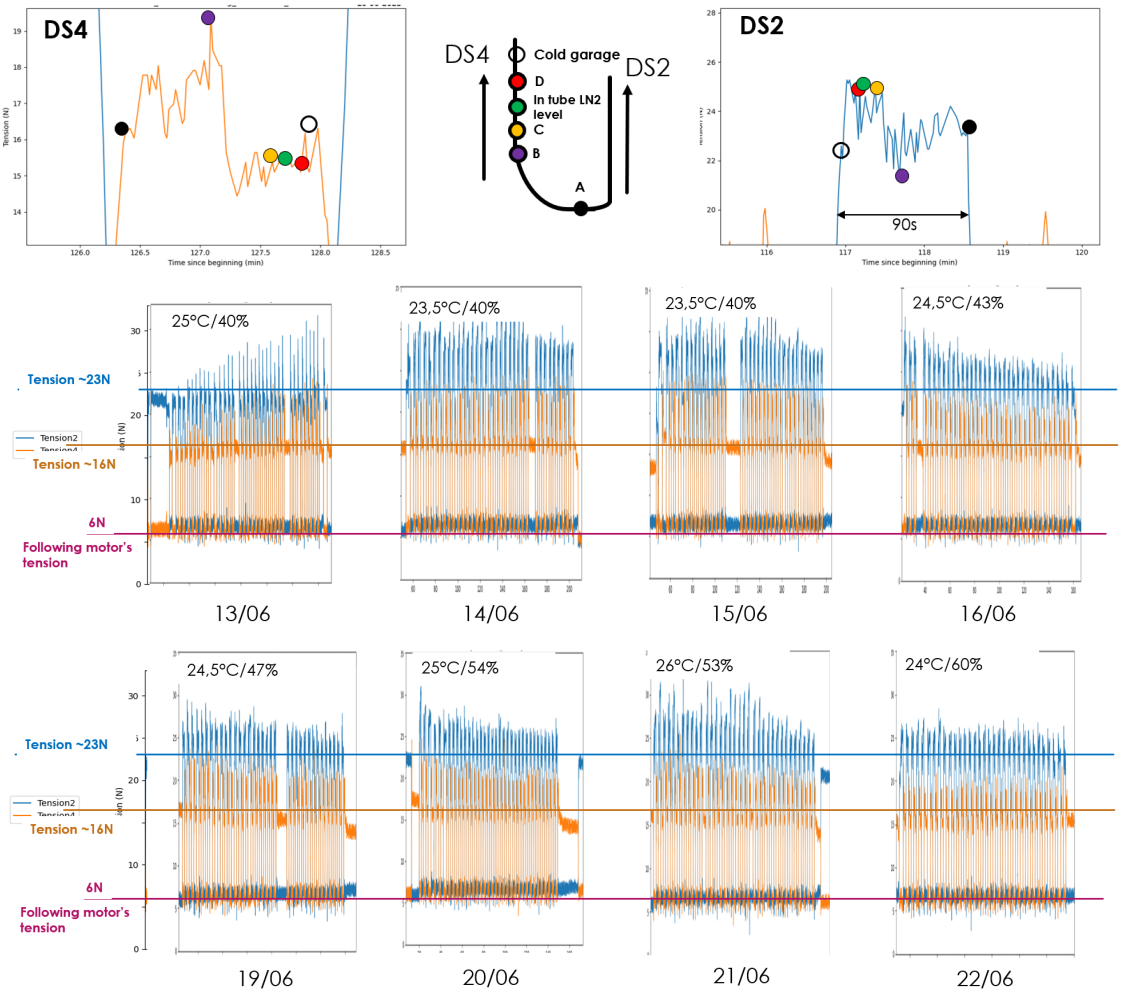

FIGURE 3.16. : Stress test measurements for the calibration system showing the evolution of tension during the 8 days as a function of time. Top : Example for one pull from position A to reference (called garage) position (left) and for one pull from reference position to A (right). Center and bottom : Tension measured along the 8 days of stress test.

As a summary, thanks to these long duration LN_2 tests, it was possible to evaluate the robustness of the calibration system under some stress conditions above the requirements of DS20k as well as the possibility to move the source from a position where it stayed a

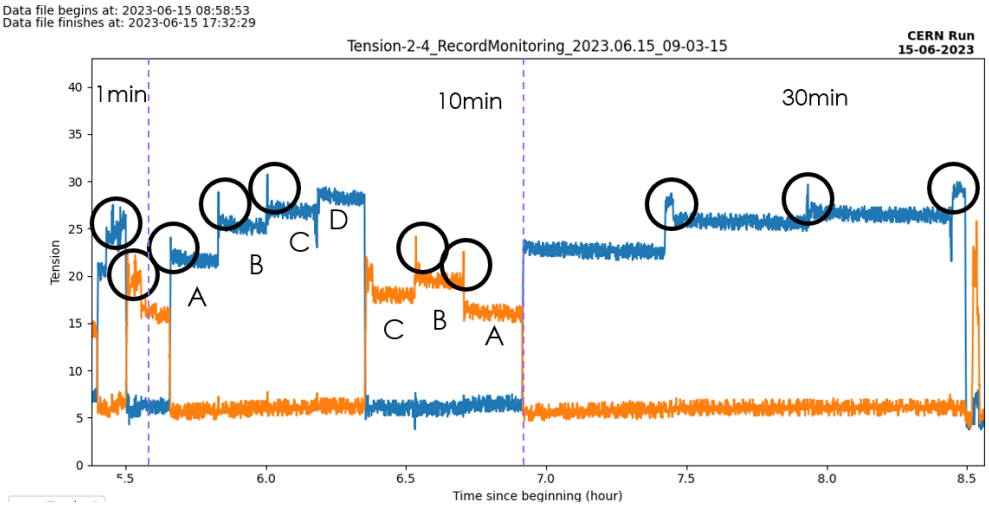

FIGURE 3.17. : Tension needed to move the source in a long-stay test with $\text{CERN}_{\text{cryo}}$ with 1 min, 10 min and 30 min stay at the same position.

day, addressing situation C2. The stability of the calibration system performance (using the final design for the motorised systems) under such conditions was demonstrated.

Long tests at 88 K In addition to the tests with LN_2, other tests were conducted at LAr temperature with the same mock-up. For this test, only the bended parts of the tube (monitored by PT100 B) were at LAr temperature during the whole run. This time, humidity at both exits of the tubes was measured thanks to sensors, and monitored. Again, stress and long-stay tests were conducted, very similar results as in the 77 K tests were obtained.
With 88 K, the main focus was put on better understanding the impact of gN_2 flux variation from 0 to 250 L/h on the humidity at both ends of the tube. The outcome of the test is that there is a threshold effect from the gN_2 flux on the humidity inside the tubes. The test suggested that in DS20k, O(300) L/h will be needed to remove the humidity in case the source is located at the bottom of the tube.

In addition, an extreme scenario was attempted. Humidity was introduced on purpose in the tube by stopping the gN_2 flux, and by blowing in the tube during several minutes to saturate the gas with humidity. Ice was formed, gradually clustering on the tube internal surface and forming an ice ring. Despite these very unfavorable conditions, the source was not blocked. The tension increased of 20 N with respect to normal operation when first trying moving the source. When flushing at 120 L/h for 90 minutes, the humidity fell down from 100% to 0%. The extra tension observed when moving the source gradually decreases when doing few back and forth. Continuing flushing at 120 L/h during 12 h, the ice turned into frost. The tension was again comparable to the normal running condition, see Figure 3.17.

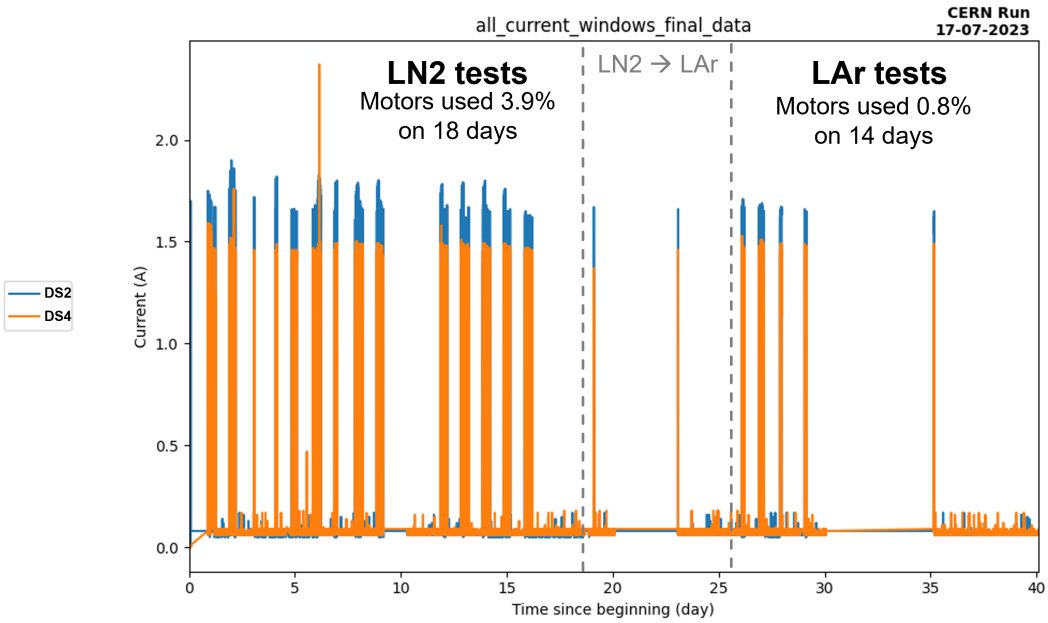

FIGURE 3.18. : Motor current as a function of time along the LN_2 and LAr test performed at CERN.

As a summary, Figure 3.18 shows the current needed to run the motors (linked to the tension applied on the ropes) during the long tests at both LN_2 and LAr temperatures. Note that the motorised systems were used above or at level of what is required during the DS20k calibration – where the motorised systems will be used 1.2% of the time. The stability of the motorised systems consumption can be appreciated in Figure 3.18, assessing the robustness of the whole system.

3.3.2. Test of the full-scale geometry at room temperature

Figure 3.19 left shows the scale-one mock-up (called $CPPM_{Scale1}$) whose purpose is to mimic the full-scale design with a transparent plastic tube to study the behaviour of the source inside it. It is made of 11 segments aligned with 3D printed sleeves, the different segments are bended, reproducing the bends sequencing in DS20k with accurate curvature radii ; only the straight parts are shorten to fit inside the lab workshop. The rope follows the 15 bends of the final tube. A pseudo-source of 5.5 cm length, 2.2 cm diameter and weighting about 100 g is attached at each side to each rope coming from the two motors. At each extremity, the mock-up tube is equipped with the final version of the motorised system and its monitoring, the same as the ones used for $CPPM_{cryo}$.

During the tests, the source travelled more than 2 x 4 times in the $\approx$ 15 m tube, leading to $>$ 100 m travelled distance. Figure 3.19 right (top and bottom) exhibits the [70, 80] N tension needed to move the source in the multi-bended tube. At departure from

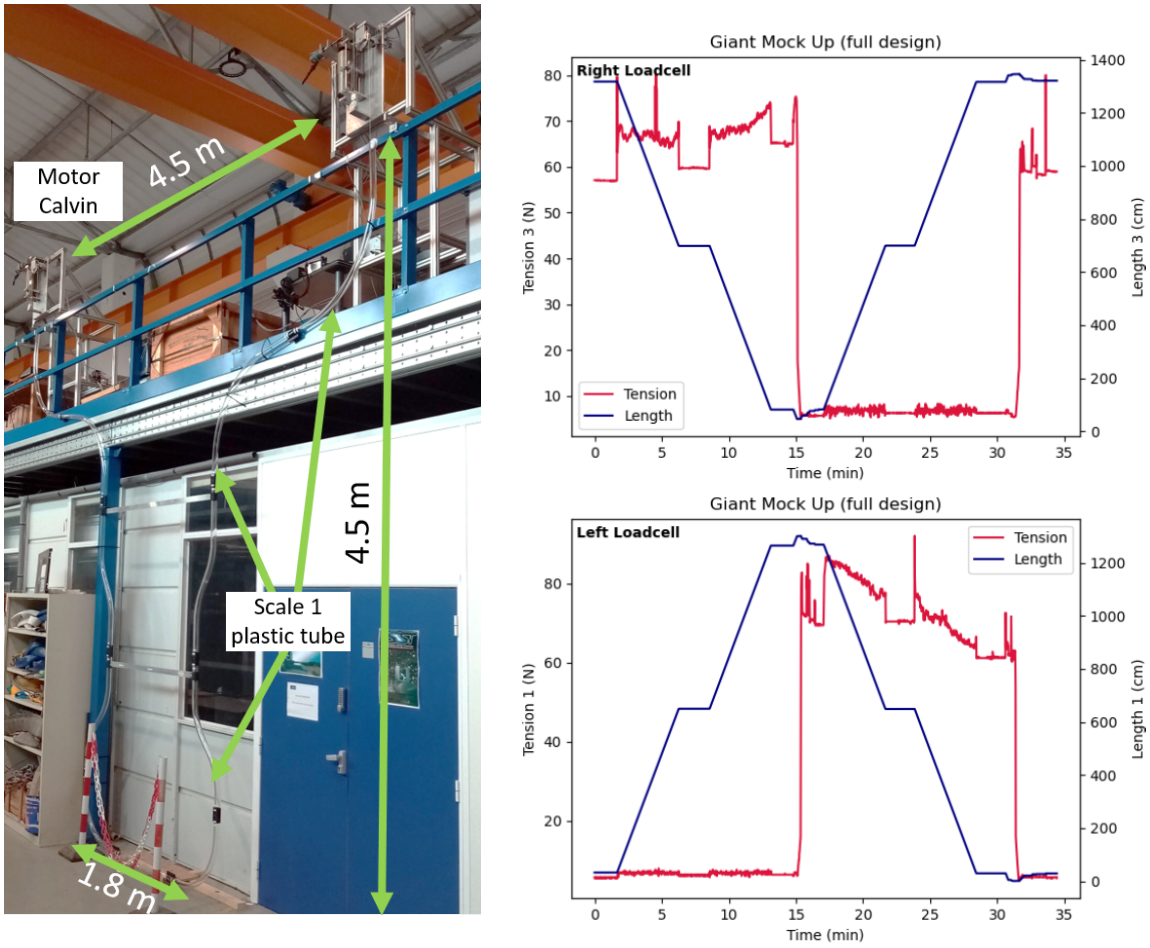

FIGURE 3.19. : Left : Scale-one mock-up installed at CPPM. Right : Tension of the motor system as measured from the right (top right) and left (bottom right) loadcells along the course of the pseudo-source in the plastic tube. The right scale shows the length of the right (top right) and left (bottom right) rope in cm.

stopped position, the tension could reach - exceptionnally - 90 N, this is still well below the maximum possible tension of 150 N. The number of bends, the total length of the tube and the tube material (plastic) may all be responsible for the larger tension needed with respect to $CPPM_{cryo}$. Figure 3.19 right also depicts an asymetry of the pattern of the tension needed to pull the source between left and right loadcells measurements, yet such asymmetry did not compromise the precise positioning of the source or its speed inside the tube, addressing situation D1.

3.3.3. Discussion

Each of the three different mock-ups presented in this section faced one of the challenges related to the design of DS20k. Yet, cross-tests were also performed to prove that the operation of the calibration system as a whole is safe (combining design, cryogenic environment and material limitations).
First, different materials were used for the tube placed in each mock-ups (plastic in $CPPM_{Scale1}$, titanium in $CPPM_{cryo}$ and stainless steel in $CERN_{cryo}$) because of design evolutions at the moment of the tests. Thanks to a set of three 4 m tubes with two bends each (design corresponding to the one used in $CPPM_{cryo}$), each manufactured with a different material, the values of the tension measured in each mock-up could be directly compared. A motorised system was installed at each end of the tubes and the tension needed to move the source was monitored. A comparison between the tension measured for the three tubes with the same U-shape is proposed in Figure 3.20. The plastic tube is the one giving the highest and most fluctuant tension, around 19 N. On the contrary, the stainless steel tube (final material for the calibration system) gives the lower tension, around 13 N (30% less). Extrapolating this reduction to the $CPPM_{Scale1}$ results gives a maximum tension around 60 N instead of 90 N for the final calibration system. This strengthens the statement that DS20k will be able to face the D1 and D2 challenges.
Second, a warm to cold tension ratio of 0.8 has been measured in $CPPM_{cryo}$. Therefore the maximum tension expected for the final system should be around (1 / 0.8) x 60 N = 75 N. It is still extremely reasonnable as it is half of the maximum tension value to be provided by the motorised system, of 150 N.

In addition, the stress tests performed with both $CPPM_{cryo}$ and $CERN_{cryo}$ showed the robustness of the motorised systems, even though the conditions were more extreme than what is planned in DS20k : the travelled distance was higher than in DS20k, the number of tensions switches (which may actually cause the higher degradation of the system) was more than five times higher than with the final system, and the hermeticity at the entrance of the tube was poor.

Also, the present Chapter mentions tests performed using tubes with 3 cm diameter. Tests performed with both 3 cm diameter stainless steel tubes and 5 cm diameter stainless steel tubes have been conducted at room temperature, again by asking the motorised systems to move the source throughout O(10) back and forth. The expected result of the test

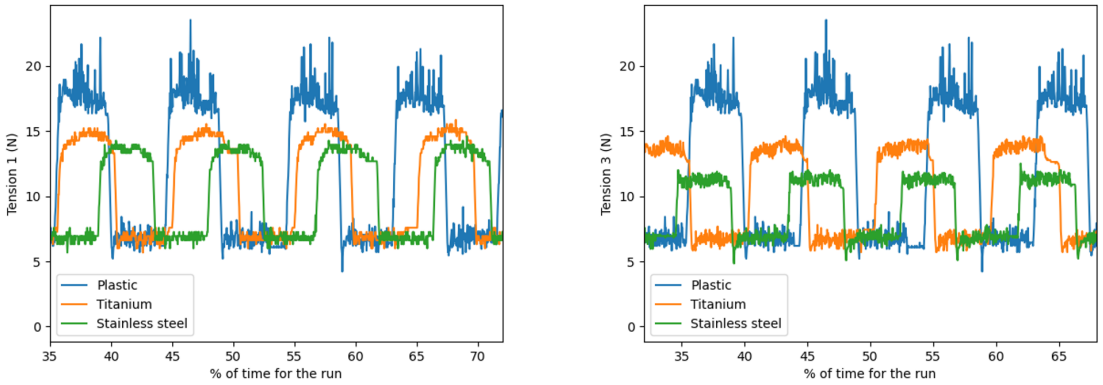

FIGURE 3.20. : Tension measured at warm with U-shape tube made of different material (plastic, titanium and stainless steel). Left : left motor (called #1) is pulling. Right : right motor (called #3) is pulling.

is no or feeble impact on the tension to apply on the ropes to let the source travel in the tube. The tests confirmed this hypothesis as shown in Figure 3.21 that displays the tension pattern measured during one set of back and forth travels in the tube. One can see that motorised sytems need to pull the source using slightly ($\approx$ 3 N, 20 % increase of tension) more tension with 5 cm (green curve) than with 3 cm (orange curve) diameter tube. The larger tension might be due to tube irregularity effects. To finish, in the most up-to-date scenario at the moment of writing, the final tube will be produced in several sub-parts and assembled using flanges and copper seals. We tested the impact of having such flanges on 5 cm diameter tubes at room temperature. The test did not outline an effect of the presence of such flanges on the tension (value and pattern) along the travel in the tube.

In addition to the validation tests described in this section, operation tests of sources safe handling were conducted with a mock-up of the glove boxes. These tests permitted the elaboration of a safe and complete procedure for source integration, including a set of protections preventing the source or the ropes to fall in the tube.

As a summary, the joint results of the mock-up test demonstrated the safe operability of the calibration system. Table 3.16 summarises the results obtained from each mock up and compares them with the requirements of DS20k, strenghtening the latter statement.

This chapter aimed at presenting the prospective calibration programme of DS20k, and more specifically the simulation of DS20k external calibration. Calibration is a key step towards high quality science data collection allowing a rich variety of physics analyses. Among them, a specific refined calibration at low energy for both ER and NR events permits to extend the WIMP search down to 1 GeV/c^2 and to other light dark matter candidates, as proven by DS50 [56, 66, 89, 90]. The study presented in Chapter 4 relies on the strength of DS50 recent results to motivate the sensitivity projection of DS20k for

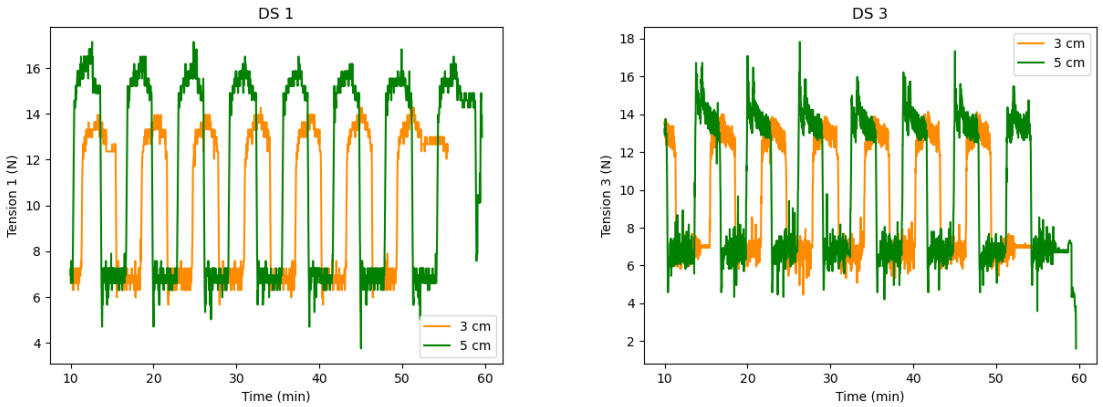

FIGURE 3.21. : Tension measured at warm with U-shape tube made of different stainless steel with different internal diameter (3 cm in orange and 5 cm in green). Left : left motor (called #1) is pulling. Right : right motor (called #3) is pulling.

low mass dark matter search.

	DS-20k	$CPPM_{cryo}$	$CERN_{cryo}$		$CPPM_{Scale1}$
	General				
Goals	NA	Cold behav.	Robust at cold		bends scale 1 :1
	Conditions				
Temperature (K)	88	**77**	**77**	**88**	290
Usage time / run (days)	30	0.3	18	14	0.3
Location	LNGS	CPPM	CERN		CPPM
	Mechanics				
Tube total length (m)	20	~ 4	~ 3		$\sim$15
Tube thickness (mm)	1.5	1.65	1.5		1.5
Tube internal diameter (mm)	30	30	33		30
Tube Material	SS	Ti	SS		Plastic
Nb of bends / tube (ϕ=40cm)	14, 15	2	1		**15**
Source length (cm)	TBD	3	5		5
Source diameter (cm)	TBD	1	2.5		2.5
	Requirements / Performance				
Speed of the source (cm/s)	> 1	3	1		2
Position accuracy (cm)	± 1	± 1	1		± 1
Tension (N)	< 150	25-40	15-30		60-90
Ice formation (block)	No	No	Yes but sublimated	No	NA NA
Total distance for all sources (m)	160 (/yr)	> 100	800	100	> 100
Total nb of back&forth / tube	4 (/yr)	44	280	35	>6

TABLE 3.16. : Characteristics of the final guide tube system and how they are addressed by the three mock-ups. Requirements from DS20k are put in red at the bottom. In green are the outcome of the mock-ups tests. Note that the speed of the source was adjusted for each set-up which explains the difference between $CPPM_{cryo}$, $CERN_{cryo}$ and $CPPM_{Scale1}$.

4. DarkSide-20k sensitivity to light dark matter particles

Summary

Double phase TPCs are primarily designed to search for high mass ($> 10\,\mathrm{GeV/c^2}$) WIMPs interacting with the nucleus of the target material. To do so, such experiments collect a combination of prompt scintillation photons and localised ionisation electrons in order to be able to perform a set of analysis selections that enable to clean the data from background. However, such analysis strategy is only possible above a certain energy threshold that depends on the detector material and design, where the scintillation is efficient enough.

It is still possible to search for dark matter below this threshold by considering only the ionisation charge signal. In the case of argon double phase TPCs, this method was proven to be successful by the DarkSide-50 (DS50) experiment in 2018, that reached world best limits on WIMP search in the low WIMP mass range [68]. A re-analysis of the data further strengthened the results [56, 89]. On top, the analysis of low energy deposits allows to search for other low mass dark matter candidates, also proven by DS50, reaching world best limits in galactic ALP, dark photon and light dark matter searches [90, 91].

In light of the success of DS50 low mass dark matter searches, the DarkSide-20k (DS20k) experiment is expected to dramatically enhance the accessible phase spaces by increasing the exposure by several orders of magnitude while decreasing the background level per unit mass compared to DS50. In that respect, I assessed the sensitivity of DS20k to low mass dark matter candidates. First, Section 4.1, further motivates the study. Then Section 4.2 presents in details the analysis method of low energy deposits, in particular the detector response model and the signal and background modelling. This leads to the sensitivity estimates of DS20k in Section 4.3 towards future low mass dark matter search. Finally, Section 4.4 assesses the robustness of DS20k sensitivity against experimental assumptions.

4.1. Motivations

The DS20k low mass sensitivity study originated from the success of DS50 in modelling its low energy background. Thus, the present section describes the DS50 analysis method that lead in 2023 to world best limits on the WIMP-nucleon spin independent cross section of interaction in the [1.2, 3.6] $\mathrm{GeV/c^2}$ mass range.

The DS50 experiment operated in the Hall C of LNGS in the last decade. During the second data-taking campaign from 2015 to 2018, the TPC was filled with low-radioactivity argon extracted from deep underground, with reduced activity of cosmogenic isotopes, especially for the ^{39}Ar β decays. Traces of residual β-decays of ^{85}Kr at the same level than ^{39}Ar were also observed – it was unexpected, hence no removal of krypton from the UAr was attempted. These two isotopes are assumed to be uniformly distributed in the TPC. The TPC active mass is 46.4 ± 0.7 kg. Two arrays of 19 classical photo-multiplier

tubes (PMTs) are installed at both ends of the TPC.

In this analysis, the only energy observable is the number of detected electrons N_{e^-}, defined as the corrected number of S2 photo-electrons (pe) divided by the S2 yield [1]. After ionisation electrons have been drifted across the liquid bulk with a 200 V/cm electric field (maximum drift time of 376 μs at an electron drift speed of 0.93 mm/μs), they are extracted and drifted in the gas pocket by means of 2.8 and 4.2 kV/cm electric fields respectively. Note that, given the relative small size of the TPC, almost all electrons reach the gas pocket as the electron lifetime was measured to be $\approx$ 10 ms, almost 30 times longer than the maximum drift time [66].

4.1.1. DarkSide-50 low mass analysis strategy

In the low energy regime with the single information of the number of ionisation electrons released in the interaction, the dark matter search cannot be background free. Indeed, because of the S1 inefficiency below O(30) electrons, the S1 Pulse Shape Discrimination (see Chapter 2) cannot be used to distinguish ER background from NR : the search becomes background-dominated. Hence, the DS50 experiment put a strong effort in modelling its low energy background.

First, one needs to identify and characterise the background sources. Then, the energy distribution of each background source is either computed or simulated and transformed into ionisation spectra by taking into account the detector response model and its calibration. The method is schemed on Figure 4.1 : starting from energy spectra, selections are performed (single scatter events in the energy region of interest and in the fiducial volume), and the resulting spectra are transformed into ionisation spectra thanks to the calibration. Then, quenching effects (ER : Fano factor and NR : quenching fluctuations), detector effects (single electron resolution measured to be 27%, electron lifetime of $\approx$ 10 ms and xy resolution taken as 1 cm) and specific corrections due to the instrument (S2 radial dependency) are applied.

As said, the selections applied to the DS50 data and the background model are single scatter events in the energy region of interest and in the fiducial volume. The energy region of interest is [0.06, 21] keV_{ee} = [0.6, 393] keV_{NR}, corresponding to [4, 170] N_{e^-} range. The upper bound of the N_{e^-} range is at high number of electrons, where one does not expect signal, in order to constrain the PMTs background, dominant from N_{e^-} = 50. The lower bound of the N_{e^-} range is the limit under which the background is not understood (see Section 4.1.2). The fiducial volume is defined as the volume below the seven central PMTs of DS50. With this definition, the fiducial volume is $\approx$20 kg.

[1] The S2 yield is measured to be g_2=23 $\pm$ 1 pe / e^- [68].

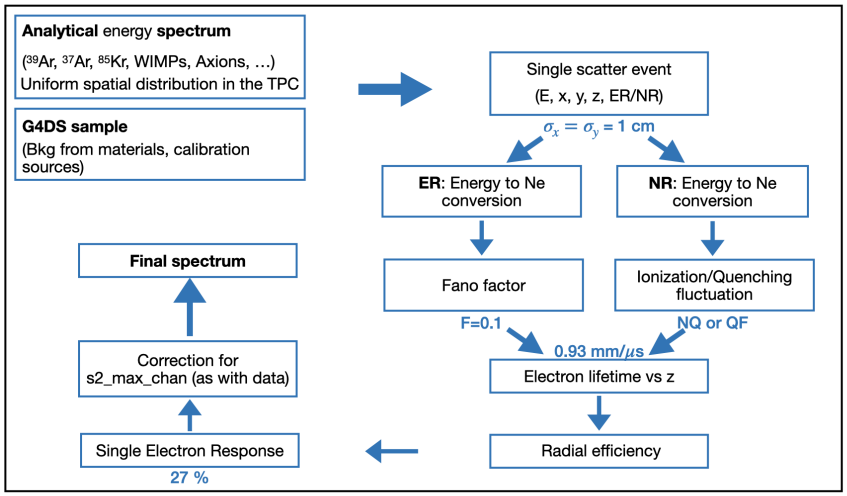

FIGURE 4.1. : Schematic representation of the analysis method used in DS50.

4.1.2. Background model

DS50 witnessed two internal background sources in the first 70 days of UAr campaign. First, the residual ^{39}Ar from the UAr volume, which was expected and measured with an activity of 0.73±0.11 mBq/kg. Second, the unexpected ^{85}Kr, measured with a corrected activity of 1.84±0.12 mBq/kg (^{85}Kr having a short decay time, $\tau_{1/2}$∼10.8 yr, the early-measured activity was corrected and averaged over the 650 live days of the DS50 dataset) [56]. The ionisation spectra are obtained from the analytical computation of β decays energy spectra of ^{39}Ar and ^{85}Kr, including atomic exchange and screening effects [92, 93]. Systematics on the shape come from the uncertainty on the atomic exchange, screening effects and Q-value (1% for ^{39}Ar and 0.4% for ^{85}Kr), and from the detector response (ER ionisation yield). The expected internal background N_{e^-} spectra for ^{39}Ar and ^{85}Kr and their associated systematics are shown in Figure 4.2 left. Note that the Q-value uncertainty is too small hence not illustrated on the plot.

For external backgrounds, the main sources of X-ray and γ backgrounds are the radioactive contaminants (^{238}U, ^{235}U, ^{232}Th, ^{60}Co, ^{54}Mn and ^{40}K) in the materials of the cryostat and the PMTs, whose activities have been measured in a dedicated material screening campaign. The energy spectra are simulated using g4ds, and predicted rates of 0.59±0.04 mHz and 3.5±0.4 mHz are obtained for cryostat and PMTs respectively [56]. Systematics from the detector response and the Monte Carlo statistical uncertainty are propagated to the spectra. The external background (nominal and associated systematics) from PMTs and the cryostat is shown on Figure 4.2 right.

DS50 observed one last background component, dominant at low number of electrons, called "spurious electron background", whose origin is unknown. This background is not well understood thus not modelled in the DS50 analysis. However, thanks to a cut on the time difference between two consecutive events in the dataset, its contribution was

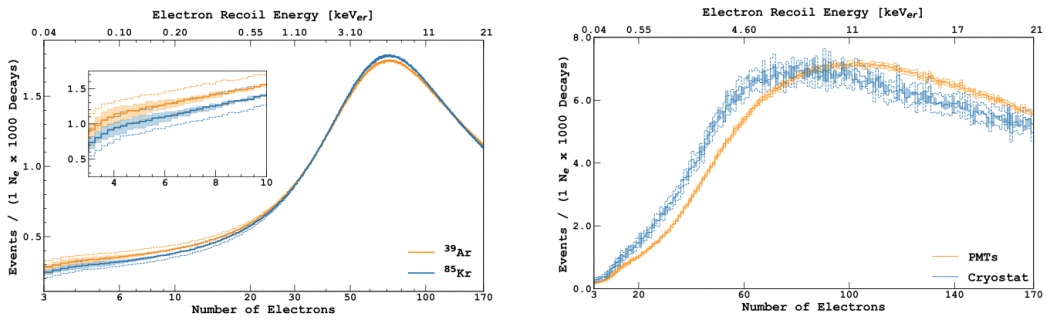

FIGURE 4.2. : N_{e^-} distribution of background spectra in DS50 per N_{e^-} and per 1,000 decays. Left : Internal background from argon (in orange) and krypton (in blue), shaded areas correspond to systematics from atomic exchange and screening effects while dashed lines correspond to systematics from ER ionisation yield. Right : External background from PMTs (in orange) and cryostat (in blue), shaded area corresponds to systematics from the detector response and dashed lines correspond to uncertainties from the Monte Carlo statistics. From [56].

lowered to negligible values from $N_{e^-} = 4$, hence the lower bound of the region of interest of the low mass analysis.

The fitted background model corresponding to 12 ton×day exposure of DS50 in the [4, 170] N_{e^-} range is shown in Figure 4.3 top. DS50 data are shown in black dots, and the fitted contributions from the four background components are shown. At the bottom of the plot, one can see the comparison between data and fitted model (with associated uncertainty in shaded area) and appreciate the good agreement between both. Figure 4.3 bottom left confirms that claim as the pulls from the background-only fit are centred on 0 and normally distributed which validates the background model. Figure 4.3 bottom right shows the individual nuisance parameters (NPs) post fit values and their correlations from the background-only fit. As expected, the normalisation (called "A") of similar background components are anti-correlated. ER ionisation yield post-fit error improved compared to the pre-fit as its model depends on few calibration points at low energy.

4.1.3. DarkSide-50 search for light dark matter particles

Using low energy data, DS50 is sensitive to low mass dark matter candidates, and especially to WIMPs below 10 GeV/c^2. Searching for WIMPs interacting with the nucleus with a pure NR signal allows DS50 to scan the [1.2, 10] GeV/c^2 WIMP mass range. Similarly to high mass WIMP search, the limits are shown in the (m_χ, σ_{SI}) phase space, m_χ being the WIMP mass and σ_{SI} the spin independent cross section of interaction between the WIMP and a nucleon. The limits are computed using a Binned Profile Likelihood method. Figure 4.4 shows the limits of DS50 compared to the ones of other experiments. DS50 leads the WIMP search in the [1.2, 3.6] GeV/c^2 mass range. This

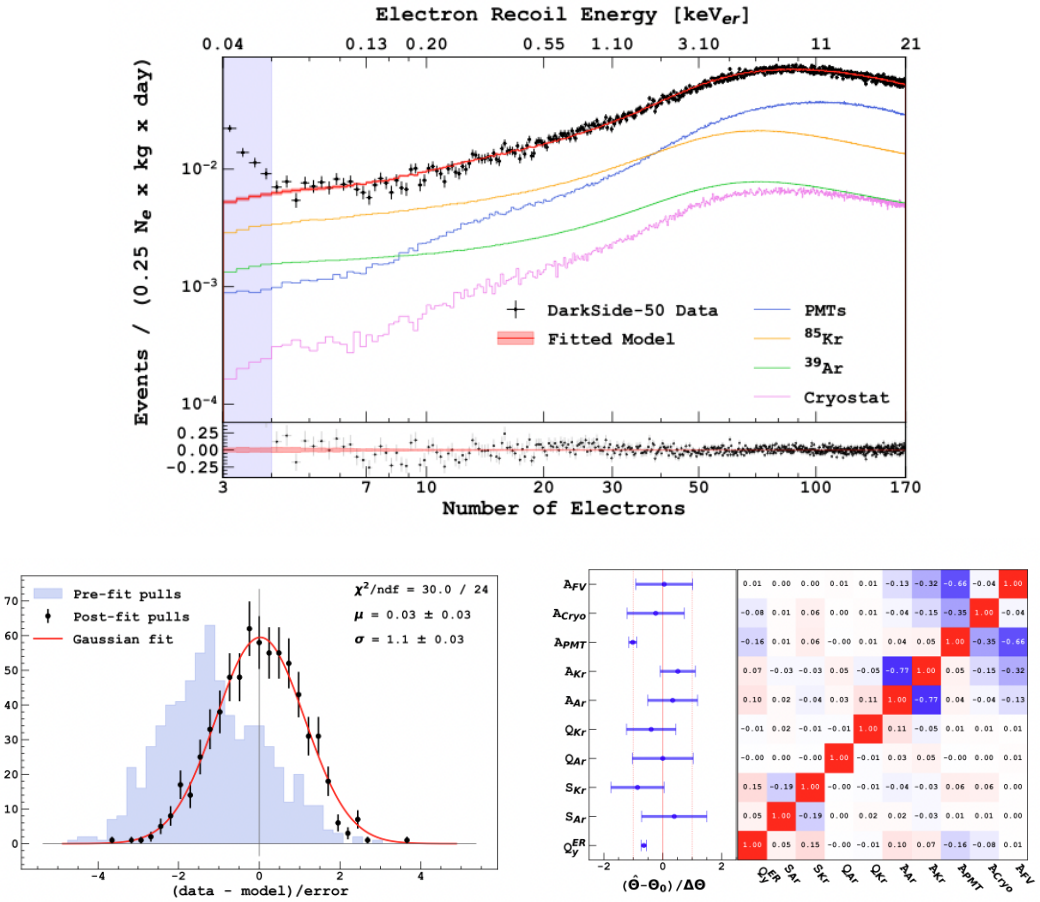

FIGURE 4.3. : Top : DS50 fitted background model and its four contributions from internal and external backgrounds. Bottom left : Background only fit pulls. Bottom right : NPs pulls and correlation matrix from the background-only fit. From [56].

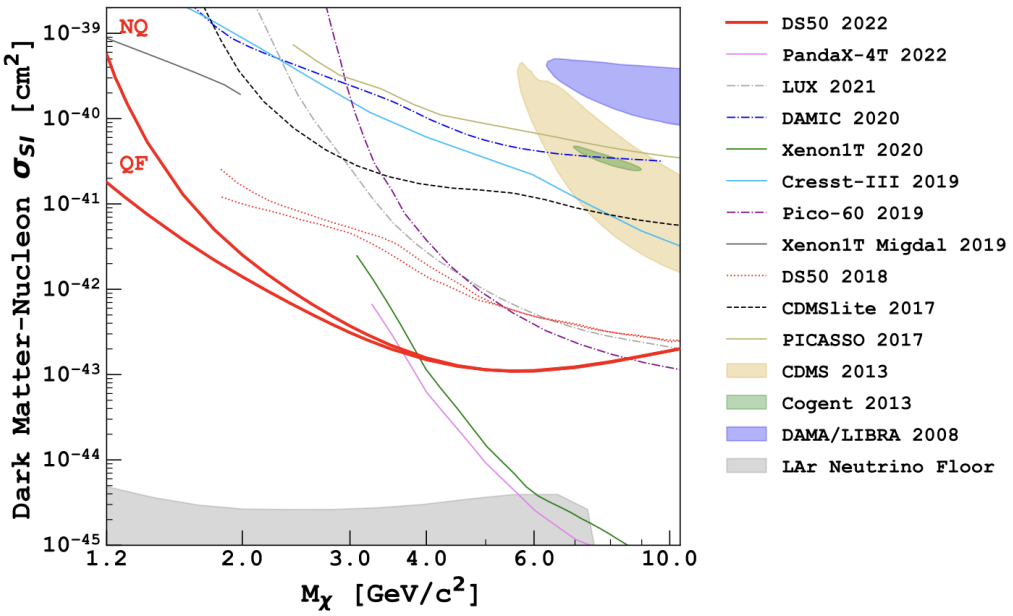

FIGURE 4.4. : DS50 90% C.L. exclusion limits on the WIMP-nucleon spin independent cross section of interaction using a Binned Profile Likelihood method. QF and NQ stand for "Binomial quenching fluctuations" and "No quenching fluctuations" for the modelling of quenching in the NR case. World best limits are set in the [1.2, 3.6] GeV/c^2 mass range. From [56].

strong result demonstrates the ability of liquid argon double phase TPCs to search for low mass dark matter candidates by only using information from the ionisation charge.

By considering the potential so-called Migdal effect in NR (atomic effect consisting in the emission of an electron following a NR), the detection threshold can be lowered thanks to the higher ionisation yield in ER. Hence, with the Migdal effect, DS50 could search for WIMPs down to 40 MeV/c^2. Figure 4.5 shows the limits placed by DS50 on the WIMP search using the Migdal effect. In the QF scenario, DS50 improves the search compared to other experiments on the whole mass range below 3.6 GeV/c^2. In the NQ scenario, DS50 improves the search compared to other experiments in the [1.2, 3.6] GeV/c^2 and below 0.6 GeV/c^2.

In addition, DS50 could search for other dark matter candidates interacting with argon electrons [2], such as the so-called "Light Dark Matter" (LDM), that has masses below 1 GeV/c^2 and scatters-off argon shell electrons via weak interaction. The cross section of interaction between LDM and electrons, $\bar{\sigma_e}$, depends on the momentum transfer q, taken into account thanks to a dark matter form factor F_{DM}, that depends on the mass of the

[2]The considered dark matter candidates are listed yet not presented in the present section, as my PhD work focused on the DS20k experiment. More information on these candidates, such as the interaction rate (key for setting limits), as well as DS50 limits, are given in Section 4.3.

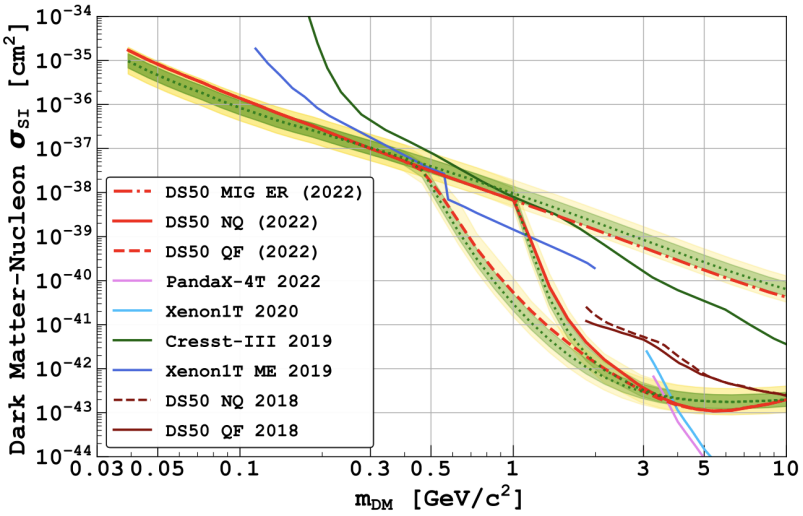

FIGURE 4.5. : DS50 90% C.L. exclusion limits on the WIMP-nucleon spin independent cross section of interaction using the Migdal effect. QF and NQ stand for "Binomial quenching fluctuations" and "No quenching fluctuations" for the modelling of quenching in the NR case. World best limits are set in the 40 MeV/c^2 – 3.6 GeV/c^2 mass range. From [89].

mediator of the interaction. These two scenarii give different limits for DS50. At the time of publication, the DS50 experiment set the world best limits on $\bar{\sigma_e}$ in the [16, 56] MeV/c^2 mass range for a heavy mediator and above 80 MeV/c^2 for a light mediator [90].

DS50 is also sensitive to other dark matter signals absorbed by shell electrons of argon. The absorption is observable thanks to the mono-energetic signal released at the particle rest mass. Axion-Like-Particles (ALPs, mass m_A) or Dark Photons (DP, mass $m_{A'}$) are two dark matter candidates that can be observed using such absorption effect. For ALPs, the interaction rate depends on the ALP-electron coupling strength g_{Ae}, while the one between DP and electrons depends on the strength of the kinetic mixing κ between the photon and dark photon. Thus, upper limits on ALPs and DP are set on g_{Ae} and κ, respectively. Stronger limits are set by DS50 on both g_{Ae} and κ in the [0.03, 0.2] keV/c^2 mass range [90]. It is worth noting that such limits were the first direct detection limits set by argon target material detector for the ALP and DP dark matter candidates.

Last, DS50 is sensitive to sterile neutrinos, that may scatter off shell electrons of argons and transform into the active state electronic neutrinos ν_e. The mixing rate depends on $|U_{e4}|^2$, that parametrises the mixing (it is a PMNS-like matrix element that includes sterile states). The sensitivity of DS50 to sterile neutrinos has been computed [90], however the NuSTAR experiment already placed best indirect constraints to sterile neutrinos down to $|U_{e4}|^2 = 10^{-13}$ at 20 keV/c^2 [94].

To conclude, thanks to an excellent background description down to 4 electrons using four background components, DS50 could set the world best limits on the direct detection

of several dark matter candidates including the flagship WIMP.

Given this success with a small-size TPC, it is clear that the 1,000 times larger successor of DS50, DarkSide-20k, is expected to drastically enhance the low mass dark matter search.

4.2. DarkSide-20k ionisation only analysis

The design of DS20k is described in Chapter 2. The key ingredients for the low mass analysis are however listed in Table 4.1 and justified here. DS20k will use purified liquid argon extracted from the same underground mine as DS50 in Colorado, USA, so the same ^{39}Ar activity as measured in DS50 is assumed (i.e. 0.73 mBq/kg). Cryogenic distillation in Aria, Sardinia, Italy (not used for DS50) may reduce the ^{39}Ar activity and this will be considered in Section 4.4. The multiple distillation column system from Urania (Colorado, USA) will remove traces of ^{85}Kr observed in DS50. As a consequence, a factor 100 lower activity than in DS50 (i.e. 18.6 μBq/kg) is assumed (unless otherwise stated, see Section 4.4).

The TPC active volume, before fiducialisation, is 1,000 larger than the one of DS50 : the TPC of DS20k will be filled with 49.7 t of low radioactivity liquid argon. As a consequence, the maximum drift time will increase from 376 μs in DS50 to 3.76 ms in DS20k [3], causing a larger part of the drifting electrons to be absorbed before reaching the gas pocket (11% in average). For the electron lifetime in the TPC, a value of 15.8 ms, as used in g4ds, is assumed [86]. The impact on the sensitivity in case a worse lifetime would be achieved is discussed in Section 4.4.

At the top of the TPC of DS20k, SiPMs will detect photo-electrons, instead of PMTs for DS50. The use of SiPMs allow to reduce the background contamination from the photo electronics per unit mass thanks to their much smaller radio-activity.

In the same vein, in DS20k, the walls of the TPC are in PMMA with excellent radio-purity properties. To shape the electric field, conductive rings are formed by painting the inner walls with Clevios, avoiding the insertion of a metal field cage structure and thus minimising the amount of passive material. Therefore the external radioactive contamination should be much reduced compared to the structure of the DS50 TPC.

As for the DS50 analysis, selection cuts are applied (Section 4.2.1) and the simulation of N_{e^-} spectra is obtained by introducing a realistic description of the detector response (Section 4.2.2). The background model is established using the currently measured activities (Section 4.2.3) and fitted with a binned profile likelihood considering a set of 15 nuisance parameters (Section 4.2.4). Benefiting from the very large volume of DS20k, one expects quick competitive results for the low mass search hence the nominal scenario assumes one year of data-taking. The relevant detector model parameters are the xy position resolution of 3 cm and the single electron charge resolution of 23%. The latter

[3] Both DS50 and DS20k have the same drift, extraction and luminescence fields. As a consequence, the same electron drift speed as DS50 is assumed for DS20k.

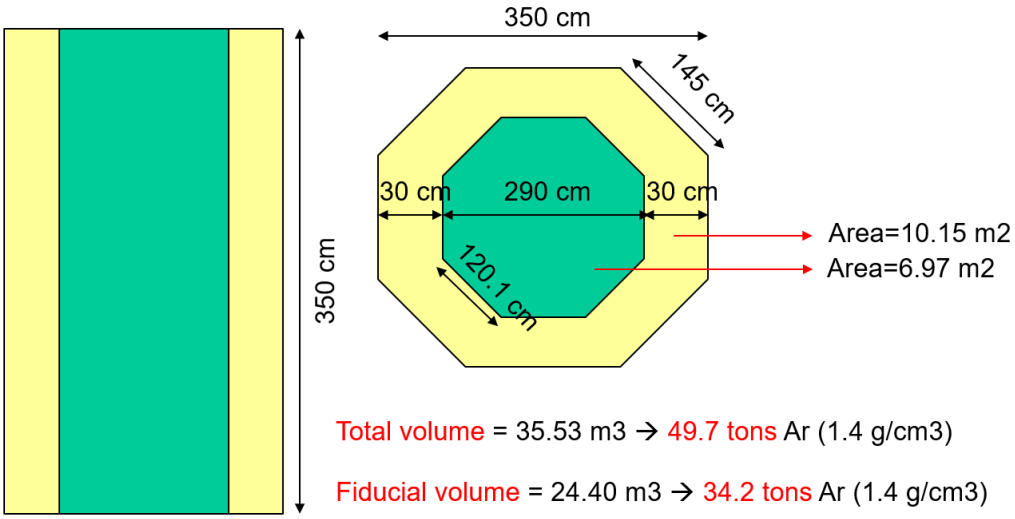

FIGURE 4.6. : Fiducial volume (shown in green) definition for the low mass analysis of DS20k.

comes from a study of noise and reconstruction effects using dedicated DAQ simulation tools.

4.2.1. Selections

4.2.1.1. Fiducialisation

A S2-only dataset does not permit to estimate the z-position of the interaction in the TPC, as it is usually estimated thanks to the time difference between the arrival of the prompt S1 (inefficient in the low energy case) and the delayed S2. Hence, the fiducialisation is only possible in the xy plane thanks to the array structure of the SiPMs. In the nominal scenario, as schemed in Figure 4.6, 30 cm in radius around all vertical walls are removed from the active volume of the TPC, defining the ficucial volume with a mass of 34 tons. This definition leads to a signal efficiency of 68.7%. The impact of increasing the fiducial volume to increase the signal efficiency is discussed in Section 4.4.

4.2.1.2. Isolated S2 pulses

In a time sequence of S2 pulses, the dark matter candidates pulses that should be considered in the analysis are single scatters, i.e. single interaction deposits in the bulk of the detector. Without information from S1, a single scatter is defined as one and only one S2 pulse. In a 3.5 m high detector like DS20k, pile-up needs to be taken into account : two S2 pulses from two different interactions (at two different times and positions in the TPC), arriving at the SiPMs level separated by a time $\Delta T < T_{drift}^{max} = 3.7$ ms (T_{drift}^{max} is the maximum electron drift time in the TPC) cannot be distinguished from a multiple scatter originating from the same background particle. Therefore, for the low mass analysis, the

considered S2 pulses dataset is S2s isolated from their closest neighbours in time, i.e. separated from the previous and next S2 pulse by more than T_{drift}^{max}. Such single scatter definition introduces some dead-time because of pile-up.

In the prospective analysis, simulation tools don't take into account the pile up (the single scatter selection is the Monte Carlo truth). Indeed, a proportion of events passing the single scatter selection at simulation level (on the basis of the Monte Carlo truth, and independently for signal and all different backgrounds) wouldn't pass such selection with real data because of pile-up. A dedicated study is performed to estimate the dead-time induced by the 3.7 ms maximum drift time in the TPC. It is done thanks to a collaboration tool (called the *event mixer*) that produces a realistic random time sequence of background S2 pulses that takes into consideration the expected activities and interaction probabilities of each background component. A veto time window of 3.7 ms before and after each reconstructed scatter is added to the dead-time. The dead-time computation procedure is detailed here :

1. 30 s of full background sample is generated in the TPC with g4ds and the event mixer, using all background sources (internal, external and spurious electrons, see Section 4.2.3) and assuming activity rates from Figure 4.7 top. Before any selection cut, the total rate from internal and external backgrounds is 80 Hz (0.0016 Hz/kg of UAr) in the TPC ;

2. the deposits are clusterised in order to mimic the number of scatters ;

3. the realistic time series of S2 pulses at SiPMs level is defined as the cluster time plus the drift time calculated from the cluster $z-$position. Figure 4.7 center shows the time distribution of these S2 pulses ;

4. for each time t_0, veto time windows in the range [t_0 −3.7 ms, t_0 +3.7 ms] are added to the dead-time, taking care of possible overlaps between them, as shown by the red boxes in Figure 4.7 bottom. All pulses falling in such windows, including pulses at t_0, are rejected.

A live time of 51% is found. This is taken into account in the following by considering a total exposure×efficiency in the fiducial volume of 34.2×0.51=17.4 ton.yr for 1 year of data taking. This approach ensures well isolated S2 events, and allows to have conservative estimates of the sensitivity.

4.2.1.3. Region of interest

Strong from the DS50 experience, the analysis assumes that the background of DS20k will be understood at least from $N_{e^-} = 4$. As shown later (Section 4.2.3), there has been an effort to model the spurious electron background, hence the possibility to reduce the lower bound of the region of interest from 4 to 2 electrons. However, the upper bound remains the same. The region of interest for the DS20k prospective analysis is thus [2, 170] N_{e^-} in the ultimate scenario, or [4, 170] N_{e^-} in the conservative scenario.

Summary	mass [kg]	up238U [Bq]	mid238U [Bq]	low238U [Bq]	232Th [Bq]	235U [Bq]	Cs-137 [Bq]	Co-60 [Bq]	K-40 [Bq]
TPC PDM (PDU + cables)	2.9E+2	2.7E+1	1.2E+1	3.6E+2	8.3E+0	1.2E+0	1.1E+0	1.2E+0	2.2E+2
VETO PDM (PDU + cables)	6.7E+01	5.6E+00	2.9E+00	8.3E+01	2.3E+00	3.2E-01	2.8E-01	2.7E-01	3.6E+01
TPC reflector	2.7E+2	5.3E-1	4.1E-1	2.0E+0	1.0E-1	2.8E-2	7.6E-2	2.2E-1	1.5E+0
TPC OP	1.62E+3	5.51E+0	2.98E+0	5.51E+0	6.65E+0	2.54E-1	9.58E-1	1.45E+0	1.26E+1
Grid Support Frame	7.0E+2	7.0E-1	5.1E-1	7.0E-1	5.8E-1	3.2E-2	6.0E-1	2.2E+0	3.4E-1
TPC structure	2.0E+3	3.6E+0	9.9E-2	2.4E+0	1.5E-1	1.6E-1	4.9E-2	4.4E-1	8.1E-1
calibration fiber	2.2E-2	1.8E-01	1.8E+00	2.4E+01	9.7E-02	8.3E-03	5.7E-02	4.8E-02	2.7E+00
Gd-PMMA	1.2E+04	1.2E+01	1.1E+01	1.2E+01	4.0E+00	5.3E-01	2.4E+00	1.3E+00	1.0E+02
Veto reflector	5.0E+01	7.1E-02	7.7E-02	1.7E-01	3.7E-02	3.3E-03	2.7E-03	3.5E-02	7.1E-02
SS vessel	1.2E+04	2.1E+01	8.8E+00	6.2E+01	3.3E+01	9.6E-01	5.0E+00	1.3E+01	4.9E+01

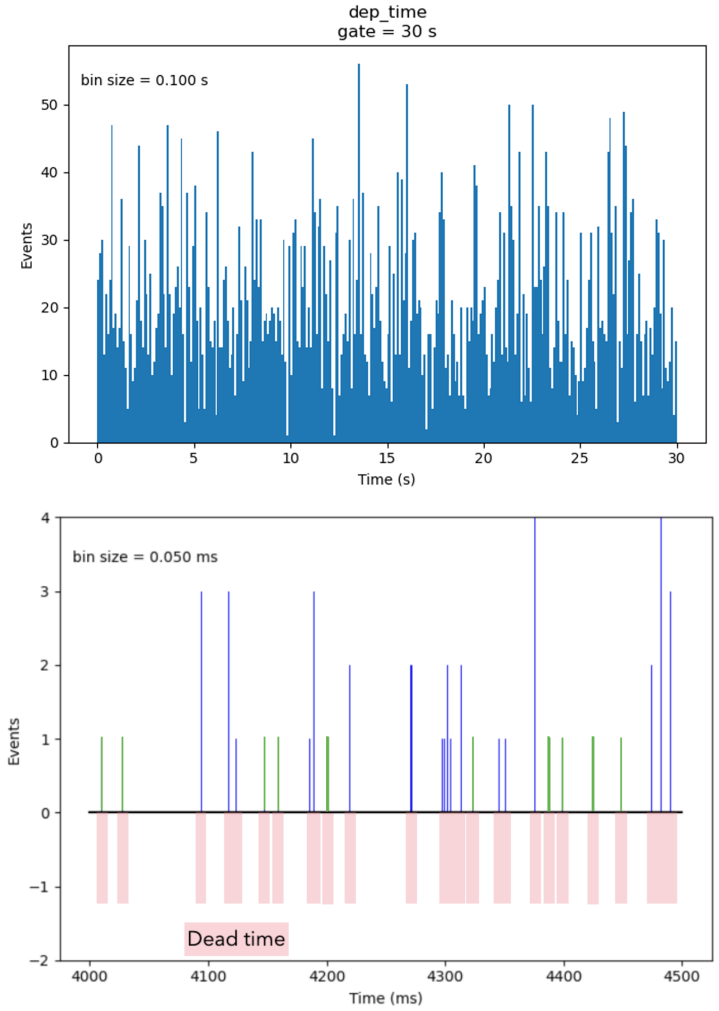

FIGURE 4.7. : External background activities estimated by screening campaigns within the collaboration, as of April 2024 (top), time distribution of events generated with the event mixer (center) and illustration of the isolation procedure (bottom). In the latter, peaks are S2 pulses. The single scatter pulses which are isolated within 3.7 ms are coloured in green, while all others (multiple scatters or single scatters with a neighbour within 3.7 ms) are coloured in blue. One maximum drift time veto window is added before and after each scatter (labelled as dead-time).

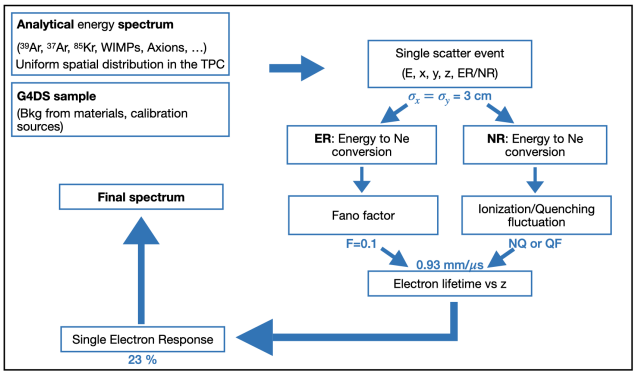

FIGURE 4.8. : Schematic representation of the detector model for DS20k.

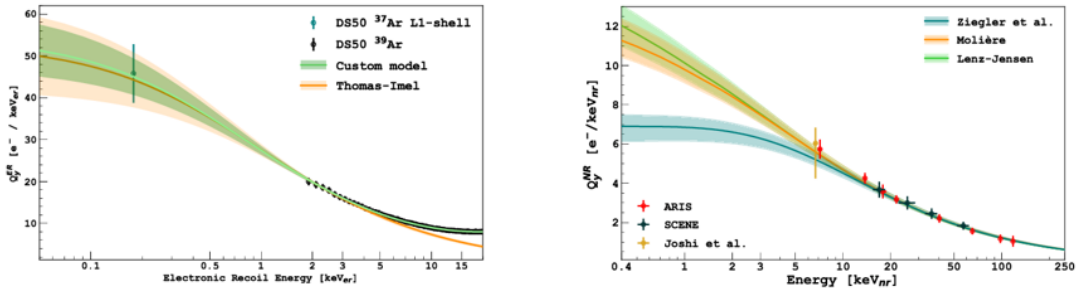

FIGURE 4.9. : ER and NR ionisation yields measured by the DS50 experiment [66].

4.2.2. DarkSide-20k detector response model

The ionisation spectra of each background, shown in terms of number of electrons N_{e^-}, are obtained from initial truth level energy spectrum of particles issued from a radioactive decay. To transform the energy spectra into ionisation spectra, several steps are implemented to take into account instrumental effects on the N_{e^-} distribution. Figure 4.8 shows the detector model adopted for DS20k.

Energy spectra are converted into N_{e^-} distributions using the ionisation yield for ER and NR, measured in low energy calibration campaign of DS50 [66] and shown in Figure 4.9. NR ionisation yield is about 7 e^- / keV_{NR} at 500 eV_{NR}. This allows the lower bound of the energy region of interest to be at low (O(1)) number of electrons. Quenching associated to ER (Fano factor [95]) and quenching NR are then considered. The former has been measured to be 0.10±0.03 [66]. There is no model existing for the latter, therefore two situations are considered : a conservative one assuming no fluctuations (NQ) or binomial fluctuations (QF) between detectable (ionisation electrons and excitons) and undetectable quanta (e.g. phonons). The choice of binomial fluctuations ensures that the number of produced quanta does not exceed the maximum one, equivalent to the ratio between the deposited energy and the average work function (19.5 eV) in liquid argon.

The detector parameters of interest in the prospective low mass analysis of DS20k are shown in Figure 4.8. They are listed in Table 4.1. Their impact on the DS20k sensitivity is discussed in Section 4.4.

TPC active mass	49.7 ton
Electron drift speed	0.93 mm/μs
Maximum drift time	3.76 ms
Electron lifetime	15.8 ms
xy position resolution	3 cm
Single electron resolution	23%

TABLE 4.1. : Relevant DS20k detector model parameters for the low mass analysis.

4.2.3. DarkSide-20k background model

In order to build a background model, one needs to estimate the activity of the radio-components present in each background and their energy spectrum. Depending on the nature of the background, internal or external to the TPC volume, the energy spectrum can be described analytically or requires Monte Carlo simulations using g4ds [82, 86].

4.2.3.1. Internal background

The same internal background components as in DS50 are considered for this analysis, however with different specific activities. Indeed, as already justified in the introduction of the present Section, the same ^{39}Ar activity as in DS50 is assumed (i.e. $\mathrm{A}(^{39}Ar) = 0.73$ mBq/kg), because the UAr comes from the same underground mine as for DS50 UAr campaign. On the contrary, the ^{85}Kr activity is taken reduced compared to what was measured in DS50 thanks to Urania extraction column. The ^{85}Kr activity is thus assumed to be 100 times lower than the one of DS50 (i.e. $A\,(^{85}Kr) = 18.6$ μBq/kg). The energy spectra of ^{39}Ar and ^{85}Kr are analytically computed including recent calculations of the corrections due to atomic exchange and screening effects [92, 93]. Below 200 eV, a linear uncertainty on this correction is considered, from 25% at 0 eV down to 0% at 200 eV. Further systematics on the shape come from the uncertainty on the Q-value (1% for ^{39}Ar and 0.4% for ^{85}Kr), and from the detector response, dominated by the uncertainty on the ionisation response.

Figure 4.10 shows the internal background ionisation spectra expected in DS20k per 1,000 decays $\times$ 0.25 N_{e^-}. The spectrum shape of ^{39}Ar and ^{85}Kr are similar as their Q-value are close to one another (565 keV for ^{39}Ar and 687 keV for ^{85}Kr). Both internal background spectrum shape are similar to DS50 (see Figure 4.2 top left), albeit with a peak positioned at slightly lower N_{e^-}, reflecting that a larger part of the drifting electrons are absorbed along their longer path (10 times longer drift time in the DS20k TPC). The contribution from all uncertainties is visible in the small inset of Figure 4.10.

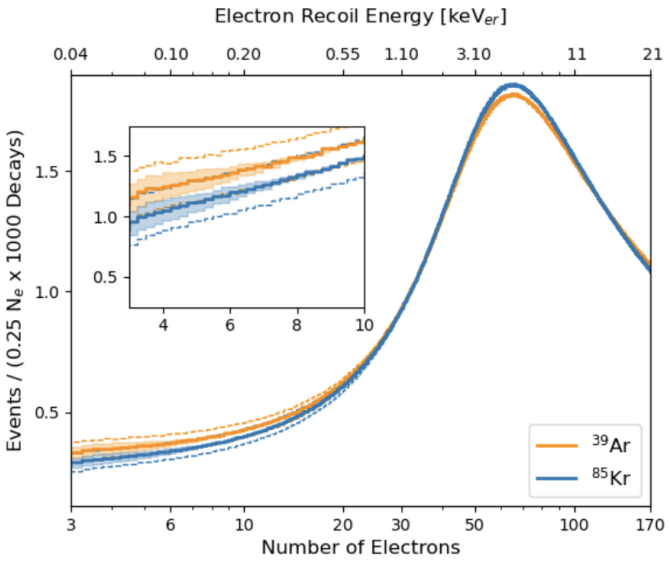

FIGURE 4.10. : Internal background spectra in N_{e^-} after including the detector response model : ^{39}Ar and ^{85}Kr.

4.2.3.2. External background

External backgrounds contributions are predicted thanks to Monte Carlo simulations. 10^9 (resp. 10^8) decays of all radio-contaminants shown in Figure 4.7 top with their associated activities have been simulated with g4ds for the photo-electronics (regrouping TPC SiPMs, veto SiPMs, optical planes stainless steel supporting structure, grid and its support frame), the TPC structure (regrouping the PMMA walls, the lateral reflectors, the anode and the cathode) and the stainless steel vessel.

Figure 4.11 shows the contribution from the three groups of external backgrounds. As expected due to the absence of z-cut in the FV definition, the contribution from the TPC SiPMs and the associated electronics is fully dominating the external background, followed by the one from the anode and the cathode. The contribution from the stainless steel vessel is completely negligible. The contribution from the TPC SiPMs is however significantly (a factor 27 per unit of fiducial UAr mass or a factor 2.7 per surface area) lower than the DS50 PMTs. The contribution from the walls and the vessel is also significantly reduced compared to the DS50 cryostat. Overall the external background level is reduced by a factor 2.5 per surface area (i.e. a factor 25 per unit of fiducial UAr mass) with respect to DS50, validating the extreme care taken to consider radio-pure material in the design of the inner detector. Uncertainties on the external backgrounds are due to the detector response and from Monte Carlo statistics.

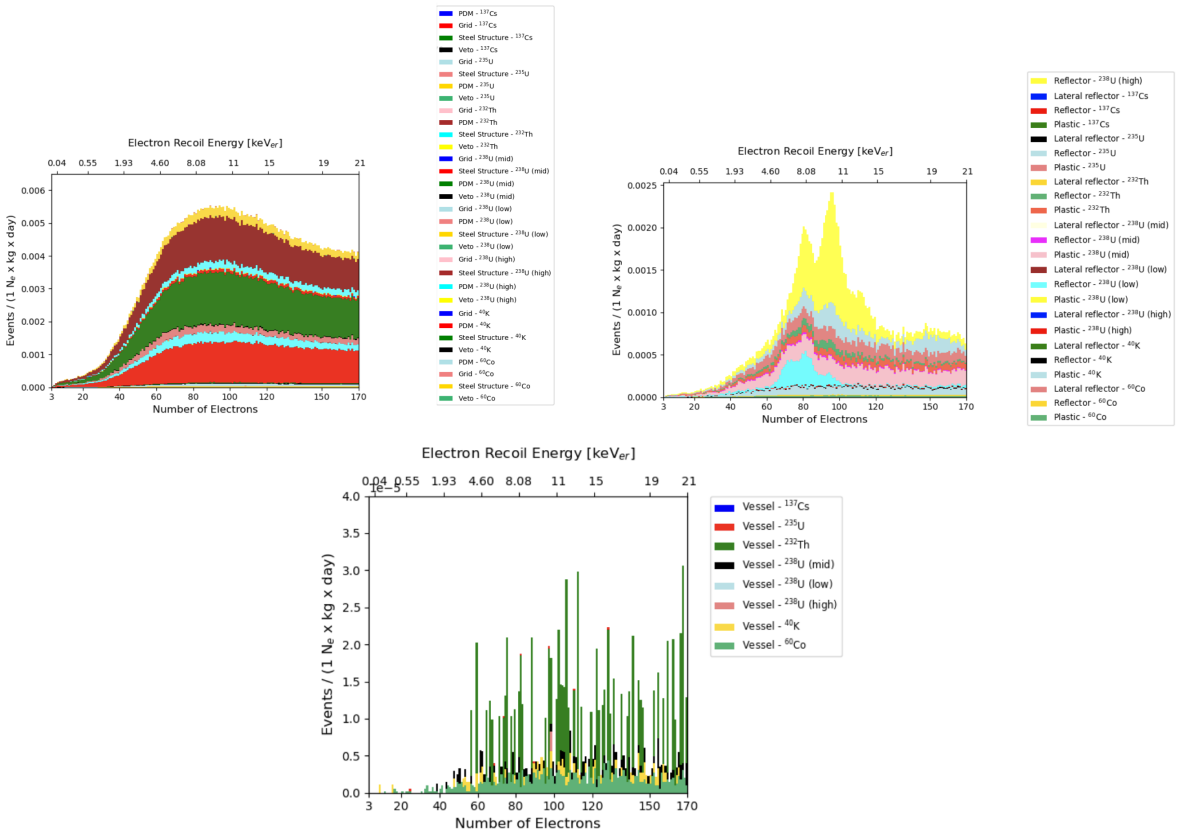

FIGURE 4.11. : External background spectra in N_e–, after including the detector response model : background from photo-electronics, regrouping TPC SiPMs, veto SiPMs, optical planes stainless steel supporting structure, grid and its support frame (top left) ; background from the TPC structure, regrouping the PMMA walls, the lateral reflectors, the anode and the cathode (called reflectors) (top right) ; and from the stainless steel vessel (bottom). The stacked spectra in the energy region of interest and in the fiducial volume are scaled by the measured activity of Figure 4.7 top.

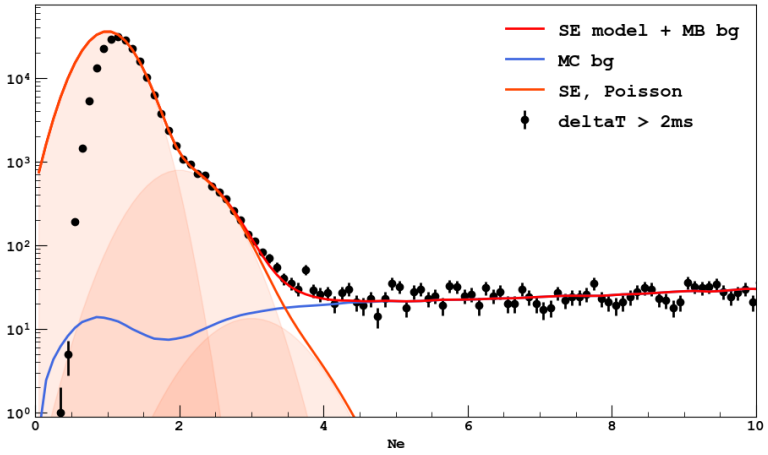

FIGURE 4.12. : Fit of the SE peak with model + background. The background (blue) is generated with Monte Carlo simulations. The model (red) is the convolution of a Poisson distribution with a Gaussian smearing for the single electron response. The individual peaks corresponding to Ne=1,2,3 are shown in shaded orange. The dataset (black dots) corresponds to the DS50 data selection.

4.2.3.3. Spurious electron background

"Spurious" electrons (SEs) are a major component of the background at low number of electron ($N_{e^-} < 4$) that needs to be estimated. They have been observed by DS50 but also by xenon experiments relying on the same technology [96, 97, 98, 99]. Their origin is for now unknown, hypotheses are ionisation electrons trapped by impurities and released later, or delayed electrons extraction at the interface between the liquid and the gas [100]. The model is built on DS50 data by the DS50 collaboration.

It has been shown that the N_{e^-} distribution of SEs can be described by a Poisson distribution whose mean is noted as μ_{se}. In addition, there is an observed correlation in time and space between SEs and a preceding high-energy (therefore highly-ionising) event (defined as *the parent event*). The mean number of SEs following a parent is also described by a Poisson distribution whose mean is referred as μ_N.

The shape of the SE peak, after the data selection including fiducialisation, can be fitted with a Poisson distribution smeared by a Gaussian term (accounting for the single electron resolution) on top of the background model generated for the low-mass DS50 analysis (including ^{39}Ar, ^{85}Kr and gamma rays from the PMTs and the cryostat). Figure 4.12 shows an example of such fit. Note that the model is unable to fully describe the shape of the $N_{e^-} = 1$ gaussian peak due to the trigger or pulse finder efficiency, failing for low electroluminescence signals. It has been proven that the shape (in N_{e^-}) of the SE background does not depend on the time difference ΔT between the SE event and its parent.

In addition, it has been shown that the SE spectra has a peculiar time profile. The SE event rate per unit time as a function of the event lifetime ΔT is shown in Figure 4.13. Fits

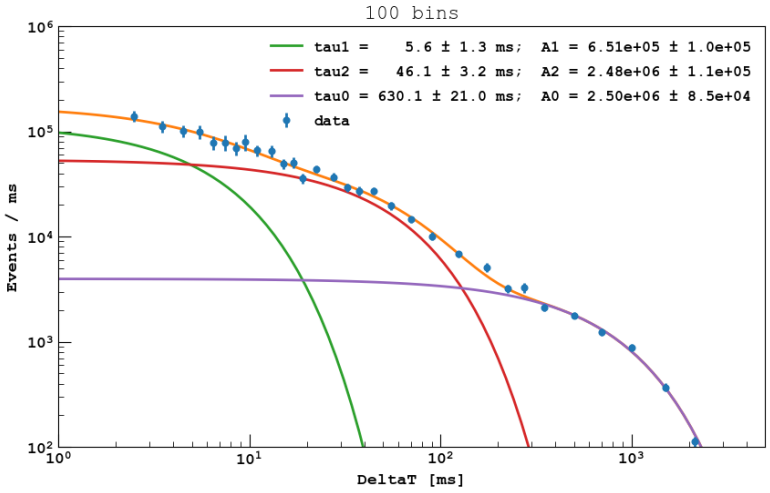

FIGURE 4.13. : Triple exponential fit (orange) of the SE event rate per unit time as a function of the event lifetime.

with a triple exponential are performed in order to precisely determine the characteristic times τ_i and the amplitudes A_i of the three components. Three decay time constants are visible : two are describing correlated components with $\tau_1 \sim 5$ ms and $\tau_2 \sim 50$ ms ; the third component ($\tau_0 \sim 630$ ms, $1/\tau_0 \sim 1.58$ Hz, compatible with the DS50 trigger rate) accounts for uncorrelated events.

Last but not least, it has been checked that the average number of SE increases linearly with the parent drift time, which is expected under the assumption that electrons are trapped on electro-negative impurities during their drift towards the anode and impurities are uniformly distributed in the bulk.

All these observations drive the extrapolation from DS50 data to DS20k :

- The SE ionisation spectrum model for DS20k low mass analysis is a Poisson distribution convoluted with Gaussian of sigma $\sigma_{SER} = 0.23$ and with a time profile with 3-components as in DS50 data ;
- As the SE are expected to come from trapped electrons from highly ionising particles, the scaling factor from DS50 to DS20k includes a trigger rate ratio $\frac{T_{DS20k}}{T_{DS50}}$;
- As the average number of SE increases linearly with the parent drift time, the scaling factor from DS50 to DS20k includes a maximum drift length ratio $\frac{L_{DS20k}}{L_{DS50}}$.

The absolute SE event rates of the three components are obtained by scaling the ones measured in DS50 by the ratio between the predicted (DS20k) vs measured (DS50) overall event rates and by the ratio between the drift lengths. Dividing by the active mass of the detectors, one can compute the specific rate (r^{corr}_{DS20k}, event rate per unit

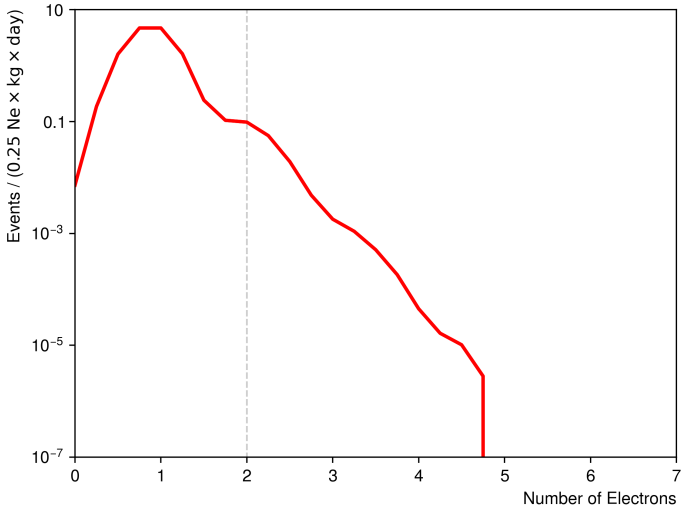

FIGURE 4.14. : N_{e^-} distribution for the SE background as extrapolated from DS50 data.

mass) predicted in DS20k as :

$$r_{DS20k} = r_{DS50} \times \frac{M_{DS50}}{M_{DS20k}} \times \frac{T_{DS20k}}{T_{DS50}} \times \frac{L_{DS20k}}{L_{DS50}}, \tag{4.1}$$

where r_{DS50} is the specific rate in DS50, M_i is the active mass, T_i the trigger rate and L_i the drift length of experiment i (i = DS50 or DS20k).

Finally, the model for SE ionisation spectrum is obtained with toy-Monte Carlo simulation, uniformly distributed in the TPC volume. The impact of electron lifetime is accounted for in the final determination of the shape and amplitude of the SE peak. A shape systematic is inferred by varying the mean of the Poisson distribution within the fit errors. A normalisation systematic is inferred from the A_i fits (3%) and raised to 20% to take into account uncertainty from extrapolation. As seen later, this normalisation is set to be conservative, yet has no impact on the sensitivity. The toy-Monte Carlo SE background spectrum is shown in Figure 4.14 : it is non-negligible at low number of electrons, and drops to negligible values for $N_{e^-} \geq 5$.

4.2.3.4. Neutrino background

With such a large exposure, DS20k sensitivity is expected to approach the neutrino fog. Hence, the neutrino background was considered in this analysis.

As energy spectrum input for the neutrino flux, the most recent estimates including radiative corrections (computed by members of the collaboration) are used, shown

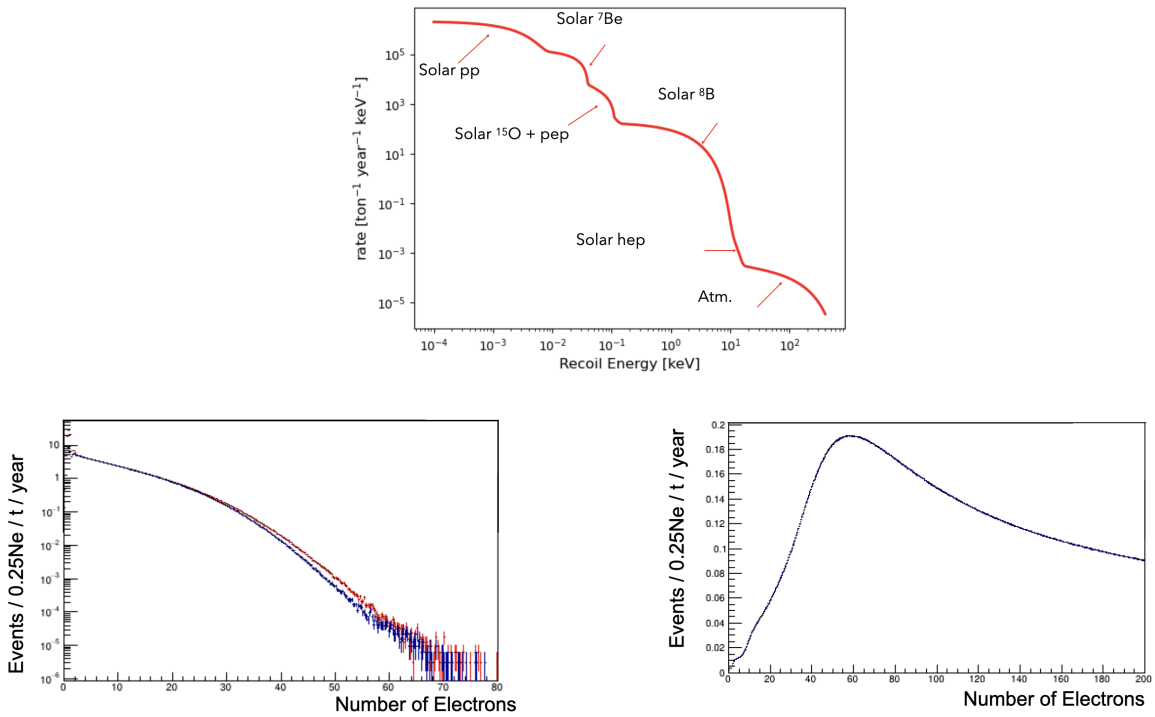

FIGURE 4.15. : CEνNS neutrino background energy distribution (top) and corresponding N_{e^-} spectra (bottom) : interaction with the nucleus via CEνNS (left) for both QF (red) and NQ (blue) quenching fluctuations and elastic scattering off argon electrons (right).

in Figure 4.15 top. Both interactions with the nucleus via CEνNS (Coherent Elastic Neutrino-Nuclear Scattering, NR) and with the electrons via elastic scattering ν-ES (ER) components are considered, and shown in Figure 4.15 bottom left and right, respectively. For CEνNS, both QF and NQ cases are considered for NR quenching fluctuations. At low N_{e^-} (for $N_{e^-} < 30$), the CEνNS contribution is dominating.

A normalisation systematic of 10% is considered for the neutrino flux, applied to both ER and NR contributions. A shape systematic is also attributed to the neutrino CEνNS and ν-ES spectra, from the NR and ER ionisation yield respectively.

4.2.3.5. Other contributions

Surface contamination from radon, resulting from the lowest ^{238}U segment (^{210}Pb-^{210}Bi-^{210}Po), might impact the analysis. Assuming the activity measured by DEAP-3600 on TPB and PMMA surfaces (260 μBq/m^2) [77], this translates to 4.3 mBq/kg for layers of 50-μm thickness (assuming a flat distribution in depth). This has to be compared with the 1.2 mBq/kg used for bulk simulations for the lower part of the ^{238}U decay chain (called ^{238}U low), already included in the gamma background estimate.

Using simulations, it has been estimated that a radon contamination equivalent to a ^{238}U

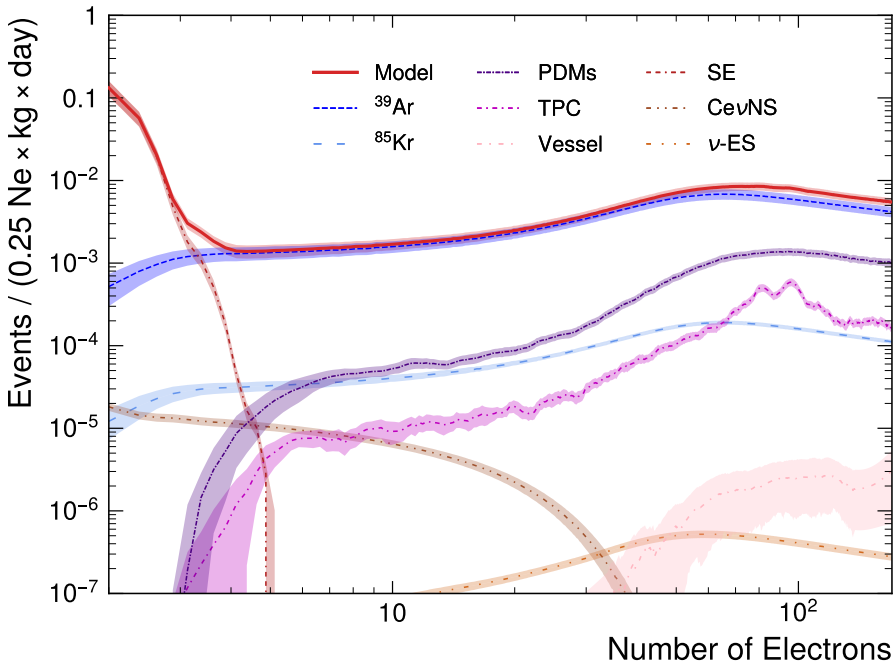

FIGURE 4.16. : Pre-fit N_{e^-} distribution for all backgrounds (dashed lines) and associated uncertainties (shaded areas, see Table 4.2 in Section 4.2.4) in the [2, 170] N_{e^-} range. The summed background model is shown in red.

low bulk one of 4.3 mBq/kg from the anode and cathode corresponds to 4.7% of the entire gamma-ray background rate from TPC components (which is sub-dominant with respect to the ^{39}Ar background) in the [2, 170] N_{e^-} range. It is therefore neglected in the following.

Finally, the NR background level, originating from radiogenic and cosmogenic neutrons, is expected to be negligible with respect to the ER background, hence not modelled in this analysis.

4.2.3.6. Summary

Figure 4.16 shows the pre-fit N_{e^-} distribution for all backgrounds and associated uncertainties (quantified in Table 4.2, see Section 4.2.4). At $N_{e^-} \leq 3$, the SE background dominates over other contributions and becomes negligible from $N_{e^-} = 4$, where it is already a factor 18 lower than the ^{39}Ar background. At $N_{e^-} \geq 4$, thanks to the reduction of the external background with respect to DS50, ^{39}Ar is largely dominating over the other background components. The external γ-ray background is dominated by the contribution of TPC PDMs. The contribution from the neutrino background is subdominant (two orders of magnitude lower than others), even at low N_{e^-}.

4.2.4. Background only fit

The fitting procedure [56] is based on a binned profile likelihood, described by Eq. (4.2) :

$$\mathcal{L} = \prod_{i \in bins} \mathcal{P}(n_i | m_i(\mu_s, \Theta)) \times \prod_{\theta_i \in \Theta} \mathcal{G}(\theta_i | \theta_i^0, \Delta\theta_i) \times \prod_{i \in bins} \mathcal{G}\left(m_i(\mu_s, \Theta) | m_i^0(\mu_s, \Theta), \delta m_i(\mu_s, \Theta)\right) \tag{4.2}$$

The first term is the Poisson probability of observing n_i events in the ith-bin given the expected ones $m_i(\mu_s, \Theta)$, μ_s being the signal strength and Θ the set of (15) nuisance parameters. The second term is a product of Gaussian penalty terms to account for the nuisance parameters (θ_i^0 and $\Delta\theta_i$ are the nominal central values and uncertainties, respectively), which can be correlated. The last term of Eq. (4.2) accounts for the statistical uncertainties in each bin of the simulated sample with respect to the nominal value.

The NPs are accounting for normalisation and shape uncertainties, as already mentioned in Section 4.2.3. The list of all NPs is detailed in Table 4.2. For the NPs related to the internal ^{39}Ar and ^{85}Kr backgrounds, a 15% initial uncertainty is used. A 10% initial uncertainty on the normalisation is used for the neutrino background[4], and for all external background components (Photo-Electronics, TPC structure and vessel), similarly to DS50. As a sanity test, it has been checked (doubling and halving this initial uncertainty of 10%) that this does not affect the results. Indeed, the SiPMs and TPC structure backgrounds normalisations are largely constrained by the pseudo-data fit (see later), while the vessel has a very small contribution. For the SE background, a 20% initial uncertainty on the normalisation is conservatively assumed, which has no impact on the results. Furthermore, multiplying the SE shape systematic uncertainty by a factor five does not affect the limit. In total 15 nuisance parameters are considered in the fit.

In the following, an Asimov fit is performed in the [2, 170] N_{e^-} range where pseudo-data are the sum of all backgrounds. Figure 4.17 top shows the post-fit background-only model. Compared to the pre-fit situation (Figure 4.16), the uncertainty is significantly reduced thanks to the large exposure, leading to large pseudo-data statistics. Figure 4.17 bottom left shows the post-fit values of the nuisance parameters. They are all centred on 0 – as expected from an Asimov fit. Big constraints are set on the NPs attached to the ER ionisation yield, to the normalisation and shape of the ^{39}Ar background, to the normalisation and shape of the SE background, and to the normalisation of the background from SiPMs and from TPC structure, as the high-statistics pseudo-data provide additional information with respect to the original assumptions. As expected, no constraint is set on the three smallest backgrounds (from ^{85}Kr, vessel and neutrinos) nor on the NR yield. Figure 4.17 bottom right shows the correlation between the NPs. The background being dominated by the contributions from ^{39}Ar, SE, SiPMs and TPC structure, the largest

[4]This is quite conservative for neutrinos, as for the fully dominant source of neutrinos from ^8B, the flux has been measured with a 4% uncertainty [101]. The same NP is used for the CEνNS and ν-ES contributions.

	Source uncertainty	Affected components
Amplitude	5% on the exposure	WIMP, ^{39}Ar, ^{85}Kr, SE, PDMs, Vessel, TPC, ν-ES, CEνNS
	15% on ^{39}Ar activity	^{39}Ar
	15% on ^{85}Kr activity	^{85}Kr
	20% on SE normalisation	SE
	10% on activity from PDMs	PDMs
	10% on activity from the vessel	Vessel
	10% on activity from the TPC	TPC
	10% on neutrinos normalisation	Neutrinos
Shape	spectral shape from atomic exch. + screening effects	^{39}Ar
	spectral shape from atomic exch. + screening effects	^{85}Kr
	1% on the ^{39}Ar-decay Q-value	^{39}Ar
	0.4% on the ^{85}Kr-decay Q-value	^{85}Kr
	SE spectral shape	SE
	spectral shape from ER ionization response unc.	^{39}Ar, ^{85}Kr, PDMs, Vessel, TPC, ν-ES
	spectral shape from NR ionization response unc.	WIMP, CEνNS

TABLE 4.2. : List of systematics included in the binned profile likelihood. Their sources and the impacted signal and background components they affect are listed. The exposure affects equally all spectra, but the ionisation response depends on the recoil type. WIMP-nucleon interaction is impacted by the NR ionisation response uncertainty.

correlation is observed between the four associated normalisation NPs, which are all largely anti-correlated with the exposure NP.

4.3. DarkSide-20k sensitivity to light dark matter particles

4.3.1. Signal models

4.3.1.1. Weakly Interacting Massive Particles

Assuming the Standard Halo Model (SHM, see Chapter 1 for more computational details), Figure 4.18 shows the energy spectra distributions (left) for a few of the considered WIMP masses and the N_{e^-} spectra (right) generated after considering the detector response model. The low WIMP masses populate mainly the very first bins of the N_{e^-} distribution.

Figure 4.19 shows the signal N_{e^-} distribution compared to the background model, for a 2 GeV/c^2 WIMP mass, a cross-section approximatively corresponding to the lowest cross-section excluded by DS20k at this mass ($\sigma_{SI} = 3.10^{-44}$cm^2, see later) and assuming binomial quenching fluctuations. The signal is non-zero below $N_{e^-} \approx 50$. Thanks to the high volume of DS20k, the signal could be simulated for lower WIMP masses than what was considered in DS50 : the research range can be extended down to $m_\chi = 0.8$ GeV/c^2.

The WIMP scattering on argon atoms can be accompanied by an additional ionisation component originating from the potential release of an electron in NR, this is called the Migdal effect. This theoretical prediction [102] is still pending experimental evidence, though recent results on xenon atom might indicate that it is overestimated [103]. This electron recoil component, in addition to the NR one, increases the probability of exceeding the detection threshold, thus opening a window of exploration for WIMPs with masses down to a few tens of MeV/c^2 [89]. Figure 4.20 shows in green dashed-double-dotted lines the signal N_{e^-} distribution compared to the total background model, for a 540 MeV/c^2 WIMP mass, a cross-section of 1.10^{-38}cm^2 and assuming binomial quenching fluctuations for the pure NR part.

4.3.1.2. Light dark matter particles interacting with electrons

Apart from the " classical" WIMPs, several other dark matter candidates exist and can be constrained by the future DS20k data (like DS50 did in 2023 [90]) when considering a S2-only analysis : light dark matter (LDM) fermion or scalar boson with masses below one GeV/c^2, pseudo-scalar ALPs, vector-boson dark photons and sterile neutrinos. These candidates will interact with shell electrons –being absorbed, elastically scattering or inelastically scattering– all resulting in the ionisation of argon atoms. The different candidates and their interaction are summarised in the following, where some parameters

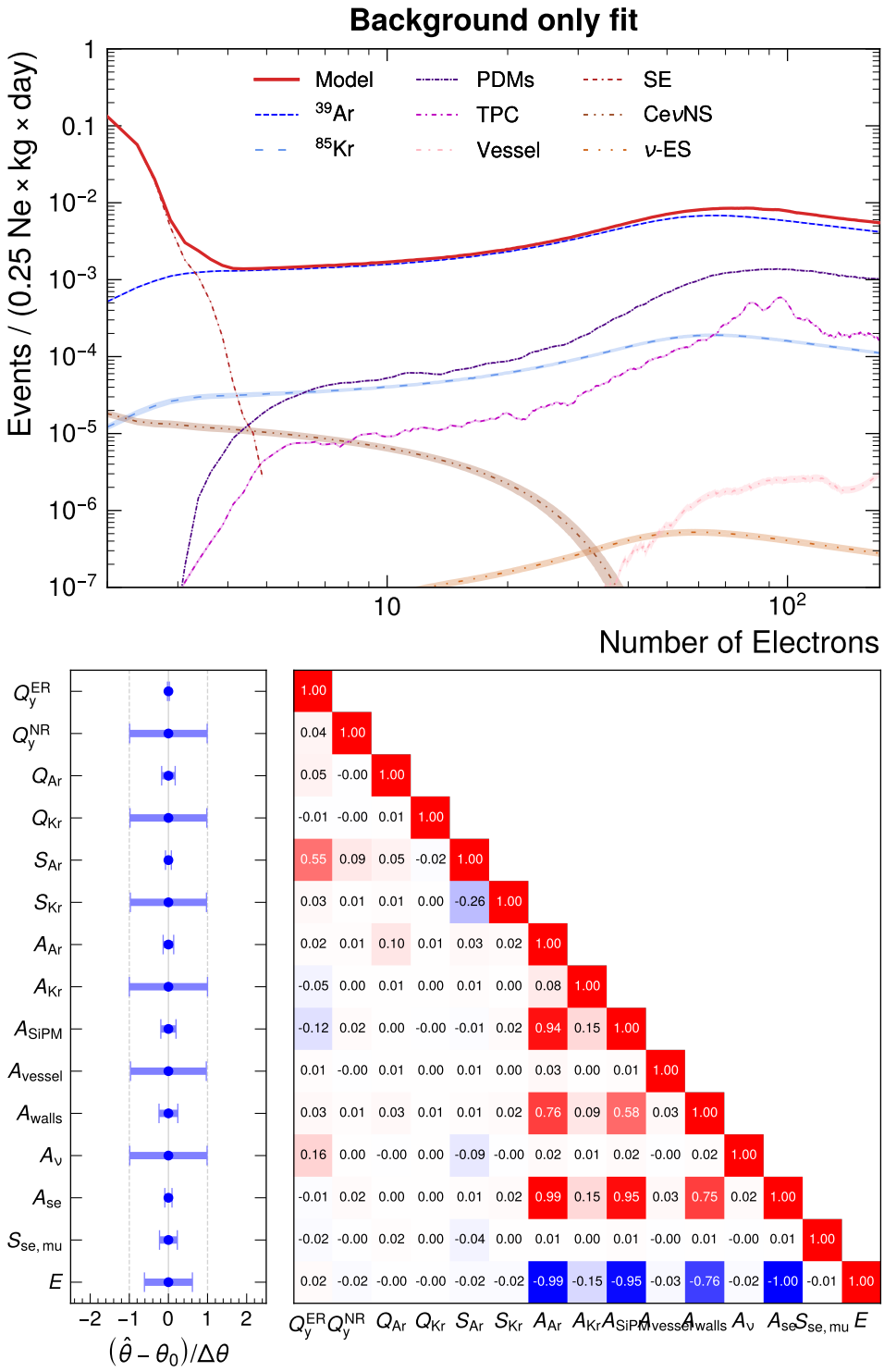

FIGURE 4.17. : Top : Post-fit background-only model and associated uncertainties (dashed lines and shaded areas) in the [2, 170] N_{e^-} range. The summed background model is shown in red. Bottom : post-fit nuisance parameters compared to the nominal values (left) and correlation matrix (right) from the background-only fit. Error bars are normalised to the prefit size of each of the nuisance parameter penalty terms.

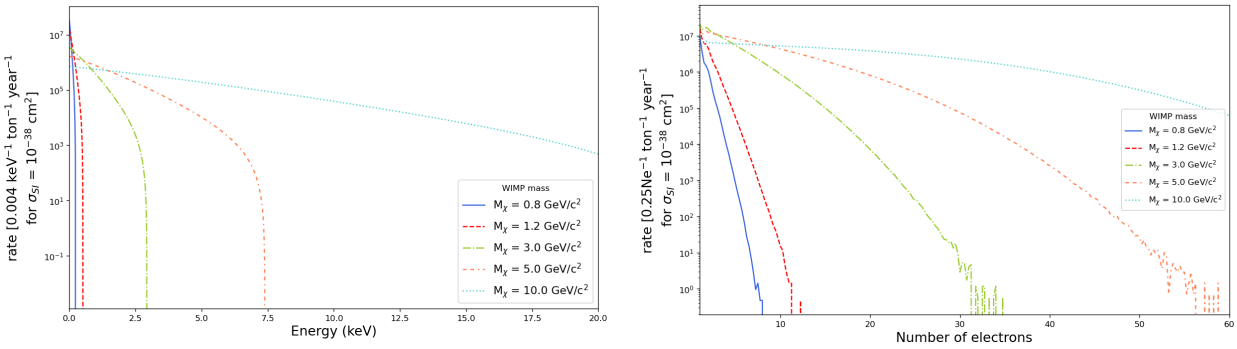

FIGURE 4.18. : WIMP NR signal energy distribution (left) and corresponding N_{e^-} spectra (right) for five WIMP masses ([0.8, 1.2, 3, 5, 10] GeV/c^2).

often occur such as the number of target atoms per unit mass N_T, the orbital shell parameters of electrons in atoms (n, l), the local mass density of dark matter ρ_{DM} and the reduced mass of a (A, B) system $\mu_{A,B}$:

- **Light Dark Matter (LDM) :** LDM are weakly interacting particles with low mass ($< 1\,\mathrm{GeV/c^2}$), hence interacting with shell electrons instead of the nucleus of atoms. The mediator of the weak-like interaction is a vector, it can be heavy or light, resulting in different signal rates. The difference in signal rates is encapsulated in a dark matter form factor, F_{DM}, that has a different mathematical expression for both cases.
  - If the vector mediator is heavy (its mass is larger than αm_e, with α the fine structure constant and m_e the mass of the electron), the dark matter form factor is a constant of the momentum transfer q : $F_{DM}(q) \sim 1$;
  - If the vector mediator is light (its mass is less than αm_e), the dark matter form factor depends on the momentum transfer q : $F_{DM}(q) \sim \left(\frac{\alpha m_e}{q^2}\right)^2$.

  In both cases, the signal rate can be computed as

$$\frac{dR}{d\ ln\ E_{er}} = N_T \frac{\rho_{DM}}{m_\chi} \times \frac{\bar{\sigma}_e}{8\mu_{\chi e}^2} \times \sum_{nl} \int |f_{ion}^{nl}(k', q)|^2 |F_{DM}(q)|^2 \eta(v_{min}) q dq, \qquad (4.3)$$

  where $|f_{ion}^{nl}(k', q)|$ is the ionisation form factor that models the effects of bound electrons in the (n, l) shell and outgoing final state and k' is the electron recoil momentum. This differential rate depends on the cross section of interaction between the LDM and shell electrons $(n,\ l)$, $\bar{\sigma}_e$, hence the sensitivity plots are shown in the (m_χ, $\bar{\sigma}_e$) phase space. Figure 4.20 shows the expected signal from a 100 MeV/c^2 LDM in the heavy ($\bar{\sigma}_e = 5.10^{-40}$ cm^2, yellow densely-dotted line) and light ($\bar{\sigma}_e = 5.10^{-36}$ cm^2, red dotted line) mediator scenarii. Likewise the WIMP signal, the spectra are confined at the low N_{e^-} range.

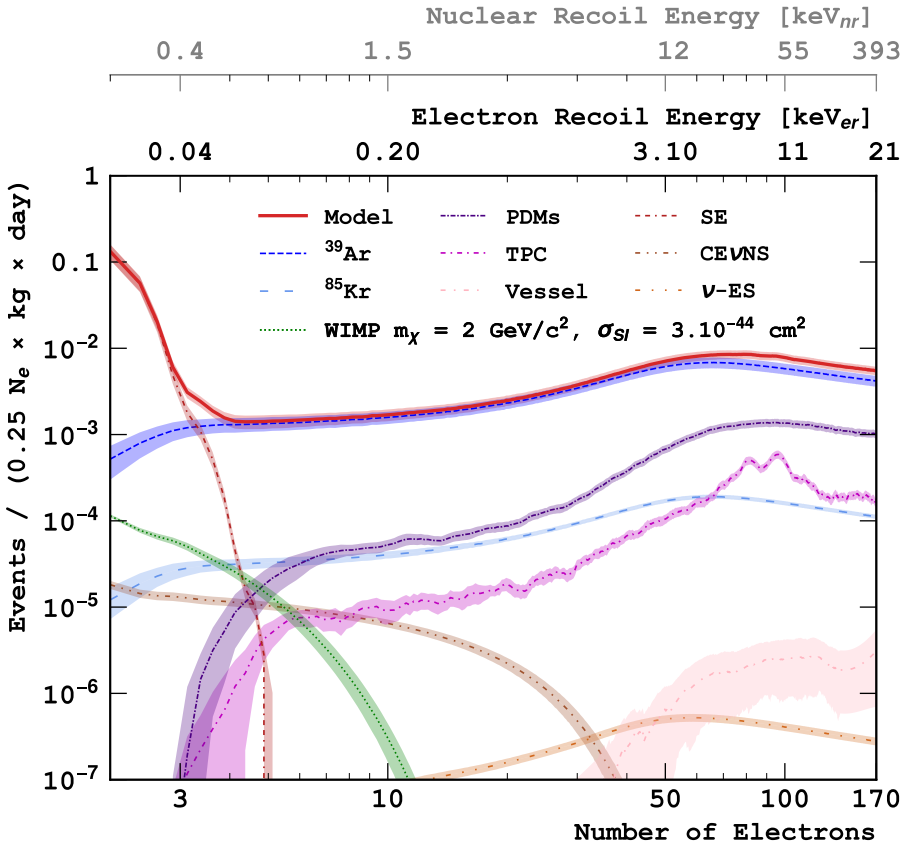

FIGURE 4.19. : Pre-fit N_{e^-} distribution for the signal and all backgrounds, and associated uncertainties (dashed lines and shaded areas) in the [2, 170] N_{e^-} range. The corresponding ER and NR energy scales are indicated at the top. A typical signal is super-imposed, corresponding to a WIMP mass of 2 GeV/c^2 with cross section of interaction $\sigma_{SI} = 3.10^{-44}$ cm^2, assuming binomial quenching fluctuations. The summed signal+background model is shown in red.

- **Axion-Like-Particles (ALPs) :** ALPs are pseudo-scalar dark matter candidates that could be absorbed by shell electrons of argon. Their differential rate on argon target per unit mass depends on their mass m_A and the square of ALP-electron coupling strength g_{Ae} :

$$R = N_T \frac{\rho_{DM}}{m_A} \times \frac{3 m_A^2 g_{Ae}^2}{16 \pi \alpha m_e^2} \sigma_{pe}(m_A c^2) c, \tag{4.4}$$

where $\sigma_{pe}(m_A c^2)c$ is the cross section of the photo-electric effect in argon, evaluated at the particle rest energy $m_A c^2$. Figure 4.20 shows an example of expected signal from galactic ALPs of mass $m_A = 0.3\,\mathrm{keV/c^2}$ and coupling strength $g_{Ae} = 5.10^{-13}$ in blue dashed line. One can see that the signal from ALP at a peculiar mass is monochromatic (as expected from the contribution of the photoelectric effect).

- **Dark Photon (DP) :** DP are vector-boson dark matter candidates. They can be absorbed by shell electrons of argon, similarly to ALPs. Their differential rate on argon target per unit mass depends on their mass $m_{A'}$ and κ^2, the square of the strength of the DP-photon kinetic mixing, like

$$R = N_T \frac{\rho_{DM}}{m_{A'}} \times \kappa^2 \sigma_{pe}(m_{A'} c^2) c, \tag{4.5}$$

where $\sigma_{pe}(m_{A'}c^2)$ is the cross section of the photo-electric effect in argon, evaluated at the particle rest energy $m_{A'}c^2$. Figure 4.20 shows, with a pink dashed-dotted line, an example of expected signal from DP of mass $m_A = 0.3\,\mathrm{keV/c^2}$ and coupling strength $g_{Ae} = 1.10^{-15}$. Similarly to ALPs, the signal from DP at a peculiar mass is monochromatic.

- **Sterile neutrino (ν_s) :** ν_s are a dark neutrino state interacting via gravitation and mixing with active states $\nu_{e,\mu,\tau}$. The differential ionisation rate is parametrised by σ_{nl}, the cross section between ν_s and an electron in a given orbital (n, l), as well as the ν_s mass m_ν and the mixing angle between electron neutrino active state and sterile state $|U_{e4}|^2$:

$$\frac{dR}{dE_{er}} = N_T \frac{\rho_{DM}}{m_\nu} \times \sum_{nl} 2(2l+1) \int \frac{d\sigma_{nl}}{dE_{er}} \left(v, m_\nu, |U_{e4}|^2\right) f(v)\ v\ dv \tag{4.6}$$

Figure 4.20 shows, with a grey double-dashed-double-dotted line, an example of expected signal from ν_s of mass $m_\nu = 10\,\mathrm{keV/c^2}$ and mixing angle $|U_{e4}|^2 = 5.10^{-3}$. The ν_s is localised in the low N_{e^-} range of the ionisation spectra.

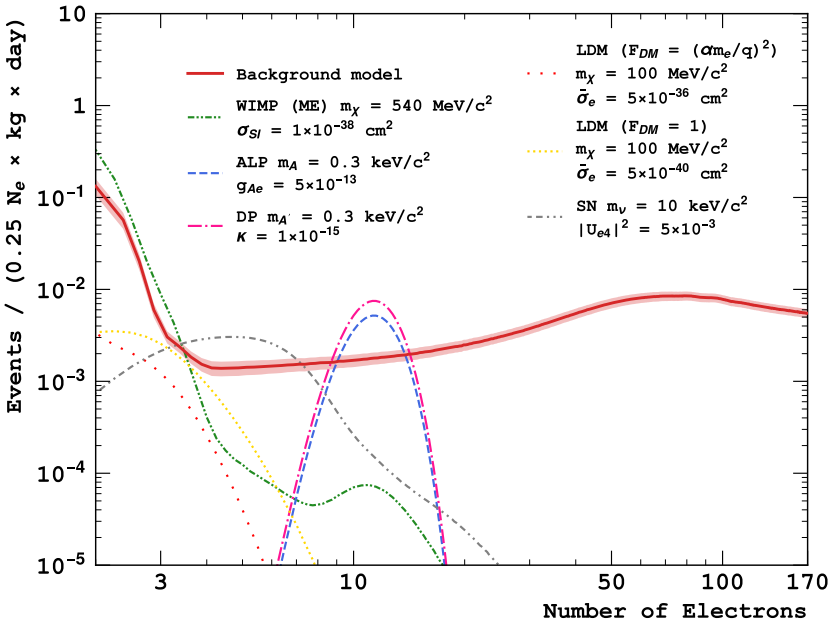

FIGURE 4.20. : DS20k N_{e^-} spectrum background model (red line) with its uncertainties (red shaded area) compared to expected ionization spectra of illustrative mass values for DM candidates : WIMP including the Migdal effect (ME) and with quenching fluctuations (QF) for the NR signal (dashed-dotted green line), light dark matter (LDM) for an heavy (dotted red line) and light (dotted yellow line) mediator, axion-like particle (ALP, dashed blue line), dark photon (DP, dashed-dotted pink line) and sterile neutrino (SN, dashed-dotted grey line).

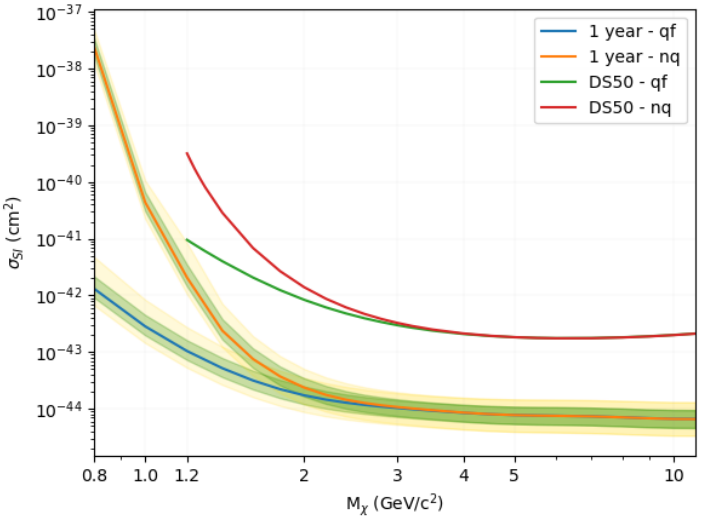

FIGURE 4.21. : DS20k 90% C.L. expected limits on spin independent WIMP-nucleon cross section with the 1-σ (green shaded area) and 2-σ (yellow shaded area) bands. Both non-quenching (NQ) and quenching (QF) fluctuations models are considered. The DS50 expected limits from [56] are also shown for comparison.

4.3.2. DarkSide-20k sensitivity to Weakly Interacting Massive Particles

Figure 4.21 shows the 90% C.L. expected limits on spin independent WIMP-nucleon cross section computed with the CLs technique in the range above 0.8 GeV/c^2 with the 1-σ and 2-σ bands. An improvement of sensitivity by a factor 30 to 100 (a factor 100 at low mass (1.2 GeV/c^2) and 35 at high mass (10 GeV/c^2)) with respect to DS50 (expected sensitivity) is obtained in the QF scenario. In the NQ scenario, the gain is similar at high WIMP mass and more significant at the lowest WIMP masses (up to factor 180 at 1.2 GeV/c^2).

Overall, DS20k will be sensitive to σ_{SI} values below 10^{-42} cm^2 for WIMP masses above 0.8 GeV/c^2, within one year of exposure time.

The impact of the systematic uncertainties is assessed by removing gradually NPs by group in the fit. This is shown in Figure 4.22, by choosing to remove the systematics in the following order : first on ER yield (orange line), then on ^{39}Ar background (green line), then on SE background (red line) and finally all the rest (purple line). As expected, the main impact comes from the uncertainties on the detector response (ER ionisation yield) and on the main background (^{39}Ar). The measured degradation impact of the systematics on the limit is of 60% compared to a limit only considering statistical uncertainties (purple line of Figure 4.22).

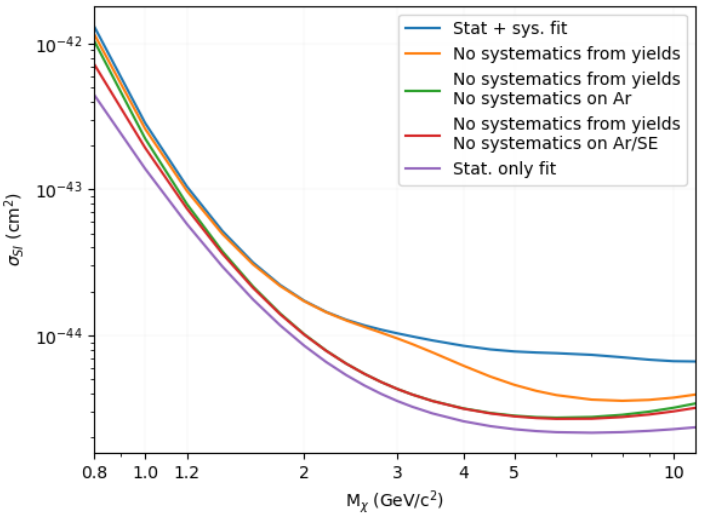

FIGURE 4.22. : Impact of the systematic uncertainties on the DS20k 90% C.L. expected limits on spin independent WIMP-nucleon cross sections. From top to bottom curves : gradual removal of systematics by group (ER yield, ^{39}Ar background, SE background, rest), as explained in the text. The QF scenario for signal fluctuation is assumed.

A comparison with the DS50 fitting strategy (fit in the [4, 170] N_{e^-} range, where the SE background can be neglected) is shown in Figure 4.23. With both strategies, the NPs attached to the main background components (^{39}Ar, SE, photo-electronics and TPC structure) are well constrained by the fit (like shown in Section 4.2.4 for the [2, 170] N_{e^-} fit range). The fit starting from $N_{e^-} = 4$ reduces the sensitivity at low mass as the signal decreases with N_{e^-}, but the limit is more robust against the SE modelling. Indeed, including or not the SE background in the fit changes the sensitivity at most by 20% for the lowest WIMP masses, as seen in the Figure (orange and green curves). Using such fit strategy, an improvement of sensitivity by a factor 27 at low mass (1.2 GeV/c^2) to 35 at high mass (10 GeV/c^2) with respect to DS50 is obtained in the QF scenario. This roughly scales like the square root of the exposure ratio between DS20k and DS50 ($\sim$ 25), which is the statistical expectation, as discussed later.

Comparison of the DS20k sensitivity to WIMPs (with both fitting strategies) with existing experiments is proposed in Figure 4.24 top (resp. bottom) in the mass range between 0.8/c^2 and 10 GeV/c^2 and assuming binomial quenching fluctuations in NR (resp. no fluctuations).

Above a WIMP mass of 5 GeV/c^2, Xenon dual-phase TPC experiments are already providing the best limits based on analyses using either S2 only signals [104, 57] or S1+S2 optimised for ^8B solar neutrinos searches [105, 106]. No prospective studies seem

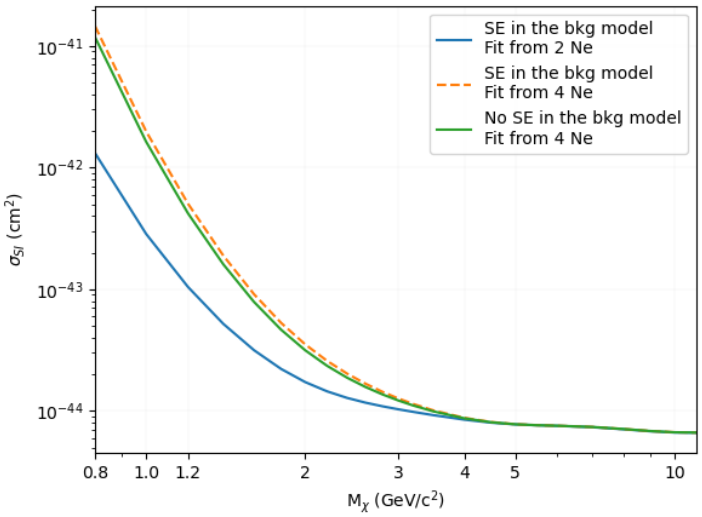

FIGURE 4.23. : DS20k 90% C.L. expected limits on spin independent WIMP-nucleon cross section for a lower bound of the N_{e^-} cut set to 2 (blue) and 4 (orange). In the latter case, the SE background is negligible and plays a minor role (green). The QF scenario for signal fluctuation is assumed.

available for such low mass searches, but prospects for high mass WIMP searches with Xenon detectors [83, 84] foresee to marginally improve these limits below 5 GeV/c^2.

The expected DS20k sensitivity is significantly improving over the existing limits in the mass range below 4 GeV/c^2. As shown in Appendix B, other technologies will also be competitive in this low-mass region in the coming years provided the current working prototypes can be scaled-up to an exposure above 10 kg×yr. The most promising efforts are using :

- Cryogenic bolometer using Germanium (Ge) sensors. The most sensitive in the 1-5 GeV/c^2 mass range is Super-CDMS based on cryogenic thermal phonon technology using HV sensors [58], presently under construction at SNOLAB and that should start taking data in Autumn 2023. Eight Ge HV detectors are foreseen for a total exposure of 36 kg×yr. The CDEX collaboration, based on p-type point contact (PPC) Ge detectors, has obtained first results with 1 and 10 kg detectors. The next generation project aims for a 50 kg detector CDEX-50 [107].

- Skipper CCDs. Present results are obtained with few CCDs for a total mass of O(0.01) kg, see e.g. the latest DAMIC results [108]. The most ambitious plan is to run with O(1) kg mass using 50 CCDs with the DAMIC-1K detector [60].

- Spherical gas proportional counter : First results have been obtained with 10 kg×day exposure with the NEWS-G detector in 2017 [109]. Future fully electroformed

detectors are under preparation and could extend the exposure to 20 kg×yr [61].

In the GADMC collaboration, a detector specifically designed for the search of light dark matter has been designed (however not yet under construction phase). It is called DarkSide-LowMass (DS-LM) [118]. DS-LM assumes a 10 times reduced internal ^{39}Ar activity thanks to Aria. In one year of exposure, it has a slightly better sensitivity than the one of DS20k with the same fitting strategy ($N_{e^-} \geq 4$), as seen in Appendix B.

Sensitivity plots shown in the present chapter are computed for one year of data collection, however DS20k should take data for a decade. Hence the evolution of the DS20k 90% C.L. limits on σ_{SI} with respect to the exposure time has been studied. Figure 4.25 shows the sensitivity increase at two WIMP masses (1.2 GeV/c^2 and 10 GeV/c^2) for science data collection times from 0.1 year to 10 years, fitting the background model in the range [2, 170] N_{e^-} and assuming the QF scenario for NR. As expected thanks to the high statistics that will constrain the main NPs, the sensitivity improves with the square root of the running time. Consequently, after 10 years of data taking, one expects a factor ≈ 3 improvement (on the whole mass range) compared to the limits shown up to now. The 90% C.L. expected exclusion limit of DS20k after 10 years is shown in Figure 4.26, in the QF scenario and using the ultimate fit scenario. One can see that around ≈ 5 GeV/c^2, DS20k is expected to reach the neutrino fog.

Note that DS20k should reach (and slightly improve) the sensitivity of DS50 after only one day of data collection.

When including the Migdal effect in the signal model, an improvement by a factor 30 compared to DS50 is seen on the upper limit cross section, independent on the WIMP mass considered. DS20k is expected to improve current limits above 40 MeV/c^2, after only one year of science data collection as shown in Figure 4.27 left and right, assuming QF and NQ quenching fluctuations respectively.

4.3.3. Sensitivity to other light dark matter particles

The same analysis as in Section 4.3.2 has been performed for the five already mentioned signal models interacting with electrons : LDM (for a heavy and a light mediator), ALP, dark photon and sterile neutrino.

In the conservative fit scenario (i.e. the same as used for DS50), the sensitivity improvements compared to DS50 can be summarised as :

- LDM : an improvement by a factor 15 at low mass (15 MeV/c^2) to 30 at high mass (1 GeV/c^2) on the cross section, independent of the assumption made on the form factor ($F_{DM} \sim 1$ or $F_{DM} \sim \left(\frac{\alpha m_e}{q}\right)^2$). This is similar to the WIMP NR case ;
- ALP : an improvement by a factor 4 at low mass (0.025 keV/c^2) to 13 at high mass (20 keV/c^2) on g_{Ae}. The improvement at low mass is lower than the WIMP NR case, as the event rate scales with g_{Ae}^2 ;

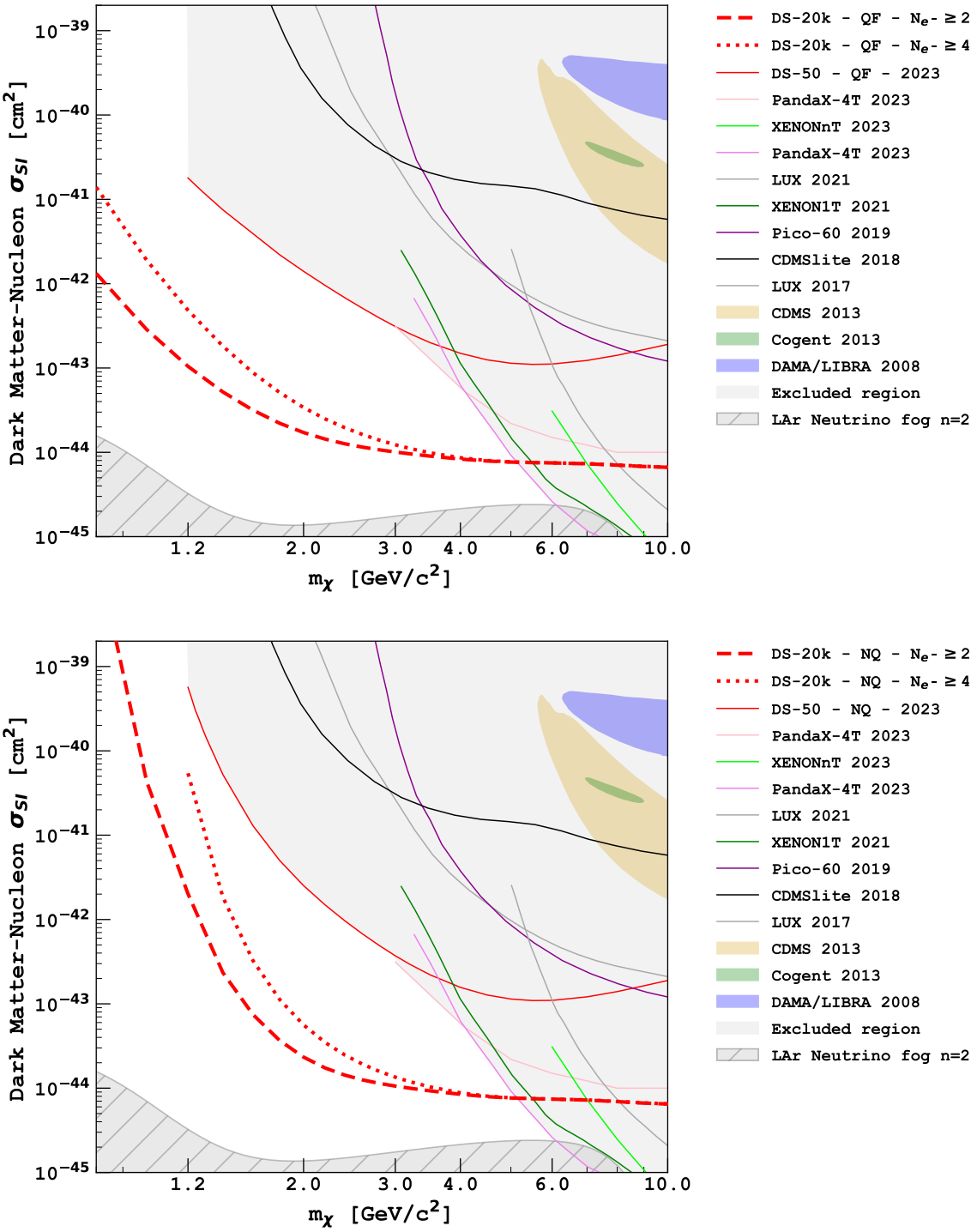

FIGURE 4.24. : Expected DS20k 90% C.L. exclusion limits for spin-independent WIMP NR with quenching fluctuations (QF) are shown as bold red lines (dotted : fit from $N_{e^-} = 4$, dashed : fit from $N_{e^-} = 2$). One year of data is assumed. They are compared to the published 90% C.L. limits from DS50 [56] and from other experiments [75, 106, 104, 105, 110, 111, 112, 113], with currently excluded parameter space shaded in light grey, as well as claimed discovery from Refs [114, 115, 116]. The neutrino fog for LAr experiments with index $n = 2$ [117] is also shown.

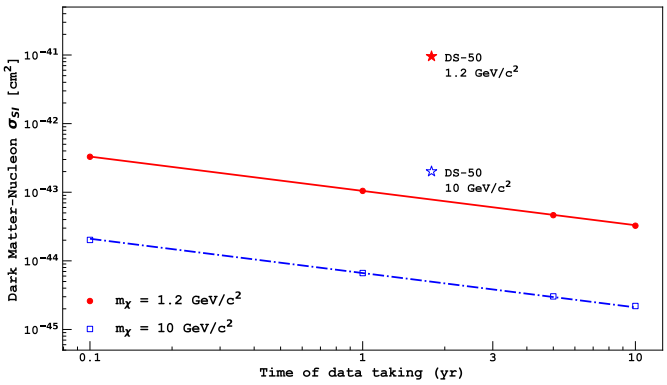

FIGURE 4.25. : DS20k 90% C.L. expected limits on spin independent WIMP-nucleon cross section for two WIMP masses (1.2 GeV/c^2 (red full lines) and 10 GeV/c^2 (blue dashed-dotted lines)) for a lower bound of the N_{e^-} cut set to 2. The QF scenario for NR quenching fluctuation is assumed. The lines are $1/\sqrt{\text{time}}$ functions passing through the 1 year points. The DS50 results are indicated with stars for these two WIMP masses.

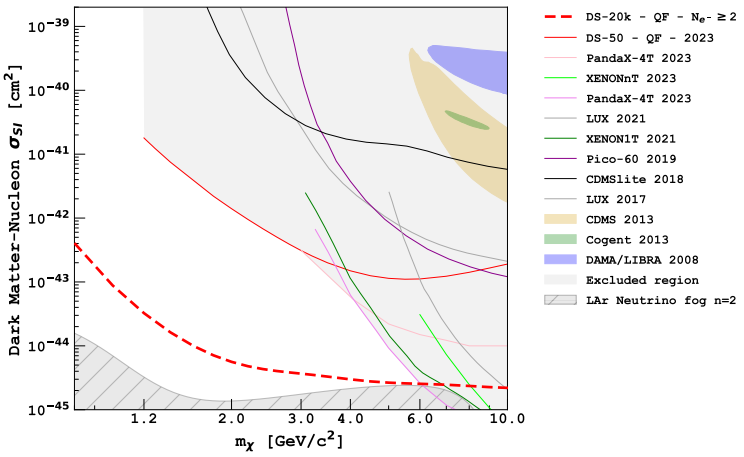

FIGURE 4.26. : Expected DS20k 90% C.L. exclusion limits for spin-independent WIMP NR with quenching fluctuations (QF) are shown as bold dashed red line (fit from $N_{e^-} = 2$). Ten years of data are assumed. They are compared to the published 90% C.L. limits from DS50 [56] and from other experiments [75, 106, 104, 105, 110, 111, 112, 113], with currently excluded parameter space shaded in light grey, as well as claimed discovery from Refs [114, 115, 116]. The neutrino fog for LAr experiments with index $n = 2$ [117] is also shown.

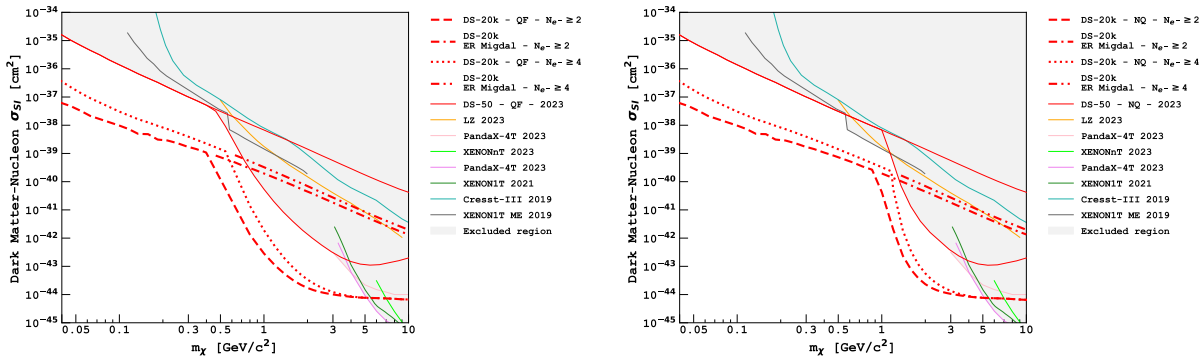

FIGURE 4.27. : Expected DS20k upper limits at 90% C.L. for spin-independent WIMP–nucleon cross-section when considering the Migdal effect and binomial quenching fluctuations (QF, left) or without quenching fluctuations (NQ, right) for the NR signal (bold red lines, dotted : fit from $N_{e^-} = 4$, dashed : fit from $N_{e^-} = 2$). One year of data is assumed. These results are compared to the published 90% C.L. limits from DS50 [89] and other experiments [75, 106, 104, 119, 105, 32, 120], with currently excluded parameter space shaded in light grey.

- Dark Photon : an improvement by a factor 4 at low mass (0.025 keV/c^2) to 13 at high mass (20 keV/c^2) on κ. The improvement at low mass is lower than the WIMP NR case, as the event rate scales with κ^2 ;
- Sterile Neutrino : an improvement by a factor 30 at low mass (7 keV/c^2) to 70 at high mass (35 keV/c^2) on $|U_{e4}|^2$. This would improve further on the existing direct limits set by a high-precision measurement of the ^{63}Ni β spectrum [121].

These improvements over DS50 limits are significant for all considered signal models. The improvement in the cross section limits at the lowest masses roughly scales like the square root of the exposure ratio between DS20k and DS50 ($\sim$25), as discussed in Section 4.3.2. It is interesting to note that DS50 already has the world best limits in some part of the mass spectra.

Comparison of the DS20k sensitivity (for both fitting strategies discussed in Section 4.3.2, i.e. fit starting from $N_{e^-} = 2$ or from $N_{e^-} = 4$, which reduces the sensitivity at low mass but is more robust against the SE modelling) with published limits from previous experiments is proposed in Figure 4.28. DS20k is expected to explore more than order of magnitude uncharted phase space in one year, for LDM, ALP and DP dark matter candidates. Like DS50, DS20k can set best direct limits on the mixing angle $|U_{e4}|^2$, however this phase space is already discarded by indirect dark matter search from the NuSTAR experiment [94], which looks for anomalous X-ray lines from radiative sterile neutrino DM decays.

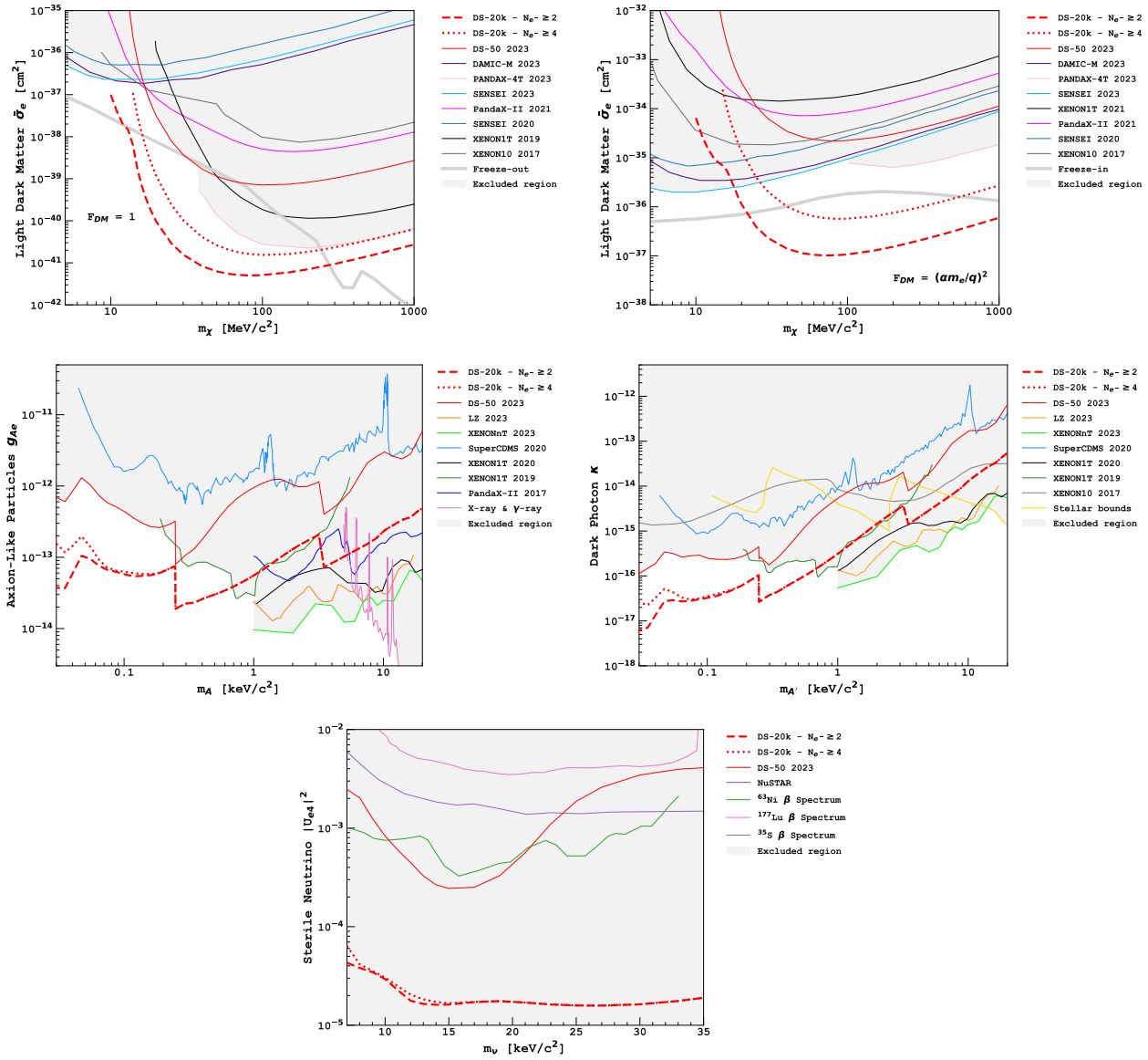

FIGURE 4.28. : Expected DS20k upper limits at 90% C.L. for various signal models (bold red lines, dotted : fit from $N_{e^-} = 4$, dashed : fit from $N_{e^-} = 2$). One year of data is assumed. These results are compared to the published 90% C.L. limits from DS50 [90] and other experiments [104, 122, 123, 124, 57, 125, 120, 126, 127, 121, 128, 129, 130, 131, 132, 133, 134] and astrophysical constraints [135, 136, 137, 94], with currently excluded parameter space shaded in light grey. Top left and right : light dark matter cross-section for an heavy and light mediator, respectively. Thick lines show cross-sections giving the relic DM abundance through freeze-in or freeze-out production mechanisms [138]. Center left : ALPs. Center right : dark photon. Bottom : sterile neutrino.

4.4. Impact of experimental assumptions on DarkSide-20k sensitivity

In this section[5], the impact of nominal assumptions used to compute the 90% C.L. cross-section limits (Section 4.3) is studied (assuming the QF scenario for NR quenching fluctuations). Several variations from the nominal assumptions are considered :

- Reduction of ^{39}Ar activity : though it is reasonable to assume the same ^{39}Ar activity as in DS50 (0.73 mBq/kg), it is also possible that the ^{39}Ar in DS20k is further reduced thanks to Urania and Aria. Two hypotheses are considered : 50% and 90% reduction. In the former case, ^{39}Ar is still dominating the background for all N_{e^-}, whereas in the later ^{39}Ar is above SiPMs background only for $N_{e^-} < 8$. Moreover, the live time increases from 56% to 64% and 71%, respectively. As a result, the sensitivity improves by a factor 1.5 at the lowest WIMP masses to 1.8 around 7 GeV/c^2 (resp. 3.4 to 4.6) for 50% (resp. 90%) ^{39}Ar activity reduction, as seen in Figure 4.29 top left.

- Increase of ^{85}Kr activity to DS50 level : though it is reasonable to assume that ^{85}Kr will be negligible in DS20k after the cryogenic distillation in Urania, a worst case scenario could be that DS20k measures the same activity of ^{85}Kr as in DS50 (1.9 mBq/kg). In this case the live time would drop from 56% to 28% and ^{85}Kr would be the dominant background. The sensitivity would degrade by a factor ∼2.7 (resp. ∼3.9) for a WIMP mass of 1.2 (resp. 8) GeV/c^2, as shown in Figure 4.29 top right.

- Electron lifetime : in case the electron lifetime would be twice worse than the nominal value of 15.8 ms, a larger part of the drifting electrons would be absorbed before reaching the gas pocket (from 11% in average in the nominal scenario to 20%). As shown in Figure 4.29 bottom left, the sensitivity would degrade for the lowest masses (by at most a factor 2 at 0.8 GeV/c^2), and would not change by more than 8% above 3 GeV/c^2.

- Single electron charge resolution : the nominal single electron charge resolution of 23% comes from a study of noise and reconstruction effects. Considering the SE background for this peculiar check, a scenario considering a pessimistic increase to 50% single electron charge resolution have been considered. It impacts the sensitivity at the lowest masses, as the SE background populates more N_{e^-} bins with a worse single electron resolution. In the conservative fit scenario (fitting from $N_{e^-} = 4$), the impact is at most 30-40% in the [0.8, 2] GeV/c^2 mass range and decreases to < 10% for $m_\chi \geq 3$ GeV/c^2. In the ultimate scenario (fitting from $N_{e^-} = 2$), the impact is a factor 2 at 1 GeV/c^2, 1.6 at 2 GeV/c^2 and decreases to ≤ 15% for $m_\chi \geq 3$ GeV/c^2.

[5]For historical reasons, this section uses an older background model (external background from an old version of g4ds and without SE) giving 56% of live time, and a fit from $N_{e^-} = 4$.

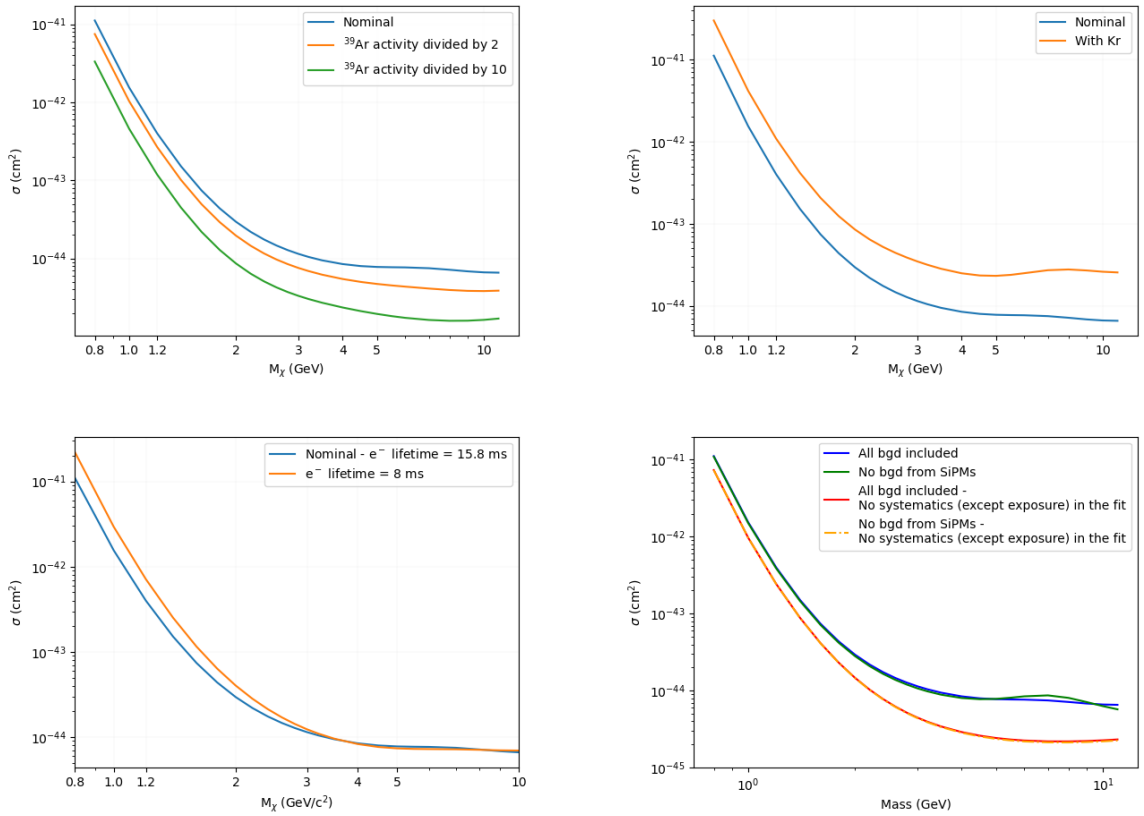

FIGURE 4.29. : Evolution of the DS20k 90% C.L. expected limits on spin independent WIMP-nucleon cross sections under different hypotheses : reduction of ^{39}Ar background (top left), presence of ^{85}Kr (top right), decrease of electron lifetime (bottom left), removal of SiPMs background (bottom right) See text for more details.

- *xy* resolution : the position resolution is not known precisely and a value of 3 cm is assumed. Scenarii considering 2 cm and 5 cm have also been considered. Even in the worst case scenario, the impact on sensitivity is less than 3%.
- FV definition : external background events are removed if they deposit their energy less than ∼30 cm away from the vertical walls of the TPC. It is possible to reduce this value to 20 or 10 cm to gain on signal acceptance (from 69% to 78% and 89% respectively) at the price of increasing the external background coming from the TPC walls per unit of mass by 10% and 50% respectively. The dominant SiPMs background is only marginally increased, by $< 2\%$ per unit of mass, as it comes from the top and bottom of the TPC. The gain on the sensitivity is at maximum 10% in both cases.

Table 4.3 presents a summary of the variation of all the input parameters and their impact on the cross-section limit for two different WIMP masses (1.2 GeV/c^2 and

Value	Hypothesis							
	^{39}Ar		^{85}Kr	El. life	El. reso.	$x-y$ reso.	FV	Exposure
Nominal	DS50		DS50/100	15.8 ms	23%	1 cm	30 cm	1 yr
Change	×0.5	×0.1	DS50	8 ms	50%	5 cm	10 cm	3 yr
m_χ (GeV/c^2)	$\sigma_{\text{Change}}/\sigma_{\text{Nominal}}$							
1.2	0.67	0.30	2.7	1.8	0.66	1.0	0.9	0.6
6	0.57	0.23	3.3	0.94	1	0.98	0.9	0.6

TABLE 4.3. : Impact of assumptions for ^{39}Ar and ^{85}Kr activity, electron lifetime, single electron resolution, xy resolution, fiducial volume and exposure on the DS20k 90% C.L. cross-section limit at two reference masses (1.2 GeV/c^2 and 6 GeV/c^2). The QF scenario for signal fluctuation is assumed. A value lower (greater) than one means that sensitivity improves (degrades) with respect to nominal sensitivity of Figure 4.21.

6 GeV/c^2). The highest degradation of the DS20k sensitivity is at most of a factor of 3.3 in case ^{85}Kr is present in the TPC bulk, as it would become the main background component. On the other hand, the highest gain is of a factor of 4.3 in case ^{39}Ar activity is reduced by a factor of 10, as it is currently the main background component above four electrons. This assesses the robustness of the conclusion that DS20k can significantly improve over DS50 sensitivity for WIMP NR signal.

In principle, the external background could be further reduced, e.g. by considering other discriminating variables (like position x, y and possibly time distribution (hence z) of the S2 pulse) and/or by using the neutron veto detector information. However, under the nominal assumptions, the background in the analysis is largely dominated by the internal ^{39}Ar, which is uniformly distributed in the TPC. As a consequence, the possible gain in sensitivity with an improved analysis (multi-variate analysis using position variables and/or cutting on veto variables) is marginal, as shown in Figure 4.29 bottom right. For this plot, an extreme scenario removing completely the SiPMs background has been considered as it is the one that would be removed by a three dimensional fiducialisation. The maximum gain over the whole mass range is 6%. Around 7 GeV/c^2, the sensitivity is even lowered, which is attributed to the fact that correlations between the NPs are changed, as without SiPMs background ^{39}Ar is almost the unique background source. This has been checked (i) removing the SiPMs background normalisation NP in the fit, and (ii) removing all systematics. In the latter case, the sensitivity without SiPMs background is better over the whole mass range, by at most 3%, as shown in the plot (orange and red lines). The analysis has been redone reducing the ^{39}Ar activity by 50% (resp. 90%) : in this case, the maximal gain in sensitivity when the SiPMs background is removed is 9% (resp. 18%).

Hence, thanks to all these checks, one can claim that the sensitivity of DS20k is robust against the detector model assumptions and that a refined analysis method should not improve much the result.

4.5. Conclusion

The DarkSide-20k experiment will be key in the direct search for WIMPs below $10\,\mathrm{GeV/c^2}$ and other light dark matter candidates. The present chapter demonstrated that DS20k should quickly (in one year) and significantly improve (more than one order of magnitude improvement for a variety of dark matter candidates) the current direct search for low mass dark matter. In particular, after one exposure year, DS20k will be sensitive to WIMP-nucleon spin-independent cross sections of interaction below 1.10^{-42} $\mathrm{cm^2}$ for WIMP masses above 800 $\mathrm{MeV/c^2}$ and down to 7.10^{-45} $\mathrm{cm^2}$ at $10\,\mathrm{GeV/c^2}$. With the full 10 years exposure, the sensitivity of DS20k will reach the neutrino fog around $5\,\mathrm{GeV/c^2}$. The present chapter also proved the stability of the sensitivity of DS20k against a variety of experimental assumptions.

Of course, the sensitivity of an experiment also depends on the signal model. In direct detection, the dark matter halo is commonly modelled by the Standard Halo Model (see Chapter 1), a convenient model because of its simplicity (e.g. the velocity distribution after the change of frames has an analytical expression). The next chapter assesses the theoretical uncertainties of the sensitivity of DS20k, in both low mass WIMP and high mass WIMP regimes, that are originating from the dark matter halo modelling.

5. Impact of the dark matter halo model on the sensitivity of DarkSide-20k

Summary

The present chapter assesses the systematic uncertainties of the sensitivity of DarkSide-20k coming from the modelling of the Milky Way dark matter halo. Indeed, all sensitivity plots (e.g. Figure 1.12, Figure 2.6 or Figure 4.24) are considering a dark matter halo model, called the Standard Halo Model (SHM), which is simplistic and whose astrophysical parameters are not consistently set. The first goal of the present chapter is to justify that one needs to consider better motivated dark matter halo models than the SHM (Section 5.1). Then, Section 5.2 proposes to investigate the individual effect of each of the four astrophysical parameters (ρ_0, v_c, v_0 and v_{esc}) on the sensitivity of DS20k. In addition, halo models beyond the simple isothermal isotropic spherically symmetric case are studied in Section 5.3 and their impact on the DS20k sensitivity is shown.

In this study, the exclusion limits of DarkSide-20k are taken as figure of merit for the sensitivity even if discovery potential limits could have also been taken. Both high mass (see Chapter 2) and low mass (see Chapter 4) sensitivities are considered. At high mass ([15 GeV/c^2, 10 TeV/c^2]), the sensitivity is computed for the full exposure of DS20k, i.e. 200 ton $\times$ years, whereas at low mass ([0.8 GeV/c^2, 11 GeV/c^2]), the sensitivity is computed for one year of data taking (similarly to Chapter 4). At low mass, the fit of the background model is chosen to be in the range [4, 170] N_{e^-} (see Chapter 4 for more details). In order to ease the reading, the sensitivity in the High Mass regime will be called HM, while the sensitivity in the Low Mass regime will be called LM.

5.1. Motivations for going beyond the Standard Halo Model

The Standard Halo Model is a simple and handy model chosen by dark matter experiments to compare one another, thus to assess the competitiveness of each detector in different mass regions of the WIMP search. Yet, it is important to use a well-suited model to reject parameters space regions at best –which is the first aim of these exclusion limits.

First, having a Maxwellian speed distribution for the galactic dark matter halo is the consequence of an over-simplistic halo model. Indeed, as introduced in Chapter 1, the SHM was built assuming a maximally symmetric system : a spherical and isotropic halo. Thus, the energy $\mathcal{E}$ of the system is the only relevant degree of freedom. An example of distribution depending only on the energy is the well-known Maxwell-Boltzmann distribution (see also Eq. (1.6)) which also describes an isothermal system :

$$f_{MB}(\mathcal{E}) = \frac{1}{K} e^{-\mathcal{E}/k_B T}, \tag{5.1}$$

k_B being the Boltzmann constant, T the temperature of the gas halo and K the normalisation constant. The energy of each particle is $\mathcal{E}(\vec{r}, \vec{v}) = m\Phi(\vec{r}) + \frac{1}{2}\, m\, \vec{v}^2$, with m the mass of the dark matter particle, $\vec{v}$ its velocity and $\Phi(\vec{r}) = \Phi(r)$ the gravitational potential of the halo at position $\vec{r}$, so :

$$f_{MB}(\mathcal{E}) = \frac{1}{K} e^{-\frac{m\overrightarrow{v}^2}{2k_BT}} e^{-\frac{m\Phi(r)}{k_BT}} \tag{5.2}$$

As the Maxwell-Boltzmann describes an isothermal system, the term k_BT/m can be seen as the square of a velocity dispersion σ_{MB} : one obtains the gaussian distribution of velocity $f_{gal}^{\text{No cut}}(\overrightarrow{v})$ (Eq. (5.3), with new normalisation constant K_r) :

$$f_{gal}^{\text{No cut}}(\overrightarrow{v}) = \frac{1}{K_r} e^{-\frac{\overrightarrow{v}^2}{2\sigma_{MB}^2}} \tag{5.3}$$

$f_{gal}^{\text{No cut}}(\overrightarrow{v})$ is normalised to 1. One may also want to take into account the mass distribution of the halo, needed for dynamics-based estimates for example, generically called here $f(\overrightarrow{r}, \overrightarrow{v})$. The normalisation condition of this probability distribution function gives :

$$\int d^3\overrightarrow{v} \int d^3\overrightarrow{r}\, f(\overrightarrow{r}, \overrightarrow{v}) = M_{tot}^{DM}, \tag{5.4}$$

or

$$\int d^3\overrightarrow{v}\, f(\overrightarrow{r}, \overrightarrow{v}) = \rho(r), \tag{5.5}$$

where M_{tot}^{DM} is the total mass of the dark matter halo and $\rho(r)$ is the dark matter mass density distribution, which depends on the radial distance to the center of the galaxy. One can simultaneously integrate $f(\overrightarrow{r}, \overrightarrow{v})$ and the Poisson equation to obtain -with G the universal gravitational constant :

$$\rho(r) \propto \frac{\sigma_{MB}^2}{Gr^2}. \tag{5.6}$$

Furthermore, it is possible to obtain this result with another simple description of the halo, often used to obtain the $1/r^2$ dependency of $\rho(r)$. In order to reproduce the measurements of the circular velocity of stars in galaxies performed in the last century, the mass distribution is tuned so that the circular velocity v_c becomes constant at some point. That gives the following computation, with a the acceleration of stars sensitive to the spherically symmetric gravitational potential, v_c the circular velocity of the stars and $M(r)$ the mass of the galaxy enclosed inside radius r :

$$a(r) = \frac{v_c^2}{r} = \frac{M(r)G}{r^2}, \tag{5.7}$$

which gives :

$$v_c = \sqrt{\frac{M(r)G}{r}} \sim \text{cst} \tag{5.8}$$

Thus one expects $M(r) \sim$ r and consequently :

$$M(r) \xrightarrow[r\to\infty]{} \infty \tag{5.9}$$

Another consequence of this model is the divergence of the mass density at radii going to 0. Indeed :

$$M(r) = \int_0^r \rho(r) d^3\overrightarrow{r} \tag{5.10}$$

$$M(r) = \int_0^r \rho(r) 4\pi r^2 dr \sim r, \tag{5.11}$$

thus $\rho(r) \sim \frac{1}{r^2}$

$$\rho(r) = \frac{\rho_0}{r^2}, \tag{5.12}$$

therefore :

$$\rho(r) \xrightarrow[r\to 0]{} \infty \tag{5.13}$$

As a conclusion, the isothermal model is at most an effective intermediate-scale model describing dark matter halos.

Furthermore, as done in Figure 1.9-left, one has to artificially cut the Maxwellian velocity distribution, $f_{gal}^{\text{No cut}}(\overrightarrow{v})$, at the local escape speed because it doesn't naturally drop down to 0 before reaching this velocity limit. Such sharp cut is not physical, thus one should at least consider a smooth (often taken as exponential [139]) cut-off of the velocity distribution before v_{esc}, or consider other models implying velocity distribution that naturally vanishes before the escape velocity.

Besides, the accepted values of the astrophysical parameters of interest in the signal computation are quite old with respect to the data that space missions collected since dark matter experiments agreed on using these peculiar estimates (like GAIA which scans the Milky Way [140]). More problematically, they were determined independently from one another while they should have mutual dependency [141] (see Section 5.2.2).

In the computation process of the sensitivity of an experiment, the first step is the computation of the expected rate of signal events in the volume of the detector. In the case of dark matter direct search with NR interaction, it is done thanks to Equation (1.37), reminded here (quantities noted with an apostrophe being defined in the terrestrial frame) :

$$\frac{\mathrm{d}R_{coll}}{\mathrm{d}E_r}(E_r) = M_{tot,DMDD}\frac{\rho_0}{m_\chi} \cdot \frac{\sigma_0 A^2 F^2(q)}{2\mu^2} \int_{v'_{min}}^{v'_{max}} \frac{f_\oplus(\overrightarrow{v'}, t)}{|\overrightarrow{v'}|} \mathrm{d}^3\overrightarrow{v'} \tag{5.14}$$

In Eq. (5.14), the mass of the WIMP and of the target nucleus (in μ), the differential cross section of interaction and the differential rate of events are particle physics

parameters. On the contrary, the mass density of the WIMP at the local position ρ_0, the maximum WIMP velocity in the lab frame v'_{max}, the WIMP velocity distribution in the lab frame $f_{\oplus}(\overrightarrow{v'}, t)$ are (or derive from) astrophysical parameters. Yet, the exclusion limits of dark matter direct detection experiments are computed in the (M_χ, σ_{SI}) frame. This is therefore for a peculiar (fixed) astrophysical framework (composed of the WIMP velocity distribution $f_{gal}(\vec{v})$ and of astrophysical parameters ρ_0, v_{esc}, v_c, and v_0), on which there is limited knowledge.

On the one hand, if one wants to determine the theoretical systematic uncertainties from the signal modelling of an experiment, one can try to take more recent (with more statistics in data) estimates of the value of the four astrophysical parameters (ρ_0, v_{esc}, v_c, and v_0) taken in the SHM. Then, plot a band around the official limit testifying which amount of parameters space it might be wrongly accepting or rejecting with an experiment because of the lack of knowledge on the galaxy kinematics. This is done in Section 5.2.

On the other hand, one can play with the input velocity distribution. Using better suited dark matter halo models in the Milky Way would improve the WIMP galactic velocity distribution $f_{gal}(\vec{v})$ thus improve the estimate of the rate of events and in the end the sensitivity. Here, the method and its impact on the sensitivity of DS20k (in terms of exclusion power) is presented in Section 5.3.

5.2. Impact of galactic parameters in the Standard Halo Model framework

The current recommended conventions for direct dark matter experiments are [43] :

$$\rho_0 = 0.3\,(\mathrm{GeV/c^2})/\mathrm{cm^3},\ v_{esc} = 544\,\mathrm{km/s} \text{ and } v_0 = v_c = 238\,\mathrm{km/s}\ .$$

The purpose of the present section is to assess the impact of astrophysical uncertainties on dark matter direct detection exclusion limits. The followed method is to directly vary astrophysical parameters in their uncertainty band and observe the effects on the exclusion limits. To begin with, Section 5.2.1 proposes to vary these parameters independently, keeping the Maxwellian velocity distribution for the halo model, so that one can assess the effect of each individual parameter on the exclusion limit. To go further, Section 5.2.2 applies three consistent sets of parameters, derived by Ref. [141] thanks to a method that considers the dynamics of the dark matter halo, to a Maxwellian velocity distribution and shows he effect on the sensitivity of DS20k.

5.2.1. Uncertainty on kinematic parameters and their independent variation

The relevant astrophysical parameters in the signal rate computation are :

- ***The local dark matter density*** ρ_0. The rate of events increases linearly with the WIMP density. Thus the number of signal events scales with ρ_0.

- ***The escape velocity at the position of the Sun*** v_{esc}. It contributes to both the upper bound of the integral in the differential rate computation and the cut of the tail of the velocity distribution if the considered model goes beyond v_{esc}.

- ***The circular velocity at the position of the Sun*** v_c. It contributes to the velocity distribution of the WIMP as seen on Earth, $f_\oplus(\overrightarrow{v'})$ (see Eq. (1.26)) when substituting $\overrightarrow{v}$ to $\overrightarrow{v'}+\overrightarrow{v_\oplus}(t)$. Indeed, $\overrightarrow{v_\oplus}(t) = \overrightarrow{v_{\oplus/\text{galaxy}}}(t) = \overrightarrow{v_{\oplus/\odot}}(t)+\overrightarrow{v_{\odot/\text{galaxy}}} = \overrightarrow{v_{\oplus/\odot}}(t)+\overrightarrow{v_c}+\overrightarrow{v_{pec}}$, $\overrightarrow{v_{pec}}$ being the peculiar velocity of the Sun around its circular orbit. In the following, the convention $\overrightarrow{v_{pec}}$ = (11., 12., 7.) km/s will be used, such that $\overrightarrow{v_\odot}$ = (11., 12. + v_c, 7.) km/s.

- ***The most probable WIMP velocity at the position of the Sun*** v_0. It is where the velocity distribution peaks in the galactic frame and it parametrises the width of the SHM distribution.

As these four parameters are involved in the differential rate of signal events, changing the astrophysics framework will change the shape of the exclusion limit. The purpose of the following discussion is to evaluate how much each of the parameters will affect individually the exclusion limits. However, as already mentioned, they all dynamically correlate to one another and to the mass and velocity density distributions (hence, they depend on the halo modelling itself).

The ranges of variation for the parameters were chosen broad, in order to be conservative, on the basis of measurements using recent datasets from galactic surveys :

- local dark matter density, ρ_0, in the range [0.13, 0.6] GeV/c^2/cm^3 around a nominal value of 0.3 GeV/c^2/cm^3, where the lower (resp. upper) bound comes from RAVE (resp. microlensing) data analyses [141, 142] (see [143] for a recent review) ;

- escape velocity, v_{esc}, in the range [437, 643] km/s around a nominal value of 544 km/s, where both bounds come from Gaia data analyses [144, 145] ;

- circular velocity at the sun position, v_c, in the range [178, 252] km/s around a nominal value of 238 km/s, where the lower (resp. upper) bound come from RAVE (resp. Gaia) data analyses [141, 146] ;

- most probable WIMP velocity, v_0, in the same range as v_c, as in the SHM both values are taken equal : [178, 252] km/s around a nominal value of 238 km/s ;

In order to assess the impact of each parameter on the behaviour of the limit, parameters were changed one by one and set to the three following values :

1. the lower bound of the uncertainty band (dashed-dotted lines in plots) ;

2. the SHM nominal value of the parameter (full lines in plots) ;

3. the upper bound of the uncertainty band (dashed lines in plots).

Figure 5.1 first shows the impact of the variation of the velocity parameters on the terrestrial WIMP velocity distribution. The WIMP velocity distribution is only affected by the change of v_0, v_c and v_{esc} as the local dark matter density acts on the differential rate rather than on the WIMP velocity distribution itself.

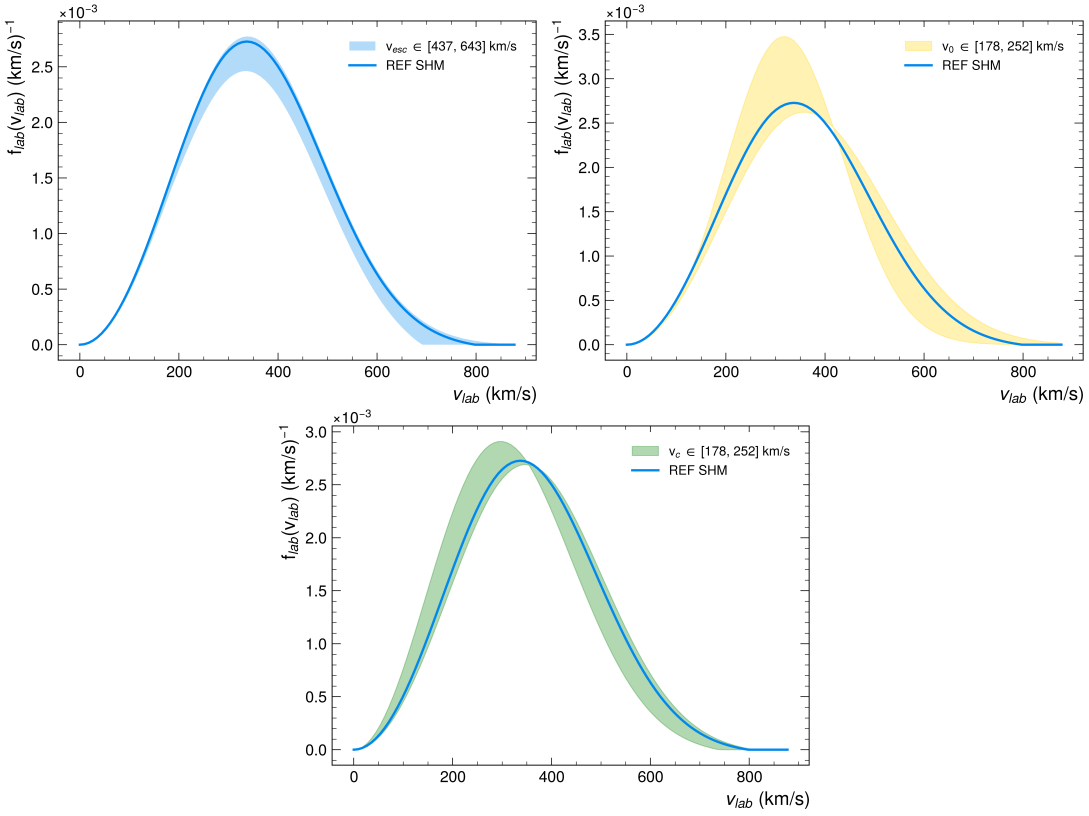

FIGURE 5.1. : In the SHM framework, impact on the normalised WIMP velocity distribution in the Earth frame of (top left) the galactic escape velocity v_{esc}, (top right) the most probable galactic WIMP velocity v_0 and (bottom) the galactic circular velocity at the position of the Sun v_c.

In order to estimate the impact of the WIMP signal theoretical uncertainties on the sensitivity of DS20k, the HM (resp. LM) limit is re-computed for each bound of the velocity distribution of Figure 5.1. The results are shown in Figure 5.2 (resp. Figure 5.3). As said before, the differential rate of signal events scales linearly with the mass density of WIMPs at the position of the Sun, hence the vertical shift of the exclusion limit when modifying ρ_0 (a twice larger ρ_0 will induce a twice larger $\frac{dR_{coll}}{dE_r}$ and in the end a twice lower value for the upper limit, corresponding to a rejection power enhanced by a factor

2).
The effects from the velocities are fainter as they induce small modifications of the differential rate computation. The main role played by the escape velocity and the circular velocity is confined at low WIMP masses. The reason for this effect is that the minimal WIMP mass needed to perform a recoil in the detection volume depends on v_{esc} and v_c. Solving Eq. (5.15) for a given experimental energy threshold E_T and mass of the detector material nucleus (i.e. for a given experiment) gives [147] :

$$v_{min}(E_T, m_{\chi,min}, m_N) = v_{esc} + v_c + v_\odot, \tag{5.15}$$

and taking $m_\chi = m_{\chi,min}$ and $E_r = E_T$ in Eq. (1.20) :

$$\sqrt{\frac{E_T m_N}{2\mu^2_{min}}} = v_{esc} + v_c + v_\odot \tag{5.16}$$

In order to provide a physical sense to this result, one can imagine that a light WIMP would need a very high speed in order to be able to move a heavy nucleus. If one removes a part of the tail of the velocity distribution, it is less and less probable that a light WIMP has a high speed thus less and less probable for a WIMP to recoil on a nucleus (or make it move enough so that it is visible by the detector).

On top, v_c plays a role in the rest of the WIMP mass range of the exclusion limit as it intervenes in the change of frame from the WIMP halo rest frame to the Earth frame (it is hidden in $\overrightarrow{v_{\odot/\text{ galaxy}}}$). To finish, v_0 parametrises the width of the bell distribution, thus the larger the v_0, the more populated the high-velocity tail of the galactic VPDF before the sharp cut. Again, the effect is relevant at low to medium WIMP masses, i.e. in the [15, 120] GeV/c^2 range in the HM regime and [0.8, 4] GeV/c^2 mass range in the LM regime.

As the impact from velocities is dominant in the low mass bound of Figure 5.2 (HM regime), one could have expected that the velocities would play a bigger role in the highest masses of the LM sensitivity of Figure 5.3. However, as the analysis is completely different, the same global behaviour is observed in both regimes.

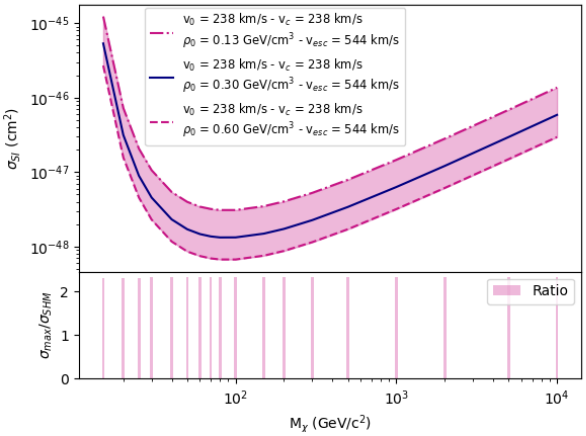

(a) ρ_0 effect.

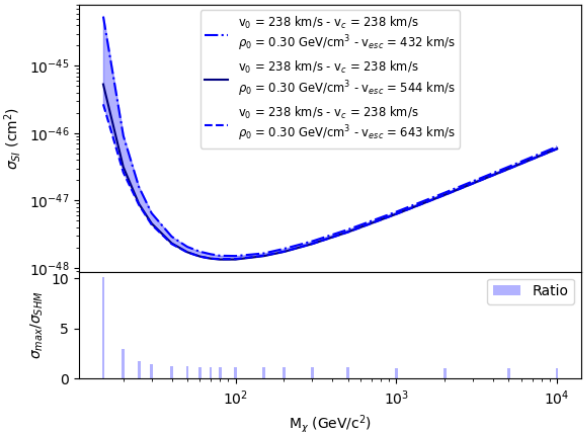

(b) v_{esc} effect.

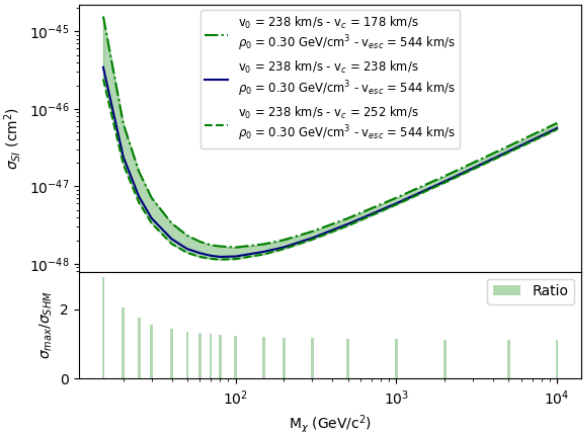

(c) v_c effect.

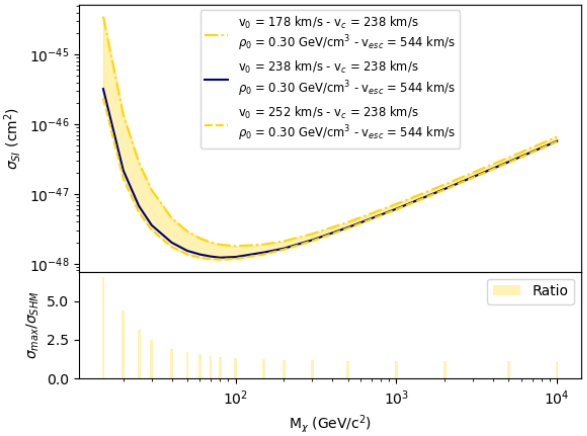

(d) v_0 effect.

FIGURE 5.2. : DS20k HM sensitivity varying independently the SHM parameters ρ_0 (top left), v_{esc} (top right), v_c (bottom left) and v_0 (bottom right). The low panel plots quantify the ratio between the worst limit set on the cross section and the nominal limit computed with the SHM for each WIMP mass.

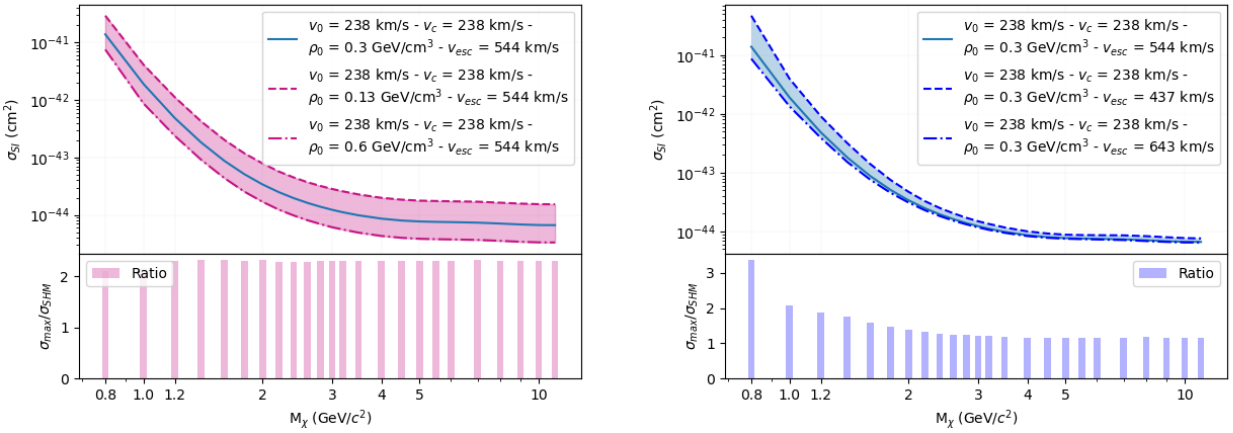

(a) ρ_0 effect.

(b) v_{esc} effect.

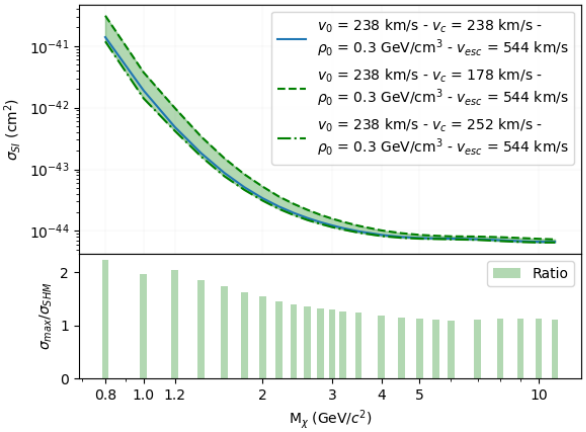

(c) v_c effect.

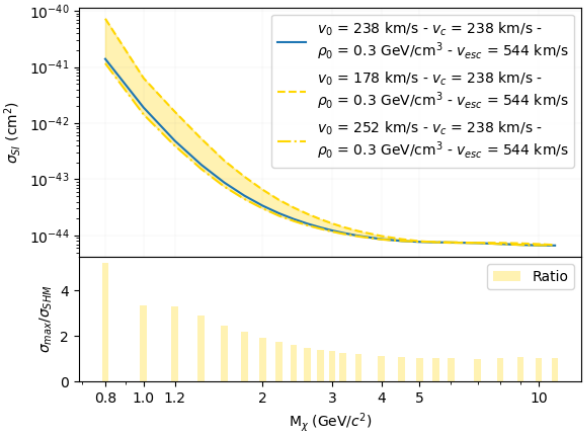

(d) v_0 effect.

FIGURE 5.3. : DS20k LM sensitivity varying independently the SHM parameters ρ_0 (top left), v_{esc} (top right), v_c (bottom left) and v_0 (bottom right). The low panel plots quantify the ratio between the worst limit set on the cross section and the nominal limit computed with the SHM for each WIMP mass.

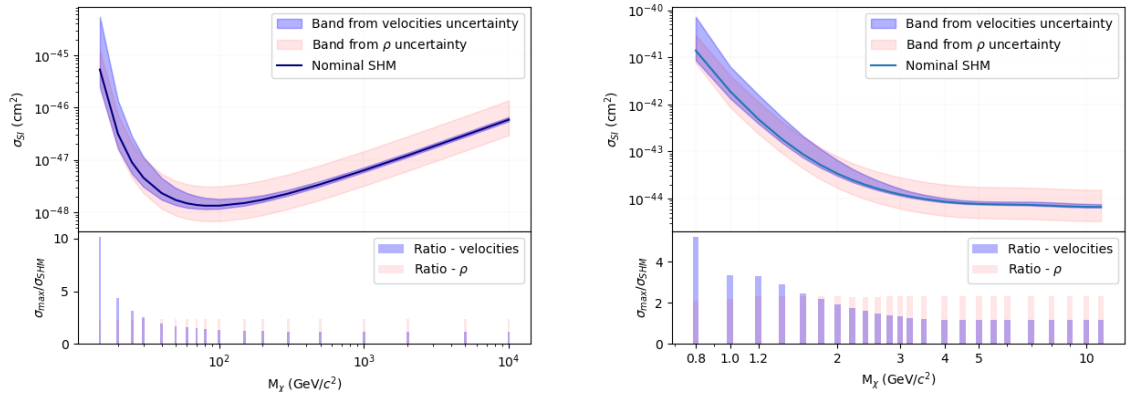

FIGURE 5.4. : In the SHM framework, impact of the astrophysical kinematics on the sensitivity of DS20k, at HM (left) and LM (right). The blue band gathers the impacts of the uncertainty of v_c, v_0 and v_{esc} local velocities on the limit while the red band only accounts for the impact of the uncertainty on ρ_0. The solid blue line is the the limit as assessed with the nominal SHM. The ratio plot shows the ratio between the least conservative limit and the limit from the nominal SHM for each point in mass.

In order to better compare the straightforward impact of ρ_0 and the more complicated impact of the velocities, Figure 5.4 left (HM regime) and right (LM regime) compares directly the effect of ρ_0 and the combined effect from the velocities. In the HM (resp. LM) regime, the impact of ρ_0 is dominant in the whole mass range except below $50\,\mathrm{GeV/c^2}$ (resp. below $1.6\,\mathrm{GeV/c^2}$), where the effect of v_0 overcomes the one of the dark matter density. At maximum in the HM (resp. LM) regime, the sensitivity as computed with the SHM is 10 x (resp. 5.2 x) less conservative than the upper bound of the systematic uncertainties. At high WIMP masses ($m_\chi > 100$ GeV/c^2 (HM) and $m_\chi > 4$ GeV/c^2 (LM)), the combined effect of the three velocity parameters almost vanishes. Hence the width of the exclusion band is given by the width of ρ_0 uncertainty interval. In these high mass ranges, the total uncertainty on the four astrophysical parameters induce a loss of rejection power of about 2.3 x (HM and LM) compared with the central one considering the nominal values of the parameters of the SHM.

5.2.2. Consistent variations of Standard Halo Model parameters

As already mentioned, the four astrophysical parameters needed to compute the differential rate of signal events in a dark matter direct detection (ρ_0, v_{esc}, v_c and v_0) depend on each other. In Section 5.2.1, these parameters were varied independently in order to assess their individual influence on DS-20k exclusion limits. To go further, one may want to take galactic dynamics into account in order to build relevant sets of parameters.

To give a hint of the interplay of the four parameters, the considered halo is the isotropic spherically symmetric isothermal halo (i.e. the Maxwell-Boltzmann halo, like the one of SHM). Here is what was obtained in Section 5.1 when describing the SHM :

$$\rho(r) \propto \frac{\sigma_{MB}^2}{r^2} \propto \frac{v_0^2}{r^2} \tag{5.17}$$

Thus, $\rho_0 = \rho(r = R_\odot)$ and v_0 are correlated. Plus, as already obtained in the context of the SHM :

$$\rho(r) = \int d^3\overrightarrow{v}\, f_{gal}(\overrightarrow{v}, r), \tag{5.18}$$

and

$$f_{MB}(\overrightarrow{v}, r) = \frac{1}{K} e^{-\frac{m\overrightarrow{v}^2}{2k_BT}} e^{-\frac{m\Phi(r)}{k_BT}} \tag{5.19}$$

Combining Eq. (5.18) and (5.19) :

$$\rho(r) = \int d^3\overrightarrow{v}\, \frac{1}{K} e^{-\frac{m\overrightarrow{v}^2}{2k_BT}} e^{-\frac{m\Phi(r)}{k_BT}} \tag{5.20}$$

Thus, $\rho(r)$ is correlated with both $\Phi(r)$ and the value of v_0.
Besides, in spherically symmetric galaxies, the escape velocity is :

$$v_{esc}(r) = \sqrt{2(\Phi(r_{max}) - \Phi(r))}, \tag{5.21}$$

r_{max} being the radius at which the spherically symmetric potential $\Phi(r)$ is at its maximum value. r_{max} defines the radius up to which the halo still has a gravitational influence. With Eq. (5.21), one halo defined -at least- by its gravitational potential correlates to v_{esc}, $\rho(r)$ and thus to v_0 (and v_c which is taken equal as v_0).

The goal of the present subsection is to compute the sensitivity of DS20k using consistent sets of parameters that take into account the dynamics of the dark matter halo. Yet, deriving a self-consistent astrophysical framework by building an ergodic velocity distribution function goes beyond the scope of this study. Fortunately, one can rely on existing studies.

Ref. [148] performed an analysis of the RAVE data to estimate the value of the escape velocity v_{esc} using different priors on the halo concentration and on the circular velocity at the position of the Sun v_c. Ref. [148] obtained estimated v_{esc} to be $v_{esc} = 533^{+54}_{-41}$ km/s and $v_{esc} = 511^{+48}_{-35}$ km/s by considering as prior $v_c = 220\,$km/s and $v_c = 240\,$km/s, respectively. In addition, Ref. [148] also let the circular velocity free in the fit, obtaining jointly $v_c = 196^{+26}_{-18}$ km/s and $v_{esc} = 537^{+44}_{-55}$ km/s.

Ref. [141] translated the three latter estimates of v_{esc} in terms of the other parameters needed in the event rate computation. To achieve so, they used a self-consistent velocity probability distribution function and a Likelihood method. The consistent estimates of the astrophysical parameters computed by Ref. [141] are presented in Table 5.1. It is

worth noting that the simultaneous fit of v_c and ρ_0 gives significantly lower values than many other estimates of the same galactic parameters.

Assumption on v_c	v_c (km/s)	v_{esc} (km/s)	ρ_0 (GeV/c^2/cm^3
$v_c = 220$ km/s	220	533^{+54}_{-41}	$0.37^{+0.02+0.04}_{-0.03-0.04}$
$v_c = 240$ km/s	240	511^{+48}_{-35}	$0.43^{+0.05}_{-0.05}$
Free v_c	196^{+26}_{-18}	537^{+44}_{-55}	$0.25^{+0.14}_{-0.12}$

TABLE 5.1. : Estimates of relevant astrophysical parameters for DMDD signal rate computation as translated by Ref [141] from astrophysical derivations of the escape speed from Ref. [148].

In the present thesis, the three sets of astrophysical parameters shown in Table 5.1 will be applied on a Maxwellian velocity distribution function, as done in direct dark matter search experiments. However, it is worth stressing once more that these parameters not only depend on each other but also on the assumption made for the velocity distribution function itself to derive the parameters. Figure 5.5 left (resp. right) shows the impact of the three latter consistent sets of astrophysical parameters, in the SHM framework, on the HM (resp. LM) sensitivity of DS20k. The main change in the limit is vertical, i.e. comes from the estimate of the dark matter density. In two of the three cases (the two cases where the circular velocity at the position of the Sun v_c has a reasonable value), the sensitivity as computed with the SHM is conservative. In the last case (where no prior on v_c is put in the fit), the set of astrophysical parameters gives a lower sensitivity (up to a factor 6.6 at 15 GeV/c^2 (HM) and 7.3 at 0.8 GeV/c^2 (LM)). It is due to the low value obtained for ρ_0, and thus a very low sensitivity compared to the nominal one.

With this illustrative example, this section addressed the impact that a consistent set of parameters can have on the sensitivity estimate of DS20k. The aim of the present thesis was not to build a model that permits to derive a completely consistent astrophysical framework of the dark matter halo but rather to introduce the importance to model at best the signal, that is partly determined by the kinematics of our galaxy.

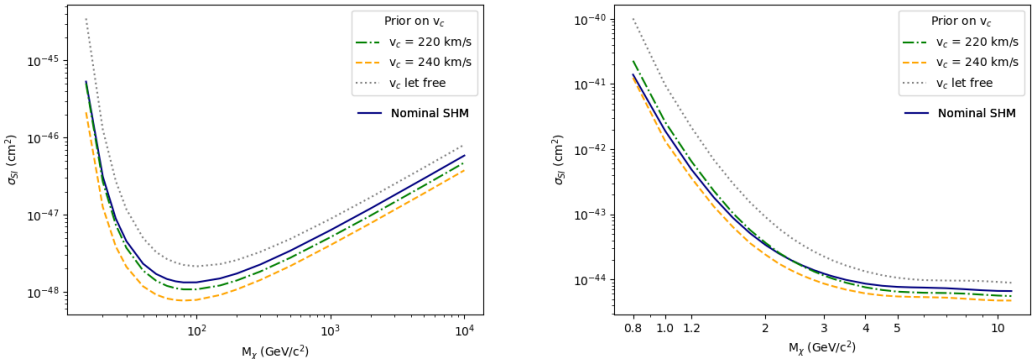

FIGURE 5.5. : In the SHM framework, impact of three consistent sets of astrophysical parameters on the sensitivity of DS20k [141] (see text for more details), at HM (left) and LM (right). The solid blue line is the limit as assessed with the nominal SHM.

5.3. Dark matter halo velocity distributions beyond the Maxwellian case

As said in Section 5.1, the isothermal isotropic spherically symmetric halo itself is not physically motivated. Hence it may be interesting to consider dark matter velocity distributions beyond Maxwellian distribution.

5.3.1. Analytical velocity distributions

There exists other viable dark matter halo analytical velocity distributions than the Maxwellian distribution. They are better suited than a Maxwellian distribution because they come from fits of N-body cosmological simulations. Even though they are better motivated than the SHM, using them is less relevant than taking the output of cosmological simulations themselves as proxy for the model of the galactic dark matter halo –hence not presented in the main content of the present thesis. However, the study of the behaviour of the HM sensitivity using a Tsallis [149] velocity distribution and a generalised Maxwellian [150] velocity distribution are shown and discussed in Appendix C.

5.3.2. Velocity distributions from N-body cosmological simulations

In the context of taking closer-to-reality dark matter halo velocity distributions, it is possible to take the VPDF of simulated halos as input for the event rate computation. This permits to take into account more complex and realistic features like streams, clumps, dark disk (which is not done by a pure bell-shaped distribution) resulting from (sometimes violent) accretion history processes [151, 152, 153, 154]. However, given that a cosmological simulation cannot provide information on the local dark matter

density, this approach can only lead to qualitative conclusions about the goodness of the approximation of a Maxwellian velocity distribution.

In order to have Milky Way-like dark matter halo VPDF, one has to select halos with the correct mass and size. It also implies extrapolating from simulated galaxies to the actual Milky Way. These simulations can be Dark Matter Only (DMO) simulations or dark matter + baryons simulations. They follow the accretion of halos over time and one of their outputs is the 3-vector velocity of each dark matter particle of the halo (say, n particles). Thus, the velocity distribution in the galactic frame can be inferred from the three velocity components of each simulated particle in the galactic frame :

$$v = \sqrt{v_x^2 + v_y^2 + v_z^2} \tag{5.22}$$

This v is then a histogram of the speed of n dark matter particles in the galactic frame. For instance, in the case of the SHM, each of the three velocity components of the halo follows a gaussian distribution with width v_0. To change frame and obtain the velocity distribution in the Earth (lab) frame, one only has to express the WIMP velocity on Earth as a function of the WIMP velocity in the galactic frame following Equation (1.23). In order to obtain the speed distribution histogram of the WIMP in the Earth frame, one has again to perform :

$$v' = \sqrt{v_x'^2 + v_y'^2 + v_z'^2} \tag{5.23}$$

In the peculiar case of this thesis, the data from 3D cosmological simulations are taken from Ref. [155]. In particular, the two selected halos are the so-called Halo B and Mochima halo.
The Mochima halo (resp. Halo B) is modelled by a zoom-in simulation, performed in [155] (resp. in [156]). First, initial conditions are generated with low and uniform resolution in the simulation box. These initial conditions are then evolved down to z = 0 (i.e. down to present times) in the box. Then, halos are selected if they are Milky Way-like galaxies candidates and the simulation of the halo is performed again, with the same seed of initial conditions but with increased resolution (the number of particles in the box is increased but the total mass is conserved). This resolution increased when approaching the center of the galaxy. Again, the box is evolved down to z = 0. At this step, if low resolution particles dropped into the inner part of the galaxy, they are included in the initial condition and the simulation is done again. These last three steps are done until the last requirement is fulfilled. New initial conditions are set, including for the baryonic gas : the hydrodynamic simulation is performed down to z = 0. The Mochima galaxy and Halo B are obtained after this zoom-in process selecting a Milky Way - size galaxy.

The velocity distributions resulting from both simulations are taken as input and integrated in the computation process of DS20k exclusion limit. The value of the dark matter mass density is kept to $\rho_0 = 0.3$ (GeV/c^2)/cm^3. First, Figure 5.6 and Figure 5.7 respectively show the velocity distributions of the Mochima halo and Halo B in the galactic (left plot) and Earth frames (right plot). The Mochima halo (Figure 5.6) has a

velocity distribution which drops down to 0 way before the SHM. Its escape velocity at the position of the Sun was computed as $v_{esc}^{Mochima} = 484$ km/s [155]. The bump that one can see in its velocity distribution in the galactic frame comes from different non-linear processes of accretion in the history of the halo formation. The Halo B (Figure 5.7) is more similar to SHM than Mochima. Indeed, first, its escape velocity is $v_{esc}^{Halo\ B} = 535$ km/s, closer to the 544 km/s of the SHM than Mochima. Plus, although Halo B displays a bump in the galactic velocity distribution, it is less intense than the one of Mochima. None of the two bumps are visible in the Earth frame distributions that are smoothed by the change of frame.

Figures 5.8 and 5.9 respectively show the expected exclusion limits at HM and LM obtained with Mochima (left) and Halo B (right). The exclusion limit computed with the SHM is displayed for comparison in full blue line. At HM, both limits computed with cosmological simulations results are 2.8 (Halo B) to 14 (Mochima halo) times more conservative than the SHM below 100 GeV/c^2. At LM, limits computed with simulated VPDF are 2.1 (Halo B) to 3.6 (Mochima) times more conservative than the SHM below 4 GeV/c^2. Like in the case of reduced v_{esc} and v_c, this sensitivity decrease is observed because the higher and the more populated the velocity tail, the lower the WIMP mass threshold to induce a recoil, the larger the rejected phase space. This effect is stronger for the Mochima halo as it drops down to 0 significantly before the SHM at high WIMP speed.
Above $m_\chi = 100$ GeV/c^2 (HM) and $m_\chi = 4$ GeV/c^2 (LM), the limits converge to the same value, giving the same rejection power to DS20k.

Using such cosmological simulations is a first step towards studying the impact of refined features that the Milky Way dark matter halo is suspected to have, such as clumps, streams or a dark disk. Such features are observed in most cosmological simulations of Milky Way-like galaxies and can be modelled in the same vein as the Tsallis or generalised Maxwellian distributions (see Appendix C) can model some VPDF simulations. Motivated by N-body cosmological simulations, such phenomena are expected to be present in our galaxy and thus are expected to better model the dark matter halo. More dedicated models to further study this effect or to see the impact of the presence of the large Magellan cloud on the WIMP halo VPDF may be biased (Which peculiar density should one take to simulate these features ? Which kinematics to take ? How important are these features at the Sum position ?, etc). Such studies go beyond the scope of this work.

5.4. Conclusions

After exploring the impact from different sources of astrophysical uncertainties on the sensitivity of DS-20k, it is interesting to gather all the effects into systematic uncertainty bands from the theoretical modelling of the signal around the nominal sensitivity assessed using the SHM. It also allows to compare all the methods directly.

This is performed in Figure 5.10 for the HM (top) and LM (bottom) sensitivity. On

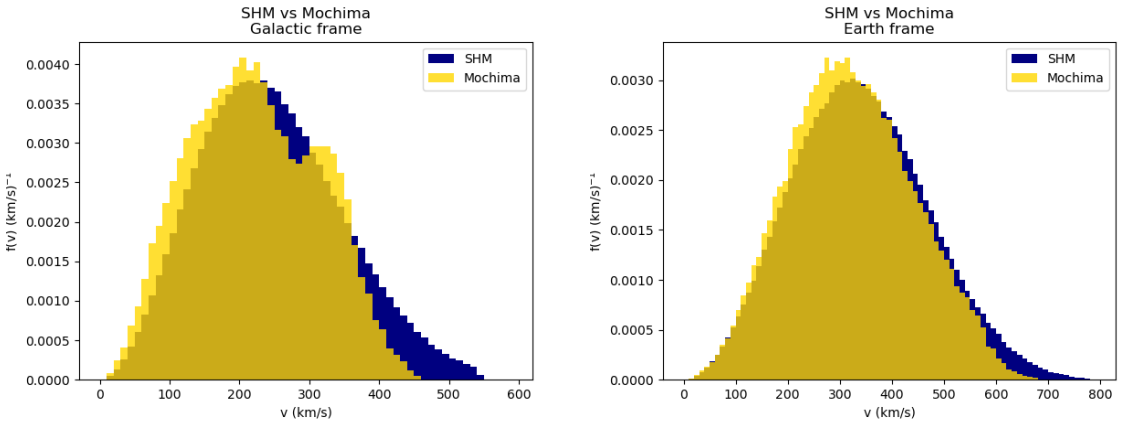

FIGURE 5.6. : Left : Velocity distribution of the Mochima halo (yellow) in the galactic frame (direct result of the simulation of [155]). Right : Velocity distribution in the Earth (lab) frame (change of frame done as if the Mochima halo was our Milky Way). For comparison, the SHM case is shown in blue.

these plots, there are three different bands :

- A red band (labelled 'Independent variation of parameters', left plots), that outlines the uncertainty on the limit coming from the uncertainty on the astrophysical parameters ρ_0, v_{esc}, v_c and v_0. The major part of the band is coming from the lack of knowledge on ρ_0 ;
- A green band (labelled 'Dependent variation of parameters', left plots), that shows the sensitivity of DS20k obtained by taking three consistent sets of astrophysical parameters, as advised by [141] ;
- A yellow band (labelled 'N-body simulations', right plots), that takes simulated WIMP halo VPDF as input for the signal computation, allowing for qualitative discussion of choice of the Maxwellian VPDF modelling of the local dark matter halo.

To conclude, the main impact comes from the lack of knowledge on ρ_0, the dark matter density at the position of the Sun, but its effect is linear thus maybe not problematic (if comes a doubt about dark matter detection, experiments can run their detector longer and see if a less dense halo is accepted or not). In the case of a dark matter halo whose velocity distribution is described by a Maxwellian distribution but with consistent set of astrophysical parameters (green band), two out of three sets of parameters result in stronger sensitivity than the SHM. To finish, the two models using cosmological simulations lead to a weaker sensitivity than the nominal one, especially in the lower mass ranges.
Hence, the SHM (both its Maxwellian velocity distribution and its accepted values for

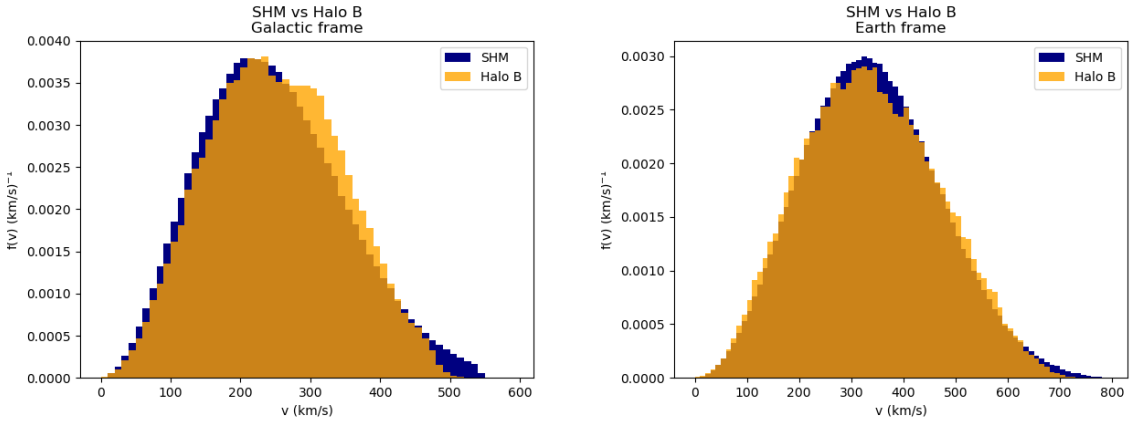

FIGURE 5.7. : Left : Velocity distribution of the Halo B (orange) in the galactic frame (direct result of the simulation of [156]). Right : Velocity distribution in the Earth (lab) frame (change of frame done as if the Mochima halo was our Milky Way). For comparison, the SHM case is shown in blue.

the astrophysical parameters) is not the best motivated model both from theoretical and observational sides, and can result in too optimistic sensitivity estimates for dark matter direct detection experiments. It remains however handy to compute comparison plots showing the race for dark matter detection such as the one of Figure 1.12, provided all caveats described in this chapter are kept in mind.

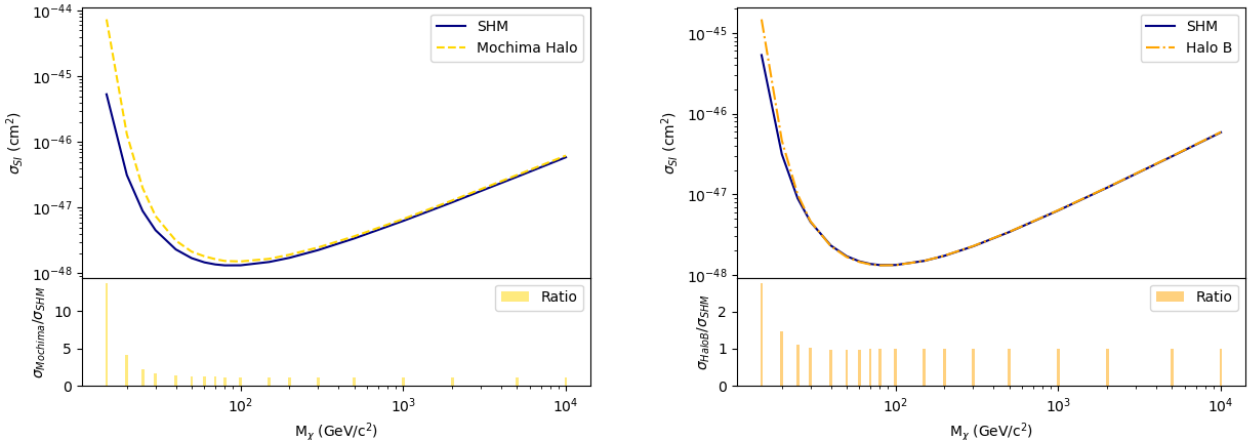

FIGURE 5.8. : The expected 90 % C.L. exclusion limit of DS20k for 10 years exposure at HM. Left : The yellow dashed line is the limit computed taking the velocity distribution of Mochima as input and the blue line is the reference one computed with SHM. Right : The orange dashed-dotted line is the limit computed taking the velocity distribution of the halo B as input and the blue line is the reference one computed with SHM. The bottom part of the plot shows the ratio between the exclusion limit computed with simulated halo and the one computed with SHM.

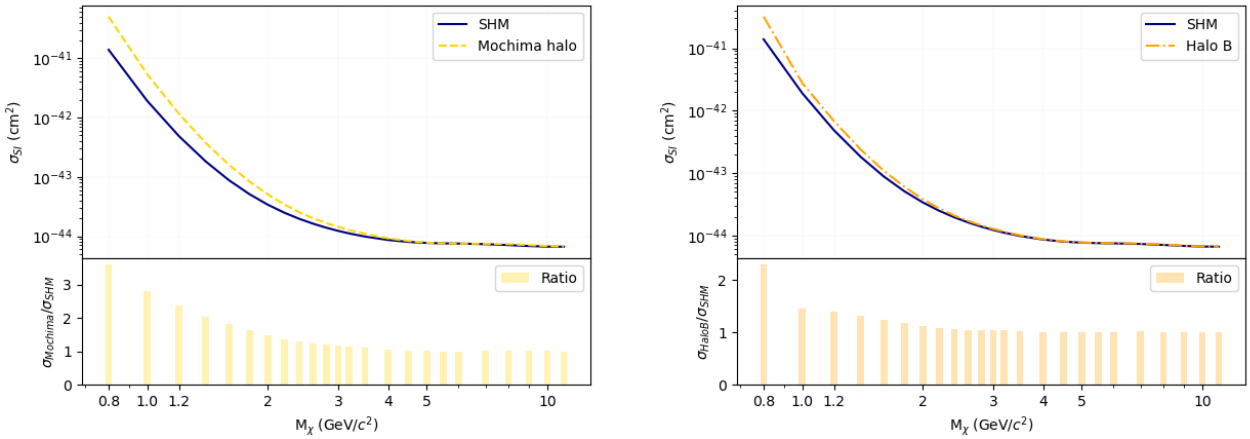

FIGURE 5.9. : The expected 90 % C.L. exclusion limit of DS20k for 1 year exposure at LM. Left : The yellow dashed line is the limit computed taking the velocity distribution of Mochima as input and the blue line is the reference one computed with SHM. Right : The orange dashed-dotted line is the limit computed taking the velocity distribution of the halo B as input and the blue line is the reference one computed with SHM. The bottom part of the plot shows the ratio between the exclusion limit computed with simulated halo and the one computed with SHM.

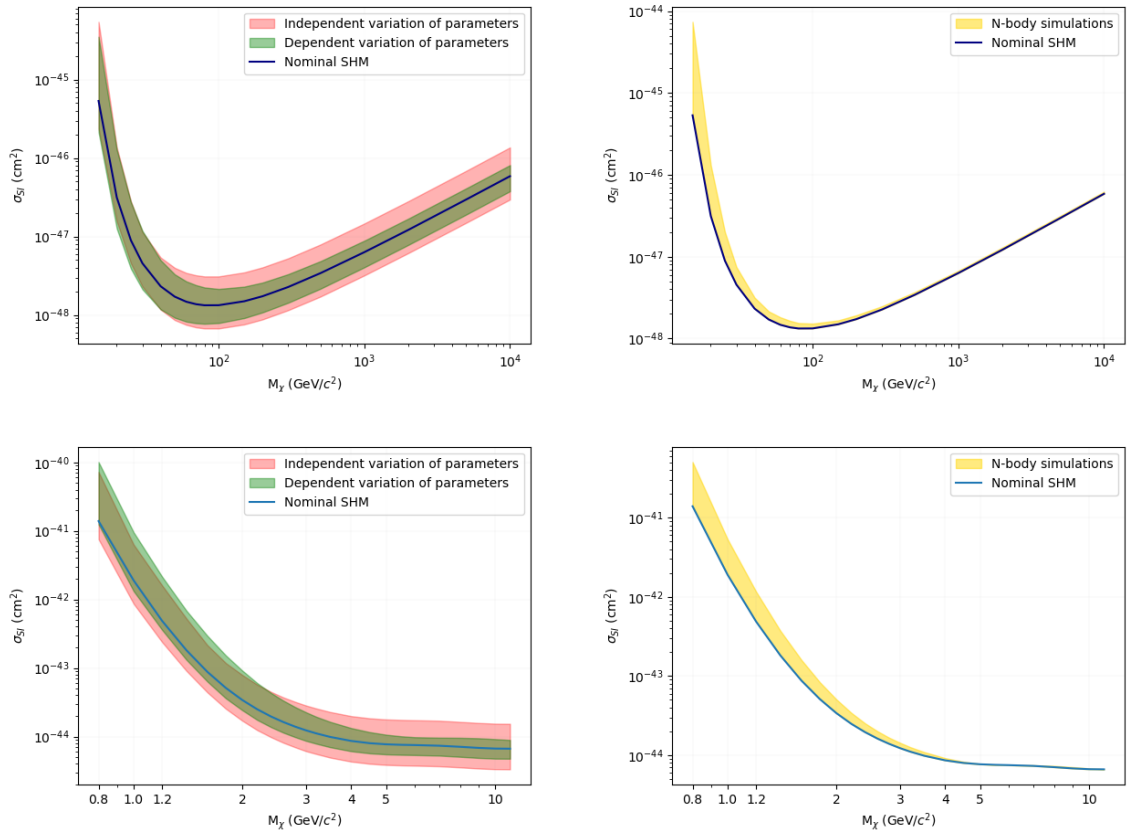

FIGURE 5.10. : Sensitivity of DarkSide-20k as estimated by its 90 % C.L. exclusion limit, computed with the SHM (full blue line). The systematic uncertainties on the limit originating from the modelling of the WIMP signal is shown as a band for three cases : in the left panels : the independent variation of the four astrophysical parameters of interest (red), an example of a dependent variation of these astrophysical parameters (green), and in the right panels : WIMP signal originating from a simulated halo (yellow). The top (resp. bottom) plots show the high mass (resp. low mass) sensitivity.

Conclusions

Dark matter remains one of the main puzzles of fundamental physics. Since its indirect proof of existence inferred from astrophysical observations almost a century ago, its very nature is still a major question mark. The near future in the field of dark matter will be exciting as a variety of promising experiments are currently operating or under final construction phase to search for these unseen particles. DarkSide-20k is one of them, primarily built to perform background-free search for Weakly Interacting Massive Particles between $10\,\mathrm{GeV/c^2}$ and $10\,\mathrm{TeV/c^2}$. By making use of 50 t of purified underground argon in a double phase TPC, and ultimately reaching 200 ton $\times$ year of exposure, DarkSide-20k should have a leading role in the direct search for dark matter. It is presently under construction and should start taking data in 2027.

The first part of this PhD work prepared the calibration of the DarkSide-20k TPC with external sources, both from an analysis and from a technical standpoints. The calibration is key in the conception of an experiment as it eventually permits the deep understanding of the detector response to signal and backgrounds. This is especially the case for DarkSide-20k, whose calibration comes with a set of challenges as it will be the largest TPC ever built for dark matter search purposes. The simulation of the calibration proved the feasibility of the external calibration within one month, reaching enough statistics for a reliable calibration, and without adverse impact from the external calibration system on the detector performances. In parallel, the hardware tests proved that the calibration system will be safely operable in a cryogenic environment.

The sensitivity of DarkSide-20k to low mass dark matter particles was assessed for the first time. To this end, the detector response model at low mass as well as the expected background components were modelled, building on the success of DarkSide-50. This work demonstrated that DarkSide-20k will have the potential to probe more than one order of magnitude of uncharted spin independent cross sections of WIMP interaction with nucleons within one year of physics data collection. Searching for the existence of low mass WIMPs will be possible below cross sections of 10^{-42} cm^2 for WIMP masses above $0.8\,\mathrm{GeV/c^2}$, and down to 7×10^{-45} cm^2 at $10\,\mathrm{GeV/c^2}$. Ultimately, after 10 years of data taking, DarkSide-20k should reach the neutrino fog around $5\,\mathrm{GeV/c^2}$. Capitalising on the potential atomic Migdal effect, DarkSide-20k should be able to set the strongest limits to spin independent cross sections of WIMP interaction with nucleons for WIMPs above $40\,\mathrm{MeV/c^2}$ and below $\approx 5\,\mathrm{GeV/c^2}$. In addition, DarkSide-20k will be able to search for direct interaction between light dark matter particles and shell electrons of argon. These dark matter particles are the light dark matter (with heavy and light mediator models), the galactic ALP, the dark photon and the sterile neutrino. Best direct limits

on all of them would be placed after only one year of data taking, after commissioning. These very good prospects further strengthen the physics reach of DarkSide-20k.

Last, this work quantified the impact of the galactic dark matter halo modelling on the DarkSide-20k sensitivity to high mass and low mass WIMPs, through three different methods. Two of them (one naive, one refined) assess the impact of the local kinetics of the galaxy by varying the four astrophysical parameters at use in the WIMP-nucleons event rate computation. The third method qualitatively assesses the impact of the dynamics of the galaxy by considering refined local dark matter velocity distributions, as modelled by N-body cosmological simulations. As expected, the impact is more important near the detection threshold for all methods.

Thanks to the multi-ton $\times$ year exposures employed by direct search for dark matter experiments –such as the 200 ton $\times$ year of DarkSide-20k– it will soon be possible to probe cross sections of interaction with target nuclei down to the neutrino floor. While this work partly demonstrated DarkSide-20k promising future, the latter still needs to be built, commissioned, and calibrated to ensure high-quality scientific data collection and to realise its full potential. Looking forward to seeing the DarkSide-20k experiment under operation, and ultimately the adaptation of this PhD work with a real-life detector !

Bibliography

[1] Jan H. Oort. « The force exerted by the stellar system in the direction perpendicular to the galactic plane and some related problems ». In : *Bulletin of the astronomical institutes of the Netherlands* VI (1932), p. 249-287.

[2] Fritz Zwicky. « Die Rotverschiebung von extragalaktischen Nebeln ». In : *Helvetica Physica Acta* 6 (1933), p. 110-127.

[3] Yann Mambrini. « Particles in the Dark Universe : A Student's Guide to Particle Physics and Cosmology ». Springer International Publishing, 2021. doi : 10.1007/978-3-030-78139-2.

[4] Vera C. Rubin et W. Kent Ford Jr. « Rotation of the Andromeda Nebula from a Spectroscopic Survey of Emission Regions ». In : *Astrophys. J.* 159 (1970), p. 379-403. doi : 10.1086/150317.

[5] The Gaia Collaboration. « Gaia Data Release 3 - Catalogue validation ». In : *Astron. Astrophys.* 674 (2023), A32. doi : 10.1051/0004-6361/202243790. arXiv : 2206.05989 [astro-ph].

[6] Yongjun Jiao et al. « Detection of the Keplerian decline in the Milky Way rotation curve ». In : *Astron. Astrophys.* 678 (2023), A208. doi : 10.1051/0004-6361/202347513. arXiv : 2309.00048 [astro-ph].

[7] Urmas Haud et Jaan Einasto. « Galactic models with massive corona I. Method ». In : *Astron. Astrophys.* 223 (1989), p. 89-94.

[8] Laurent Chemin, W. J. G. de Blok et Gary A. Mamon. « Improved Modeling of the Mass Distribution of Disk Galaxies by the Einasto Halo Model ». In : *Astron. J.* 142 (2011), p. 109. doi : 10.1088/0004-6256/142/4/109. arXiv : 1109.4247 [astro-ph.CO].

[9] Anne M. Green. « Dark matter in astrophysics/cosmology ». In : *SciPost Phys. Lect. Notes* (2022), p. 37. doi : 10.21468/SciPostPhysLectNotes.37. url : https://scipost.org/10.21468/SciPostPhysLectNotes.37.

[10] Douglas Clowe, Anthony Gonzalez et Maxim Markevitch. « Weak lensing mass reconstruction of the interacting cluster 1E0657-558 : Direct evidence for the existence of dark matter ». In : *Astrophys. J.* 604 (2004), p. 596-603. doi : 10.1086/381970. arXiv : astro-ph/0312273.

[11] N. Aghanim et al. « Planck 2018 results. VI. Cosmological parameters ». In : *Astron. Astrophys.* 641 (2020). [Erratum : Astron.Astrophys. 652, C4 (2021)], A6. doi : 10.1051/0004-6361/201833910. arXiv : 1807.06209 [astro-ph.CO].

[12] Bernard Carr et al. « Primordial black hole constraints for extended mass functions ». In : *Phys. Rev. D* 96 (2017), p. 023514. DOI : 10.1103/PhysRevD.96.023514. arXiv : 1705.05567 [astro-ph.CO].

[13] Peter W. Higgs. « Broken Symmetries and the Masses of Gauge Bosons ». In : *Phys. Rev. Lett.* 13 (1964). Sous la dir. de J. C. Taylor, p. 508-509. DOI : 10.1103/PhysRevLett.13.508.

[14] F. Englert et R. Brout. « Broken Symmetry and the Mass of Gauge Vector Mesons ». In : *Phys. Rev. Lett.* 13 (1964). Sous la dir. de J. C. Taylor, p. 321-323. DOI : 10.1103/PhysRevLett.13.321.

[15] G. S. Guralnik, C. R. Hagen et T. W. B. Kibble. « Global Conservation Laws and Massless Particles ». In : *Phys. Rev. Lett.* 13 (1964). Sous la dir. de J. C. Taylor, p. 585-587. DOI : 10.1103/PhysRevLett.13.585.

[16] Marco Battaglieri et al. « US Cosmic Visions : New Ideas in Dark Matter 2017 : Community Report ». In : juill. 2017. arXiv : 1707.04591 [hep-ph].

[17] Stephen P. Martin. « A Supersymmetry primer ». In : *Adv. Ser. Direct. High Energy Phys.* 18 (1998). Sous la dir. de Gordon L. Kane, p. 1-98. DOI : 10.1142/9789812839657_0001. arXiv : hep-ph/9709356.

[18] Pierre Fayet. « About R-parity and the supersymmetric standard model ». In : (déc. 1999). Sous la dir. de Mikhail A. Shifman, p. 476-497. DOI : 10.1142/9789812793850_0027. arXiv : hep-ph/9912413.

[19] Jonathan L. Feng. « The WIMP paradigm : Theme and variations ». In : *SciPost Phys. Lect. Notes* 71 (2023), p. 1. DOI : 10.21468/SciPostPhysLectNotes.71. arXiv : 2212.02479 [hep-ph].

[20] Graciela Gelmini et Paolo Gondolo. « DM Production Mechanisms ». 2010. arXiv : 1009.3690 [astro-ph.CO].

[21] Gianfranco Bertone et Dan Hooper. « History of dark matter ». In : *Rev. Mod. Phys.* 90 (2018), p. 045002. DOI : 10.1103/RevModPhys.90.045002. arXiv : 1605.04909 [astro-ph.CO].

[22] R. D. Peccei et Helen R. Quinn. « Constraints Imposed by CP Conservation in the Presence of Instantons ». In : *Phys. Rev. D* 16 (1977), p. 1791-1797. DOI : 10.1103/PhysRevD.16.1791.

[23] Marco Fabbrichesi, Emidio Gabrielli et Gaia Lanfranchi. « The Dark Photon ». 2020. arXiv : 2005.01515 [hep-ph].

[24] Wan-lei Guo, Zhi-zhong Xing et Shun Zhou. « Neutrino Masses, Lepton Flavor Mixing and Leptogenesis in the Minimal Seesaw Model ». In : *Int. J. Mod. Phys. E* 16 (2007), p. 1-50. DOI : 10.1142/S0218301307004898. arXiv : hep-ph/0612033.

[25] Jean-Philippe Bruneton et Gilles Esposito-Farese. « Field-theoretical formulations of MOND-like gravity ». In : *Phys. Rev. D* 76 (2007). [Erratum : Phys.Rev.D 76, 129902 (2007)], p. 124012. DOI : 10.1103/PhysRevD.76.129902. arXiv : 0705.4043 [gr-qc].

[26] Mordehai Milgrom. « MOND theory ». In : *Can. J. Phys.* 93 (2015), p. 107-118. DOI : 10.1139/cjp-2014-0211. arXiv : 1404.7661 [astro-ph.CO].

[27] Tia Miceli. « A search for dark matter appearing as missing transverse energy at CMS ». In : *J. Phys. Conf. Ser.* 485 (2014). Sous la dir. de Myriam Mondragón et al., p. 012030. DOI : 10.1088/1742-6596/485/1/012030.

[28] Jan Conrad et Olaf Reimer. « Indirect dark matter searches in gamma and cosmic rays ». In : *Nature Phys.* 13 (2017), p. 224-231. DOI : 10.1038/nphys4049. arXiv : 1705.11165 [astro-ph.HE].

[29] M. G. Aartsen et al. « Search for annihilating dark matter in the Sun with 3 years of IceCube data ». In : *Eur. Phys. J. C* 77 (2017). [Erratum : Eur.Phys.J.C 79, 214 (2019)], p. 146. DOI : 10.1140/epjc/s10052-017-4689-9. arXiv : 1612.05949 [astro-ph.HE].

[30] S. Adrian-Martinez et al. « First results on dark matter annihilation in the Sun using the ANTARES neutrino telescope ». In : *JCAP* 11 (2013), p. 032. DOI : 10.1088/1475-7516/2013/11/032. arXiv : 1302.6516 [astro-ph.HE].

[31] Marc Schumann. « Direct Detection of WIMP Dark Matter : Concepts and Status ». In : *J. Phys. G* 46 (2019), p. 103003. DOI : 10.1088/1361-6471/ab2ea5. arXiv : 1903.03026 [astro-ph.CO].

[32] CRESST Coll. « First results from the CRESST-III low-mass dark matter program ». In : *Phys. Rev. D* 100 (2019), p. 102002. DOI : 10.1103/PhysRevD.100.102002. arXiv : 1904.00498 [astro-ph.CO].

[33] EDELWEISS Coll. « Performance of the EDELWEISS-III experiment for direct dark matter searches ». In : *JINST* 12 (2017), P08010. DOI : 10.1088/1748-0221/12/08/P08010. arXiv : 1706.01070 [physics.ins-det].

[34] I. Alkhatib et al. « Light Dark Matter Search with a High-Resolution Athermal Phonon Detector Operated Above Ground ». In : *Phys. Rev. Lett.* 127 (2021), p. 061801. DOI : 10.1103/PhysRevLett.127.061801. arXiv : 2007.14289 [hep-ex].

[35] XENON Coll. « The XENONnT Dark Matter Experiment ». 2024. arXiv : 2402.10446 [physics.ins-det].

[36] PandaX Coll. « Dark Matter Search Results from the PandaX-4T Commissioning Run ». In : *Phys. Rev. Lett.* 127 (2021), p. 261802. DOI : 10.1103/PhysRevLett.127.261802. arXiv : 2107.13438 [hep-ex].

[37] LZ Coll. « First Dark Matter Search Results from the LUX-ZEPLIN (LZ) Experiment ». In : *Phys. Rev. Lett.* 131 (2023), p. 041002. DOI : 10.1103/PhysRevLett.131.041002. arXiv : 2207.03764 [hep-ex].

[38] DarkSide Coll. « DarkSide-50 532-day Dark Matter Search with Low-Radioactivity Argon ». In : *Phys. Rev. D* 98 (2018), p. 102006. DOI : 10.1103/PhysRevD.98.102006. arXiv : 1802.07198 [astro-ph.CO].

[39] J. Calvo et al. « Commissioning of the ArDM experiment at the Canfranc underground laboratory : first steps towards a tonne-scale liquid argon time projection chamber for Dark Matter searches ». In : *JCAP* 1703 (2017), p. 003. DOI : 10.1088/1475-7516/2017/03/003. arXiv : arXiv:1612.06375 [physics.ins-det].

[40] J. D. Lewin et P. F. Smith. « Review of mathematics, numerical factors, and corrections for dark matter experiments based on elastic nuclear recoil ». In : *Astropart. Phys.* 6 (1996), p. 87-112. DOI : 10.1016/S0927-6505(96)00047-3.

[41] Anne M. Green. « Astrophysical uncertainties on the local dark matter distribution and direct detection experiments ». In : 44 (1er août 2017), p. 084001. ISSN : 0954-3899, 1361-6471. DOI : 10.1088/1361-6471/aa7819. arXiv : 1703.10102[astro-ph,physics:hep-ph].

[42] Youjia Wu et al. « Uncertainties in Direct Dark Matter Detection in Light of Gaia's Escape Velocity Measurements ». In : *Journal of Cosmology and Astroparticle Physics* 2019 (11 oct. 2019), p. 034-034. ISSN : 1475-7516. DOI : 10.1088/1475-7516/2019/10/034. arXiv : 1904.04781[astro-ph,physics:hep-ph].

[43] D. Baxter et al. « Recommended conventions for reporting results from direct dark matter searches ». In : *Eur. Phys. J. C* 81 (2021), p. 907. DOI : 10.1140/epjc/s10052-021-09655-y. arXiv : 2105.00599 [hep-ex].

[44] Jodi Cooley. « Dark Matter direct detection of classical WIMPs ». In : *SciPost Phys. Lect. Notes* (2022), p. 55. DOI : 10.21468/SciPostPhysLectNotes.55.

[45] Richard H. Helm. « Inelastic and Elastic Scattering of 187-Mev Electrons from Selected Even-Even Nuclei ». In : *Phys. Rev.* 104 (1956), p. 1466-1475. DOI : 10.1103/PhysRev.104.1466.

[46] Gintaras Duda, Ann Kemper et Paolo Gondolo. « Model Independent Form Factors for Spin Independent Neutralino-Nucleon Scattering from Elastic Electron Scattering Data ». In : *JCAP* 04 (2007), p. 012. DOI : 10.1088/1475-7516/2007/04/012. arXiv : hep-ph/0608035.

[47] N. Fornengo et S. Scopel. « Temporal distortion of annual modulation at low recoil energies ». In : 576 (déc. 2003), p. 189-194. ISSN : 03702693. DOI : 10.1016/j.physletb.2003.09.077. arXiv : hep-ph/0301132.

[48] V Chepel et H Araújo. « Liquid noble gas detectors for low energy particle physics ». In : *Journal of Instrumentation* 8 (2013), R04001-R04001. ISSN : 1748-0221. DOI : 10.1088/1748-0221/8/04/R04001.

[49] Julien Billard et al. « Direct detection of dark matter—APPEC committee report ». In : *Rept. Prog. Phys.* 85 (2022), p. 056201. DOI : 10.1088/1361-6633/ac5754. arXiv : 2104.07634 [hep-ex].

[50] MIMAC Coll. « Dark Matter Directionality Detection performance of the Micromegas-based μTPC-MIMAC detector ». In : *Nucl. Instrum. Meth. A* 1021 (2022), p. 165412. DOI : 10.1016/j.nima.2021.165412. arXiv : 2003.11812 [physics.ins-det].

[51] DarkSide-20k Coll. « Constraints on directionality effect of nuclear recoils in a liquid argon time projection chamber ». In : *Eur. Phys. J. C* 84 (2024), p. 24. doi : 10.1140/epjc/s10052-023-12312-1. arXiv : 2307.15454 [physics.ins-det].

[52] R. Bernabei et al. « The DAMA/LIBRA apparatus ». In : *Nucl. Instrum. Meth. A* 592 (2008), p. 297-315. doi : 10.1016/j.nima.2008.04.082. arXiv : 0804.2738 [astro-ph].

[53] R. Bernabei et al. « New results from DAMA/LIBRA ». In : *Eur. Phys. J. C* 67 (2010), p. 39-49. doi : 10.1140/epjc/s10052-010-1303-9. arXiv : 1002.1028 [astro-ph.GA].

[54] P. -A. Amaudruz et al. « Design and Construction of the DEAP-3600 Dark Matter Detector ». In : *Astropart. Phys.* 108 (2019), p. 1-23. doi : 10.1016/j.astropartphys.2018.09.006. arXiv : 1712.01982 [astro-ph.IM].

[55] R. L. Workman et al. « Review of Particle Physics ». In : *PTEP* 2022 (2022), p. 083C01. doi : 10.1093/ptep/ptac097.

[56] DarkSide-50 Coll. « Search for low-mass dark matter WIMPs with 12 ton-day exposure of DarkSide-50 ». In : *Phys. Rev. D* 107.6 (2023), p. 063001. doi : 10.1103/PhysRevD.107.063001. arXiv : 2207.11966 [hep-ex].

[57] XENON Coll. « Light Dark Matter Search with Ionization Signals in XENON1T ». In : *Phys. Rev. Lett.* 123 (2019), p. 251801. doi : 10.1103/PhysRevLett.123.251801. arXiv : 1907.11485 [hep-ex].

[58] SuperCDMS Coll. « A Strategy for Low-Mass Dark Matter Searches with Cryogenic Detectors in the SuperCDMS SNOLAB Facility ». In : *Snowmass 2021*. Mars 2022. arXiv : 2203.08463 [physics.ins-det].

[59] Julien Billard. « Conseil scientifique de l'IN2P3 ». Report. 2023.

[60] A. E. Chavarria. « DAMIC at SNOLAB ». In : *Journal of Physics : Conference Series* 1342 (2020), p. 012057. doi : 10.1088/1742-6596/1342/1/012057.

[61] NEWS-G Coll. « DarkSPHERE : Exploring light dark matter with a spherical proportional counter electroformed underground at the Boulby Underground Laboratory ». 2023. arXiv : 2301.05183 [hep-ex].

[62] K. Rielage et al. « Update on the MiniCLEAN Dark Matter Experiment ». In : *Phys. Procedia* 61 (2015). Sous la dir. de Frank Avignone et Wick Haxton, p. 144-152. doi : 10.1016/j.phpro.2014.12.024. arXiv : 1403.4842 [physics.ins-det].

[63] The Global Argon Dark Matter Collaboration. *DarkSide-20k Technical Design Report*. Rapp. tech. INFN, 2021.

[64] V. Chepel et H. Araujo. « Liquid noble gas detectors for low energy particle physics ». In : *JINST* 8 (2013), R04001. doi : 10.1088/1748-0221/8/04/R04001. arXiv : 1207.2292 [physics.ins-det].

[65] D. -M. Mei et al. « A Model of Nuclear Recoil Scintillation Efficiency in Noble Liquids ». In : *Astropart. Phys.* 30 (2008), p. 12-17. DOI : 10.1016/j.astropartphys.2008.06.001. arXiv : 0712.2470 [nucl-ex].

[66] DarkSide-50 Coll. « Calibration of the liquid argon ionisation response to low energy electronic and nuclear recoils DarkSide-50. » In : *Phys. Rev. D* 104 (2021), p. 082005. DOI : 10.1103/PhysRevD.104.082005. arXiv : 2107.08087 [physics.ins-det].

[67] Tadayoshi Doke et al. « Absolute Scintillation Yields in Liquid Argon and Xenon for Various Particles ». In : *Jap. J. Appl. Phys.* 41 (2002), p. 1538-1545. DOI : 10.1143/JJAP.41.1538.

[68] DarkSide-50 Coll. « Low-Mass Dark Matter Search with the DarkSide-50 Experiment ». In : *Phys. Rev. Lett.* 121 (2018), p. 081307. DOI : 10.1103/PhysRevLett.121.081307. arXiv : 1802.06994 [astro-ph.HE].

[69] DarkSide Coll. « Results From the First Use of Low Radioactivity Argon in a Dark Matter Search ». In : *Phys. Rev. D* 93 (2016). [Addendum : Phys.Rev.D 95, 069901 (2017)], p. 081101. DOI : 10.1103/PhysRevD.93.081101. arXiv : 1510.00702 [astro-ph.CO].

[70] DarkSide Coll. « Separating ^{39}Ar from ^{40}Ar by cryogenic distillation with Aria for dark-matter searches ». In : *Eur. Phys. J. C* 81 (2021), p. 359. DOI : 10.1140/epjc/s10052-021-09121-9. arXiv : 2101.08686 [physics.ins-det].

[71] DarkSide-20k Coll. « Measurement of isotopic separation of argon with the prototype of the cryogenic distillation plant Aria for dark matter searches ». In : *Eur. Phys. J. C* 83 (2023), p. 453. DOI : 10.1140/epjc/s10052-023-11430-0. arXiv : 2301.09639 [physics.ins-det].

[72] M. Miyajima et al. « Average energy expended per ion pair in liquid argon ». In : *Phys. Rev. A* 9 (1974), p. 1438-1443. DOI : 10.1103/PhysRevA.9.1438.

[73] T. Doke et al. « Estimation of the fraction of electrons escaping from recombination in the ionization of liquid argon with relativistic electrons and heavy ions ». In : *Chemical Physics Letters* 115 (1985), p. 164-166. ISSN : 0009-2614. DOI : https://doi.org/10.1016/0009-2614(85)80671-0.

[74] D. F. Anderson. « Photosensitive Dopants for Liquid Argon ». In : *Nucl. Instrum. Meth. A* 242 (1986), p. 254. DOI : 10.1016/0168-9002(86)90217-2.

[75] XENON Coll. « First Dark Matter Search with Nuclear Recoils from the XENONnT Experiment ». In : *Phys. Rev. Lett.* 131 (2023), p. 041003. DOI : 10.1103/PhysRevLett.131.041003. arXiv : 2303.14729 [hep-ex].

[76] Julie Rode. « DarkSide : Searching for dark matter with liquid argon ». Thèse de doct. Laboratoire de Physique Nucléaire et de Hautes Énergies, France, Sorbonne U., 2022.

[77] DEAP-3600 Coll. « Search for dark matter with a 231-day exposure of liquid argon using DEAP-3600 at SNOLAB ». In : *Phys. Rev. D* 100 (2019), p. 022004. DOI : 10.1103/PhysRevD.100.022004. arXiv : arXiv:1902.04048 [astro-ph.CO].

[78] DEAP-3600 Coll. « First results from the DEAP-3600 dark matter search with argon at SNOLAB ». In : *Phys. Rev. Lett.* 121 (2018), p. 071801. DOI : 10.1103/PhysRevLett.121.071801. arXiv : arXiv:1707.08042 [astro-ph.CO].

[79] Daniel Z. Freedman. « Coherent Neutrino Nucleus Scattering as a Probe of the Weak Neutral Current ». In : *Phys. Rev. D* 9 (1974), p. 1389-1392. DOI : 10.1103/PhysRevD.9.1389.

[80] XENON Coll. « First Measurement of Solar ^{8}B Neutrinos via Coherent Elastic Neutrino-Nucleus Scattering with XENONnT ». Août 2024. arXiv : 2408.02877 [nucl-ex].

[81] PandaX Coll. « First Indication of Solar ^{8}B Neutrino Flux through Coherent Elastic Neutrino-Nucleus Scattering in PandaX-4T ». Juill. 2024. arXiv : 2407.10892 [hep-ex].

[82] DarkSide. gitlab.in2p3.fr:darkside/g4ds.git. 2021.

[83] LZ Coll. « Projected WIMP sensitivity of the LUX-ZEPLIN dark matter experiment ». In : *Phys. Rev. D* 101 (2020), p. 052002. DOI : 10.1103/PhysRevD.101.052002. arXiv : 1802.06039 [astro-ph.IM].

[84] Xenon Coll. « Projected WIMP sensitivity of the XENONnT dark matter experiment ». In : *JCAP* 11 (2020), p. 031. DOI : 10.1088/1475-7516/2020/11/031. arXiv : 2007.08796 [physics.ins-det].

[85] XENON Coll. « Dark Matter Search Results from a One Ton-Year Exposure of XENON1T ». In : *Phys. Rev. Lett.* 121.11 (2018), p. 111302. DOI : 10.1103/PhysRevLett.121.111302. arXiv : arXiv:1805.12562 [astro-ph.CO].

[86] DarkSide Coll. « Simulation of argon response and light detection in the DarkSide-50 dual phase TPC ». In : *JINST* 12.10 (2017), P10015. DOI : 10.1088/1748-0221/12/10/P10015. arXiv : arXiv:1707.05630 [physics.ins-det].

[87] Marie van Uffelen et al. (DarkSide-20k calibration group). « Guide tube system for external source calibration in DarkSide-20k ». docdb/4334. 2024.

[88] DarkSide Coll. « CALIS—A CaLibration Insertion System for the DarkSide-50 dark matter search experiment ». In : *JINST* 12 (2017), T12004. DOI : 10.1088/1748-0221/12/12/T12004. arXiv : 1611.02750 [physics.ins-det].

[89] DarkSide-50 Coll. « Search for Dark-Matter–Nucleon Interactions via Migdal Effect with DarkSide-50 ». In : *Phys. Rev. Lett.* 130.10 (2023), p. 101001. DOI : 10.1103/PhysRevLett.130.101001. arXiv : 2207.11967 [hep-ex].

[90] DarkSide-50 Coll. « Search for Dark Matter Particle Interactions with Electron Final States with DarkSide-50 ». In : *Phys. Rev. Lett.* 130.10 (2023), p. 101002. DOI : 10.1103/PhysRevLett.130.101002. arXiv : 2207.11968 [hep-ex].

[91] DarkSide-50 Coll. « Constraints on Sub-GeV Dark-Matter–Electron Scattering from the DarkSide-50 Experiment ». In : *Phys. Rev. Lett.* 121.11 (2018), p. 111303. DOI : 10.1103/PhysRevLett.121.111303. arXiv : 1802.06998 [astro-ph.CO].

[92] S. J. Haselschwardt et al. « Improved calculations of beta decay backgrounds to new physics in liquid xenon detectors ». In : *Phys. Rev. C* 102 (2020), p. 065501. DOI : 10.1103/PhysRevC.102.065501. arXiv : 2007.13686 [hep-ex].

[93] X. Mougeot et C. Bisch. « Consistent calculation of the screening and exchange effects in allowed β^- transitions ». In : *Phys. Rev. A* 90 (2014), p. 012501. DOI : 10.1103/PhysRevA.90.012501. URL : https://link.aps.org/doi/10.1103/PhysRevA.90.012501.

[94] B. M. Roach et al. « NuSTAR Tests of Sterile-Neutrino Dark Matter : New Galactic Bulge Observations and Combined Impact ». In : *Phys. Rev. D* 101.10 (2020), p. 103011. DOI : 10.1103/PhysRevD.101.103011. arXiv : 1908.09037 [astro-ph.HE].

[95] U. Fano. « Ionization Yield of Radiations. 2. The Fluctuations of the Number of Ions ». In : *Phys. Rev.* 72 (1947), p. 26-29. DOI : 10.1103/PhysRev.72.26.

[96] D. Yu. Akimov et al. « Observation of delayed electron emission in a two-phase liquid xenon detector ». In : *JINST* 11 (2016), p. C03007. DOI : 10.1088/1748-0221/11/03/C03007.

[97] ZEPLIN-II Collaboration. « Measurement of single electron emission in two-phase xenon ». In : *Astropart. Phys.* 30 (2008), p. 54-57. DOI : 10.1016/j.astropartphys.2008.06.006. arXiv : 0708.0768 [physics.ins-det].

[98] XENON100 Collaboration. « Observation and applications of single-electron charge signals in the XENON100 experiment ». In : *J. Phys. G* 41 (2014), p. 035201. DOI : 10.1088/0954-3899/41/3/035201. arXiv : 1311.1088 [physics.ins-det].

[99] XENON Collaboration. « Emission of single and few electrons in XENON1T and limits on light dark matter ». In : *Phys. Rev. D* 106 (2022), p. 022001. DOI : 10.1103/PhysRevD.106.022001. arXiv : 2112.12116 [hep-ex].

[100] Peter Sorensen. « Electron train backgrounds in liquid xenon dark matter search detectors are indeed due to thermalization and trapping ». In : (fév. 2017). arXiv : 1702.04805 [physics.ins-det].

[101] SNO Coll. « Combined Analysis of all Three Phases of Solar Neutrino Data from the Sudbury Neutrino Observatory ». In : *Phys. Rev. C* 88 (2013), p. 025501. DOI : 10.1103/PhysRevC.88.025501. arXiv : 1109.0763 [nucl-ex].

[102] A.B. Migdal. « Ionization of atoms accompanying α- and β-decay ». In : *J. Phys. USSR* 4 (1941), p. 449.

[103] Jingke Xu et al. « Search for the Migdal effect in liquid xenon with keV-level nuclear recoils ». In : *Phys. Rev. D* 109 (2024), p. L051101. DOI : 10.1103/PhysRevD.109.L051101. arXiv : 2307.12952 [hep-ex].

[104] PandaX Coll. « Search for Light Dark Matter with Ionization Signals in the PandaX-4T Experiment ». In : *Phys. Rev. Lett.* 130 (2023), p. 261001. DOI : 10.1103/PhysRevLett.130.261001. arXiv : 2212.10067 [hep-ex].

[105] XENON Coll. « Search for Coherent Elastic Scattering of Solar ^{8}B Neutrinos in the XENON1T Dark Matter Experiment ». In : *Phys. Rev. Lett.* 126 (2021), p. 091301. DOI : 10.1103/PhysRevLett.126.091301. arXiv : 2012.02846 [hep-ex].

[106] PandaX Coll. « Search for Solar ^{8}B Neutrinos in the PandaX-4T Experiment Using Neutrino-Nucleus Coherent Scattering ». In : *Phys. Rev. Lett.* 130 (2023), p. 021802. DOI : 10.1103/PhysRevLett.130.021802. arXiv : 2207.04883 [hep-ex].

[107] CDEX-50 Coll. « Projected sensitivity of the CDEX-50 experiment ». 2023. arXiv : 2012.02169 [hep-ex].

[108] DAMIC Coll. « Results on low-mass weakly interacting massive particles from a 11 kg-day target exposure of DAMIC at SNOLAB ». In : *Phys. Rev. Lett.* 125 (2020), p. 241803. DOI : 10.1103/PhysRevLett.125.241803. arXiv : 2007.15622 [astro-ph.CO].

[109] NEWS-G Coll. « First results from the NEWS-G direct dark matter search experiment at the LSM ». In : *Astropart. Phys.* 97 (2018), p. 54-62. DOI : 10.1016/j.astropartphys.2017.10.009. arXiv : 1706.04934 [astro-ph.IM].

[110] LUX Coll. « Improving sensitivity to low-mass dark matter in LUX using a novel electrode background mitigation technique ». In : *Phys. Rev. D* 104 (2021), p. 012011. DOI : 10.1103/PhysRevD.104.012011. arXiv : 2011.09602 [hep-ex].

[111] LUX Coll. « Results from a search for dark matter in the complete LUX exposure ». In : *Phys. Rev. Lett.* 118 (2017), p. 021303. DOI : 10.1103/PhysRevLett.118.021303. arXiv : 1608.07648 [astro-ph.CO].

[112] SuperCDMS Coll. « Low-mass dark matter search with CDMSlite ». In : *Phys. Rev. D* 97 (2018), p. 022002. DOI : 10.1103/PhysRevD.97.022002. arXiv : 1707.01632 [astro-ph.CO].

[113] PICO Coll. « Dark Matter Search Results from the Complete Exposure of the PICO-60 C_3F_8 Bubble Chamber ». In : *Phys. Rev. D* 100 (2019), p. 022001. DOI : 10.1103/PhysRevD.100.022001. arXiv : 1902.04031 [astro-ph.CO].

[114] CDMS Collaboration. « Silicon Detector Dark Matter Results from the Final Exposure of CDMS II ». In : *Phys. Rev. Lett.* 111 (2013), p. 251301. DOI : 10.1103/PhysRevLett.111.251301. arXiv : 1304.4279 [hep-ex].

[115] CoGeNT Coll. « CoGeNT : A Search for Low-Mass Dark Matter using p-type Point Contact Germanium Detectors ». In : *Phys. Rev. D* 88 (2013), p. 012002. DOI : 10.1103/PhysRevD.88.012002. arXiv : 1208.5737 [astro-ph.CO].

[116] DAMA/LIBRA Coll. « Final model independent result of DAMA/LIBRA-phase1 ». In : *Eur. Phys. J. C* 73 (2013), p. 2648. DOI : 10.1140/epjc/s10052-013-2648-7. arXiv : 1308.5109 [astro-ph.GA].

[117] Ciaran A. J. O'Hare. « New Definition of the Neutrino Floor for Direct Dark Matter Searches ». In : *Phys. Rev. Lett.* 127 (2021), p. 251802. DOI : 10.1103/PhysRevLett.127.251802. arXiv : 2109.03116 [hep-ph].

[118] DarkSide Coll. « Sensitivity projections for a dual-phase argon TPC optimized for light dark matter searches through the ionization channel ». In : *Phys. Rev. D* 107 (2023), p. 112006. DOI : 10.1103/PhysRevD.107.112006. arXiv : 2209.01177 [physics.ins-det].

[119] XENON Coll. « Search for Light Dark Matter Interactions Enhanced by the Migdal Effect or Bremsstrahlung in XENON1T ». In : *Phys. Rev. Lett.* 123 (2019), p. 241803. DOI : 10.1103/PhysRevLett.123.241803. arXiv : 1907.12771 [hep-ex].

[120] LZ Coll. « Search for new physics in low-energy electron recoils from the first LZ exposure ». In : *Phys. Rev. D* 108 (2023), p. 072006. DOI : 10.1103/PhysRevD.108.072006. arXiv : 2307.15753 [hep-ex].

[121] E. Holzschuh et al. « Search for heavy neutrinos in the beta spectrum of Ni-63 ». In : *Phys. Lett. B* 451 (1999), p. 247-255. DOI : 10.1016/S0370-2693(99)00200-2.

[122] SENSEI Coll. « SENSEI : Direct-Detection Results on sub-GeV Dark Matter from a New Skipper-CCD ». In : *Phys. Rev. Lett.* 125 (2020), p. 171802. DOI : 10.1103/PhysRevLett.125.171802. arXiv : 2004.11378 [astro-ph.CO].

[123] PandaX-II Coll. « Search for Light Dark Matter-Electron Scatterings in the PandaX-II Experiment ». In : *Phys. Rev. Lett.* 126 (2021), p. 211803. DOI : 10.1103/PhysRevLett.126.211803. arXiv : 2101.07479 [hep-ex].

[124] Rouven Essig, Tomer Volansky et Tien-Tien Yu. « New Constraints and Prospects for sub-GeV Dark Matter Scattering off Electrons in Xenon ». In : *Phys. Rev. D* 96 (2017), p. 043017. DOI : 10.1103/PhysRevD.96.043017. arXiv : 1703.00910 [hep-ph].

[125] XENON Coll. « Emission of single and few electrons in XENON1T and limits on light dark matter ». In : *Phys. Rev. D* 106 (2022), p. 022001. DOI : 10.1103/PhysRevD.106.022001. arXiv : 2112.12116 [hep-ex].

[126] DAMIC-M Coll. « First Constraints from DAMIC-M on Sub-GeV Dark-Matter Particles Interacting with Electrons ». In : *Phys. Rev. Lett.* 130 (2023), p. 171003. DOI : 10.1103/PhysRevLett.130.171003. arXiv : 2302.02372 [hep-ex].

[127] SENSEI Coll. « SENSEI : First Direct-Detection Results on sub-GeV Dark Matter from SENSEI at SNOLAB ». In : *Preprint* (déc. 2023). arXiv : 2312.13342 [astro-ph.CO].

[128] J. L. Mortara et al. « Evidence against a 17-keV neutrino from S-35 beta decay ». In : *Phys. Rev. Lett.* 70 (1993), p. 394-397. DOI : 10.1103/PhysRevLett.70.394.

[129] Stefan SCHONERT et al. « Experimental limits for heavy neutrino admixture deduced from Lu-177 beta decay and constraints on the life time of a radiative neutrino decay mode ». In : *Nucl. Phys. B Proc. Suppl.* 48 (1996). Sous la dir. d'A. MORALES, J. MORALES et J. A. VILLAR, p. 201-203. DOI : 10.1016/0920-5632(96)00238-1.

[130] Changbo FU et al. « Limits on Axion Couplings from the First 80 Days of Data of the PandaX-II Experiment ». In : *Phys. Rev. Lett.* 119 (2017), p. 181806. DOI : 10.1103/PhysRevLett.119.181806. arXiv : 1707.07921 [hep-ex].

[131] T. ARALIS et al. « Constraints on dark photons and axionlike particles from the SuperCDMS Soudan experiment ». In : *Phys. Rev. D* 101 (2020). [Erratum : Phys.Rev.D 103, 039901 (2021)], p. 052008. DOI : 10.1103/PhysRevD.101.052008. arXiv : 1911.11905 [hep-ex].

[132] Haipeng AN et al. « Direct Detection Constraints on Dark Photon Dark Matter ». In : *Phys. Lett. B* 747 (2015), p. 331-338. DOI : 10.1016/j.physletb.2015.06.018. arXiv : 1412.8378 [hep-ph].

[133] E. APRILE et al. « Excess electronic recoil events in XENON1T ». In : *Phys. Rev. D* 102 (2020), p. 072004. DOI : 10.1103/PhysRevD.102.072004. arXiv : 2006.09721 [hep-ex].

[134] E. APRILE et al. « Search for New Physics in Electronic Recoil Data from XENONnT ». In : *Phys. Rev. Lett.* 129 (2022), p. 161805. DOI : 10.1103/PhysRevLett.129.161805. arXiv : 2207.11330 [hep-ex].

[135] Nicolás VIAUX et al. « Neutrino and axion bounds from the globular cluster M5 (NGC 5904) ». In : *Phys. Rev. Lett.* 111 (2013), p. 231301. DOI : 10.1103/PhysRevLett.111.231301. arXiv : 1311.1669 [astro-ph.SR].

[136] Ricardo Z. FERREIRA, M. C. David MARSH et Eike MÜLLER. « Do Direct Detection Experiments Constrain Axionlike Particles Coupled to Electrons ? » In : *Phys. Rev. Lett.* 128 (2022), p. 221302. DOI : 10.1103/PhysRevLett.128.221302. arXiv : 2202.08858 [hep-ph].

[137] Haipeng AN, Maxim POSPELOV et Josef PRADLER. « New stellar constraints on dark photons ». In : *Phys. Lett. B* 725 (2013), p. 190-195. DOI : 10.1016/j.physletb.2013.07.008. arXiv : 1302.3884 [hep-ph].

[138] Rouven ESSIG et al. « Direct Detection of sub-GeV Dark Matter with Semiconductor Targets ». In : *JHEP* 05 (2016), p. 046. DOI : 10.1007/JHEP05(2016)046. arXiv : 1509.01598 [hep-ph].

[139] Katherine FREESE, Mariangela LISANTI et Christopher SAVAGE. « Annual Modulation of Dark Matter : A Review ». In : 85 (1er nov. 2013), p. 1561-1581. ISSN : 0034-6861, 1539-0756. DOI : 10.1103/RevModPhys.85.1561. arXiv : 1209.3339[astro-ph,physics:hep-ph].

[140] 2020. URL : https://gaia-mission.cnes.fr/fr.

[141] J. Lavalle et S. Magni. « Making sense of the local Galactic escape speed estimates in direct dark matter searches ». In : *Phys. Rev. D* 91 (2015), p. 023510. doi : 10.1103/PhysRevD.91.023510. arXiv : 1411.1325 [astro-ph.CO].

[142] F. Iocco et al. « Dark Matter distribution in the Milky Way : microlensing and dynamical constraints ». In : *JCAP* 11 (2011), p. 029. doi : 10.1088/1475-7516/2011/11/029. arXiv : 1107.5810 [astro-ph.GA].

[143] Y. Wu et al. « Uncertainties in Direct Dark Matter Detection in Light of Gaia's Escape Velocity Measurements ». In : *JCAP* 10 (2019), p. 034. doi : 10.1088/1475-7516/2019/10/034. arXiv : 1904.04781 [hep-ph].

[144] Gaia Coll. « Gaia Data Release 2 : *Summary of the contents and survey properties* ». In : *Astron. Astrophys.* 616 (2018), A1. doi : 10.1051/0004-6361/201833051. arXiv : 1804.09365 [astro-ph.GA].

[145] Gaia Coll. « Gaia Early Data Release 3 ». In : *Astron. Astrophys.* 650 (2021), p. C3. doi : 10.1051/0004-6361/202039657e. arXiv : 2012.01533 [astro-ph].

[146] J. Bovy. « A purely acceleration-based measurement of the fundamental Galactic parameters ». 2021. arXiv : 2012.02169 [astro-ph.GA].

[147] Stefano Magni. « Astrophysical aspects of dark matter direct detection ». These de doctorat. Montpellier, 13 nov. 2015.

[148] Til Piffl et al. « The RAVE survey : the Galactic escape speed and the mass of the Milky Way ». In : *Astron. Astrophys.* 562 (2014), A91. doi : 10.1051/0004-6361/201322531. arXiv : 1309.4293 [astro-ph.GA].

[149] Constantino Tsallis. « Possible Generalization of Boltzmann-Gibbs Statistics ». In : *J. Statist. Phys.* 52 (1988), p. 479-487. doi : 10.1007/BF01016429.

[150] F. S. Ling et al. « Dark Matter Direct Detection Signals inferred from a Cosmological N-body Simulation with Baryons ». In : *JCAP* 02 (2010), p. 012. doi : 10.1088/1475-7516/2010/02/012. arXiv : 0909.2028 [astro-ph.GA].

[151] J. Diemand et al. « Clumps and streams in the local dark matter distribution ». In : *Nature* 454 (2008), p. 735-738. doi : 10.1038/nature07153. arXiv : 0805.1244 [astro-ph].

[152] Volker Springel et al. « The Aquarius Project : the subhalos of galactic halos ». In : *Mon. Not. Roy. Astron. Soc.* 391 (2008), p. 1685-1711. doi : 10.1111/j.1365-2966.2008.14066.x. arXiv : 0809.0898 [astro-ph].

[153] Mark Vogelsberger et al. « The fine-grained phase-space structure of Cold Dark Matter halos ». In : *Mon. Not. Roy. Astron. Soc.* 385 (2008), p. 236. doi : 10.1111/j.1365-2966.2007.12746.x. arXiv : 0711.1105 [astro-ph].

[154] Amina Helmi, Simon D. M. White et Volker Springel. « The Phase-space structure of cold dark-matter halos : Insights into the galactic halo ». In : *Mon. Not. Roy. Astron. Soc.* 339 (2003), p. 834. doi : 10.1046/j.1365-8711.2003.06227.x. arXiv : astro-ph/0208041.

[155] Luis Arturo Nunez de Villavicencio Castine. « From cosmological simulations to dark matter detection : baryonic physics and spiral galaxy formation : dark matter distribution features : detection of dark matter toward the Sun with the ANTARES neutrino telescope ». These de doctorat. Aix-Marseille, 12 déc. 2019.

[156] Pol Mollitor, Emmanuel Nezri et Romain Teyssier. « Baryonic and dark matter distribution in cosmological simulations of spiral galaxies ». In : *Mon. Not. Roy. Astron. Soc.* 447 (2015), p. 1353-1369. DOI : 10.1093/mnras/stu2466. arXiv : 1405.4318 [astro-ph.GA].

[157] PICASSO Coll. « Final Results of the PICASSO Dark Matter Search Experiment ». In : *Astropart. Phys.* 90 (2017), p. 85-92. DOI : 10.1016/j.astropartphys.2017.02.005. arXiv : 1611.01499 [hep-ex].

Appendices

A. The simulation of the DS20k calibration : additional content

A.1. Meeting DAQ requirements and calibration procedure

In section 3.2.2, the time needed to perform the calibration corresponds to a certain statistics of events in the TPC. For the ER case especially, two possibilities were considered depending on the available time to perform the ER calibration : either the calibration shifter waits until the collection of 10,000 pure ER SS events in the TPC , or the shifter waits until the collection of 1,000 pure ER SS with energy in the photoelecric peak of the decaying source. The former option gives ER calibration spectra as presented in Figures 1 and 2. The latter consideration gives ER calibration spectra as shown in Figures 3 and 4, respectively showing the SS energy spectra as seen in the TPC when the source is placed on the side and at the bottom of the TPC, zoomed around the photoelectric peak and in linear y-scale. Considering calibration events in the photoelectric effect energy peak would help the study of the detector energy reconstruction. Finally, waiting for 1,000 SS events with the initial energy of the photon would take one full week for the whole ER calibration run, which is still reasonable.

A.2. Background induced by the calibration pipes in TPC and veto : ArDM stainless steel scenario

Section 3.2.3 presents the fraction of NR and ER background in the TPC induced by the presence of the calibration tubes inside the inner veto. The results of the simulation are presented in the best case scenario, though. In this Appendix, the estimation of the background contamination in the TPC from the calibration pipes are shown. They come from the same set of simulations, yet the weightings consider the ArDM stainless steel case instead of the LZ stainless steel case. Table 1 shows the radiocontaminators measured in ArDM-type stainless steel and their respective neutron yields. In total the ArDM stainless steel contamination is 24 times higher than the one of the LZ stainless steel.
Tables 2 and 3 respectively show the NR and ER background induced in the TPC, per 10 years of data taking. Like in Section 3.2.3, the upper limits in Table 3 come from the null-result obtained in the ER background simulation, simulating 1e7 decays per radiocontaminant.
The same conclusion as LZ stainless steel case is obtained : the NR and ER background induced in the TPC because of the presence of the tubes in the veto is totally negligible compared to the background budget of DS20k of 0.1 events / 10 years of data collection.

A.3. Material activation from neutrons

Neutron activation of the detector was evaluated with Monte-Carlo simulations for AmC and AmBe neutron sources, already mentioned in Chapter 3. In the calibration history,

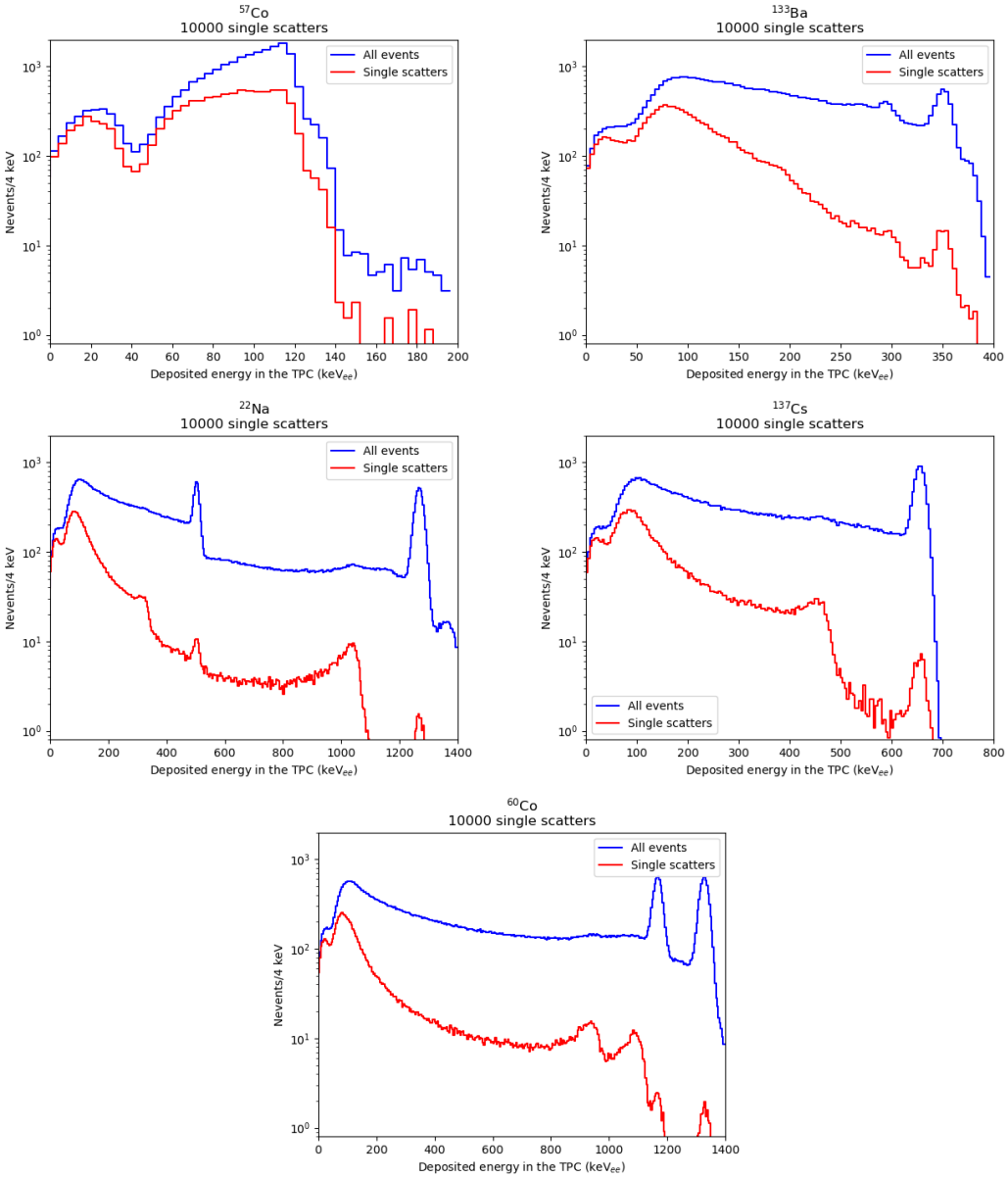

FIGURE 1. : Number of events measured inside the TPC for five sources of photons (placed on the side of the TPC) as a function of the energy deposited in the TPC (keV$_{ee}$). From left to right and top to bottom : ^{57}Co, ^{133}Ba, ^{22}Na, ^{137}Cs, ^{60}Co. The integral of each red curve is 10,000 (these spectra are normalised to 10,000 SS events). The spectra are log-scaled and have a 4 keV$_{ee}$ binning. The expected energy resolution of DS20k is applied.

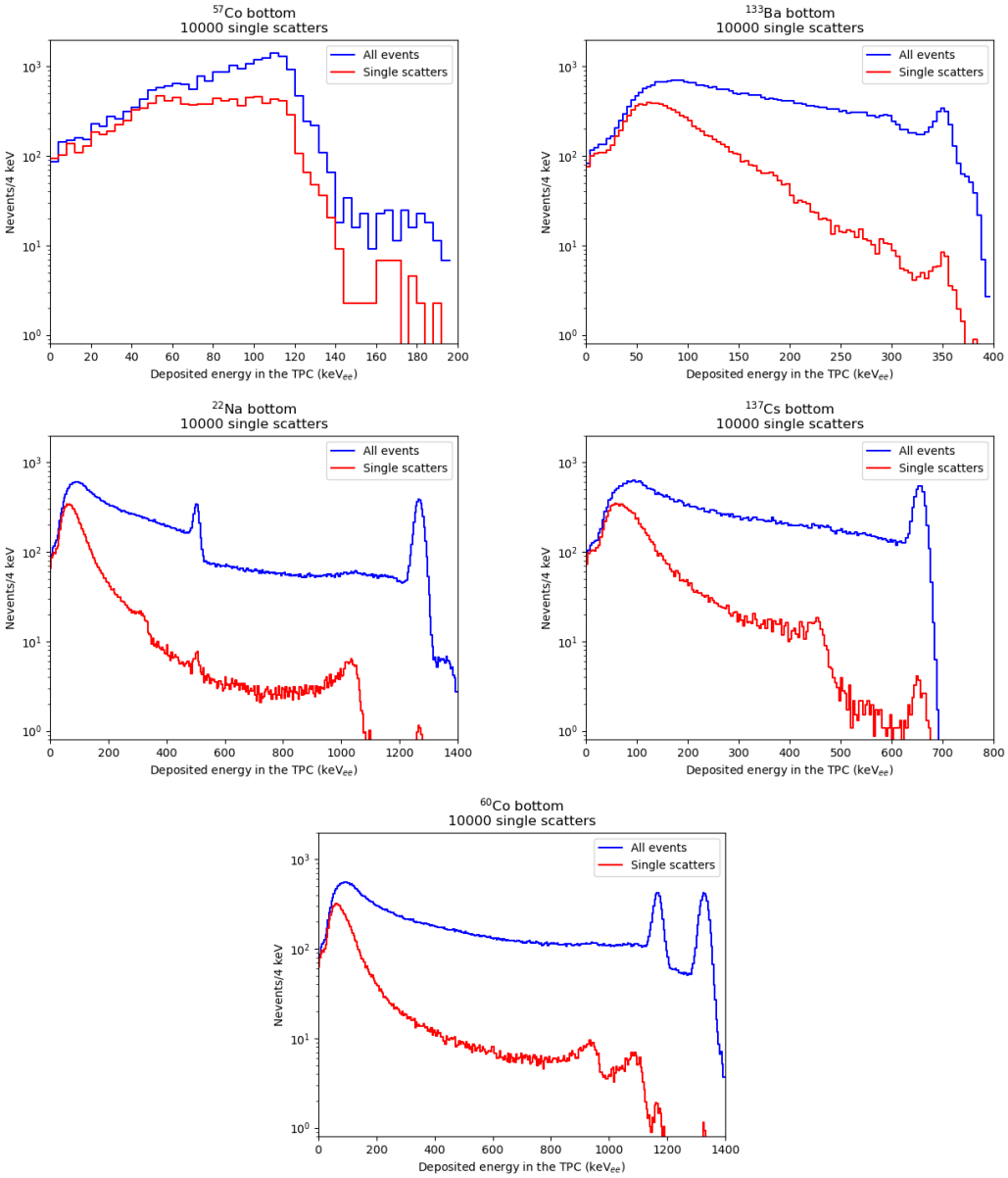

FIGURE 2. : Number of events occurring inside the TPC for five sources of photons (situated at the bottom of the TPC) as a function of the energy deposited in the TPC (keV$_{ee}$). From left to right and top to bottom : ^{57}Co, ^{133}Ba, ^{22}Na, ^{137}Cs, ^{60}Co. The integral of each red curve is 10,000 (these spectra are normalised to 10,000 SS events). The spectra are log-scaled and have a 4 keV$_{ee}$ binning. The expected energy resolution of DS20k is applied.

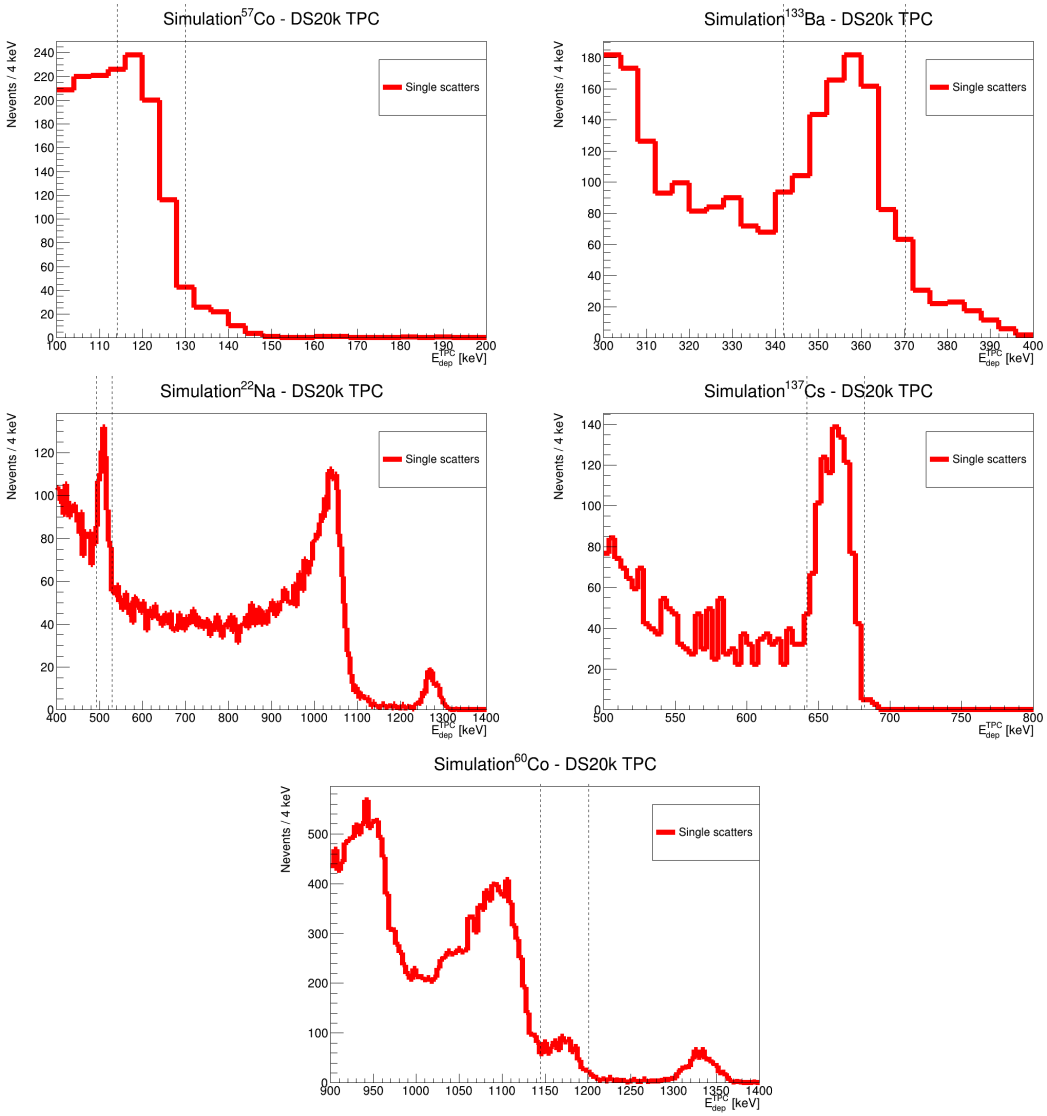

FIGURE 3. : Number of events occurring inside the TPC after exposure of five sources of photons (placed on the side of the TPC) as a function of the energy deposited in the TPC (keV). From left to right and up to down : ^{57}Co, ^{133}Ba, ^{22}Na, ^{137}Cs, ^{60}Co. The spectra are zoomed on the energy peaks, and normalised so that there are 1,000 SS in the peak (peak depicted by the dashed lines). Prospective energy resolution of DS20k is applied.

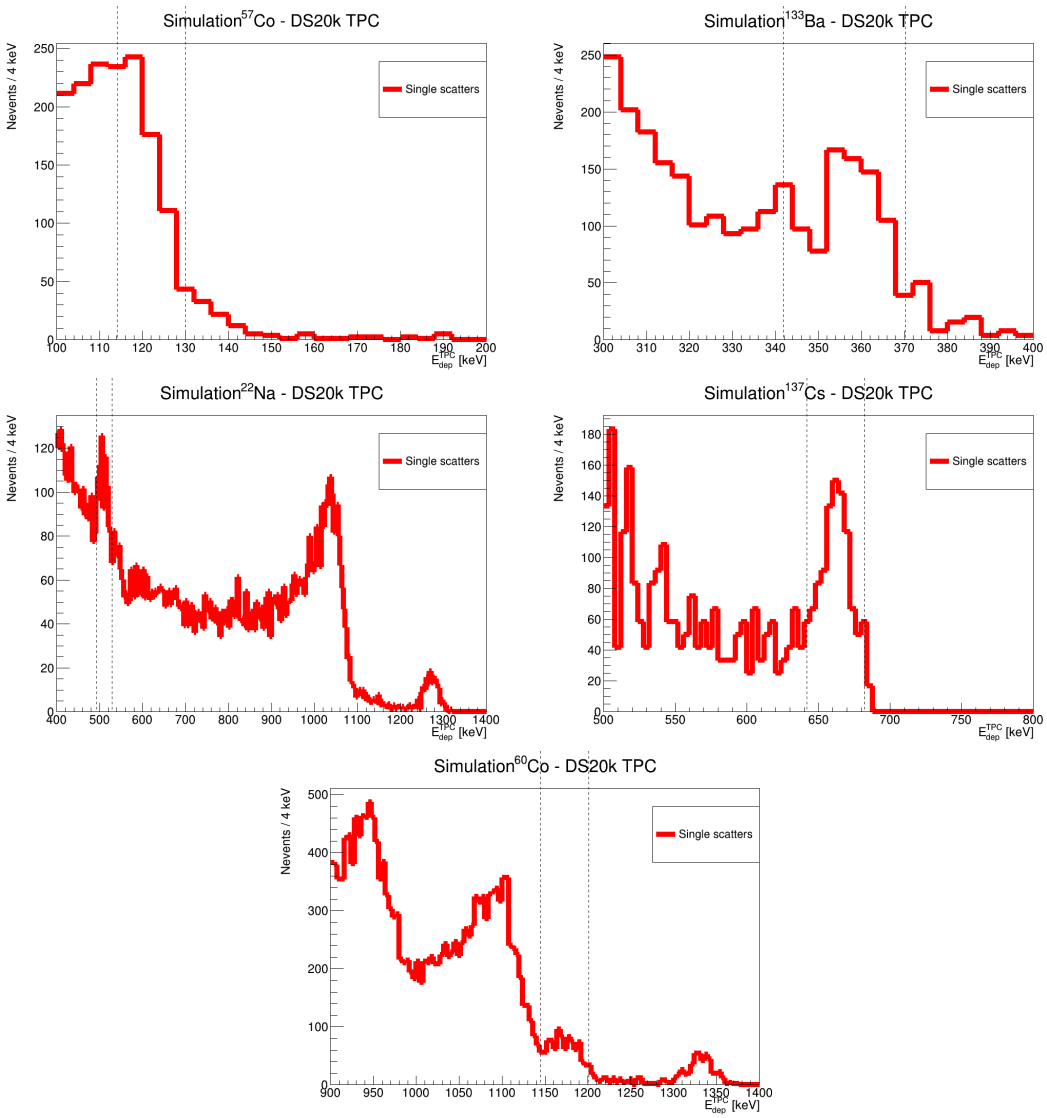

FIGURE 4. : Number of events occurring inside the TPC after exposure of five sources of photons (placed at the bottom of the TPC) as a function of the energy deposited in the TPC (keV). From left to right and up to down : ^{57}Co, ^{133}Ba, ^{22}Na, ^{137}Cs, ^{60}Co. The spectra are zoomed on the energy peaks, and normalised so that there are 1,000 SS in the peak (peak depicted by the dashed lines). Prospective energy resolution of DS20k is applied.

Element	^{238}U Upper	^{238}U Middle	^{238}U Lower	^{232}Th	^{235}U	^{40}K	^{60}Co	^{137}Cs
Contamination (mBq/kg)	50	50	50	20	2.3	6.4	13	1.5
Photon producer ?	Yes	Yes	Yes	Yes	Yes	Yes	Yes	Yes
Neutron producer ?	Yes	Yes	Yes	Yes	Yes	No	No	No
Neutron yield (neutron/decay)	1.1 x 10^{-9}	4.8 x 10^{-7}	1.06 x 10^{-9}	1.8 10^{-6}	3.7 x 10^{-7}	No	No	No

TABLE 1. : For stainless steel, assuming ArDM-type stainless steel : contamination sources inside the tubes and their respective contamination levels (mBq/kg), background production and neutron yield.

Element	^{238}U Upper	^{238}U Middle	^{238}U Lower	^{232}Th	^{235}U
Contamination (mBq/kg)	50	50	50	20	2.3
Neutron yield (neutron/decay)	1.1 x 10^{-9}	4.8 x 10^{-7}	1.06 x 10^{-9}	1.8 10^{-6}	3.7 x 10^{-7}
Events/10years	3.5 x 10^{-7}	1.5 x 10^{-4}	3.5 x 10^{-7}	2.3 x 10^{-4}	5.3 x 10^{-6}

TABLE 2. : NR background rates induced by the radioactive contamination of the stainless steel tubes, assuming ArDM-type stainless steel, after normalisation (which includes the neutron production rate of the three radioactive elements).

Element	^{238}U Upper	^{238}U Middle	^{238}U Lower	^{232}Th	^{235}U	^{40}K	^{60}Co	^{137}Cs
Contamination (mBq/kg)	50	50	50	20	2.3	6.4	13	1.5
Events/10years	< 183	< 183	< 183	< 73	< 8	< 23	< 47	< 5.5

TABLE 3. : ER background rates induced by the radioactive contamination of the stainless steel tubes, assuming ArDM-type stainless steel, after normalisation.

the so-call DD-generator (for Deuteron-Deuteron generator) of monochromatic neutrons was also considered (neutrons of 2.45 MeV). Some of the activated isotopes de-excite quickly and result in prompt gammas. On the contrary, some others have long lifetimes and might present experimental background. The most important component is the activation of argon, as isotopes would decay directly in the target volume and such events cannot be fiducialised. Note that this study has been done using a previous version of the detector veto geometry, but the same TPC argon volume. Conclusions should hence remain similar.

Three activated isotopes of argon were identified : ^{37}Ar, ^{39}Ar and ^{41}Ar, having respectively 35.04 days, 269 years and 109.34 minutes of half-life. The production rates for ^{37}Ar and ^{39}Ar are well below μBq/kg level (respectively 10^{-7} and 10^{-12} Bq/kg), hence are negligible and do not present any danger for the experimental goals. Neutron capture on ^{40}Ar results in prompt gammas with a total energy of 6.1 MeV, concurrent with the transition to ^{41}Ar isotope, which is radioactive and undergoes β-decay with a Q-value of $\sim$2.5 MeV. It is produced in the target volume during neutron calibration at the rate of 0.28 mBq/kg. Similar activities are expected from ^{39}Ar (0.73$\pm$0.11 mBq/kg) and ^{85}Kr (0.020$\pm$0.001 mBq/kg), however given the relatively short half-life of ^{41}Ar of 1.83 hours, most of the activated target atoms will decay within a day after the calibration run.

B. DarkSide-20k sensitivity prospects to light dark matter particles : additional plots

Chapter 4 compares the sensitivity projection of DarkSide-20k to low mass WIMPs to the research results of other experiments. However, other experiments using different technologies are foreseen to be constructed in the coming years. With Figure 5, the present appendix compares the WIMP sensitivity projections of these experiments to the one of DarkSide-20k after one year of data collection, assuming binomial quenching fluctuations for the NR response model.

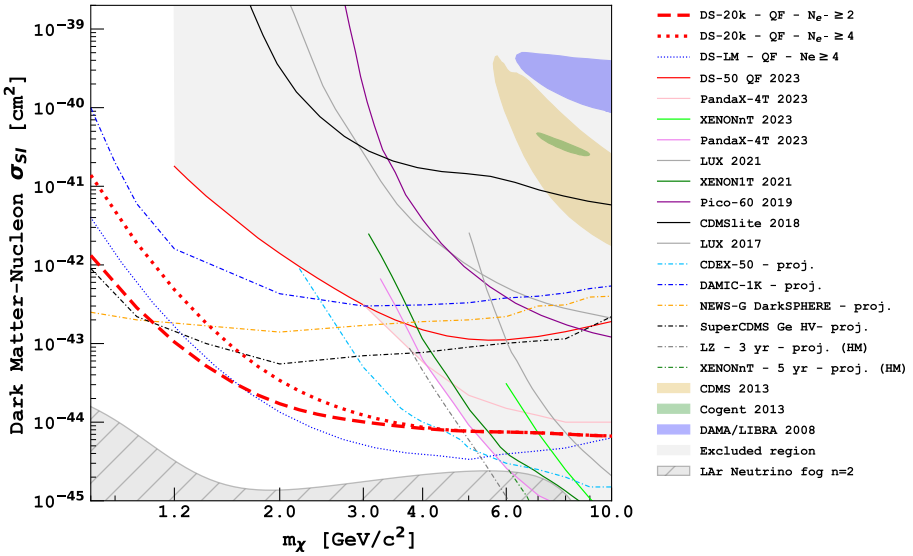

FIGURE 5. : Overview of published (full lines) and expected (dashed lines) 90% C.L. limits for spin-independent WIMP NR. DS20k expected limits are presented with bold dashed red lines (fit in the [2, 170] N_{e^-} range) and bold dotted lines (fit in the [4, 170] N_{e^-} range), assuming QF scenario. Limits set by DS50 are shown with full red lines [56]. Best published limits of xenon TPC experiments (PandaX [106, 104], Xenon [105, 119], LUX [110, 111]) and LZ [83]/Xenon-nT [84] high-mass prospects are shown. Prospects of the DS-LM experiment are shown in dotted blue lines in the top plot [118]. Results and/or prospects of experiments sensitive in the low-mass regime but using different technologies (CDMSLite [112], SuperCDMS [58], CRESST-III [32], PICO [113], PICASSO [157], DAMIC [108, 60], CDEX [107], NEWS-G [61]) are also shown. Past claimed discoveries [114, 115, 116] are shown as coloured contours. The neutrino fog for LAr experiments with index $n = 2$ [117] is shown in striped grey.

C. Analytical velocity distributions beyond the SHM

The present appendix proposes to consider other motivated dark matter halo velocity distributions, such as the Tsallis [149] and the Generalised Maxwellian [150] velocity distributions. These two distributions take usual input parameters such as $|\overrightarrow{v}|$, v_{esc}, v_c, v_0, ρ_0 but also specific parameters whose value are estimated from fits of N-body cosmological simulations of galaxy formations in the Universe (see Section 5.3.2).

A Tsallis distribution is a distribution with form :

$$f_{gal}^{Tsallis}(\overrightarrow{v}) = \frac{1}{N_{esc}(q)} \left(1 - \frac{\overrightarrow{v}^2}{v_0^2}\right)^{\frac{q}{1-q}} \quad \text{if } |\overrightarrow{v}| < v_{esc}, \tag{.1}$$

with $N_{esc}(q)$ the norm of $x \mapsto \left(1 - \frac{\vec{x}^2}{v_0^2}\right)^{q/1-q}$. It takes one additional parameter compared with the SHM : the q parameter. The Tsallis distribution is bell-shaped, the q-parameter guides the width of the distribution as shown in Figure 6 left [1]. The larger the q, the wider the distribution. The SHM is retrieved at limit q $\to$ 1. The " $f_{gal}(v) = 0$ if $v < v_{esc}$ " requirement is kept in Figure 6 left, but there is a relationship between v_0, v_{esc} and the q parameter :

$$q = 1 - \frac{v_0^2}{v_{esc}^2} \tag{.2}$$

Thus fixing a certain value for the q-parameter forces the value of v_{esc}.

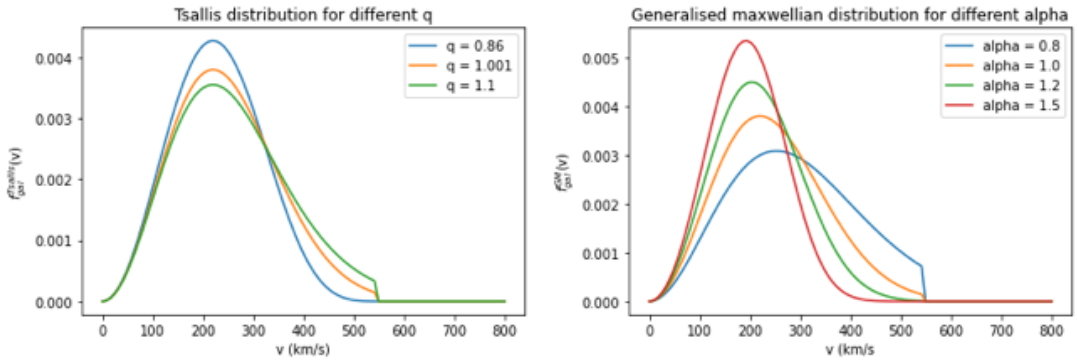

FIGURE 6. : Left : A Tsallis distribution with different values for its q-parameters. Right : A generalised maxwellian distribution with different values for the α-parameter. In both plots, the v_0 parameter is taken as 220 km/s, and v_{esc} as 544 km/s.

The generalised Maxwellian distribution has the form :

[1] For historical reasons, in the present Appendix, the nominal value of v_0 and v_c is set to the former recommendation, i.e. v_0 = 220 km/s and v_c = 220 km/s.

$$f_{gal}^{GM}(\overrightarrow{v}) = \frac{1}{N_{esc}(\alpha)} e^{-\left(\frac{\overrightarrow{v}^2}{v_0^2}\right)^{\alpha}} \quad \text{if } |\overrightarrow{v}| \text{ ,} < v_{esc} \tag{.3}$$

with $N_{esc}(\alpha)$ the norm of $x \mapsto e^{-\left(\frac{\vec{x}^2}{v_0^2}\right)^{\alpha}}$. It is a bell-shaped distribution as well, the α parameter playing with the width of the distribution. The shape of a generalised Maxwellian distribution with different values for the α parameter is shown in Figure 6 right. The SHM is retrieved when $\alpha = 1$.

The values of the q and α parameters are derived from fits of N-body cosmological simulations. It has been done in Ref. [155] using Halo B, and the result is used in the present thesis : q = 0.864 and $\alpha = 1.232$.
Eq. (.1) and (.3) give the shape of the dark matter halo VPDF in the galactic frame, but in the purpose of assessing the sensitivity of terrestrial experiments, one needs to perform the change of frame following Eq. (1.26), and compute the associated event rate. The WIMP velocity distribution in the galaxy expected with a Tsallis (resp. generalised Maxwellian) with parameter q = 0.864 (resp. $\alpha = 1.232$) is shown in Figure 7 left (resp. Figure 7 right). In the same plot, the velocity distribution is plotted in the lab frame.

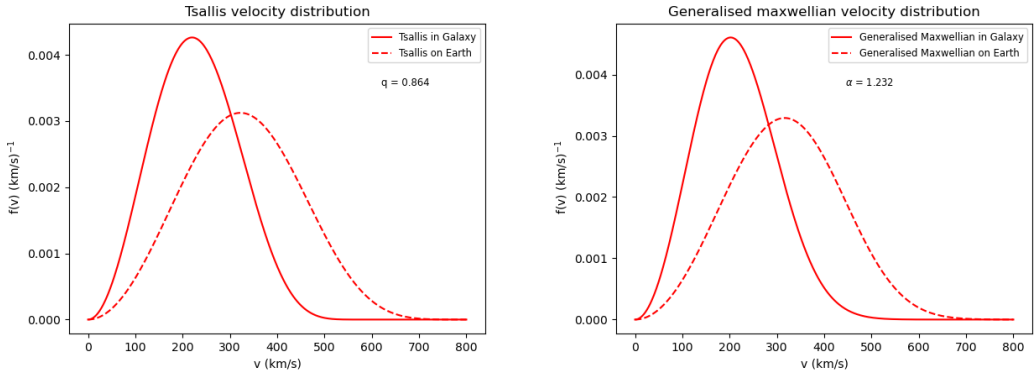

FIGURE 7. : Left : A Tsallis velocity distribution with best-fit parameter q = 0.864 from [155] as seen in the Milky Way frame (full red line) and in the Earth frame (red dashed line). Right : A generalised Maxwellian velocity distribution with best-fit parameter $\alpha = 1.232$ from [155] as seen in the Milky Way frame (full red line) and in the Earth frame (red dashed line).

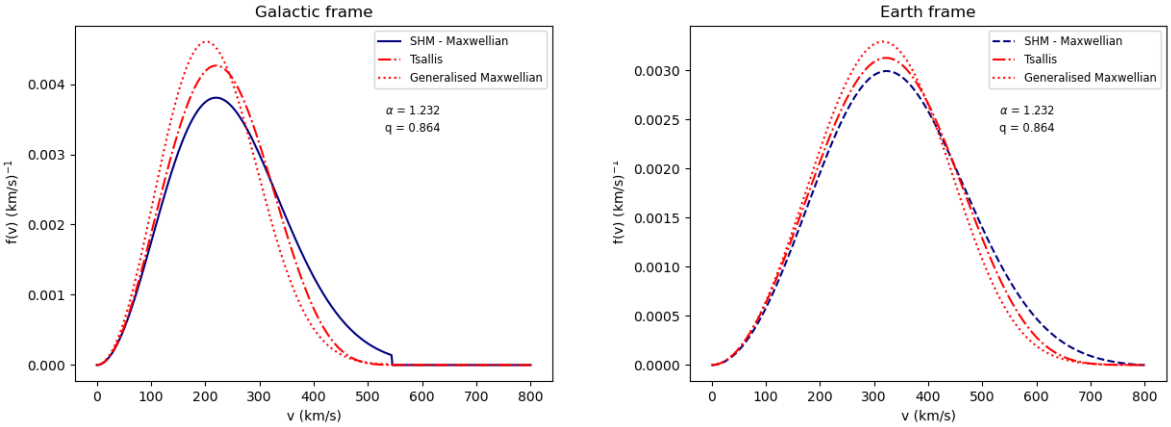

FIGURE 8. : Comparison of a Tsallis velocity distribution (with q = 0.864, red dashed dotted line), a Generalised Maxwellian velocity distribution (with $\alpha = 1.232$, red dotted line) and the regular Maxwellian velocity distribution used in the SHM (blue, full-line in the galactic frame, dashed line in Earth frame). Left : in the galactic frame. Right : in the Earth (lab) frame.

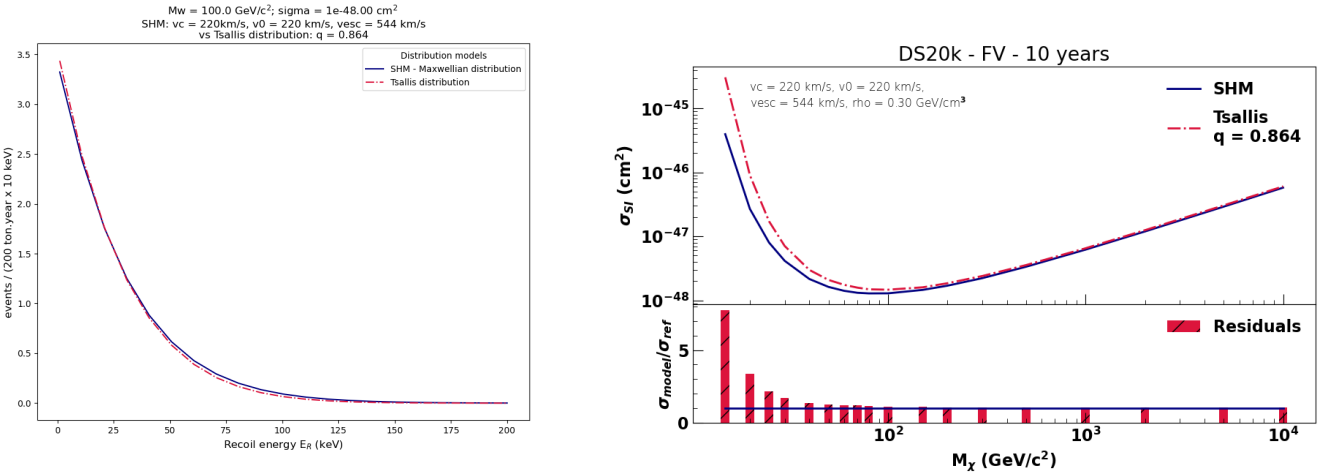

FIGURE 9. : Left : Expected rate of events computed with a Tsallis velocity distribution with parameter q = 0.864. Right : The final exclusion limit with the same distribution. For both plots, the Tsallis case is in red dash-dotted line, compared with SHM in full blue line.

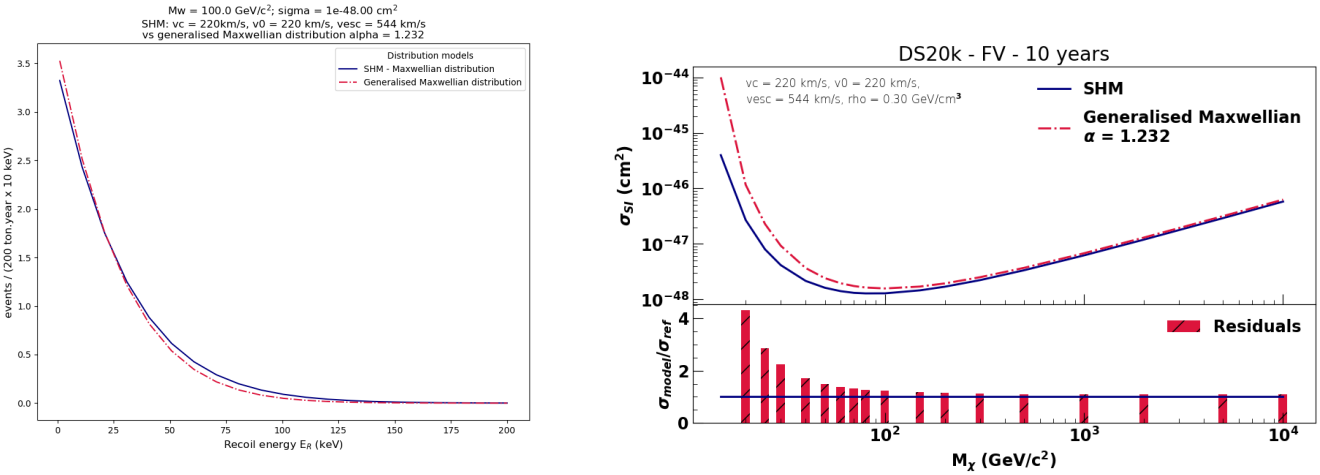

FIGURE 10. : Left : Expected rate of events computed with a generalised Maxwellian velocity distribution with parameter $\alpha = 1.232$. Right : The final exclusion limit with the same distribution. For both plots, the generalised Maxwellian case is in red dash-dotted line, compared with SHM in full blue line.

In order to better compare the three velocity distributions (SHM, Tsallis and generalised Maxwellian), Figure 8 shows the three distributions in the galactic frame (left) and on Earth (right). These distributions show very different behaviour for the three models of velocity distribution, both in the Galaxy frame and in the Earth frame. Indeed, the Tsallis and generalised Maxwellian plots, respectively represented by the red dashed dotted and simply dotted lines, drop out before the SHM (blue lines) : their tails drop naturally down to 0 around 500 km/s. Thus, they naturally respect the $f_{gal}(v > v_{esc}) = 0$ requirement (taking the usual $v_{esc} = 544$ km/s). Of course, as these distributions are PDFs, they are normalised to 1, thus the two new distributions peak upper than the SHM distribution (because they are thinner as they have a depleted velocity tail). The effects of having such different velocity distributions behaviour on the final exclusion limit in the high mass (HM) case can be seen on Figures 9 and 10. The exclusion limits obtained with these two models are more conservative than with the nominal SHM : the ratio-plot of Figure 9 (resp. Figure 10) states that a Tsallis distribution with parameter q = 0.864 (resp. generalised Maxwellian distribution with parameter $\alpha = 1.232$) implies a lower signal at low mass, leading down to 5.1 times (resp. 4.3 times) lower sensitivity than usually stated with the SHM at WIMP masses lower than 100 GeV/c^2. The reason is that the drop of the velocity distributions before v_{esc} implies a lack of events at high speed, which implies this lower rejection power in the low mass range of DS20k exclusion limit. Nonetheless, the effects at high masses are lower than 14 % (resp. 22 %) for the Tsallis (resp. generalised Maxwellian) fit.

Figures 11 (Tsallis distribution) and 12 (generalised Maxwellian distribution) propose to vary independently ρ_0, v_{esc}, v_c and v_0 parameters in the Tsallis and generalised Maxwellian frameworks respectively. To produce these bands, the value of the q and α parameters are kept to $q = 0.864$ and $\alpha = 1.232$. But, the astrophysical parameters are varied as for Figure 5.4 of Chapter 5.

The result is interesting as the SHM is just below the parameters uncertainty band of the exclusion limit computed with a Tsallis and with a generalised Maxwellian distribution. At very low WIMP masses ($m_\chi < 30$ GeV/cm^2), the superposition of both effects (change of model and change of parameters) can lower the rejection power of DS20k between 10 and 20 times the one computed when considering the original SHM. At high WIMP masses, all effects converge and the only parameter influencing the exclusion limit is ρ_0. Again, this is because ρ_0 is a global scale factor needed in the differential rate computation and does not affect the WIMP velocity distribution in a peculiar velocity region.

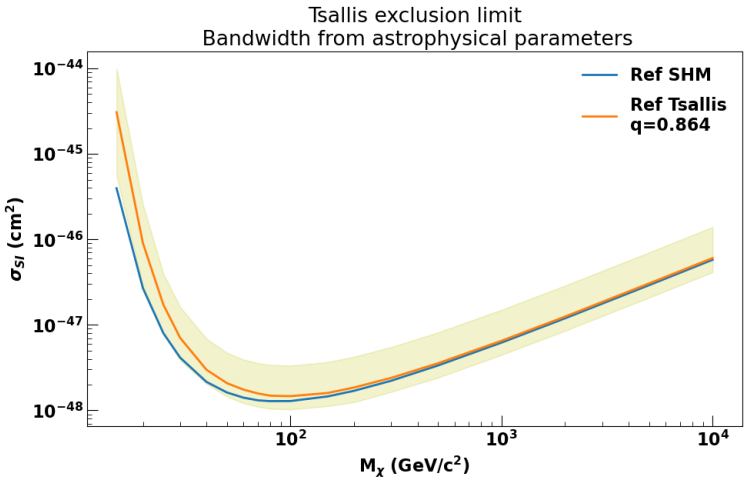

FIGURE 11. : Exclusion limit of DarkSide-20k computed with a Tsallis velocity distribution function as signal model (orange) and its uncertainty band coming from the independent variation of the four astrophysical parameter of interest in the event rate computation. The reference exclusion limit computed with the SHM and the four nominal values of the astrophysical parameters is plotted in blue.

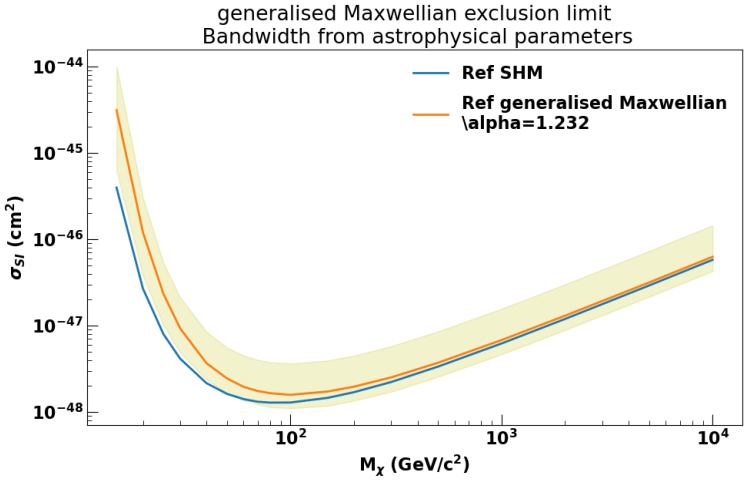

FIGURE 12. : Exclusion limit of DarkSide-20k computed with a generalised Maxwellian velocity distribution function as signal model (orange) and its uncertainty band coming from the independent variation of the four astrophysical parameters of interest in the event rate computation. The reference exclusion limit computed with the SHM and the four nominal values of the astrophysical parameters is plotted in blue.